Neutron and Photon Imaging Capabilities of Bismuth-loaded Plastic

A Dissertation Presented for the
Doctor of Philosophy
Degree
The University of Tennessee, Knoxville

Andrew W. Decker
May 2021

Copyright © 2021 by Andrew W. Decker
All rights reserved.

ACKNOWLEDGEMENTS

I want to thank God for giving me the opportunity to expand my understanding of nuclear engineering at the University of Tennessee, Knoxville, and Oak Ridge National Laboratory (ORNL). I want to thank my wife, Jill, for putting up with me throughout the past three years; I sincerely appreciate her continuous love, support, patience, and encouragement. I also wish to thank my daughters, Ashlyn and Siena, for their love, support, and understanding.

I want to also thank the members of my PhD committee, Drs. Howard Hall, John McClory, and Paul Hausladen for their guidance and support. I thank Howard Hall for his classroom instruction and his encouragement during the qualifying examinations. I thank John McClory for his willingness to potentially support my research at AFIT during a time of limited COVID access at ORNL. A special thank you to Paul Hausladen for his time and effort recording initial neutron measurements in my absence. Later, he enabled me to record my final neutron measurements, guided me through data analysis pitfalls, and developed the methodology used herein to interpolate and subtract image dark noise.

Lastly, I wish to especially thank and acknowledge the support, patience, and guidance extended to me by Dr. Jason Hayward, my committee chair, throughout my coursework and research. It was my pleasure to learn from him, and I am so grateful for all the assistance and mentorship he provided, which contributed immensely to my successful completion of this program.

ABSTRACT

Plastic scintillators utilizing iridium complex fluorophores offer substantial improvements in light yield, and their light yield is not significantly quenched in compositions with bismuth metalorganic loading at 21% weight. These advances may resolve significant capability gaps for low-cost, portable, and durable dual-particle imaging (DPI) systems for nuclear safety, security, and safeguard purposes. However, all candidate materials should first undergo investigation utilizing industry standards to quantify and evaluate their capabilities. As such, a 21% bismuth-loaded polyvinyl toluene (BiPVT) scintillator fabricated by Lawrence Livermore National Laboratory (LLNL) is computationally and experimentally evaluated as a small, pixelated radiographic array, with individual pixel dimensions of 2×2×19 mm. To facilitate direct comparisons, the same evaluations are conducted for two same-sized arrays made from EJ-200 and EJ-256 scintillator, respectively. ASTM standard test methods and practices are utilized to calculate the modulation transfer function and basic spatial resolution for each array, both from measured and simulated data. Measurements are recorded by pressure coupling all three arrays to a commercial a-Si digital radiographic panel, and the computational model replicates the experimental design. Computational and experimental results are compared for all three arrays in the x-ray and fast neutron environments. The x-ray results demonstrate equivalent performance between the evaluated BiPVT array and the more ideally manufactured EJ-200 array, while the BiPVT array outperforms a similar array made from EJ-256. The agreement between simulated and experimental x-ray results validates the applied computational methodology and suggests more ideally manufactured BiPVT arrays may significantly outperform similar arrays made from EJ-200. Experimental results in a fast neutron environment demonstrate superior performance of the BiPVT array compared to the EJ-256 array, while the EJ-200 array is found to outperform both. Additionally, the performance of a second array made from a separate 21% bismuth-loaded plastic (Ir-Bi-Plastic) is evaluated experimentally in both x-ray and neutron environments using the same radiographic panel and methodology. The Ir-Bi-Plastic array consists of 64 pixels with individual dimensions of 5×5×20 mm, and the results suggest it will outperform similar arrays made from EJ-200 in both x-ray and neutron environments. These findings suggest plastic scintillators with iridium complex fluorophores and 21% weight bismuth-loading hold promise over more traditional material alternatives for DPI applications supporting nuclear safety, security, and safeguard missions.

TABLE OF CONTENTS

Chapter One - Background 1
Introduction 1
Scintillator Materials for Radiation Imaging 2
Inorganic Scintillators 2
Organic Scintillators 3
Photon Interactions 4
Neutron Interactions 5
Chapter Two - Literature Review 7
Scintillation Photophysics and Kinematics 7
Pulse Shape Discrimination Kinematics 9
Novel Organic Scintillator Materials 12
Organometallic Scintillators 12
Nanocomposite Organics 19
Modern Radiation Imaging Techniques 20
Radiography 20
Scatter-based Imaging 22
Coded Aperture Imaging 23
Summary and Outlook 24
Chapter Three - Novel Contributions 26
Chapter Four - Preliminary Performance and Material Evaluation 28
Analytic Material Evaluation 28
Motivation 28
Analytic Calculations 28
Effective Atomic Number 29
Computational Material Evaluation 37
Motivation and Description of Work 37
Theory 37
Methodology 38
Results 41
Conclusions 52
Initial Radiographic Characterization of a BiPVT Array 52
Simulations 52
Results 58
Discussion 61
Conclusions 64
Investigation of Internal X-ray Scatter within BiPVT and EJ-200 64
Simulations 64
Results 66
Discussion 68
Chapter Five - Experiment Design Analysis and Considerations 70
Array Fabrication 70
Pixel Dimensions 70

Fabrication Process 70
BiPVT Light Collection Degradation 74
Radiation Sources 78
X-ray Source 78
Neutron Source 80
Panel Noise Discussion and Study 92
Statistical Noise 92
Thermal Noise 93
Dark Noise 93
Chapter Six - Material Analyses 105
Stopping Power and Proton Range 105
Stopping Power Theory 105
Collisional Stopping Power 107
Components of Collisional Stopping Power 108
Simulation Methodology 109
Results 112
Conclusions 123
Analyses of Expected Photon and Neutron Interactions 124
X-rays 124
D-T Neutrons 132
Proton Pixel Crosstalk Study 145
Simulations 145
Results 149
Conclusions 149
Chapter Seven - Image Analysis Theory and Application 151
Composite Image Production and Edge Response Measurement 151
Modulation Transfer Function and Spatial Resolution 153
Detector Signal-to-Noise Ratios Normalized 157
Factors Affecting Spatial Resolution 160
Inherent Unsharpness 160
Geometric Unsharpness 161
Chapter Eight - X-ray Radiography Characterization using a Bismuth-loaded Polyvinyl Toluene Array 166
Abstract 166
Introduction 166
Theory 167
Experiment and Simulation Methodology 172
Analysis and Results 178
Discussion 186
Conclusions 186
Acknowledgment 187
Chapter Nine - Simulated X-ray Radiographic Performance of a Bismuth-loaded PVT Array 188
Abstract 188

Introduction 188
Theory 190
Experiment and Simulation Methodology 192
Analysis and Results 199
Discussion 209
Conclusion 209
Acknowledgement 212
Chapter Ten - Fast Neutron Radiographc Performance of a Small Bismuth-loaded PVT Array 213
Abstract 213
Introduction 213
Theory 216
Experiment and Simulation Methodology 222
Analysis and Results 230
Discussion 242
Conclusion 242
Acknowledgement 244
Chapter Eleven - Characterization of a Novel Plastic Array in Both X-ray and Fast Neutron Environments 245
Abstract 245
Theory 245
Experiment Methodology 252
Analysis and Results 255
Discussion and Conclusion 267
Acknowledgement 268
Chapter Twelve - Conclusions and Recommendations for Future Work 269
Conclusions 269
X-Ray Environment 269
Neutron Environment 270
Ir-Bi-Plastic Array Evaluation 270
Recommendations for Future Work 270
Works Cited 272
Vita 280

LIST OF TABLES

Table 4.1. Calculated atomic percentages and other relevant material values for BiPVT, EJ-200, and EJ-256. 30
Table 4.2. Calculated material values for BiPVT, EJ-200, and EJ-256 31
Table 4.3. Calculated weight percentages and *Z*-values for BiPVT, EJ-200, EJ-256, and water. 33
Table 4.4. Calculated energy-dependent Z_{eff} values for BiPVT, EJ-200, EJ-256, and water 36
Table 4.5. List of specific material densities used in both analytic calculations and MCNP computations. 39
Table 4.6. List of element weight percentages used in both analytic calculations and MCNP computations. 40
Table 4.7. Simulated Basic Spatial Resolution (SRb) values for BiPVT and EJ-200 in x-ray fields (top) and the 14 MeV neutron field (bottom), as well as associated uncertainties. 62
Table 5.1. Simulated average energy deposition (MeV) within the three array pixels using a D-T neutron source, both from proton recoil events and photon interactions due to photoluminescence in the lead plate. 91
Table 5.2. Measured count rates from the Varex 1515DXT-I (shown graphically in Figure 5.14) panel following an offset calibration as panel temperature (unmeasured) increased. 97
Table 6.1. Mean excitation potential, I, values for specific elements in units of eV [46] 110
Table 6.2. Mean excitation potential, I, values for compounds in units of eV 111
Table 6.3. Simulated (MCNP) and calculated (Analytic) energy-dependent proton ranges (cm) for each material examined. 119
Table 6.4. Calculated energy-dependent stopping powers, *S*, for each material examined. 122
Table 6.5. For each material, the fraction of pixel cross-section wherein a 7 MeV proton scattered directly toward a pixel edge is expected to fully attenuate and deposit light within the pixel. These values are provided for various pixel cross sectional areas (cm^2) and demonstrate the importance of proton recoil range within small pixel arrays. 125
Table 6.6. Average energy (MeV) deposited per incident photon within each pixel, as estimated by MCNP6 simulations. 127
Table 6.7. Average predicted energy (MeV) deposited per pixel for each material of interest during each 0.5 sec measurement. 128
Table 6.8. Reported light yields (ph/MeV) for BiPVT, EJ-256, and EJ-200 [9, 37, 36]. 129
Table 6.9. Estimated average number of photons emitted within each 2×2 mm pixel per measurement. 130

Table 6.10. Estimated average number of photons detected within each 2×2 mm pixel per measurement. 131
Table 6.11. Calculated macroscopic cross sections and probabilities for 14.064 MeV (n,p) elastic scatter interaction within 1.9 cm of material. 134
Table 6.12. Expected rate of (n,p) reactions from incident 14.064 MeV neutrons 135
Table 6.13. Expected average number of photons detected within each pixel per 150s measurement, assuming 100% localization of energy deposition and including QE. 137
Table 6.14. Analytically derived 2-D probabilities for full energy deposition and localization of 7 MeV recoil protons for pixels within a 2×2 mm pixel for each material of interest. 143
Table 6.15. Analytically derived probabilities for full energy deposition and localization of 7 MeV recoil protons for pixels within a 2×2×19 mm pixel for each material of interest. 144
Table 6.16. Analytically derived probabilities for full energy deposition and localization of 7 MeV recoil protons for pixels within a 2×2×19 mm pixel for each material of interest. 146
Table 6.17. Expected rate of photon production within each pixel per measurement, considering the analytic probabilities of proton scatter for each material and 2×2 mm pixel in 3D space. 147
Table 6.18. Computationally derived estimates for the fraction of proton energy deposition within the center pixel of a 3×3-pixel array when exposed to 14.1 MeV. This is analogous to the analytic estimates performed above for the probability for full energy deposition and localization of 7 MeV recoil protons for pixels within a 2×2×19 mm pixel for each material of interest. 150
Table 8.1. Mean 2×2 mm pixel intensity and standard deviation measured for each array in the free-field (FF), as well as the SNRs calculated from those values. 179
Table 8.2. Experimentally and computationally determined values of SR for both material arrays, as well as the associated uncertainties. 183
Table 8.3. Experimentally and computationally determined values of dSNRn for both material arrays, as well as the associated uncertainties. 184
Table 9.1. Average 2×2 mm pixel intensity and standard deviation measured for each array when fully shielded by the 6.35 mm steel phantom. 200
Table 9.2. Average 2×2 mm pixel intensity and standard deviation measured for each array when fully shielded by the 6.35 mm steel phantom. 201
Table 9.3. Experimentally and computationally determined Nyquist values and spatial resolution (SR) for all three material arrays, as well as the associated standard deviation. 206
Table 9.4. Comparative ratios of average pixel intensity for the EJ-256 and EJ-200 arrays in the free-field and shielded environments (6.35 mm of steel). 210

Table 9.5. Computational ratios of average pixel intensities for BiPVT vs. EJ-200 and EJ-256 at 150, 270, and 370 kV, both in the free-field and a fully shielded environment (6.35 mm of steel). 211
Table 10.1. Experimentally and computationally determined $f_{10\%}$ and spatial resolution (SR) values for all three material arrays evaluated in a 370 kVp x-ray field, as well as the associated errors. 217
Table 10.2. Average 2×2 mm pixel intensity, standard deviation, and SNR measured for each array during five-second exposures in the free-field (FF). 231
Table 10.3. Average 2×2 mm pixel intensity, standard deviation, and SNR measured for each array during five-second exposures when fully shielded by the 5.08 cm tungsten phantom. 233
Table 10.4. Experimentally and computationally determined $f_{10\%}$ frequencies and spatial resolution (SR) values for all three material arrays, as well as the associated uncertainty. 239
Table 10.5. Comparative SNR, SR, and dSNRn values for all three arrays calculated from measured values of $f_{10\%}$ from the MTF and using Eq. 6. .. 243
Table 11.1. Experimentally measured average pixel intensities, standard deviations, and calculated SNR for the Ir-Bi-Plastic when exposed to the considered x-ray bremsstrahlung spectra. 257
Table 11.2. Experimentally measured average pixel intensities, standard deviations, and calculated SNR for the Ir-Bi-Plastic when exposed to 14.1 MeV neutrons at a SDD of 12.5 cm. 260
Table 11.3. Experimentally measured values of SR for the Ir-Bi-Plastic in both the 14.1 MeV neutron and 370 kVp x-ray environments. 265
Table 11.4. Experimentally measured values of dSNRn for the Ir-Bi-Plastic for both 14.1 MeV neutron and 370 kVp x-ray environments. 266

LIST OF FIGURES

Figure 2.1. Energy levels of organic molecules [22]. 8
Figure 2.2. Diagram of particle kinetic energy transfer from polymer matrix to wavelength shifting dye and reemission of lower energy fluorescent photon [9]. 10
Figure 2.3. Representation of comparable peak intensities from different particles due to the effects of ion quenching and delayed fluorescence [9]. 11
Figure 2.4. Normalized pulse heights from different particles, which demonstrate varied peak-to-tail ratios due to differing fractional contributions from delayed fluorescence [9]. 13
Figure 2.5. Display of multiple plastic scintillator tail-to-total ratios [8]. 14
Figure 2.6. Chemical structure of iridium complexes [10]. 16
Figure 2.7. Comparison of radioluminescence between standard plastic fluors (blue) and triplet-harvesting Iridium complex fluors (green) [9]. 17
Figure 2.8. ^{137}Cs pulse height spectrum obtained with a 50 cm^3 sample of Bi-loaded PVT at LLNL [9]. 18
Figure 4.1. Plot of the energy-dependent Z_{eff} values for BiPVT, EJ-200, EJ-256, and water..... 35
Figure 4.2. A graphic of the idealized spherical MCNP model used to evaluate various thicknesses, t, of material for both photon and neutron sensitivity. A F2 (surface flux tally) was utilized to assess the percentage of particle flux penetrating the material within the specific incident energy region of interest. 42
Figure 4.3. Photon interaction probability within CsI at thicknesses of 200 and 400 µm and energies between 200 keV and 2 MeV 43
Figure 4.4. Photon interaction probability within Gadox at thicknesses of 200 and 400 µm and energies between 200 keV and 2 MeV 44
Figure 4.5. Photon interaction probability within 2.54 cm and 5.08 cm thick 21% BiPVT at energies between 200 keV and 2 MeV. 46
Figure 4.6. Photon interaction rates derived both analytically and computationally (MCNP6.2) for 400 µm of CsI. 47
Figure 4.7. Photon interaction rates derived both analytically and computationally (MCNP6.2) for 400 µm of Gadox. 48
Figure 4.8. Photon interaction rates derived both analytically and computationally (MCNP6.2) for 2.54 and 5.08 cm of 21% BiPVT. 49
Figure 4.9. Photon interaction rates derived computationally via MCNP6.2 for 1.27 to 5.08 cm of 21% BiPVT..... 50
Figure 4.10. The energy-dependent interaction rates calculated from MCNP6.2 estimates of surface flux tallies and neutron counts. 51
Figure 4.11. Neutron interaction rates derived analytically via Equation 15 for 1.27 to 5.08 cm of 21% Bi-loaded PVT. 53

Figure 4.12. Neutron interaction rates derived computationally via MCNP6.2 for 1.27 to 5.08 cm of 21% BiPVT. 54
Figure 4.13. Images of duplex wire sets, where a version provided in ASTM E2002 is on the left [48], and the image on the right represents the MCNP6.2 model of tungsten duplex wires in green, polyethylene in yellow, and air in pink. This served as the IQI for all BiPVT and EJ-200 photon image computations. ... 56
Figure 4.14. An image of the IQI used for 14 MeV neutron measurements, where yellow represents either polyethylene or lead, and the MTF and SRb values are determined from contrast fluctuations computed using decreasing gap widths between the shielding material, which are consistent with established duplex wire IQI diameters. 57
Figure 4.15. Comparison of the MCNP6.2-generated BiPVT and EJ-200 radiographs of the duplex wire IQI when exposed to 150 kVp x-rays at an array thickness of 10 mm. The BiPVT image is on the left, while the EJ-200 image is on the right. All axes refer to pixel number within the arrays..... 59
Figure 4.16. Comparison of the MCNP6.2-generated BiPVT and EJ-200 radiographs of the lead slab IQI when exposed to 14 MeV neutrons at an array thickness of 15 mm. The BiPVT image is on the left, while the EJ-200 image is on the right. All image axes refer to pixel number within the array. 60
Figure 4.17. Comparison of the MCNP6.2-generated BiPVT and EJ-200 MTFs measured from duplex wire IQI radiographs, where x-ray energy is a) 150 keV, b) 270 keV, and c) 370 keV x-rays. The BiPVT MTF plots are on the left, and the EJ-200 MTF plots are on the right. 63
Figure 4.18. Conceptual image of the simulated array design used to estimate pixel crosstalk in BiPVT and EJ-200 for 150, 270, and 370 kVp x-ray fields. For each material and energy region the array was simulated at thicknesses of 10, 15, 20, or 25 mm, commensurate with the energies and thicknesses used in the duplex wire evaluations of SRb. 65
Figure 4.19. Plot of estimated pixel energy crosstalk to adjacent pixels as a fraction of total energy deposited in the central pixel. 67
Figure 5.1. BiPVT source sample (6.85×19×21 mm) provided by LLNL. 72
Figure 5.2. Images of the a) individual BiPVT pixels, adhesed to ESR using a UV-cured optically clear adhesive prior to trimming, and b) final BiPVT 4×3-pixel array face, which is placed in contact with the Varex radiographic panel. ... 73
Figure 5.3. Images of EJ-200 a) cut, polished, and stacked into uniform plates (prior to the orthogonal cut creating the pixel stacks), and b) the final EJ-200 4×3-pixel array face, which contacts the Varex radiographic panel. 75
Figure 5.4. Images of the a) BiPVT, b) EJ-200, and c) EJ-256 finished arrays mounted on a 2.5 mm tall plate of polycarbonate plastic to prevent movement between measurements. 76
Figure 5.5. Images of the a) EJ-256, b) EJ-200, and c) BiPVT arrays within the aluminum light-tight enclosure, which is affixed to the sides of a Varex PaxScan 1515DXT-I Flat Panel Detector. 77

Figure 5.6. Images of the BiPVT array, including a) a “clouding” effect within the pixels due to alumina polishing, and b) after the clouding had largely dissipated. Image ‘b)’ also shows some small residual occlusions, although their contributions, as well as the degradation in ESR reflectivity, were impossible to quantify prior to experimental evaluation. 79
Figure 5.7. Image of the Comet MXR-451/26. This RGD contains a bipolar oil-cooled x-ray tube with a tungsten anode and 5mm of beryllium beam shielding. It is designed specifically for NDA. 81
Figure 5.8. Image of the bremsstrahlung x-ray spectrum emitted by the Comet MXR-451/26 when operated at 450 kVp. 82
Figure 5.9. Simulated source spectrum for the MXR-451/26 RGD at 370 kVp. .. 83
Figure 5.10. Top-down image of the ING-27 neutron generator, as well as the relative location of the pixelated alpha detector (top), which enables accurate calculations of neutron production and directionality (bottom) from measured alpha interaction rates and localities. 85
Figure 5.11. Simulated neutron source location relative to the Varex panel, plastic arrays, concrete floor, aluminum generator housing, and lead x-ray shield. 87
Figure 5.12. Simulated D-T neutron-induced photoluminescence spectra emitted from the 6.35 mm lead x-ray shield and present within two volumes of air per 150 second exposure. These spectra were measured within two different air volumes with different materials present in the simulations to account for their specific contributions to the spectra. 88
Figure 5.13. Simulated air volumes (A and B) used to predict relative photon fluence due to source 14.064 MeV neutron interactions within the lead x-ray shield. The purpose was to estimate material-specific energy depositions from these photoemissions within each of the plastic arrays and compare those values to expected neutron energy depositions. 89
Figure 5.14. Plot of measured dark noise within the Varex 1515DXT-I panel over time as temperature increased. 95
Figure 5.15. Plot of measured dark noise within the Varex 1515DXT-I panel over time as temperature increased. Offset calibrations were utilized between Measurements A, B, and C using the ViVa software package from Varian. 98
Figure 5.16. Image of measured dark noise within the Varex 1515DXT-I panel over time as temperature increased. The image reveals a count rate bias toward the upper right quadrant of the panel. 99
Figure 5.17. Image of measured dark noise within the Varex 1515DXT-I panel over time as temperature increased. The image reveals a count rate bias toward the upper right quadrant of the panel. 100
Figure 5.18. Image of the back of the Varex 1515DXT-I panel, with the quadrants from Figure 5.17 superimposed to show relative location. This analysis fully explains the source of thermal influence which affects dark noise across the Varex panel in a nonuniform manner. 101
Figure 6.1. Conceptual diagram of the MCNP6 simulation methodology used to estimate energy-dependent proton range for the three scintillator materials.

The diagram also illustrates the relative proton populations estimated within each layer of attenuating material, with the largest population present in the layer furthest from the source. In the methodology, the centroid of the furthest layer containing protons was used to estimate the maximum proton range at that energy. 113
Figure 6.2. Estimated proton range values within liquid water for energies 1.0-14.1 MeV as reported by NIST [46], as well as the MCNP6 simulations and analytic calculations described herein for water. 114
Figure 6.3. Estimated proton range values within PVT for energies 1.0-14.1 MeV as reported by NIST [46], as well as the MCNP6 simulations and analytic calculations described herein for EJ-200. 115
Figure 6.4. Estimated energy-dependent proton range within BiPVT derived both via MCNP simulation and analytically. 117
Figure 6.5. Estimated energy-dependent proton range within EJ-256 derived both via MCNP simulation and analytically. 118
Figure 6.6. Comparative estimates of energy-dependent proton range within BiPVT, EJ-256, and EJ-200 derived via analytic methods. 120
Figure 6.7. Comparative estimates of energy-dependent total proton stopping power, *S*, within BiPVT, EJ-256, and EJ-200 derived via analytic methods. 121
Figure 6.8. Image depicting a pixel edge and the values necessary for calculating the probability of proton energy deposition within the pixel based on *R*, *d*, and *θ*. 139
Figure 6.9. Plot of expected probabilities for a 7 MeV proton to deposit all kinetic energy locally within a 2×2mm pixel of EJ-200, EJ-256, or BiPVT, based on the distance of interaction from the pixel center (0 mm) to pixel edge (1 mm). 140
Figure 6.10. Expected probabilities for 7 MeV protons to deposit kinetic energy locally based on distance from a pixel edge within a 2×2mm pixel of EJ-200 in 2-D space. This graph represents one quarter of a pixel in 2-D, which is representative of the whole due to symmetry. 141
Figure 6.11. Expected probabilities for 7 MeV protons to deposit energy locally within a 2×2 mm pixel of EJ-200 based on distance from a pixel edge and corner in 3-D space. This graph represents one quarter of a pixel, which is representative of the whole due to symmetry. 142
Figure 6.12. Depiction of the simulated methodology with incident 14.1 MeV neutrons striking the central pixel of each 3×3-pixel array. However, the pixel dimensions shown here are not representative; each material was evaluated as an array with individual pixel dimensions of 2×2×19 mm. 148
Figure 7.1. Image of initial, 4×45-pixel, composite images for a) BiPVT and b) EJ-200 measured in the 370 kVp x-ray environment. 152
Figure 7.2. This image explains the systematic process of expanding a 4×45-pixel composite image into a 23×45-pixel composite image. Specifically, the red box highlights the original 4×45-pixel image, while the arrows, dashed boxes,

and colors serve to illustrate what portions of the original image, at least for the 370 kVp x-ray measurements, are replicated to maintain the edge response. Additionally, fully shielded and fully unshielded portions are replicated to conserve the edge and broaden the image. 154
Figure 7.3. From left to right, example of a composite 23×45-pixel image imported into ImageJ. Next, the image is rotated until the IQI edge is vertical. Lastly, this enables a measurement of edge response within the highlighted ROI (yellow), which is applied consistently across all three arrays. 155
Figure 7.4. Expected Example plot of normalized edge response function (ERF) and line spread function (LSF). 156
Figure 7.5. Example modulation transfer function (MTF), including the 10% cut-off threshold ($f_{10\%}$) which determines the value of spatial resolution (SR). In the case of this example, the MTF reaches 10% at a spatial frequency of 3.4 lp/mm, which equates to a hypothetical DDA SR value of 0.147 mm. 158
Figure 7.6. Example chart for efficiency test with difference images at different energy levels [53]. 159
Figure 7.7. ASTM technique to calculate and quantify internal scatter radiation within a DDA [53]. 162
Figure 7.8. Two different source term sizes used in a hypothetical imaging system. The image demonstrates how SR is worsened when the source of radiation is larger [74]. 163
Figure 7.9. Image demonstrating the relationship between the three components of geometric unsharpness (U_g) and how their relative values affect spatial resolution. Adapted from [74]. 165
Figure 8.1. Expected Example plot of normalized edge response function (ERF) and line spread function (LSF). 169
Figure 8.2. Example modulation transfer function (MTF), including the 10% cut-off threshold which determines the value of spatial resolution (SR). In the case of this example, the MTF reaches 10% at a spatial frequency ($f_{10\%}$) of 3.4 lp/mm, which equates to a hypothetical DDA SR value of 0.147 mm. 170
Figure 8.3. Images of a) the BiPVT source sample (6.85 × 19 × 21 mm) provided by LLNL, b) the individual BiPVT pixels, adhered to ESR, prior to trimming, and c) the final BiPVT 4×3-pixel array face, which is placed in contact with the Varex radiographic panel. 173
Figure 8.4. Image of the BiPVT (green) and EJ-200 (clear) 4×3-pixel arrays affixed to the acrylic plastic. 175
Figure 8.5. Example image of one shielded MCNP6 simulation, which includes the EJ-200 (pink) and BiPVT (blue) pixel arrays, as well as the steel step wedge phantom (brown) in one of the 15 positions, relative to the arrays. The acrylic plastic layer (light blue) and ESR material (yellow) are also shown. 177
Figure 8.6. Images of the expanded a) BiPVT and b) EJ-200 23×45-pixel composite matrices. The expansion of the original 4×45-pixel composite image utilized repeating patterns at specific distances from the phantom edge to construct the expanded image response. 181

Figure 8.7. Images of the expanded a) BiPVT and b) EJ-200 23×45-pixel composite images. 182
Figure 8.8. Plot of the experimental and computational MTFs for the a) BiPVT and b) EJ-200 composite images. Expanded sections demonstrate where the MTFs cross the 10% cutoff frequency ($f_{10\%}$) for spatial resolution determination based on ASTM standards for CT system performance evaluations [67]. . 185
Figure 9.1. Example plot of normalized edge response function (ERF) and line spread function (LSF). 191
Figure 9.2. Example modulation transfer function (MTF). Values of spatial resolution (SR) are measured for the DDA at a 10% cut-off of the MTF. In the case of this example, the MTF reaches 10% at a spatial frequency of 3.4 lp/mm, which means the hypothetical DDA provides a SR of 0.294 mm. .. 193
Figure 9.3. Image of the 4×3-pixel a) EJ-200 and b) EJ-256 arrays affixed to the acrylic plastic. Each 2×2×19 mm pixel is wrapped on five sides by ESR to maximize photoluminescent light collection by the photodetector. 195
Figure 9.4. Plot of the measured BiPVT transmissivity and emissivity spectra. These data were analyzed and input into OpticStudio to facilitate simulation of the primary emission, reabsorption, reemission, and transmissivity of optical light within the BiPVT plastic. 198
Figure 9.5. Measured composite 4×45-pixel images of a 6.35 mm-thick steel phantom edge for a) EJ-256 and b) EJ-200. These images were constructed from 15 separate measurements at varying degrees of array shielding, with the phantom edge offset from the pixel alignment at a 5˚ angle. 202
Figure 9.6. Images of the expanded a) EJ-256 and b) EJ-200 23×45-pixel composite matrices. Expansion of the original 4×45-pixel composite images, shown in Figure 9.5, utilized repeating patterns at specific distances from the phantom edge, which was necessary to facilitate calculations of the steel phantom ERF for each array. 203
Figure 9.7. Simulated composite 4×45-pixel images of the 6.35 mm-thick steel phantom steel edge for a) EJ-256, b) EJ-200, and c) BiPVT. These images were assembled from 15 separate combined simulations of both MCNP6 and OpticStudio, each with varying degrees of array shielding, with the phantom edge offset at a 5˚ angle from the pixel alignment. 205
Figure 9.8. Images of the expanded a) EJ-256, b) EJ-200, and c) BiPVT 23×45-pixel composite images, computed from MCNP6 and OpticStudio. 207
Figure 9.9. Plot of the experimental and computational MTFs for the a) EJ-256 and b) EJ-200 composite images, as well as the simulated MTF for c) BiPVT. Expanded sections highlight where the MTFs cross the 10% cutoff threshold for spatial resolution (SR) determination in ASTM standards for CT system performance evaluations [67]. 208
Figure 10.1 Example plots of normalized edge response function (ERF) and line spread function (LSF). 219
Figure 10.2 Example modulation transfer function (MTF). Values of spatial resolution (SR) are measured for the DDA at a 10% cut-off of the MTF($f_{10\%}$).

In this example, the MTF reaches $f_{10\%}$ at a spatial frequency of 3.4 lp/mm, which means the hypothetical DDA provides a SR of 0.147 mm..... 220
Figure 10.3 Images of a) BiPVT source sample (6.85×19×21 mm) provided by LLNL, b) individual BiPVT pixels, adhered to ESR, prior to trimming, and c) the final BiPVT 4×3-pixel array face, which pressure-mounted to the Varex radiographic panel. 223
Figure 10.4 Image of the BiPVT (left), EJ-200 (center), and EJ-256 (right) 4×3-pixel arrays affixed to acrylic plastic. 225
Figure 10.5 Plot of the measured BiPVT transmissivity and emissivity spectra. These data were analyzed and input into OpticStudio to facilitate simulation of the primary emission, reabsorption, reemission, and transmissivity of optical light within the BiPVT plastic. 229
Figure 10.6 Measured composite 4×45-pixel images of a 5.08 cm-thick tungsten phantom edge for a) EJ-200 b) BiPVT and c) EJ-256. These images were constructed from 15 separate measurements at varying degrees of array shielding, with the phantom edge offset from the pixel alignment at a 5˚ angle. Pixel intensity normalization occurred for a total of three fully shielded measurements (two for BiPVT and one for EJ-256), as reflected in the final composite 4×45-pixel images for d) EJ-200 e) BiPVT and f) EJ-256..... 234
Figure 10.7 Images of the expanded a) EJ-200, b) BiPVT, and c) EJ-256 20×45-pixel composite matrices. Expansion of the final 4×45-pixel composite images, shown in Figure 10.6 (d-f), utilized repeating patterns at specific distances from the phantom edge, which was necessary to facilitate calculations of the tungsten phantom ERF for each array. 235
Figure 10.8 Simulated composite 4×45-pixel images of the 5.08 cm-thick tungsten phantom edge for a) EJ-200, b) BiPVT, and c) EJ-256. These images were assembled from 15 separate combined simulations of both MCNP6 and OpticStudio, each with varying degrees of array shielding, with the phantom edge offset at a 5˚ angle from the pixel alignment. 237
Figure 10.9 Images of the expanded a) EJ-200, b) BiPVT, and c) EJ-256 20×45-pixel composite images, computed from MCNP6 and OpticStudio. These are created from the original 4×45-pixel composite images, shown in Figure 10.8, using repeating patterns at specific distances from the phantom edge. 238
Figure 10.10 Plot of the experimental and computational MTFs for the a) EJ-200, b) BiPVT, and c) EJ-256 composite images. Expanded sections highlight where the MTFs cross the $f_{10\%}$ cutoff threshold for spatial resolution (SR) determination in ASTM standards for CT system performance evaluations [67]. 240
Figure 11.1. Example plots of normalized edge response function (ERF) and line spread function (LSF). 247
Figure 11.2 Example modulation transfer function (MTF). Values of spatial resolution (SR) are measured for the DDA at a 10% cut-off of the MTF ($f_{10\%}$). In this example, the MTF reaches $f_{10\%}$ at a spatial frequency of 3.4 lp/mm, which means the hypothetical DDA provides a SR of 0.147 mm..... 248

Figure 11.3 Images of the 8×8-pixel evaluated Ir-Bi-Plastic array. The segmented side is shown on the left prior to external Teflon tape wrapping. The image on the right shows the uncut face after external wrapping, which was placed in contact with the a-Si TFT array. 251
Figure 11.4 Measured composite 8×40-pixel images of a 0.635 cm-thick steel phantom edge using the 8×8-pixel Ir-Bi-Plastic array in a 370 kVp x-ray field. This image was constructed from five separate measurements at varying degrees of array shielding, with the phantom edge offset from the pixel alignment at a 5˚ angle. 258
Figure 11.5 Image of the expanded 24×40-pixel composite image of the 0.635 cm-thick steel phantom edge using the 8×8-pixel Ir-Bi-Plastic array in a 370 kVp x-ray field. Expansion of the original 8×40-pixel composite image, shown in Figure 11.4, utilized repeating patterns at specific distances from the phantom edge, which was necessary to facilitate calculations of the steel phantom ERF. 259
Figure 11.6 Measured composite 8×40-pixel images of a 5.08 cm-thick tungsten phantom edge using the 8×8-pixel Ir-Bi-Plastic array in a 14.1 MeV neutron field. This image was constructed from five separate measurements at varying degrees of array shielding, with the phantom edge offset from the pixel alignment at a 5˚ angle. 261
Figure 11.7 Image of the expanded 24×40-pixel composite image of the 5.08 cm-thick tungsten phantom edge using the 8×8-pixel Ir-Bi-Plastic array in a 14.1 MeV neutron field. Expansion of the original 8×40-pixel composite image, shown in Figure 11.6, utilized repeating patterns at specific distances from the phantom edge, which was necessary to facilitate calculations of the tungsten phantom ERF. 263
Figure 11.8 Plot of the experimental MTFs measured for 14.1 MeV neutron environment using a 5.08 cm-thick tungsten block and the 370 kVp x-ray field using a 0.635 cm-thick stell plate. Included with these MTFs is the $f_{10\%}$ cutoff frequency used for determinations of spatial resolution (SR) according to ASTM standards for CT system performance evaluations [67]. 264

CHAPTER ONE -
BACKGROUND

Introduction

The accurate detection, localization, and identification of radioactive material is vital to current and future nuclear safety, security, and safeguarding efforts. From a safety standpoint, radioactive materials are employed ubiquitously for benign purposes across several fields, including nuclear research, medicine, and power generation. Consequently, the use of such materials necessitates care and safety to ensure health risks are minimized for both radiation workers and the general public. For example, spent nuclear reactor fuel must be removed, stored, and monitored, and in cases of radioactive contamination, sources of radioactivity must be reliably located and removed. In terms of security, all produced special nuclear material (SNM) must be controlled, measured, and monitored in perpetuity to ensure proper custody. As such, identification of illicit SNM production and acquisition routes is vital to nuclear security, and transport of SNM often offers crucial opportunities for detection. Similarly, the persistent threat posed by use of a radiological dispersion device (RDD) or an improvised nuclear device (IND) necessitates a technological capability to detect, locate, and identify radioactive materials and SNM, despite the presence of significant shielding.

Due to the range of plausible safety and security challenges, the optimal technological part of the solution includes a range of radiation imaging systems with dual-particle imaging (DPI) capabilities, which means they must reliably detect and discriminate between incident neutrons and high-energy photons. Particle discrimination offers important information that a single form of radiation detection cannot provide alone [1, 2, 3, 4, 5, 6, 7]. DPI systems should also offer an attractive combination of ruggedness, portability, relatively low cost, and high detection efficiency. Fortunately, research and development into novel materials to enhance radiation imaging is of widespread interest. Most notably, recent advances in organic scintillators provide some of the most exciting prospects for expanding the practical utility and versatility of DPI systems. Specifically, novel plastic scintillators offer improved light yield, detection efficiency, and pulse shape discrimination (PSD) properties [8, 9, 10, 11, 12]. These advancements, especially when paired with the well-known advantages of plastics, such as low cost and high durability, suggest that substantial improvements to the field of portable radiation imaging, and specifically DPI, may now be attainable. Only inorganic scintillators offer comparable price, performance, and utility when compared to organic materials [13]. As such, the advantages, drawbacks, and recent advancements

related to inorganic scintillators receive some treatment herein. Of course, other alternative detection technologies for imaging exist, such as gas detectors and semiconductors; however, these detectors are excluded from this work due to their comparably high cost, complexity, and difficulty operating outside controlled laboratory conditions.

Scintillator Materials for Radiation Imaging

A scintillator refers to any material that efficiently absorbs incident particle kinetic energy and then reemits that energy as lower energy photons, typically in the visible or ultraviolet range. These reemitted photons provide detectable and measurable signals when paired with photodetectors. As such, ideal scintillators offer fast decay times, linear light yields, and a high energy conversion efficiency. These materials must also support practical detector sizes and shapes, remain transparent to reemitted photon wavelengths, and efficiently couple to photomultiplier tubes or other light sensors.

Inorganic Scintillators

Supporting a wide range of detection systems and research activities, inorganic scintillators represent a large portion of the annual detection market, with ~$350M of the market share in 2015 [13]. Despite significant research investment into the discovery of novel inorganic scintillators over the past twenty years, the most ubiquitous forms today remain NaI(Tl), CsI(Tl), LaBr3, and Lu2SiO5(Ce). Fundamentally, inorganic scintillators are high-Z crystalline lattice or ceramic structures with trace activators to increase light yield, which is defined as

$$Light\ Yield = \frac{\text{Number of scintillation photons}}{\text{MeV of particle energy deposited}}. \quad (1)$$

When compared to organics, inorganic scintillators typically offer superior light yield (~40,000 ph/MeV), linearity, and photon interaction rates; however, they are often hygroscopic and quite fragile, which limits the practicality of inorganic scintillators for some measurements outside controlled environments. Recent improvements to inorganics expanded their forms beyond just single crystals, glasses, and ceramics; they are now also manufactured as fibers, eutectics, and thin films [13]. Yet, despite these novel designs, a significant number of capability gaps may remain, including improved energy resolution, fast timing, performance scaling, and pulse shape discrimination, especially when considered at sizes practical for portable radiography. While many small inorganics offer excellent performance at small sizes, significant funding would be required to scale select crystals to larger sizes necessary for portable radiography, as well as to enable large scale production while maintaining performance uniformity.

Improved energy resolution is a consistent requirement for a variety of nuclear security missions, such as direct search, detection, and identification of nuclear materials. As such, gamma ray energy resolution of ~2% at 662 keV is desired for isotope identification and achievable with extremely small crystals; however, novel inorganics offering that resolution suffer from challenging synthesis, poor performance consistency, and prohibitive production costs. Additionally, inorganics provide extremely poor intrinsic efficiency for fast neutron detection, which means they are incapable of identifying a key signature of plutonium and other neutron-emitting SNM [13, 14].

In general, modern inorganic scintillators can also suffer from relatively slow signal decay times, which is a well-established shortcoming in traditional inorganics. Fast timing is currently sought in multiple fields, including high energy physics (HEP), medical imaging, and even homeland security. The requirement for a <1.0 ns (and, in some cases, <100ps) response time is necessary to prevent signal pile-up, as well as to improve the measured signal-to-noise (SNR) ratio for time of flight (TOF) analysis [13]. Despite focused research on the development of ultrafast inorganics to meet these needs, novel materials, such as LSO:Ce an LYSO:Ce, still remain too slow. Additionally, the few ultrafast inorganics with <1.0 ns response, such as ZnO and BaF2, offer less light output than comparable organic scintillators [13]. Therefore, despite the existence of specific inorganics that excel in some fast-timing applications, this benefit is typically counterbalanced by drawbacks in other areas.

The final challenge facing inorganic scintillators is performance scaling with size, and no substantial improvements have been made in this area in recent decades. Only a select few inorganic scintillators are still easily grown and reproduced in sizes greater than two inches while also maintaining excellent performance, so that challenge remains constant [13].

Organic Scintillators

In contrast to the high-Z lattice structure of inorganics, organic scintillators consist of low-Z hydrogen and hydrocarbon molecules, which convert incident particle energy to lower wavelength photons via bio-molecular electron transitions. Due to these properties, organic scintillators are typically less expensive, offer faster decay times (ns), and can provide n,γ discrimination [4, 7, 15, 16]. Two drawbacks to most organic materials are a low intrinsic efficiency to PE absorption, which scales as $\sim Z_{eff}^4$, and poor light yield (of order 10,000 ph/MeV) compared to inorganics [17]. The high hydrogen concentrations of organic scintillators make them efficient and portable for fast neutron detection, since a larger fraction of incident neutron kinetic energy is transferrable per interaction to hydrogen nuclei [4, 7, 10, 18]. Also, due to their molecular nature, the fluorescence mechanism is independent of the physical state of the material, so organic scintillators can be manufactured and employed for radiation detection as crystals, liquids, or plastics.

Organic crystals, such as anthracene and stilbene, can be grown in multiple ways, offer superior decay constants to many inorganics, and provide good light yields (~20,000 ph/MeV); however, they are both fragile compared to plastics and difficult to grow larger than a few inches [9, 11]. Consequently, organic crystals scintillators are less widely used compared to organic liquids and plastics.

From a chemical standpoint, organic liquid and plastic scintillators are very similar. Both typically consist of an organic matrix mixed with dissolved primary and secondary fluorescent dyes [9], which allows for easy size scaling without affecting material homogeneity. Dyes are selected due to their high solubility, bright fluorescence, low self-quenching, and spectral properties supporting energy transfer [8]. Due to their solvent matrix, however, most organic liquids remain both highly toxic and flammable throughout their lifetime, which may exclude their use in large-scale detection arrays. Although a few liquid-based detection arrays have been developed [19], they do not meet the mobility and durability requirements previously specified. In contrast, the polymer matrix of plastic scintillators allows for safe handling and simple polishing after material manufacture and curing. Consequently, plastic scintillators are the cheapest, most durable, and easily scalable detection material available, which are advantageous material properties for modern, portable radiation imaging systems. Unfortunately, traditional plastics generally suffer from poor light yields, lower interaction efficiencies, and limited spectroscopic information from gamma rays due to their low effective atomic numbers (Z_{eff}) [9, 20, p. 228, 16]. This typically results in a measurable Compton continuum at lower gamma-ray energies, without the photopeaks provided by higher density and higher-Z scintillator alternatives, such as inorganics, which can facilitate spectroscopy using a peak-based approach..

Fortunately, some novel plastic scintillators now offer notable improvements over traditional materials, specifically in the areas of light yield, gamma interaction efficiency, and pulse shape discrimination. These advancements and their implications for improving modern radiation imaging are described in detail later in this paper.

Photon Interactions

Photoelectric (PE) absorption in detectors is typically dominant at photon energies below ~400 keV. Under these circumstances, an incident photon preferentially interacts with an inner-shell electron and deposits all its energy, thereby freeing the electron (referred to as a “photoelectron”) from the orbital shell. The initial photoelectron energy is equal to the difference between the incident photon energy and the electron binding energy. The pursuant de-excitation of the electron shell results in a characteristic x-ray emission equal to the binding energy of the freed electron. Since photoelectrons travel very short distances in matter before capture, their energy is typically deposited in nearly simultaneous coincidence with the characteristic x-ray emission, which results in a full-energy peak measurement

of the incident photon within the detection medium. Lastly, the probability of PE interaction scales as ~Z_{eff}^4, so materials with higher Z_{eff} are much more useful for gamma spectroscopy.

Compton scattering (CS) is the most likely interaction for photons between ~400 keV and ~6 MeV. This occurs whenever a photon strikes a weakly bound higher-orbital electron and imparts only a portion of its total energy to the electron. In doing so, both the photon and electron are scattered, but the angles of scatter for both particles depend on the amount of energy transferred to the electron by the incident photon. As such, scattered photons and electrons are measured across a continuum of energies, unlike the discrete energies associated with photoelectric interactions. Additionally, due to its higher initial energy and the low electron binding energy, the photon is incapable of transferring the entirety of its energy to the electron. Therefore, an upper limit of the Compton continuum exists, which known as the "Compton edge." This edge represents the maximum possible energy transferrable to electrons by source photons, which occurs whenever the electron is scattered at 0 degrees from the incident photon path. In such cases, the photon scatters backwards at 180 degrees from its incident direction. These photons can also deposit energy in the detection medium, which is known as the "backscatter peak."

Pair production (PP) cannot occur for photons below 1.022 MeV and only becomes a dominant interaction in materials when photon energies exceed ~6 MeV. Under such circumstances, a photon interacting with an electron can create a positron and electron pair, with both particles possessing rest masses of 511 keV and kinetic energies equal to half of the remaining incident photon energy. These particles depart the system in opposite directions (180 degrees apart) and quickly lose kinetic energy due to Coulombic forces from the surrounding material. Once thermalized, electrons are absorbed while the positron is annihilated as it recombines with another electron. This reaction creates two more 511 keV photons, which also depart in opposite directions (180 degrees apart). If both 511 keV photons are absorbed in the detector, the event registers as a full-energy peak deposition, although single and double escape peaks are also recorded when one or both 511 keV photons escape the detector, respectively.

Neutron Interactions

As with photons, neutrons are charge neutral and, thereby, fail to directly ionize atoms, which explains their highly penetrating nature. The likelihood of neutron interaction increases as the particles lose kinetic energy, generally following a 1/v dependence for reaction cross sections across most energies. Consequently, optimal fast neutron detectors include low-Z material constituents to slow high-energy neutrons down to thermal energies in fewer interactions, thereby enabling the detection of neutron capture reaction products or material ionizations from proton recoil events. This explains the widespread use of plastic scintillators in

neutron detection, as their high hydrogen content makes them particularly useful for moderating and detecting fast neutrons.

Neutrons incident in matter are either scattered or absorbed. Neutron scattering events consist of either elastic or inelastic scattering. Elastic scattering occurs when a neutron collides with an atomic nucleus with the kinetic energy conserved, thereby resulting in a scattered neutron and nucleus. This event represents the dominant reaction type between neutrons and low-Z materials, with hydrogen offering the highest efficiency for neutron moderation. In the case of inelastic scatter, kinetic energy is transferred but not conserved. Instead, the scattered neutron leaves the nucleus in an excited state and the imparted excess energy is released as one or more gamma emissions. Therefore, in both cases of neutron scatter, the incident neutron departs the system at a lower energy, and total energy is conserved.

An absorption event occurs when a neutron is captured by a target atom, thereby producing a compound nucleus in an excited state. The likelihood of this occurrence is governed by the energy-dependent absorption cross section for the specific isotope within the detection material, which is usually inversely related to neutron energy. Consequently, absorption events are most favorable for neutrons in the thermal energy region and typically result in (n,γ), (n,α), (n,p), fission, or neutron multiplication, all of which are important reactions in neutron imaging. In terms of radiation imaging, the most common results of neutron absorption are gamma emission and proton recoil (n,p), although induced fission is likely to occur if the imaged material is fissile. Gamma emission from excited nuclei interact with detector material via competing probabilities of PE, CS, and PP. Similarly, recoil protons are simply charged particles traveling short distances before slowing to thermal energies due to Bremsstrahlung and surrounding Coulomb forces.

CHAPTER TWO -
LITERATURE REVIEW

This chapter consolidates the findings of investigations into the current state-of-the-art with respect to novel organic plastic scintillators, the primary materials considered for examination in this research. The principles, materials, techniques, and capability gaps discussed in this chapter provide the foundation for the experimental and computational research later described.

Scintillation Photophysics and Kinematics

Based upon the principles of radiation interactions in matter, indirectly ionizing particles (i.e. photons and neutrons) deposit energy in detector media, thereby principally creating energetic electrons and protons [21]. Within organic aromatic matrices, charged particles deposit energy and excite ground state molecular electrons along a track (dE/dx), thereby producing a density of molecular electrons at various excited states following ion recombination [20, p. 225], as shown in Fig 2.1.

In simple polymer plastics, this results in 75% of electrons being excited to triplet states, while only 25% are excited to singlet states [9, 10]. These states are further subdivided into finer levels based on the molecular vibrational states, with the second subscript identifying the fine structure level. Electrons excited to singlet levels above S_{10} transition within picoseconds back to the S_{10} state through nonradiative mechanisms, such as internal conversion or ionization quenching. Internal conversion releases energy through molecular vibrations, while the degree of ionization quenching is correlated to the track ionization density. Electrons excited to only slightly higher states, such as S_{11} or S_{12}, quickly deexcite to the S_{10} state, as well. As mentioned previously, three out of four electrons are excited to higher triplet states, and these similarly de-excite to the lower triplet state of T_{10}. Therefore, following a local ionization event, these processes quickly create populations of excited molecular electrons in both the S_{10} and T_{10} states [9, 10].

Without primary or wavelength shifting dyes, electrons in the S_{10} state relax either via radiative or nonradiative pathways, whereas electrons in the T_{10} state must deexcite via nonradiative mechanisms due to spin-forbidden radiance [10, 17, 22]. The presence of a primary dye, however, facilitates fast nonradiative energy transfer between the S_{10} state of the aromatic matrix to the S_{10} state of the dye.

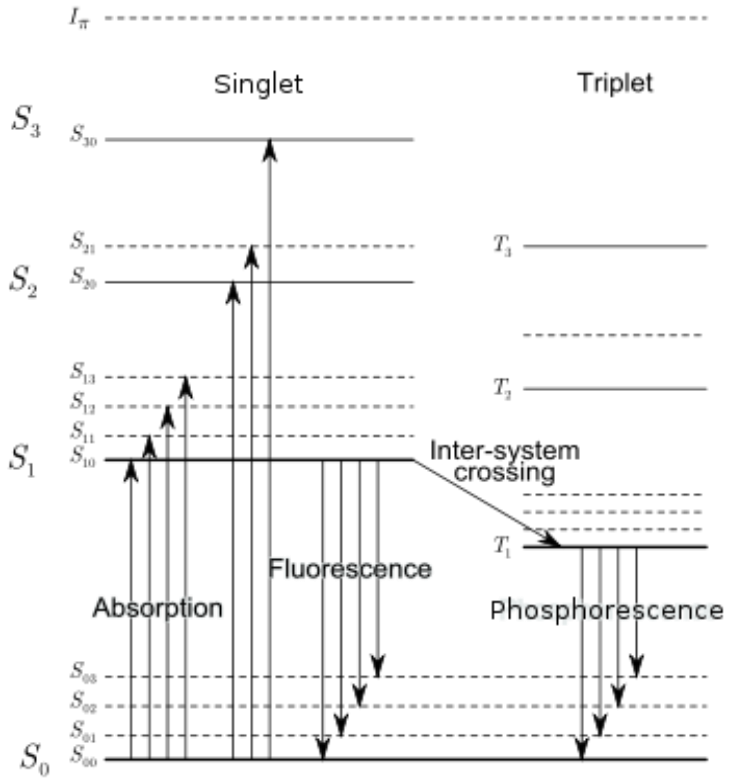


Figure 2.1. Energy levels of organic molecules [22].

Consequently, dyes are typically selected with S_{10} states just below those of the aromatic matrix (i.e., with a slightly lower electron binding energy) to facilitate this rapid transition. Additionally, electrons in the matrix T_{10} state may also transition easily to the T_{10} state of the dye before nonradiative deexcitation, although some of these electrons produce additional S_{10} states in the dye though triplet-triplet annihilation (TTA) [12]. This effect results in delayed fluorescence, since TTA occurs at a consistent and markedly slower rate than singlet deexcitation.

Based on these mechanisms, radiative deexcitation between the S_{10} and S_{00} states of the primary dye creates prompt fluorescence, or scintillation light. This emitted light from the primary dye is quickly reabsorbed by wavelength shifting dye molecules, thereby exciting those electrons to their respective S_{10} states. The subsequent radiative relaxation of these excited electrons produces the final photon emission measured by the photodetector, as shown in Fig 2.2, usually as blue light (~425 nm) [8, 22].

Consequently, primary and wavelength shifting dyes are selected to maximize the likely transfer of deposited particle kinetic energy within the aromatic matrix to a longer wavelength fluorescence, which improves scintillation light measurement by reducing self-absorption in the matrix. This occurs because the reemitted light is of lower energy than the matrix electron binding energy, which is the minimum energy required to excite molecular electrons of the detector. Additionally, wavelength shifters are also selected to produce final photon emission energies at ideal wavelengths for paired photodetectors [22].

Pulse Shape Discrimination Kinematics

PSD performance in organic detectors depends largely on detector geometry [8, 15, 23, 24]; however, the principles and processes described herein are consistent across all detector sizes and shapes. Photophysical processes occur on the order of nanoseconds, but a great deal of information can be gleaned from the measured pulse rise and decay times within organic scintillators. For the purposes of this analysis, it is useful to consider populations of S_{10} and T_{10} electrons appearing almost instantaneously due to the much faster processes of nonradiative deexcitation preceding these states (i.e., internal conversion and ion quenching) [9]. As such, when charged particles deposit energy along a track (dE/dx), the degree of ion quenching is proportional to the magnitude of dE/dx. Consequently, the absolute intensities of measured pulses decrease as dE/dx increases, which results in consistently lower pulse heights for heavier charged particles compared to pulses measured from lighter charged particles, as shown in Fig. 2.3.

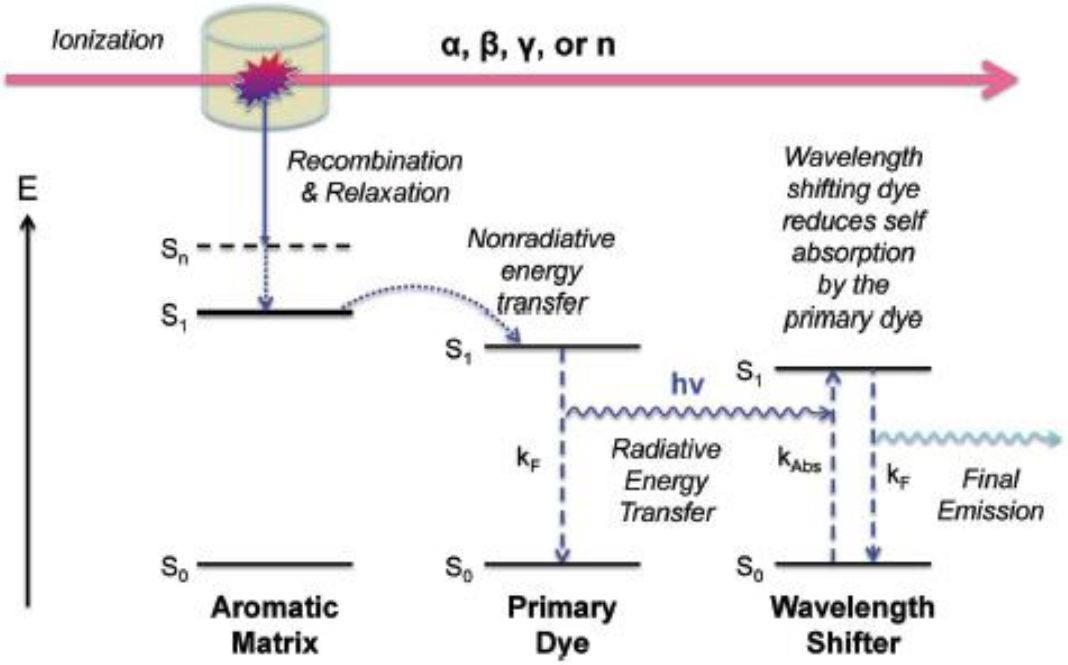


Figure 2.2. Diagram of particle kinetic energy transfer from polymer matrix to wavelength shifting dye and reemission of lower energy fluorescent photon [9].

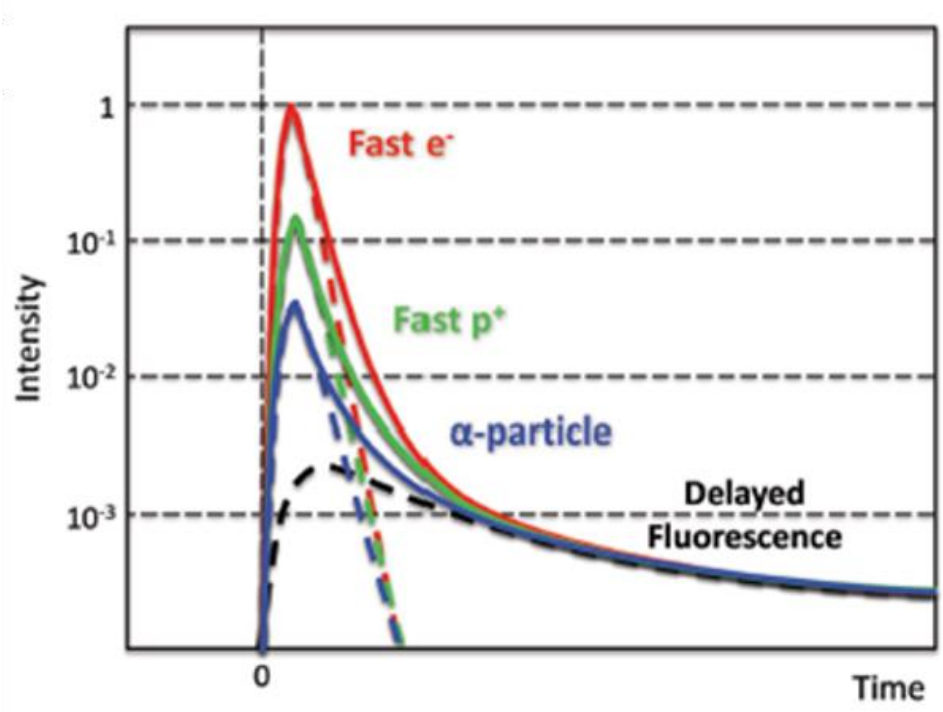


Figure 2.3. Representation of comparable peak intensities from different particles due to the effects of ion quenching and delayed fluorescence [9].

Fortunately, the rate of TTA is largely unrelated to dE/dx, so the contribution from delayed fluorescence remains relatively consistent between measured pulses from different particle types. Consequently, when compared to lighter charged particles, delayed fluorescence provides a larger fraction of the measured emission from larger, heavier charged particles, as seen in Fig. 2.4.

These differences in pulse shape can be quantified using tail-to-total ratios, which facilitate real-time discrimination between particle types in organic scintillators [8, 10, 18, 21, 23, 25]. Ratios are calculated by integrating over the total pulse, separately measuring the longer decay component (tail) of each pulse, and then discriminating between particle groups using the ratio of the two values, as demonstrated in Fig 2.5.

Therefore, the measurement and comparison of the delayed emission contribution in pulses provides the basis for pulse shape discrimination in organic plastic scintillators. This process typically results in figure-of-merit (FOM) calculations to quantify the degree of certainty when discriminating between particle populations. An alternative approach involves comparing a detector's intrinsic efficiency for a specific particle type to the likelihood of rejection for a different particle type. In this way, particle discrimination can more practically be quantified and tailored to specific detectors and experimental designs.

Novel Organic Scintillator Materials

Organometallic Scintillators

As mentioned above, the primary drawback of organic scintillators for use in gamma spectroscopy is the low Z_{eff} value of the material, which results in low PE conversion of gamma rays. To counter this shortcoming, attempts have been made to load organic scintillators with high-Z materials, most commonly tin and lead at ~10% weight [20, p. 228]. Unfortunately, while inclusion of high-Z materials increases the low energy photon sensitivity of the organic scintillator, it also degrades light yield because the high-Z constituents produce more triplet excitations and reduce the occurrence of singlets, which are the primary source of fluorescence [9]. As such, inorganic scintillators traditionally outperform organics in these regions. Until recently, these competing processes constrained the practical utility of organic scintillators, particularly plastics, to primarily neutron and high energy gamma detection; however, recent investigations into novel fluor formulations and primary dye loading may alter these long-held perceptions [8, 9, 10].

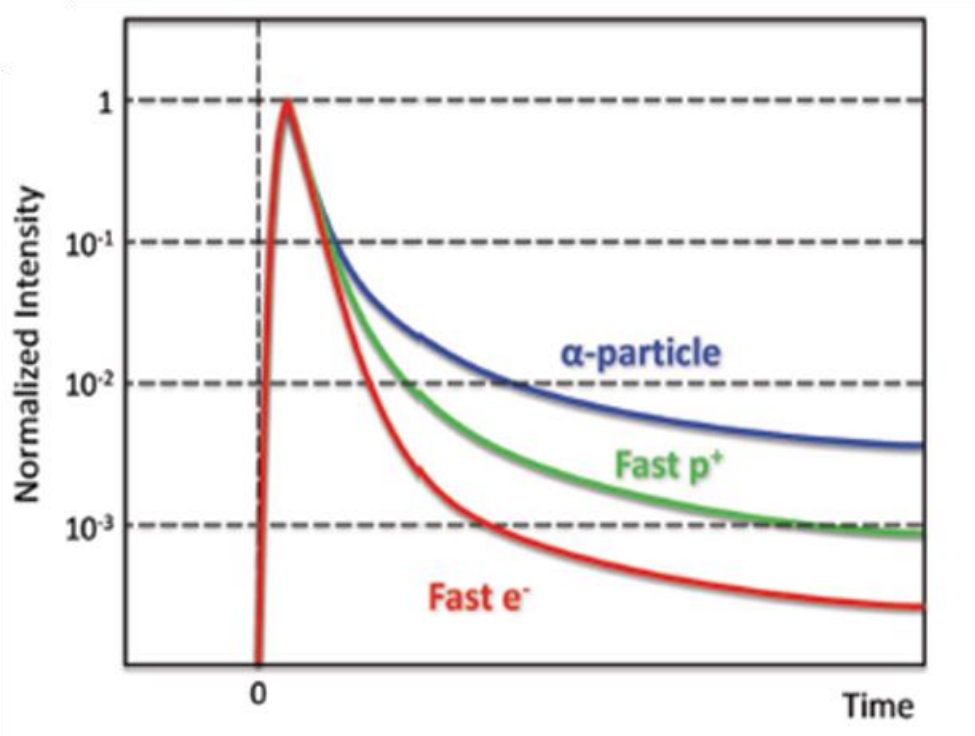


Figure 2.4. Normalized pulse heights from different particles, which demonstrate varied peak-to-tail ratios due to differing fractional contributions from delayed fluorescence [9].

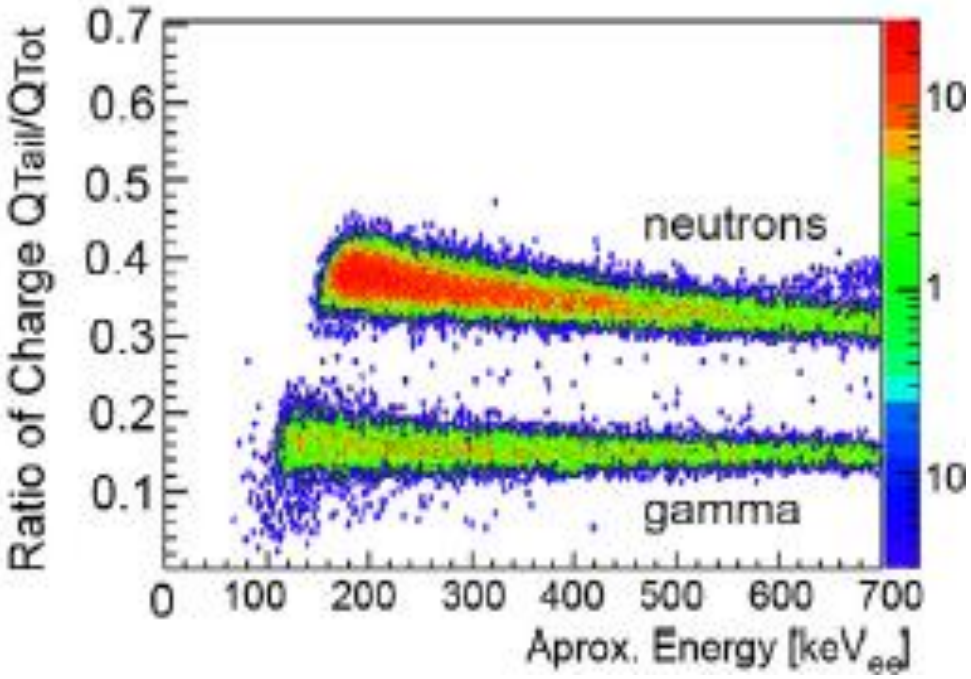


Figure 2.5. Display of multiple plastic scintillator tail-to-total ratios [8].

Organic fluors in standard plastic scintillators produce ~10,000 ph/MeV in the blue (~425 nm), which is substantially inferior to the 38,000 ph/MeV produced in NaI(Tl). However, experimental research recently established this number can be increased to ~40,000 ph/MeV in the green (~550 nm) using iridium complex fluors, shown in Fig. 2.6. These complexes leverage both singlet and triplet deexcitations via luminescence through spin-orbit coupling [3, 8, 9, 10]. This light yield improvement is demonstrated in Fig 2.7, which shows a standard plastic emitting in the blue and another one with complex fluors emitting in the green.

Based on these findings, researchers at LLNL theorized that the superior light yield from this complex fluor could mitigate the suppressed light outputs typical in high-Z loaded plastics. Consequently, they produced a 21 wt% bismuth-loaded plastic, which generates ~20,000 ph/MeV from gamma interactions [9]. This material provides 7% energy resolution for a 662 keV Cs-137 photopeak from a cm^3-scaled scintillator and 10% resolution from a 50 cm^3 sample [9], shown below in Fig 2.8.

Subsequent experiments with bismuth-loaded polyvinyl toluene (PVT) plastic provided ~25x the integrated counts from standard plastics when exposed to Am-241 [9]. Therefore, despite offering only half the light yield of standard plastic with iridium fluor, the Bi-loaded iridium fluor plastic provides improved low-energy gamma sensitivity and twice the light output of traditional plastic scintillators. However, one additional reported consequence of harvesting triplet exciton luminescence is the dramatic drop from ~ns to >µs response times due to the phosphorescent nature of triplet emissions [10]. Therefore, while the additional light yield from the iridium complex improves the signal-to-noise ratio (SNR), its use may also exclude iridium complex-loaded plastics from fast timing measurement applications. Refinement and optimization of these formulations are ongoing, and scale-up of detector sizes is expected in the near-term [9].

In addition to gamma sensitivity, incorporation of neutron-sensitive organometallics in polymer matrices is also an area of ongoing study supporting improved neutron imaging and n,γ PSD [1, 17, 19, 26, 27]. While these advancements contribute to the potential application of organic scintillators for DPI, improving the efficiency of plastics for PE absorption remains the area of greatest importance. Together, these advancements are a significant improvement to the utility of plastic scintillators for mixed-field measurements and pulse shape discrimination, which are essential requirements for DPI systems.

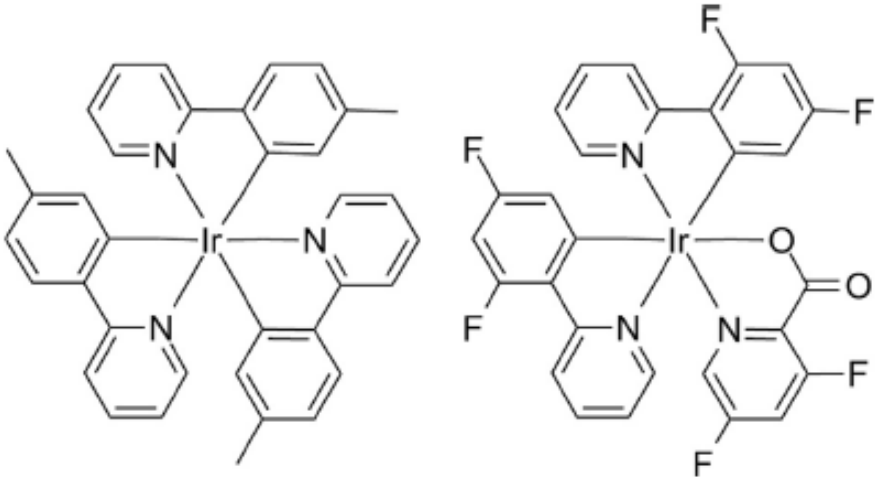


Figure 2.6. Chemical structure of iridium complexes [10].

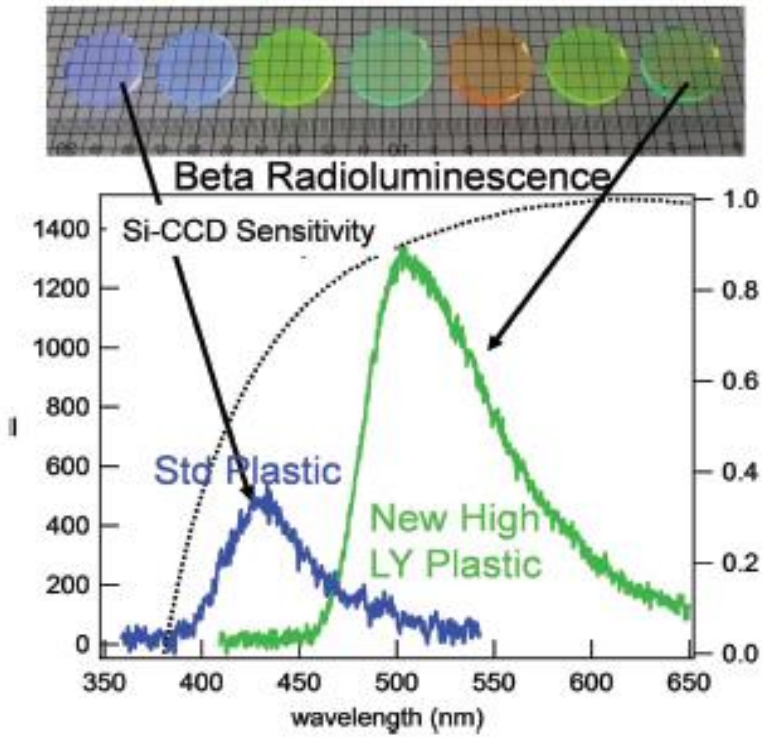


Figure 2.7. Comparison of radioluminescence between standard plastic fluors (blue) and triplet-harvesting Iridium complex fluors (green) [9].

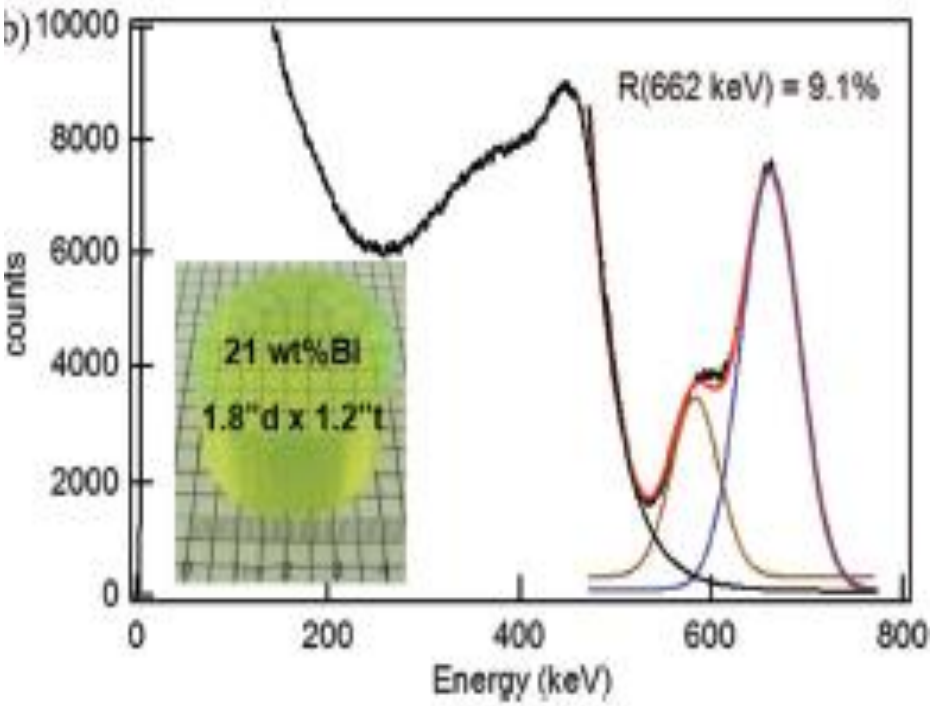


Figure 2.8. ^{137}Cs pulse height spectrum obtained with a 50 cm^3 sample of Bi-loaded PVT at LLNL [9].

Nanocomposite Organics

In addition to organometallics, significant advances have occurred in the synthesis of high-Z nanostructured materials and nanoparticles, such as BaF2, HfO2, and quantum dots (QDs). The incorporation of nanomaterials within an organic scintillator matrix is attractive for the same reasons as organometallics (higher Z_{eff}); however, nanoparticles also provide greater material stability and different potential optoelectrical properties [9, 10]. Several experiments conducted recently used traditional materials as nanoparticles, but these resulted in diminished light outputs, impractical material properties, or an inefficient energy transfer to the nanoparticles [9, 10]. Other attempts using non-emitting band-gap nanoparticles, such as Gd_2O_3, demonstrated that inorganic nanoparticles could facilitate high-energy gamma photon conversion to photoelectrons. Despite low loading levels, this experiment noticeably improved the photoelectric cross-section of the plastic, measuring a 662 keV photopeak at 11.4% resolution; however, it suffered from poor spectral overlap with the paired PMT, so investigation into scintillator performance and varying nanoparticle loading weight remains [9]. Apart from gamma detection, use of these materials has also produced marked improvement in neutron detection and neutron imagery [10, 26].

The use of inorganic QDs has also been investigated as a means of overcoming diminished light yields in nanocomposites, which is proportional to the amount of loaded non-emitting nanoparticles. QDs are ultra-small semi-conductor nanocrystals with quantum confinements effects, thereby offering tunable emissions, fast decay times, and high photoluminescent quantum efficiency. Despite these benefits, however, QDs are typically made from moderate-Z materials, loaded at low levels, and suffer from significant self-absorption. Research into the use of dyes to offset QD self-absorption properties was conducted with promising results, and future work into heavily loading (>60 wt%) QDs into small scale detectors is ongoing [9].

Nanoparticles can also be synthesized with large band-gaps to avoid quenching effects inherent in organometallics; however, despite the benefits offered by these hypothetical materials, the primary challenge still arises from bulk fabrication [10, 28]. Specifically, it is extremely difficult to produce homogenous organic mixtures with evenly distributed nanoparticles. This is due as much to the high specific surface and surface energy of the nanoparticles as to the material properties of organic polymers [9]. The ultimate result is degraded transparency due to particle aggregation, which can only be overcome through great time and care in large detector fabrication. Consequently, despite great promise in detector capabilities from loaded nanoparticles and QDs, the application of these materials to practical radiation imaging must wait until the current challenges associated with detector fabrication are overcome.

Modern Radiation Imaging Techniques

In terms of the physical processes at work, all forms of radiation imaging utilize highly penetrating radiation detectable by specific media within complex backgrounds. These forms can be further identified as active or passive imaging. Active imaging includes the use of controlled particle sources to create a stimulated emission, backscatter, coded aperture, and/or a transmission image of an object. Passive imaging utilizes particles generated within a radioactive object to determine the precise location of emittance using techniques such as coded aperture or transmission imaging. Based on this, radiography is considered active, while scatter-based forms of radiation imaging are considered passive. Most active sources consist of indirectly ionizing radiation, typically photons and neutrons. Although charged particles, such as cosmic muons and positrons, are also used [11], due to the practical limitations imposed by the more exotic radiation sources, this paper will focus exclusively on photon and neutron-based imaging. Likewise, while other forms of radiation imaging are also widely utilized, this work is limited to radiography, coded aperture, and scatter-based imaging techniques since these forms are most conducive to portable DPI systems.

Radiography

Traditional radiography involves placing an object between a source of radiation and a detection material sensitive to localized energy deposition. Early techniques paired x-ray or gamma-ray photon sources with photo-sensitive radiographic films to produce crude “shadows” of irradiated objects [29]. Despite the simplicity of early applications, the ability to visualize the contents of an object using differences in photon attenuation from differing materials and densities proved most useful, especially in medicine. However, radiographic films, despite offering good spatial resolution, consistently provided low sensitivity, so image quality suffered from unwanted background and scattering radiation. Consequently, the relatively recent development of pixelated scintillation arrays coupled to photodetectors provide notable improvements compared to film. Additionally, the incorporation of digital signal processing offers many powerful radiographic capabilities over analog images, such as accurate detection of localized events and the ability to ignore signals below a voltage threshold [29, 30]. Plastic scintillator arrays consist of small, evenly sized sections of plastic scintillator enclosed in light-tight reflective materials and coupled to a digital photodiode, such as a silicon photomultiplier (SiPM). Digital detector arrays (DDAs) can, therefore, be manufactured in a variety of sizes using whatever number and pixel size necessary to attain the desired image resolution [30, 31, 32]. Additionally, current research suggests SiPM-based measurements offer superior PSD capabilities over traditional PMTs, which further supports the utility of DPI SiPM-based pixelated arrays [18, 24, 32, 33]. Lastly, the quantum efficiency (QE) of modern a-Si DDAs tends to be higher, on average, with higher wavelength emissions. This suggests that converters emitting in the green would likely benefit from a higher QE than those emitting in the blue [34].

Photon radiography depends, first and foremost, on the interactions between source photons and orbital electrons within the detection medium. Due to dose and shielding concerns, source photons used in radiography rarely exceed an initial energy of 470 kVp, so incoming photons typically transfer energy to atomic electrons through either PE absorption or CS interactions. Even higher energies are employed in cargo radiography applications, where photons must penetrate multiple centimeters of steel to image the objects within. For man-portable radiography systems, however, x-ray energies rarely exceed 370 kVp due to both the penetrating nature of the radiation at those energies, as well as the large size of the x-ray tube and power supply needed. However, whenever source photons of energies greater than 1.022 MeV are employed, PP also becomes possible. Since all three interactions occur stochastically, the associated interaction probabilities depend (to varying degrees) on the incident photon energy and the material atomic number, Z. In general, photon interaction probabilities are positively correlated to increases in both material density and Z_{eff}. This topic will be addressed in greater detail in Chapter 4; however, it is typically believed that PE absorption scales as $\sim Z_{eff}^{4}$, so a higher material Z_{eff} results in increased rates of photon absorption and scatter.

Nuclear reactors and commercially available neutron generators are typical sources for neutron radiography. Neutrons from reactors follow a moderated Watt-fission energy distribution, while deuterium-tritium (D-T) and deuterium-deuterium (D-D) generators produce nearly isotropic sources of 14.1 and 2.45 MeV neutrons, respectively. Based upon the described differences in particle interaction types, results, and probabilities, it is extremely advantageous to utilize both forms of highly penetrating radiation in the radiographic examination of objects with unknown internal components [1, 2, 6, 7]. For example, in a nuclear non-proliferation scenario involving a dense, high-Z object suspected of containing SNM, even gamma ray imaging alone may fail to penetrate and sufficiently image the object [3, 14]. In these cases, neutrons offer improved penetration over photons as well as a significantly higher probability to induce fission within the SNM, and higher energy neutrons provide longer mean free paths [19]. The stimulated emission of neutrons from the fissile material could then be measured and imaged, which would allow for an accurate assay of the material contained inside. Conversely, when imaging comparatively low-Z and low-density objects, photon imaging is favorable over neutron imaging due to the reduced time necessary to produce the image, as well as the lower associated dose rate. Despite these benefits, neutron radiography offers superior image resolution for low-Z material features in shielded containers, which typically fail to appear in photon radiography [1, 2, 6, 19].

The recent material advancements in organic plastics are particularly applicable to radiographic purposes [3, 32, 34]. The ability of novel organometallics to detect

and discriminate between photons and neutrons could enable the rapid and practical utilization of both particle types, as well as their respective radiographic benefits. Specifically, if these materials were used in a single pixelated panel, it could provide a low-cost, portable, and durable means to holistically assess the interior of sealed containers. Furthermore, plastics containing iridium-complex fluors, which maximize light yield and high-Z loading quantum efficiencies, could support both neutron and gamma interrogation, as well as the detection of stimulated emissions from neutron interrogation [3, 9, 17].

Scatter-based Imaging

Particle scatter-based imaging is a commonly used technique for passive standoff detection of radioactive sources, such as SNM. It can be used to locate both photon and neutron emitters with some systems detecting and discriminating between both simultaneously [35]. This is particularly advantageous due to the ease by which gammas are shielded by high-Z materials and neutrons are shielded by low-Z materials. Additionally, the photon background is typically much more complex than the neutron background, and SNM emits far fewer neutrons than photons. Consequently, the ability to efficiently detect and image with both particle types helps minimize the limitations inherent to each.

In the case of photons, a Compton camera utilizes the Compton-scattering and subsequent absorption process to determine likely positional information about the source relative to the detection system. It typically functions by using time correlation to link scattering events in one detector with absorption events in another, much the same way as a single detector achieves a full energy peak. Each correlated set of interactions enables the system to refine a cone of probable source locations [35]. The cone angle (θ_γ) is determined from Klein-Nishina formula,

$$cos(\theta_\gamma) = 1 - \frac{0.511\,MeV \times E_d}{E_a(E_d + E_a)}, \quad (2)$$

where E_d is the energy deposited in the scatter and E_a is the energy deposited in the subsequent absorption. After sufficient data to reduce uncertainty, these cones are then back-projected onto a theoretical sphere surrounding the object of interest to determine a likely source location. Various Compton camera systems have been explored and documented, with most consisting of two-planes of detectors. In some cases, the material is consistent between planes. In other designs, initial detector plane consists of materials with a high probability of photon scattering, such as organic scintillators, while the second detector plane is made up of detectors with a high Z_{eff}, usually inorganic scintillators, to maximize the likelihood of PE absorption.

Similarly, neutron scatter-based imaging leverages neutron elastic scatter events to determine likely source locations. In a two-plane detector configuration, the

elastic scatter would be detected in the first plane and a second interaction in a second plane detector. The neutron scattering angle (θ_n) relates to the neutron and recoil proton energies as:

$$cos^2\theta_n = \frac{E_{n1}}{E_{n0}}, \quad (3)$$

where E_{n0} is the incident neutron energy and E_{n1} is the scattered neutron energy. From this calculation and the associated time of flight analysis, interactions in disparate detector planes can be associated accurately. Neutron scatter imaging systems use low A materials to increase the probability of scatter in one plane and absorption in the second. As such, organic scintillators have already been successfully employed for these purposes [35].

In terms of advanced material applications, the increased PE absorption capability of modern high-Z loaded organometallics or nanocomposites offers promise for scatter-based DPI systems. However, the detrimental impact of iridium complex fluors on timing response may preclude their use in scatter-based imaging, which relies heavily on fast timing pulses to adjudicate particle interactions and back-projected directionality. Additionally, these types of paneled systems remain too large to feasibly support an easily portable DPI system due to their size and weight, as well as the complexity of precise panel alignment. Consequently, scatter-based techniques are ultimately considered infeasible for a mobile DPI system at this time.

Coded Aperture Imaging

The underlying physics for coded-aperture imaging is based on pinhole camera designs, where the size of the individual hole is correlated to both angular resolution and SNR. Coded apertures are essentially masks with multiple pinholes to collimate incident radiation into multiple overlapping shadows on a detector medium, which improves the SNR over pinhole cameras while maintaining good angular resolution. However, the system requires a detector with position sensitivity to the incident radiation, which typically implies a pixelated array or a solid-state device (SSD) array. Fourier convolution of the measured shadows produces a single image of the radiation source location relative to the coded-aperture mask. Additionally, modern algorithms benefit from modified uniformly redundant array (MURA) configurations, which enable linear, hexagonal, or square coded-aperture configurations with superior angular resolution and reconstruction.

Photon-based coded-aperture imaging is widely used in a variety of industries, including space exploration, medical imaging, and nuclear decommissioning and decontamination. This area is well documented and efforts to miniaturize system components and detection media are quite advanced. Many systems utilize small detector surfaces, such as CdZnTe sensors or CsI(Tl) scintillators [29]; however, these materials, among other constraints, cannot compete with other more

affordable materials, such as plastics and liquids to support the large numbers typically needed for national security missions.

Neutron-based coded aperture applications include national security and material detection at nuclear fuel cycle facilities. Most current systems rely on large quantities of ^{3}He or BF_3-filled gas detectors or liquid scintillators, such as EJ-309. However, the size of these detectors makes them impractical in an environment where portability of radiation imaging is necessary. For both forms of radiation, scintillator-based devices have been successfully employed and are more appealing than SSD arrays due to the balance they offer with respect to cost, mobility, practicality, and detection efficiency. Both environments require detector materials offering reasonable absolute efficiencies and, in the case of neutron imaging, fast response due to time of flight measurements.

Consequently, just as in the case of radiography, the recent advances in organometallics may directly benefit the use of DPI pixelated arrays in coded-aperture systems. Due to the comparably low count rates measured by coded-aperture systems, the significantly larger timing responses expected from iridium complex loaded plastics may have much less of an impact on measurements. This will likely result in the optimal application of these materials for coded-aperture imaging systems, which typically operate over long measurement windows due to low efficiencies from distance, solid angle, and/or source intensity.

Summary and Outlook

Several modes of radiation-based imaging are available for use in future DPI systems, and two distinct methods exist to produce sensitized plastics capable of DPI. However, widespread application of DPI technology requires future systems that provide ruggedness, portability, relatively low cost, and high detection efficiency for both x-rays and neutrons. Therefore, both the technological and material options available must first be evaluated using these criteria to determine the optimal choices for future investigation.

As such, the imaging mode that best meets these requirements is transmission imaging using a DDA and associated radiation generating devices (RGDs). DDA-based DPI systems would offer the greatest portability by requiring only a single, self-contained panel for imaging purposes, as well as rapid read-out and analysis of recorded images. They would also provide higher detection efficiencies than both scatter-based and coded aperture imaging, which means shorter exposures. DDA-based systems and electronics could be ruggedized, especially when the scintillation material is a cured, stable plastic. Lastly, the cost of DDA systems can be high, but the alternative of using either a film or phosphor read-out is untenable due to the challenges addressed. Additionally, commercial DDA systems could be

adapted for DPI purposes, and the use of plastics would likely reduce overall system cost. Consequently, this technology seems the most promising approach to support future DPI applications.

In terms of the choice for DPI high-Z sensitized plastics, the most compelling prospect comes from novel organometallic-loaded plastics paired with iridium fluorophores. Specifically, organobismuth-based plastic scintillators activated with iridium complexes enable triplet-harvesting, which are expected to maximize light production pursuant to both x-ray and neutron interactions [9, 17]. Additionally, due to their shared high-Z and hydrogen concentrations, these organic scintillators offer a promising balance of particle sensitivity ideal for DPI purposes. Lastly, the green emissions from these materials, due to the iridium fluors, offer the additional benefit of improved quantum efficiency when paired with DDAs [36].

In conclusion, based upon the combined characteristics of enhanced brightness, interaction, and light collection efficiencies, plastic compositions with bismuth-loading and iridium fluorophores appear the optimal materials for future study. Furthermore, pairing these materials with DDA-based DPI transmission radiography is expected to provide improved quantum efficiency over scintillators emitting in the blue. Consequently, the subsequent research will focus on the evaluation of these materials and technology.

CHAPTER THREE -
NOVEL CONTRIBUTIONS

This research contains several scientific contributions to the field of nuclear engineering, which are all related to the radiographic performance characteristics of two novel materials when exposed separately to high-energy bremsstrahlung x-ray and fast neutron fields. The novel materials include a triphenyl bismuth-loaded polyvinyl toluene (BiPVT) and an iridium-bismuth-plastic (Ir-Bi-Plastic), both of which include 21 wt% bismuth and iridium-complex fluorophores. Both materials were also designed, manufactured, and provided by Lawrence Livermore National Laboratory (LLNL). From a small sample of BiPVT, a 4×3-pixel array was fabricated and paired with a commercial radiographic panel to support performance comparisons between the BiPVT and other available alternative plastic scintillators in the same configuration, specifically EJ-200 and EJ-256. The Ir-Bi-Plastic was supplied by LLNL as an 8×8-pixel array. The direct evaluations and performance comparisons described subsequently herein for both arrays in x-ray and fast neutron environments have never previously been performed or documented.

As such, the most notable novel contributions detailed herein are found in the experimental evaluations of edge response, modulation transfer function (MTF), and spatial resolution (SR) provided by the BiPVT and Ir-Bi-Plastic arrays in both radiation environments, as well as the comparison of those results against similar findings for the two alternative materials. Additionally, simulations of the BiPVT experiments provide insight into the physical processes occurring within the evaluated arrays, due primarily to material isotopics and incident radiation type and energy. This analysis helps us to better understand the physical reasons for each array's relative performance and facilitates reasonable predictions for performance comparisons in alternative environments. To this end, this research also describes a novel methodology to simulate array performance, which incorporates both MCNP6.2 and Zemax OpticStudio software. These simulations provide estimates of edge response for each material array, which facilitate the application of identical calculations and comparisons of array MTF and SR between experimental and simulated data. Comparisons between the simulated and experimental x-ray MTF and SR results verify the accuracy of the specific simulations, as well as the validity of the computational methodology employed. This methodology was also further leveraged to provide predictions of relative array performance for a more ideally manufactured BiPVT array.

Lastly, derivation of these results relies upon one final novel contribution, the development and implementation of a methodology to apply computed tomography processes in 1D to calculate edge response from small arrays using

composite images, both experimentally and computationally. Specifically, by conducting multiple measurements of a straight edge phantom, with each measurement recording an incrementally greater fraction of array shielding by the phantom, larger experimental and computational composite images are produced. The larger images of the straight edge phantom support evaluations of edge response in accordance with ASTM guidelines for region of interest width and height, and the agreement between SR values derived from the physical measurements and simulations of large composite arrays, demonstrates the accuracy and reliability of this approach in x-ray environments.

CHAPTER FOUR -
PRELIMINARY PERFORMANCE AND MATERIAL EVALUATION

Analytic Material Evaluation

Motivation

This section provides basic but fundamental evaluations of the materials of interest in this research, which facilitate the subsequent analysis of material characteristics governing incident particle interactions and expected light yield. Specifically, these calculations address the atomic fractions, weight percentages, and number densities of each material, as well as calculations of effective atomic number, Z_{eff}, average atomic number, $\langle Z \rangle$, and effective atomic weight, A_{eff}. The quantity Z_{eff} is particularly important for predictions of PE absorption, as mentioned in Chapter 2.

Analytic Calculations

The most fundamental value necessary for understanding particle interactions within a medium is the atomic number density of that material. For any single element, the atomic number density, N, is calculated from the equation

$$N = \frac{N_a \rho}{M_m}, \qquad (4)$$

where N_a represents Avogadro's number (6.022×10^{23} atoms/mole), ρ is the density (g/cm^3), and M_m is the molar mass (g/mol) of that element. This equation quantifies the number of atoms present within a given volume in units of atoms/cm^3. For heterogenous materials, which are those comprised of any number of elements in varying proportions, calculations of the number of atoms from each constituent element, N_i, within a cm^3 of the fictional, homogenous material can be made using

$$N_i = \frac{N_a \rho w_i}{M_i}, \qquad (5)$$

where w_i represents the weight fraction (%wt) of the specific constituent element. This equation enables calculation of the atomic percentages for each constituent element present within a heterogenous compound, and Table 4.1 provides these values for the materials of interest to this research. Of note, densities listed for EJ-200 and EJ-256 were acquired from the respective Eljen material data sheets [36, 37], and the density for BiPVT was provided by LLNL. Liquid water, although not utilized experimentally in this research, was included in Table 4.1 and in future

calculations to provide a well-characterized material allowing the comparison of any analytic or simulated results against published data. This data for water provided in Table 4.1 is consistent with the Material Compendium published by Pacific Northwest National Lab [38], which validates the analytic calculations employed for BiPVT (our novel material of interest).

From Equation 5, the *total* number, N_t, of atoms per cm^3 of any heterogenous material may be calculated as

$$N_t = N_a \rho \sum \frac{w_i}{M_i}. \qquad (6)$$

Additionally, when calculating the effective molar mass (M_{eff}) for such a material, the value is derived from the sum of the constituent molar masses using the equation

$$M_{eff} = \sum \alpha_i M_i. \qquad (7)$$

In Equation 7, α_i represents the atomic percentage of the i^{th} element to each molecule, and M_i is its molar mass of that element in units of g/mol. Using Equations 6 and 7, the effective molar masses and atomic number densities for BiPVT, EJ-200, and EJ-256 may be accurately calculated, and these values are listed below in Table 4.2.

Values calculated for water are consistent with published data [38, 39], as well as the calculated molar mass of PVT for EJ-200, using its chemical formula of $CH_2CH(C_6H_4CH_3)$ [40]. These findings support the accuracy of equivalent values calculated for both BiPVT and EJ-256.

Effective Atomic Number

For the purposes of photon attenuation, any heterogenous compound may be described as a fictitious element using an effective atomic number, Z_{eff}. However, different methods exist for calculating this value, and agreement regarding the best application of these techniques has evolved over the last 60 years [41, 42]. Consequently, different approaches will be utilized to assess the *Z*-values of each considered material for specific applications, which is consistent with past practices [42].

Beginning with a more traditional method, the first step in determining Z_{eff} for a compound requires determination of its atomic number density, which was completed in the previous section. Similarly, the number of electrons present in a cm^3 of the material from each constituent element may be calculated as

Table 4.1. Calculated atomic percentages and other relevant material values for BiPVT, EJ-200, and EJ-256.

Compound Material	Density, p (g/cm^3)	Constituent Elements	Weight Percentages	Atomic Percentages
BiPVT	1.4	Hydrogen	6.72	52.13
		Carbon	72.29	47.09
		Bismuth	21.00	0.79
EJ-200	1.023	Hydrogen	8.50	52.54
		Carbon	91.50	47.46
EJ-256	1.081	Hydrogen	8.08	52.46
		Carbon	86.93	47.38
		Lead	5.00	0.16
Water	1	Hydrogen	11.19	66.67
		Oxygen	88.81	33.33

Table 4.2. Calculated material values for BiPVT, EJ-200, and EJ-256

Material	Density, p (g/cm^3)	Effective Molar Mass, M_{eff} (g/mol)	Atomic Number Density, N ($atoms/cm^3$)
BiPVT	1.4	162.064	1.0776×10^{23}
EJ-200	1.023	118.178	9.8891×10^{22}
EJ-256	1.081	128.538	9.9430×10^{22}
Water	1	18.020	3.3429×10^{23}

$$N_{ei} = \frac{N_a \rho w_i Z_i}{M_i}, \qquad (8)$$

with Z_i representing the atomic number of the i^{th} element. From this, the total number of electrons present (N_{et}) within each gram of the fictional element, which is also known as electron density, may also be calculated as

$$N_{et} = N_a \rho \sum \frac{w_i Z_i}{M_i}. \qquad (9)$$

Material electron density is extremely important for both photon and charged particle transport since both interact with molecular and atomic orbital electrons, either directly via scatter or absorption, in the case of photons, or indirectly via Coulombic slowing, in the case of charged particles. Since the atomic number for any stable element is equal to the number of protons per atom, we can combine Equations 6 and 9 to produce an equality once thought to provide assessments of Z_{eff}, if only for predictions of relative Compton Scatter interactions [42]. However, that same expression is now referred to as the *average* Z_{eff}, $\langle Z_{eff} \rangle$ [43, 41], and it is represented mathematically as

$$\langle Z_{eff} \rangle = \frac{N_{et}}{N_t} = \frac{N_a \rho \sum w_i \frac{Z_i}{M_i}}{N_a \rho \sum \frac{w_i}{M_i}} = \frac{\sum w_i \frac{Z_i}{A_i}}{\sum \frac{w_i}{A_i}}, \qquad (10)$$

where w_i represents the weight fraction (%wt) of the i^{th} element, and Z_i and A_i are the atomic numbers and weights of the i^{th} elements, respectively. Additionally, values of $\langle A_{eff} \rangle$ may also be calculated from the similar relationship

$$\langle A_{eff} \rangle = \frac{1}{\sum \frac{w_i}{A_i}}. \qquad (11)$$

Another method used previously to determine the Z_{eff} for a heterogenous material is referred to as the Power Law rule; however, this method is now considered outdated and provides questionable scientific validity due to the span of photon energies used commonly in modern research and applications [44]. Initially, this value of Z_{eff} was found useful primarily for predicting rates of PE and PP processes [42] because these were shown experimentally as proportional to values calculated using

$$Z_{eff}{}^{2.94} = \sum \left(\frac{N_{ei}}{N_{et}} Z_i \right)^{2.94}. \qquad (12)$$

By applying Equations 10, 11, and 12 to the materials of interest in this research, values of Z and A may be calculated for each, and these are provided in Table 4.3. As mentioned earlier, water was also included to provide a well-characterized data set by which to validate the employed methodology and calculated results.

Table 4.3. Calculated weight percentages and Z-values for BiPVT, EJ-200, EJ-256, and water.

Material	Electron Density per gram (N_{te})	Average Atomic Number, $\langle Z_{eff} \rangle$	Average Atomic Weight, $\langle A_{eff} \rangle$	Effective Atomic Number (Power Law), Z_{eff}
BiPVT	4.3094×10^{23}	4.00	7.82	44.83
EJ-200	3.3356×10^{23}	3.37	6.23	5.67
EJ-256	3.4773×10^{23}	3.50	6.55	26.82
Water	3.3429×10^{23}	3.33	6.00	7.45

Analytic values of $<Z_{eff}>$ and $<A_{eff}>$ for EJ-200 and water provide good agreement with the published data [44, 41] , and the calculated electron densities for both EJ-200 and EJ-256 match the values included in their respective data sheets [36, 37].

The Power Law approach, while useful for determining values of Z_{eff} roughly proportional to PE and PP events in heterogenous materials, fails to incorporate energy-dependent cross sections for photon interactions. Therefore, a more recent technique for calculating Z_{eff} incorporates the energy-dependent mass attenuation coefficients of each constituent element. This approach is represented by the equation

$$Z_{eff} = \frac{\sum_i f_i A_i \left(\frac{\mu}{\rho}\right)_i}{\sum_j f_j \frac{A_j}{Z_j} \left(\frac{\mu}{\rho}\right)_j}, \qquad (13)$$

where f_i is the molar fraction of each element in the compound material, μ is the linear attenuation coefficient, and ρ is the density [41, 43]. Equation 13 incorporates the dynamic relationship which exists between incident photon energy and the mass attenuation coefficients of each element within the compound. As such, this methodology provides Z_{eff} values for heterogeneous compounds based upon incident photon energies. Applying Equation 13 to the materials of interest returns the data provided below in Table 4.4 and Figure 4.1.

Analytic Z_{eff} results for water, provided in Table 4.4 and shown plotted in Figure 4.1 are found to agree with published data [41], thereby validating the employed methodologies and calculated results for EJ-200, EJ-256, and BiPVT, which all appear unpublished.

Due to competing PE and CS interactions in matter, these Z_{eff} values are expected to approach $<Z_{eff}>$ in regions where CS begins to dominate, such as above 0.2 MeV for most low-Z materials [43]. This documented relationship is observable in Table 4.4 and Figure 4.1 for all four materials but especially for water and EJ-200. In contrast, EJ-256 and BiPVT, the two high-Z loaded materials, require comparatively higher photon energies before their respective Z_{eff} converge toward $<Z_{eff}>$, with peak Z_{eff} values occurring for both at 20 keV. This appears physical, since high-Z loading increases the probability of PE absorption at higher photon energies and the two are positively correlated. Therefore, the analytic results appear to reflect the observed and documented relationship between Z_{eff} and $<Z_{eff}>$, thereby further supporting the validity of the methodology and calculated results.

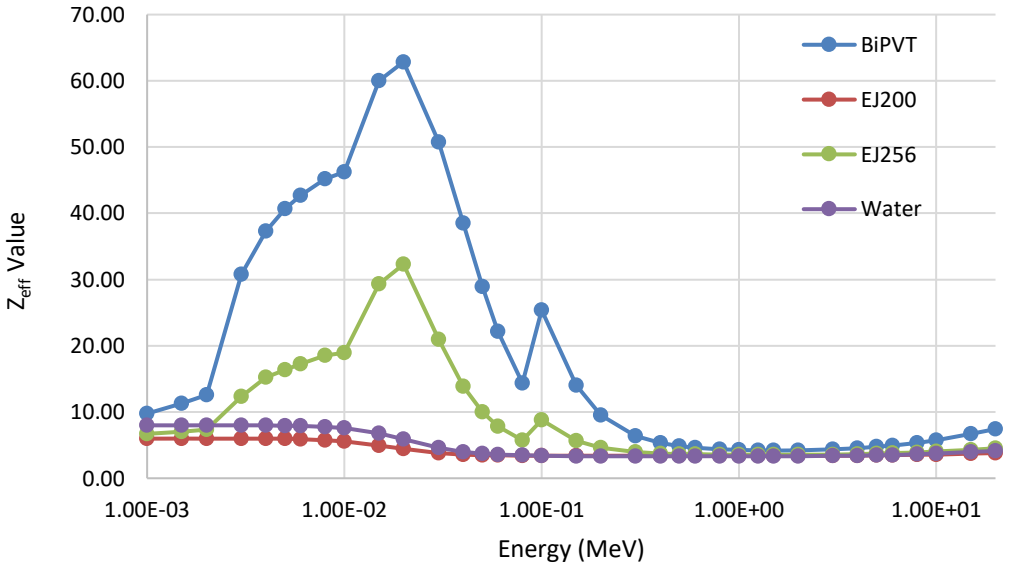


Figure 4.1. Plot of the energy-dependent Z_{eff} values for BiPVT, EJ-200, EJ-256, and water.

Table 4.4. Calculated energy-dependent Z_{eff} values for BiPVT, EJ-200, EJ-256, and water.

E	BiPVT	EJ-200	EJ-256	Water
1.00E-03	9.77E+00	5.99E+00	6.74E+00	7.99E+00
1.50E-03	1.13E+01	5.99E+00	7.05E+00	7.99E+00
2.00E-03	1.26E+01	5.99E+00	7.32E+00	7.99E+00
3.00E-03	3.08E+01	5.98E+00	1.23E+01	7.98E+00
4.00E-03	3.73E+01	5.97E+00	1.52E+01	7.97E+00
5.00E-03	4.07E+01	5.94E+00	1.64E+01	7.94E+00
6.00E-03	4.27E+01	5.90E+00	1.73E+01	7.90E+00
8.00E-03	4.52E+01	5.77E+00	1.85E+01	7.77E+00
1.00E-02	4.62E+01	5.58E+00	1.90E+01	7.57E+00
1.50E-02	6.00E+01	4.97E+00	2.93E+01	6.80E+00
2.00E-02	6.29E+01	4.41E+00	3.23E+01	5.89E+00
3.00E-02	5.07E+01	3.81E+00	2.09E+01	4.59E+00
4.00E-02	3.85E+01	3.59E+00	1.39E+01	3.98E+00
5.00E-02	2.89E+01	3.50E+00	1.00E+01	3.71E+00
6.00E-02	2.22E+01	3.46E+00	7.84E+00	3.57E+00
8.00E-02	1.43E+01	3.42E+00	5.74E+00	3.45E+00
1.00E-01	2.54E+01	3.40E+00	8.82E+00	3.40E+00
1.50E-01	1.41E+01	3.38E+00	5.67E+00	3.36E+00
2.00E-01	9.55E+00	3.38E+00	4.64E+00	3.35E+00
3.00E-01	6.36E+00	3.38E+00	3.97E+00	3.34E+00
4.00E-01	5.32E+00	3.37E+00	3.76E+00	3.34E+00
5.00E-01	4.86E+00	3.37E+00	3.66E+00	3.34E+00
6.00E-01	4.61E+00	3.37E+00	3.62E+00	3.34E+00
8.00E-01	4.37E+00	3.37E+00	3.57E+00	3.33E+00
1.00E+00	4.26E+00	3.37E+00	3.55E+00	3.34E+00
1.25E+00	4.20E+00	3.37E+00	3.54E+00	3.34E+00
1.50E+00	4.18E+00	3.37E+00	3.53E+00	3.34E+00
2.00E+00	4.21E+00	3.38E+00	3.54E+00	3.35E+00
3.00E+00	4.35E+00	3.40E+00	3.59E+00	3.38E+00
4.00E+00	4.54E+00	3.42E+00	3.65E+00	3.42E+00
5.00E+00	4.74E+00	3.45E+00	3.71E+00	3.47E+00
6.00E+00	4.94E+00	3.48E+00	3.77E+00	3.52E+00
8.00E+00	5.36E+00	3.54E+00	3.90E+00	3.62E+00
1.00E+01	5.76E+00	3.60E+00	4.03E+00	3.72E+00
1.50E+01	6.67E+00	3.73E+00	4.32E+00	3.95E+00
2.00E+01	7.43E+00	3.84E+00	4.57E+00	4.14E+00

Lastly, since photoelectric interaction rates scale at ~Z_{eff}^4, data from the Z_{eff} calculations suggest that, for all energies below 370 kVp, BiPVT will provide substantially higher x-ray interaction rates than both EJ-200 and EJ-256. This conclusion was not unexpected; however, the methodology employed herein to calculate Z_{eff} at various photon energies using the energy-dependent mass attenuation coefficients offers an alternative method to better quantify differences in expected x-ray interaction rates.

Computational Material Evaluation

Motivation and Description of Work

Detecting, locating, characterizing, and identifying unknown radiation fields is of paramount importance to the U.S. Department of Energy (DoE). Two important methods for the accurate characterization and identification of unknown radioactive materials include x-ray and fast neutron radiography. As discussed in Chapter 1, the optimal material for both imaging techniques, especially for use in man-portable systems, is organic plastic scintillators.

This section details an analysis of three scintillator materials that are either presently used or under consideration for radiography use. These materials include gadolinium-oxide (Gadox), cesium iodide (CsI), and a 21% bismuth-loaded polyvinyl toluene (BiPVT). Both Gadox and CsI are assessed in this report at thicknesses of 200 and 400 μm (because this range of thicknesses is used in commercial radiography panels) [45], while the 21% BiPVT is investigated using thicknesses between 1.27-5.08 cm, or 0.5 in to 2.0 in. The BiPVT is under development by Lawrence Livermore National Laboratory. In each case, the materials were evaluated in terms of expected sensitivity to both neutron and photon fields at discrete energies. The intended application of this research is to investigate the potential to pair the BiPVT with commercially available, low-cost amorphous silicon thin film transistor (TFT) photosensor arrays for radiography. As such, the thickness of the scintillation material is of concern because it directly affects the efficiency of photon and neutron sensing and because the overall weight and portability of the system is of interest.

Theory

a) Photons

To quantify the expected material sensitivity to photons at discrete energies, we use

$$Q = Q_0 e^{-N\mu t}, \qquad (14)$$

where Q is the total number of penetrating photons, Q_o represents the initial number of photons incident on the material, N is the material number density, μ is the total mass attenuation coefficients for interaction, and t represents the thickness of the material. Ultimately, the fraction of penetrating photons at thickness t, divided by the number of incident photons provides an approximation for the sensitivity of the material to photons at a given initial energy. Through algebraic manipulation, Equation 14 can provide this value more directly, which results in

$$1 - \frac{Q}{Q_0} = 1 - e^{-N\mu t}. \qquad (15)$$

Therefore, Equation 15 was used to theoretically evaluate each of the considered materials across a range of energies.

b) Neutrons

As discussed in Chapter 1, neutrons fail to produce direct ionization events when traveling through media due to their charge neutrality. Consequently, these particles do not interact with matter via the Coulomb force, but they instead deposit their energy discretely via collisions with other particles or atomic nuclei. Such collisions can result in either absorption or scattering events.

For the purposes of this research, MCNP6.2 is leveraged to assess the neutron sensitivity of each material, and a basic analytical solution is also provided, which is similarly rooted in Equation 15. As such, effective material cross sections were calculated for the 21% Bi-loaded PVT, which drove analytical assessments of neutron fluence penetration through the PVT.

Methodology

As discussed above, Equation 15 provides analytic values approximating the material sensitivities for photon and neutron calculations. Specific energy-dependent attenuation coefficients were drawn from NIST XCOM [39] for the constituent components of Gaddox, CsI, and BiPVT, and material-specific attenuation coefficients were calculated for each material from weight percentages provided by PNNL [38]. The same process was repeated for neutron transmission percentage calculations, with energy-dependent cross section data retrieved from the ENDF VII library. Using these calculated material attenuation coefficients and cross sections, as well as the reported densities for each material, expected theoretical determinations of photon and neutron sensitivity were calculated.

In addition to these calculations, MCNP6.2 was also used to evaluate these conclusions and refine the assessment of expected material sensitivity to both particle types. When applying both analytic and stochastic methods, the following data from Tables 4.5 and 4.6 were incorporated.

Table 4.5. List of specific material densities used in both analytic calculations and MCNP computations.

Densities, ρ (g/cm^3)		
CsI	Gaddox	PVT (21% Bi)
4.51	7.44	1.40

Table 4.6. List of element weight percentages used in both analytic calculations and MCNP computations.

Material Weight Percentages								
CsI		Gadox			BiPVT		
Cs	I	Gd	O	S	H	C	Bi
51.15%	48.85%	83.08%	8.45%	8.47%	6.72%	72.29%	21.00%

Additionally, the MCNP6.2 computations in this report utilized an idealized detector design. Specifically, the scintillator material of interest fully encapsulates the isotropic point source as a spherical shell, which was the case for evaluations using either neutrons or photons. This design maximizes particle interactions, which thereby reduces variance in the solution and statistical uncertainty; however, it is not representative of a practical experimental design. Despite this, the results are useful for rough predictions of particle interaction rates as a function of energy, although future evaluations using more conventional experimental designs must account for the distance and detector solid angle relative to the source. Figure 4.2 provides a simple schematic of the idealized detector design utilized in MCNP6.2.

To calculate the expected rate of energy-dependent particle interactions within each material, separate MCNP6.2 simulations were run using mono-energetic sources corresponding to discrete energy bins. In each case, a surface flux tally (F2) estimated the normalized flux penetrating the outer shell of the detector material, which provided convenient ratios for the flux remaining at the initial energy to the total flux escaping the detector. In other words, this value represented the percentage of particles exiting the detector material at the original source energy. However, shortcomings associated with this method include its failure to account for particles absorbed within the material, which could lead to a percentage overestimation, and particles that exit the detector material and then scatter back through it, which could produce a percentage underestimation. Consequently, this method only provides rough predictions of interaction rates.

Regardless, by multiplying the percentage value by the total number of particles crossing the outer detector surface, the fraction of penetrating particles at the original energy can be estimated. These particles are to be considered unperturbed, and by dividing this value by the total number of simulated particles entering the detector, the percentage of unperturbed particles escaping the detector can be calculated from MCNP6.2 estimates. Finally, subtracting this percentage from a value of one provides a final MCNP-derived estimate for the total percentage of particle interactions within a medium at a specific thickness and specific incident energy. In all cases, ENDF-VII/B libraries were utilized for particle interactions.

As expected, the probabilities for photon interaction decrease exponentially across the thickness of materials, and the rates of interaction within 400 µm of material are approximately twice those within only 200 µm. In both cases, the Gadox is expected to outperform the CsI across all energies for photon sensitivity.

Results

Utilizing the process described by Equation 15, analytical calculations for photon interaction rates within CsI and Gadox were conducted at material thicknesses of 200 or 400 µm, as shown in Figures 4.3 and 4.4.

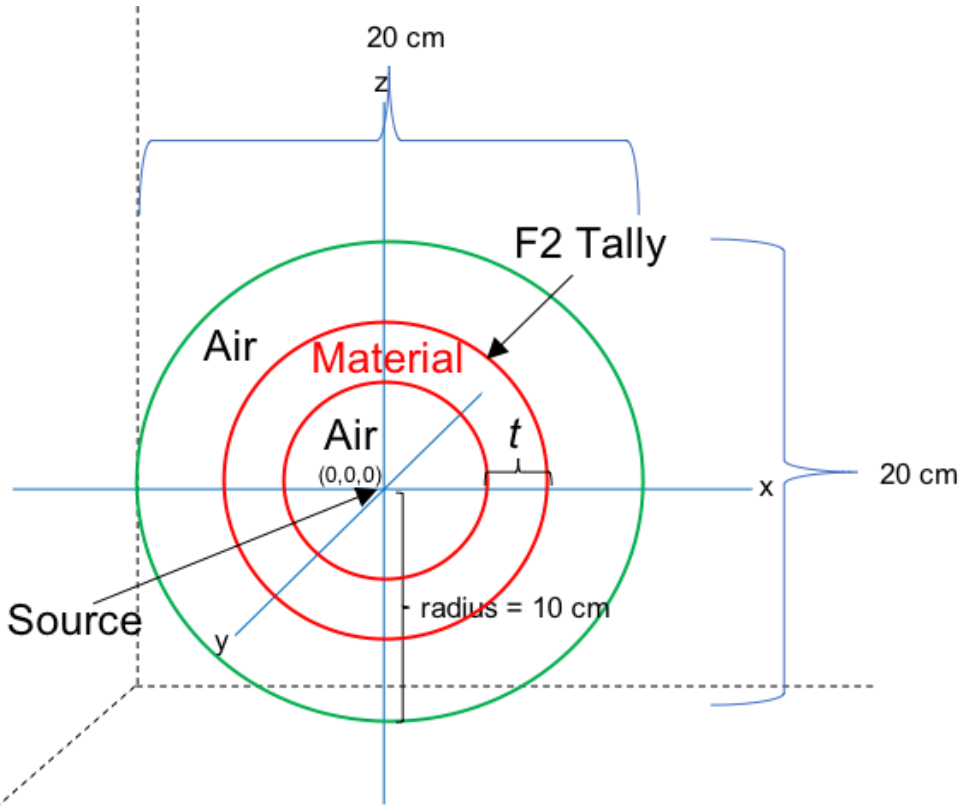


Figure 4.2. A graphic of the idealized spherical MCNP model used to evaluate various thicknesses, t, of material for both photon and neutron sensitivity. A F2 (surface flux tally) was utilized to assess the percentage of particle flux penetrating the material within the specific incident energy region of interest.

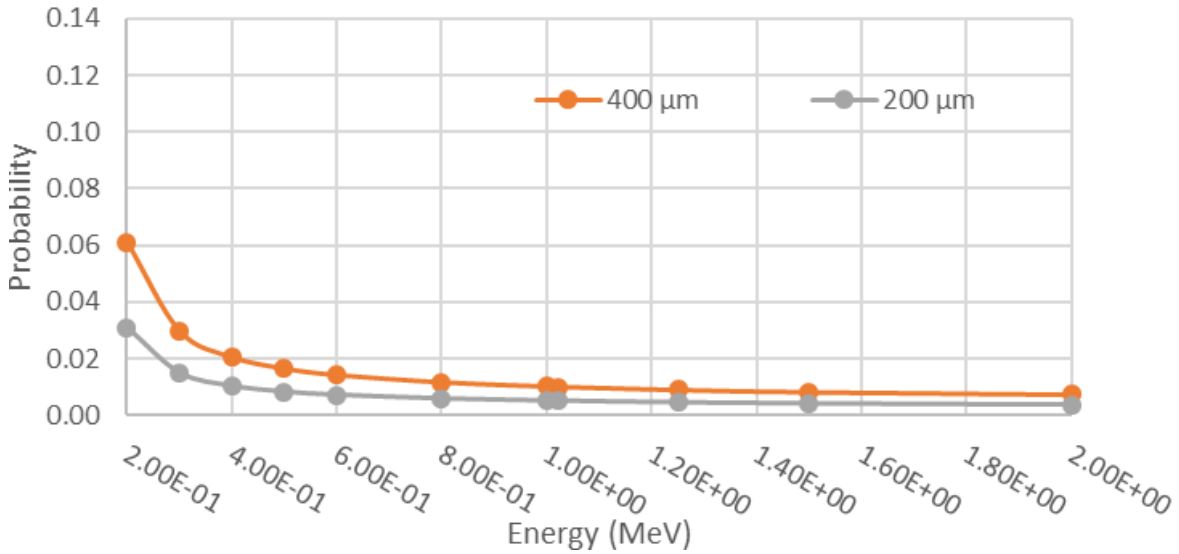


Figure 4.3. Photon interaction probability within CsI at thicknesses of 200 and 400 µm and energies between 200 keV and 2 MeV

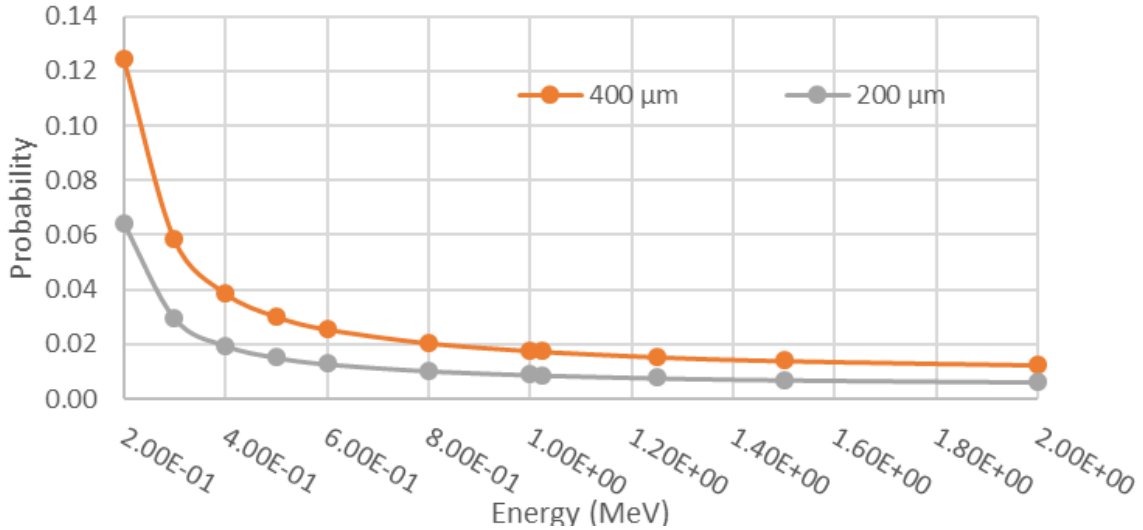


Figure 4.4. Photon interaction probability within Gadox at thicknesses of 200 and 400 µm and energies between 200 keV and 2 MeV

For the BiPVT, the same process was applied to estimate the interaction rates for photons within the material at 2.54 and 5.08 cm thicknesses. These results are provided in Figure 4.5. As shown, the BiPVT is expected to outperform both the Gadox and CsI, largely due to the differences in the considered thicknesses. These rates of interaction also decrease exponentially as expected.

MCNP6.2 was then utilized to provide a more accurate estimate for the rates of interaction within each material. Beginning with the CsI, MCNP6.2 estimates were computed for a 400 μm thickness and the results from F2 tallies agreed within 1.5% across all energy values considered, in absolute terms. In relative values, the disparity between data sets averaged ~60%, and this was likely due to some photons never penetrating the detector, which lowered the estimate of total flux. The results for both methods are presented in Figure 4.6. For the Gadox material at the same thickness, MCNP6.2 returned results within 2% of the absolute values calculated analytically, as shown in Figure 4.7. In relative terms, the data sets averaged a ~72% disparity, which was also likely due to scattered photons never penetrating the detector, which reduced the estimate of total flux present. The larger difference, therefore, in average value between the analytic and simulated data is attributed to the higher density and effective atomic number of Gadox over CsI.

Lastly, the results for both the 2.54 and 5.08 cm 21% Bi-loaded PVT were also computed and compared to analytic calculations of expected interaction rates. Figure 4.8 provides these data and demonstrates the agreement between the analytic and stochastic methods employed. From these results, a more comprehensive assessment of photon interaction rates across a wider variety of PVT thicknesses was considered. Figure 4.9 provides data for MCNP6.2-derived interaction rates, which reveals the greatest single increase in efficiency occurs between 1.27 cm and 2.54 cm.

Based on the demonstrated agreement between the analytic and computational methods used to determine photon interactions, the same computational methodology was applied to determine MCNP6.2-estimated neutron interaction rates for each material. Starting with evaluations of both Gadox and CsI at a thickness of 400 μm, the methodology described above provided the data shown in Figure 4.10. As shown, these data all fall below a one percent chance of interaction, and the uncertainty regarding these values is high due to the thickness of material used. More particles could have been run to reduce these uncertainties; however, the overall assessment of neutron sensitivity at that thickness would not change substantially. At thicknesses of less than a centimeter, these materials appear to offer no practical sensitivity to neutrons with the kinetic energies considered, which is well-documented and understood. These computations were conducted for the purposes of material analysis completeness.

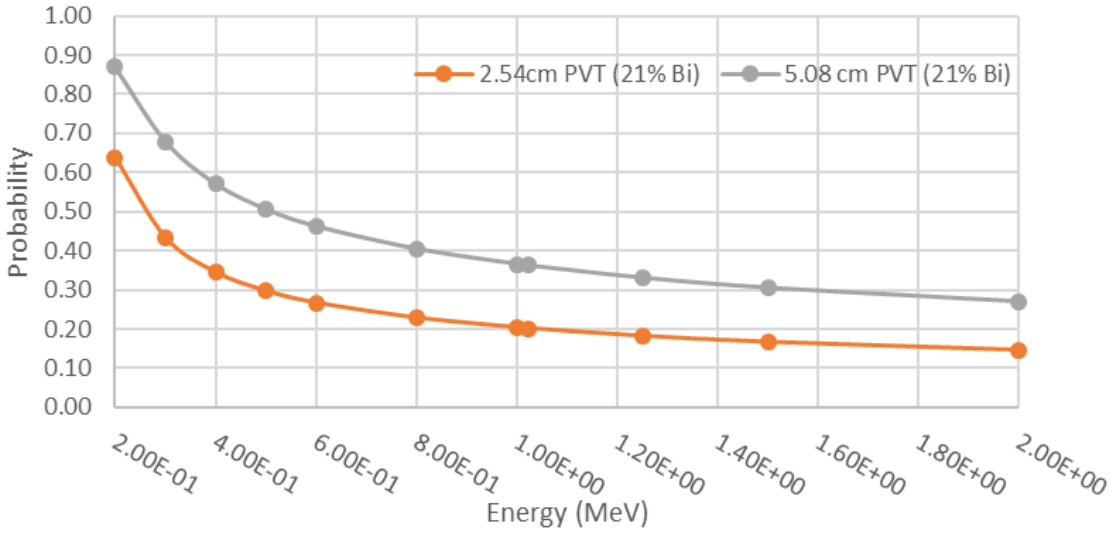


Figure 4.5. Photon interaction probability within 2.54 cm and 5.08 cm thick 21% BiPVT at energies between 200 keV and 2 MeV.

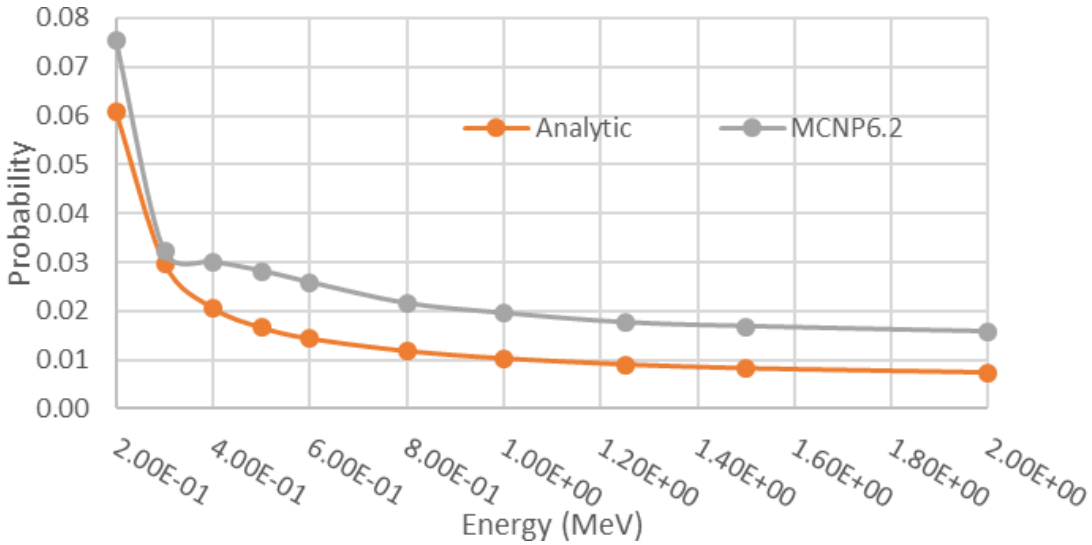


Figure 4.6. Photon interaction rates derived both analytically and computationally (MCNP6.2) for 400 μm of CsI.

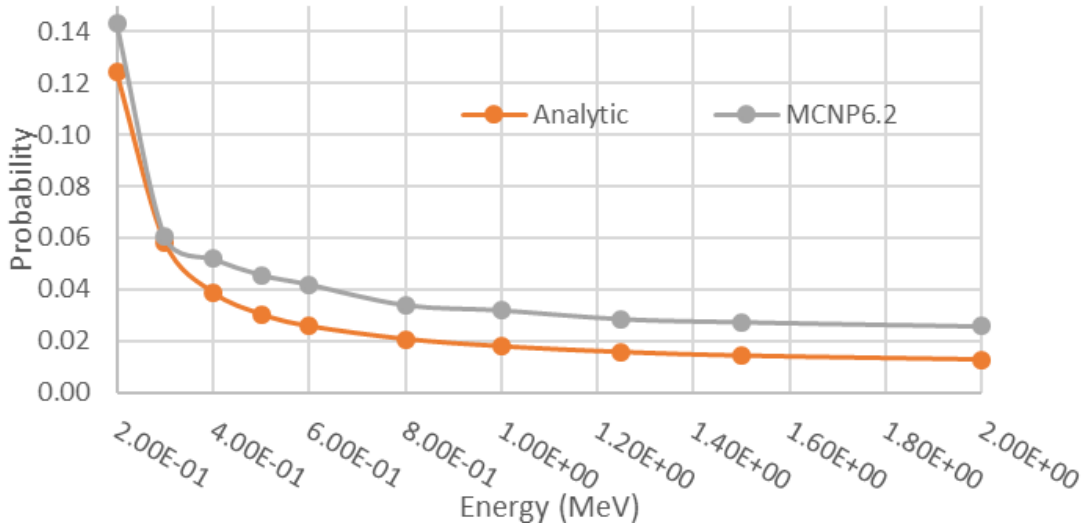


Figure 4.7. Photon interaction rates derived both analytically and computationally (MCNP6.2) for 400 μm of Gadox.

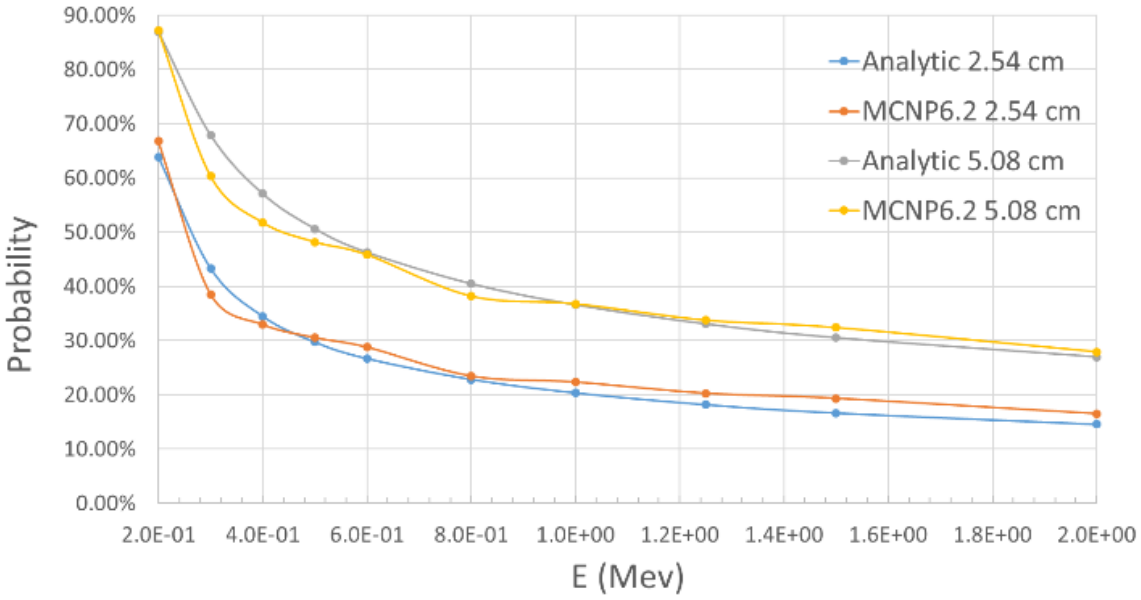


Figure 4.8. Photon interaction rates derived both analytically and computationally (MCNP6.2) for 2.54 and 5.08 cm of 21% BiPVT.

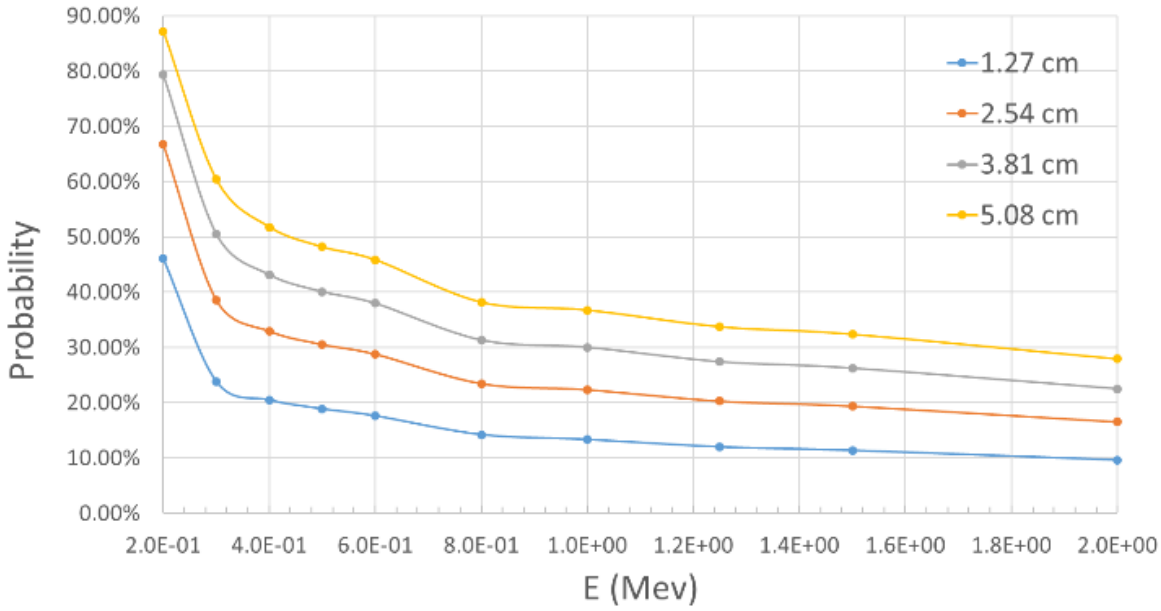


Figure 4.9. Photon interaction rates derived computationally via MCNP6.2 for 1.27 to 5.08 cm of 21% BiPVT.

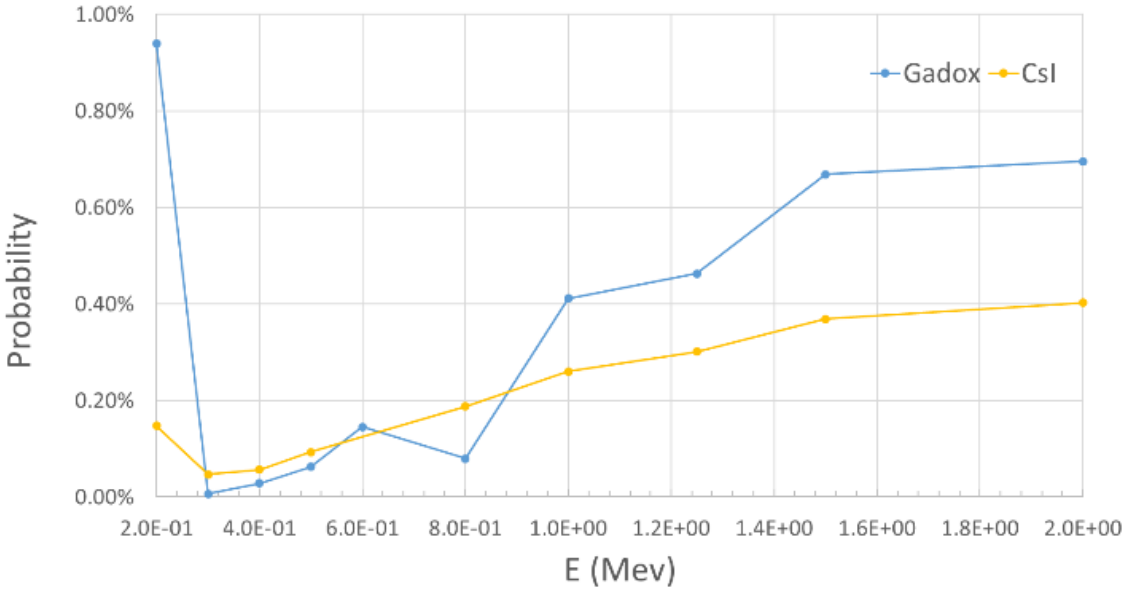


Figure 4.10. The energy-dependent interaction rates calculated from MCNP6.2 estimates of surface flux tallies and neutron counts.

Based on these simulated results, the rate of neutron interactions within BiPVT at these energies is expected to be significantly higher than those found in Gadox and CsI. This is likely due as much to the increased thickness of materials as well as the differences in its elemental composition. Figure 4.11 provides the graphical depiction of the analytically derived neutron interaction rates across energies from 6 keV to 14.1 MeV, while Figure 4.12 provides the MCNP6.2-derived computational estimate of the same values. The disparities evident between the values shown in both plots are assessed as due to the previously discussed simulation shortcomings. Additionally, as demonstrated previously for photons, both the analytical and computational results indicate that the largest gains in neutron sensitivity occur over thicknesses between 1.27 cm and 2.54 cm. This is true across all energies assessed herein.

Conclusions

Based upon the results discussed above, a thickness near one inch (2.54 cm) of 21% BiPVT appears to offer an optimal balance between neutron and photon sensitivity, while remaining relatively thin and lightweight. In addition to the sensitivities assessed herein, the 21% BiPVT also provides other characteristics making it commensurate with traditional photon scintillators. For example, it emits light wavelengths between 500-550nm, which corresponds to a 60-80% quantum efficiency in the spectral response of the TFT photodiodes [45]. This is comparable to both Gadox and CsI(Tl), which provide primary emission peaks of ~550 nm. Consequently, the 21% BiPVT appears ideally matched for its intended purpose and is, therefore, recommended for future use over the considered alternatives. For multiple reasons, such a material and thickness likely will provide optimal efficiency when paired with a TFT and utilized for x-ray and neutron radiography.

Initial Radiographic Characterization of a BiPVT Array

Simulations

These initial MCNP6.2 simulations utilize rectangular TMESH3 tallies to estimate energy deposition within pixelated arrays. For both the BiPVT and EJ-200 materials, a 2×2 mm pixel face is selected due to expected scattered proton and electron pathlengths. Specifically, based on the continuous slowing down approximation (CSDA) model used by NIST PSTAR [46] and an assumed EJ-200 density of 1.023 g/cm^3, neutron-induced 14 MeV protons recoil >2 mm. If pixel dimensions are too small, charged particles may routinely scatter beyond pixel boundaries and deposit significant portions of their energy in adjacent pixels. For example, protons scattered at 30° relative to the path of incident 14 MeV neutrons will depart at energies of ~10.5 MeV, which means they are expected to travel ~1.3

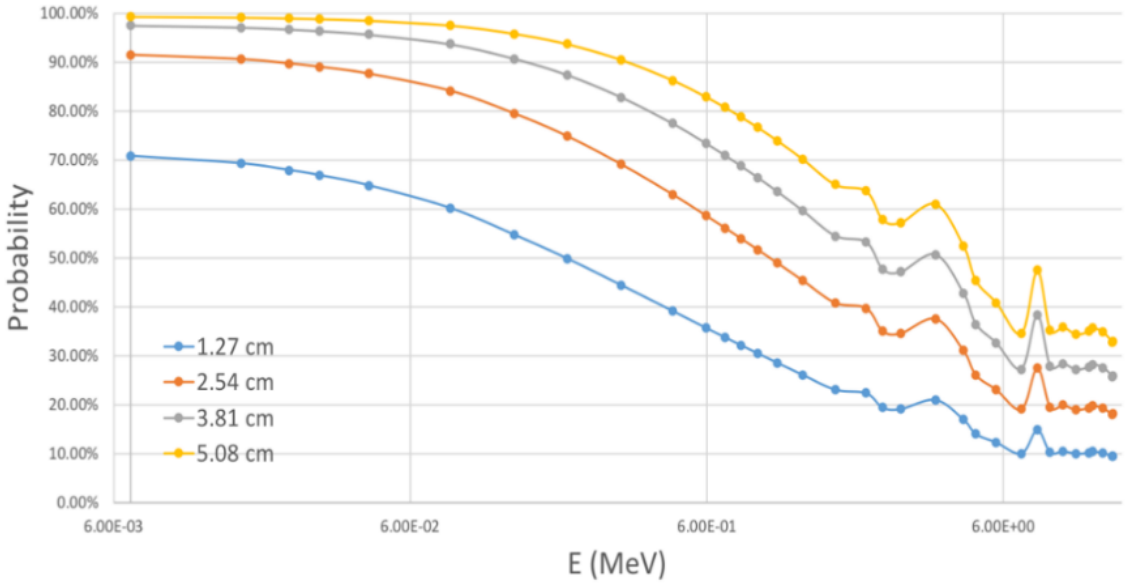


Figure 4.11. Neutron interaction rates derived analytically via Equation 15 for 1.27 to 5.08 cm of 21% Bi-loaded PVT.

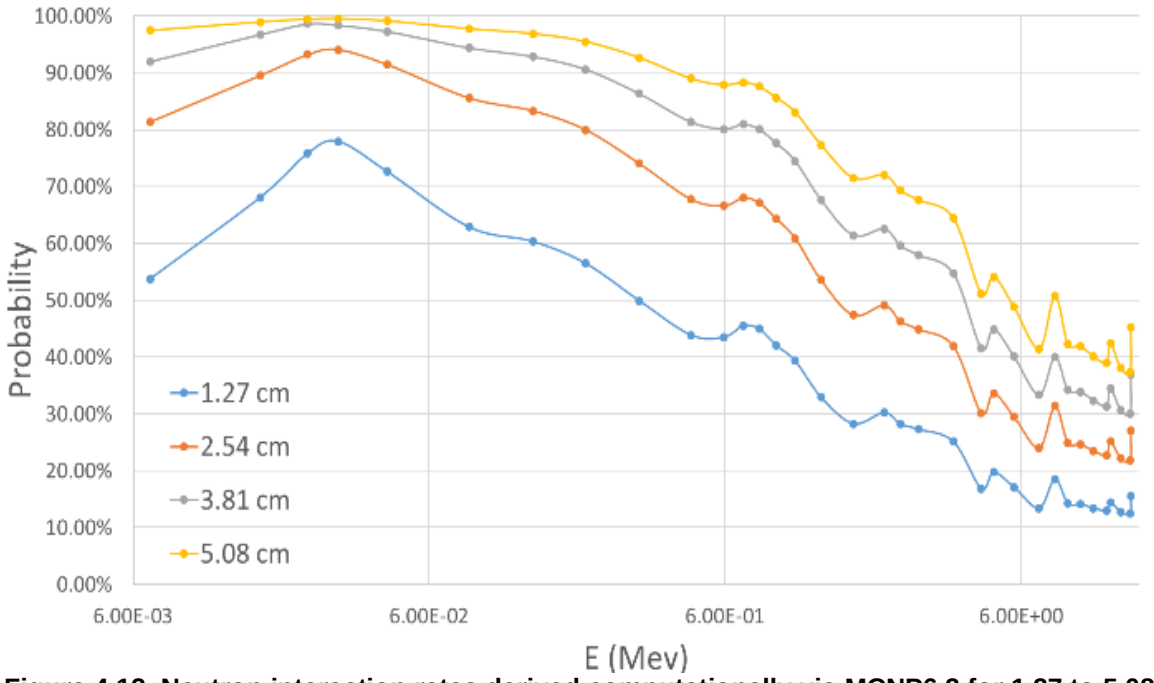


Figure 4.12. Neutron interaction rates derived computationally via MCNP6.2 for 1.27 to 5.08 cm of 21% BiPVT.

mm from the interaction site and ~0.65 mm orthogonal to the original neutron path. Therefore, protons scattered at 30° from anywhere within a pixel with a cross section <1.69 mm^2 (1.3×1.3 mm) may likely enter an adjacent pixel. Since TFT panels measuring light scintillations typically operate in integration mode, this effect would be expected to reduce the position and image resolution. Based on this understanding, a pixel dimension of 2×2 mm (4 mm^2 pixel cross section) is selected to reduce the likelihood of secondary particles depositing energy in neighboring pixels. This dimension was used for both EJ-200, as well as the BiPVT, which has a density of 1.4 g/cm^3. All simulated arrays cover a total area of 146×146 mm, thereby producing 73×73 voxels, which corresponds to the active surface area of a commercial Varex PaxScan 1515DXT-I radiographic panel.

For photon computations, the arrays are exposed to three million particles from 150, 270, or 370 kV bremsstrahlung x-ray sources. Photon energy distributions are simulated using a commercially available x-ray generator spectrum [47] equally distributed across the arrays from a point source centered on the detector at 1000 mm distance. A tungsten duplex wire image quality indicator (IQI), consistent with established standards [48, 49], is simulated in MCNP6.2, as shown in Figure 4.13. Within Figure 4.13, listed distances correspond to the wire diameters and distances between the wire pairs. Mean free path distances for 150, 270, and 370 keV photons in tungsten are 0.33, 1.29, and 2.36 mm, respectively.

For 14 MeV neutron fields, duplex wires are insufficient due to the low probability for interactions, so separate IQIs for neutron measurements are simulated using both lead and polyethylene slabs. The slabs are arranged such that the gaps between them are consistent with the spaces between the duplex wires, although all slabs are simulated with a vertical thickness of 25.4 mm from the face of the array, as shown in Figure 4.14. For reference, one mean free path for a 14 MeV neutron through lead is ~56.6 mm. Since no standards exist for fast neutron radiography, this IQI was designed to replicate the duplex wire-based system used for x-rays.

These IQI facilitate computational estimates of the modulation transfer function (MTF), which is used to determine the basic spatial resolution (SRb) values for each array, as described below. For the x-ray fields, the duplex wires provide a series of line spread functions at each diameter and equivalent spacing, while the

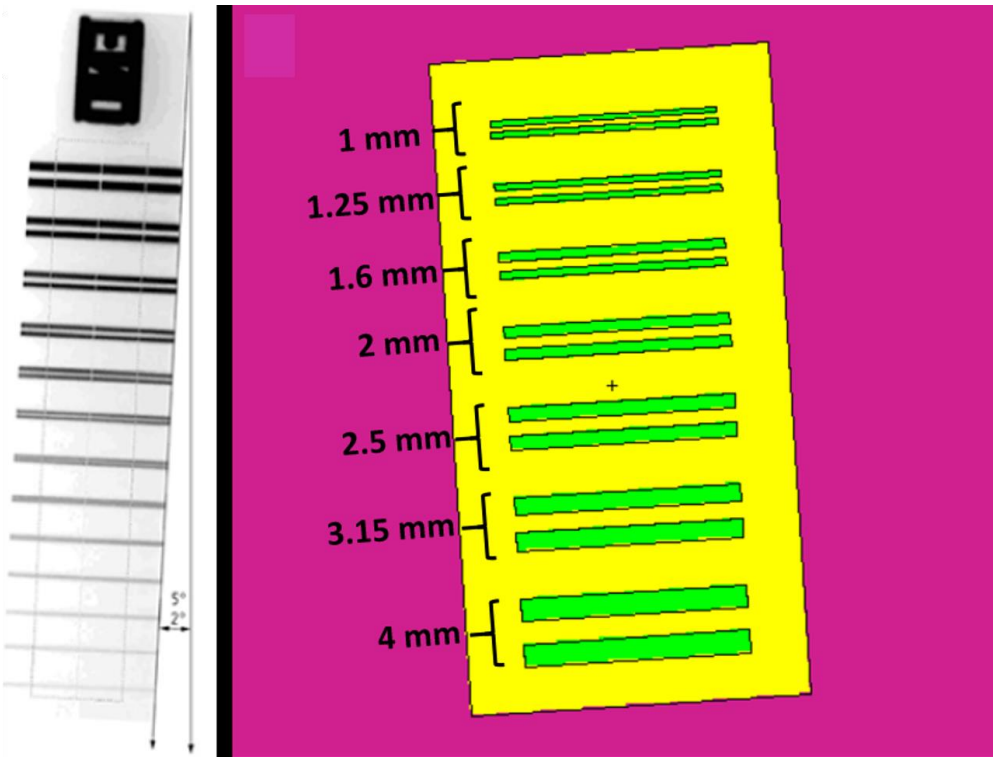


Figure 4.13. Images of duplex wire sets, where a version provided in ASTM E2002 is on the left [48], and the image on the right represents the MCNP6.2 model of tungsten duplex wires in green, polyethylene in yellow, and air in pink. This served as the IQI for all BiPVT and EJ-200 photon image computations.

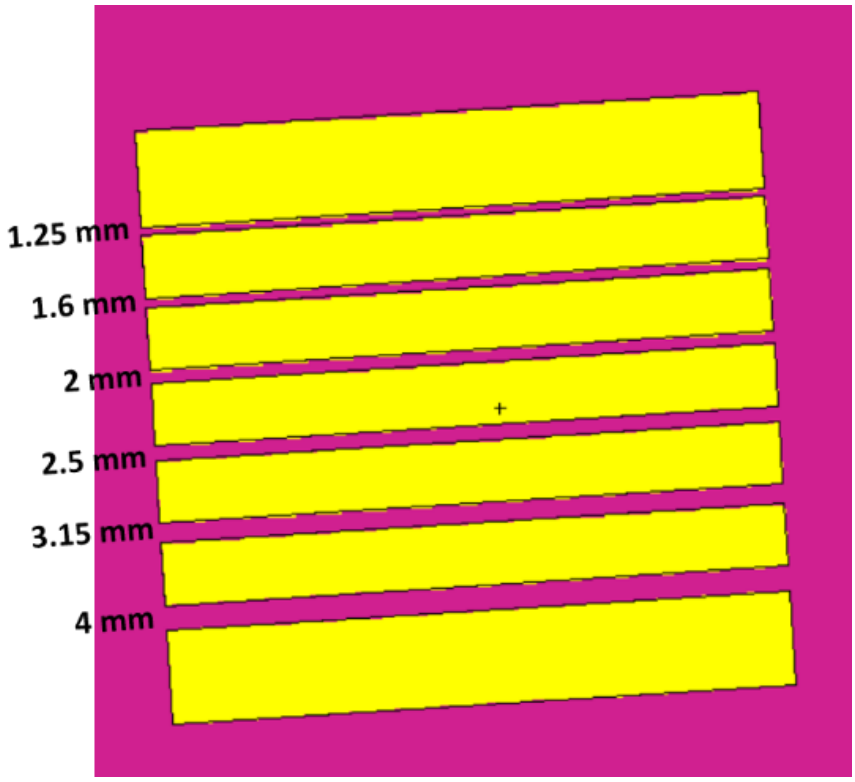


Figure 4.14. An image of the IQI used for 14 MeV neutron measurements, where yellow represents either polyethylene or lead, and the MTF and SRb values are determined from contrast fluctuations computed using decreasing gap widths between the shielding material, which are consistent with established duplex wire IQI diameters.

lead and poly slabs used in the neutron computations provide edge spread functions. Of course, these simulations fail to account for image noise, which is a limiting factor for flat panel radiography. The MTF is plotted as the normalized average modulation recorded between the duplex wires versus their thickness in line pairs per mm (lp/mm). The MTF provides a means to quantifiably evaluate spatial resolution and object contrast for an imaging system [50]. Modulation, M, is typically defined as

$$M = \frac{I_{max} - I_{min}}{I_{max} + I_{min}}, \qquad (16)$$

where I_{max} and I_{min} represent maximum and minimum pixel intensities for imaged features. ASTM standards require the IQI for radiography to be angled between 2°-5° from the pixel column line [49], so the simulated IQIs are offset at an angle of 3.5°. After the MTF is acquired, SRb values are determined using the equation

$$SRb = D_1 - \frac{(D_1 - D_2)(R_1 - 20)}{R_1 - R_2}, \qquad (17)$$

where D_1 is the diameter of the smallest wire pair with >20% resolution of the space between the two wires, D_2 is the diameter of the largest wire pair with <20% resolution of the gap, and R_1 and R_2 are the modulation values corresponding to the two wire pairs [51]. SRb is calculated from the linear interpolation of the wire pair thicknesses, using the smallest wire pair with a recorded dip in modulation between the wires of >20%. In this way, Equation 17 quantifies the degree to which an array distinguishes between image intensities for closely spaced points as an ideal detector, and calculations of SRb have an associated error of ±5% [52]. However, SRb is based on normalized modulation values that, for the purpose of direct comparisons, intentionally exclude energy, geometric, and material-dependent particle interaction efficiencies, which directly contribute to material light yields.

Results

MCNP6.2 TMESH computations produced simulated radiographic images for both the BiPVT and EJ-200 voxelated arrays at thicknesses of 10, 15, 20, and 25 mm. These images were analyzed using the MATLAB Image Processing Toolbox (v10.3) and the ImageJ Image Processing and Analysis in Java (v1.52a) software. Pixel intensity values were assigned using MCNP6.2 estimates of total energy deposition, and the predicted differences per pixel were clearly discernable in the generated images when exposed to simulated x-ray and neutron fields, as shown in Figures 4.15 and 4.16, respectively.

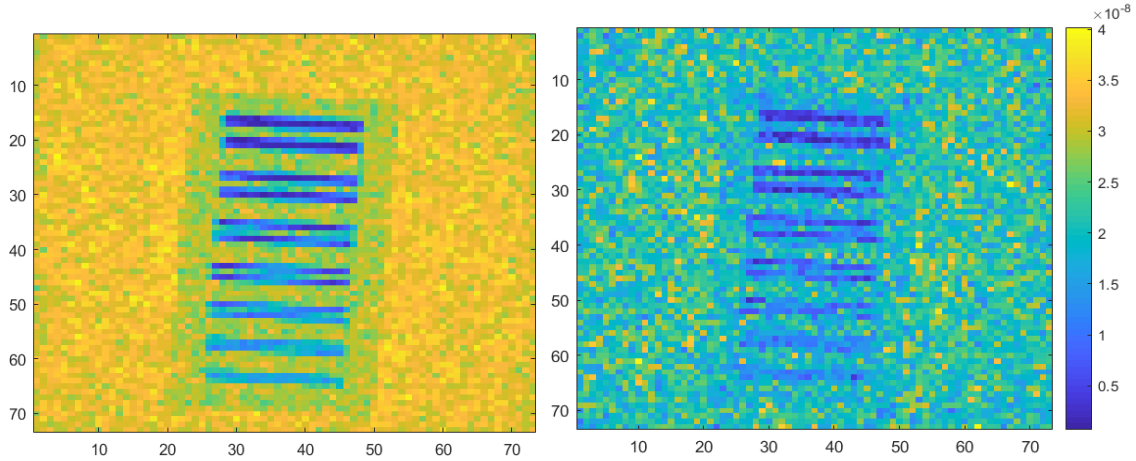


Figure 4.15. Comparison of the MCNP6.2-generated BiPVT and EJ-200 radiographs of the duplex wire IQI when exposed to 150 kVp x-rays at an array thickness of 10 mm. The BiPVT image is on the left, while the EJ-200 image is on the right. All axes refer to pixel number within the arrays.

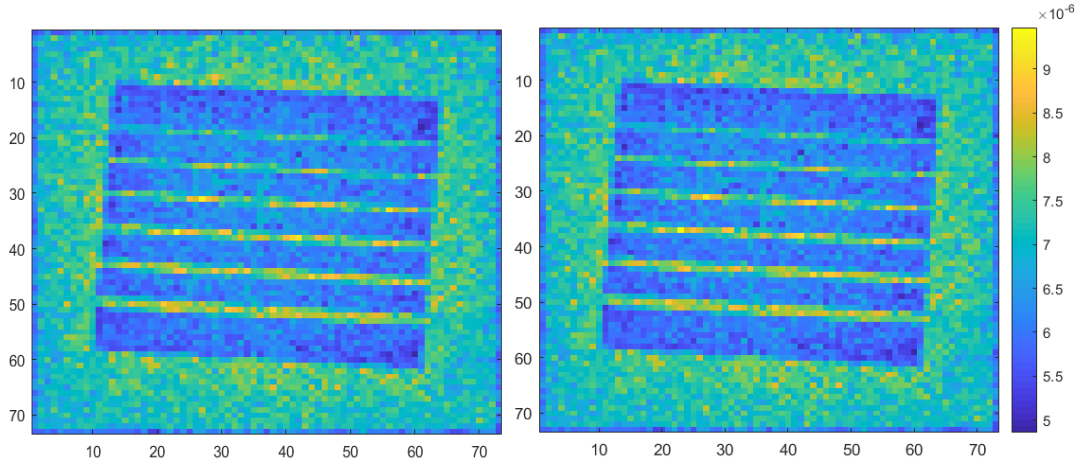


Figure 4.16. Comparison of the MCNP6.2-generated BiPVT and EJ-200 radiographs of the lead slab IQI when exposed to 14 MeV neutrons at an array thickness of 15 mm. The BiPVT image is on the left, while the EJ-200 image is on the right. All image axes refer to pixel number within the array.

MCNP6.2 estimates of x-ray energy deposition were normalized to provide MTF values using Equation 16, and the results of this analysis are provided in Table 4.7 and plotted in Figure 4.17. These calculations suggest that BiPVT and EJ-200 offer statistically equivalent SRb values at all energies and pixel depths at 150 kVp. In the 270 kVp x-ray fields, the EJ-200 is shown to provide superior SRb at pixel depths of 25 mm. Lastly, in 370 kVp x-ray fields, EJ-200 is expected to provide superior SRb to BiPVT at thicknesses of 20 and 25 mm. For all other pixel thicknesses for the x-ray distributions considered, the two materials are expected to provide statistically equivalent values of SRb. Calculated SRb values for EJ-200 and BiPVT from the computed neutron images were found to agree within the uncertainties for all thicknesses and IQI. All SRb calculation results and associated uncertainties are provided in Table 4.7.

Discussion

The inability of BiPVT to match the SRb values estimated for EJ-200 at 25 mm in the 270 kVp field and at 20 and 25mm in the 370 kVp environment is attributed to the presence of increased internal scatter within the higher-Z material. This is a recognized contribution to geometrical unsharpness in digital detector arrays (DDAs) which, combined with other factors such as scatter from the imaged object(s), degrades SRb [53]. However, since no other differences between the comparable simulations exist (i.e. energy spectra, object type or location, etc.), increased relative rates of internal detector scatter is the only reasonable conclusion. Further simulations and discussion in the following section attempt to better explain these predicted differences in resolution.

Lastly, the SRb calculations listed in Table 4.7 only account for estimates of deposited energy, so they do not include estimates of light emission, transport, quantum efficiency, or panel noise, nor do they include physical differences in pixel spacing and array geometry caused by ESR and adhesive. Consequently, the predicted SRb values for BiPVT and EJ-200 are expected to more closely agree with measured results once those simulated components of performance are added. Additionally, since SRb is calculated from the normalized modulation response, it does not provide a final conclusive evaluation of comparative array performance. Consequently, these findings justify further investigations and physical experimentation to quantitatively evaluate the comparative performance of BiPVT pixelated arrays with other alternatives.

Table 4.7. Simulated Basic Spatial Resolution (SRb) values for BiPVT and EJ-200 in x-ray fields (top) and the 14 MeV neutron field (bottom), as well as associated uncertainties.

	150 kVp		270 kVp		370 kVp	
Thickness	BiPVT	EJ-200	BiPVT	EJ-200	BiPVT	EJ-200
10mm	2.11 ± 0.11	2.09 ± 0.10	2.13 ± 0.11	2.12 ± 0.11	2.12 ± 0.11	2.08 ± 0.10
15mm	2.12 ± 0.11	2.02 ± 0.10	2.12 ± 0.11	2.07 ± 0.10	2.11 ± 0.11	2.02 ± 0.10
20mm	2.11 ± 0.11	2.02 ± 0.10	2.10 ± 0.11	2.01 ± 0.10	2.11 ± 0.11	1.92 ± 0.10
25mm	2.11 ± 0.11	2.06 ± 0.10	2.09 ± 0.10	1.91 ± 0.10	2.10 ± 0.10	1.90 ± 0.09

	Lead Target		Poly Target	
Thickness	BiPVT	EJ-200	BiPVT	EJ-200
10mm	1.94 ± 0.10	1.90 ± 0.10	2.39 ± 0.12	2.37 ± 0.12
15mm	1.95 ± 0.10	1.91 ± 0.10	2.41 ± 0.12	2.39 ± 0.12
20mm	1.99 ± 0.10	1.96 ± 0.10	2.44 ± 0.12	2.43 ± 0.12
25mm	2.07 ± 0.10	2.03 ± 0.10	3.65 ± 0.18	3.53 ± 0.18

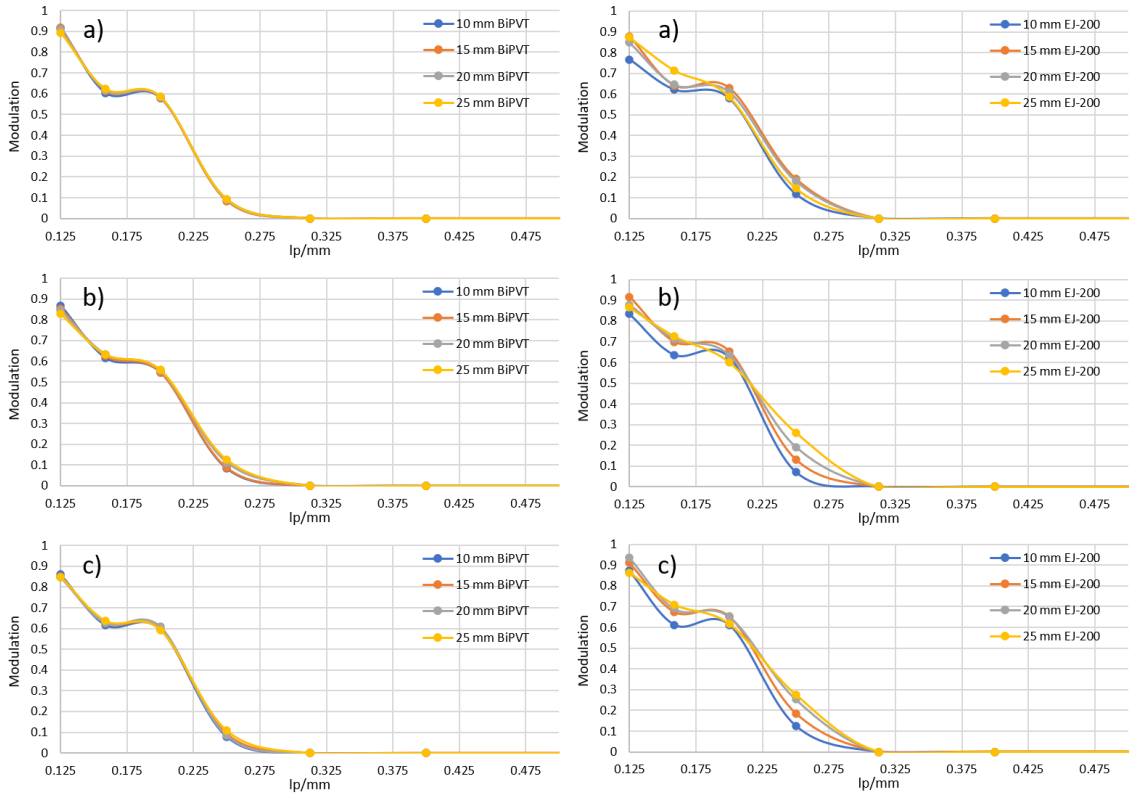


Figure 4.17. Comparison of the MCNP6.2-generated BiPVT and EJ-200 MTFs measured from duplex wire IQI radiographs, where x-ray energy is a) 150 keV, b) 270 keV, and c) 370 keV x-rays. The BiPVT MTF plots are on the left, and the EJ-200 MTF plots are on the right.

Conclusions

Of the materials evaluated, the results suggest an optimal thickness of 25 mm for experimental x-ray and neutron SRb comparisons due to the greatest disparity in x-ray SRb values occurring at that thickness. However, 20 mm offers nearly the same difference in SRb values and corresponded with the thickness of sample material provided by LLNL. Despite predictions of poorer SRb provided by BiPVT at these thicknesses, the computational comparisons conducted herein, as well as previous evaluations of interaction efficiencies, suggest BiPVT offers significantly enhanced detection performance over EJ-200 at all practical energies for portable x-ray radiography. These initial conclusions support further investigation of BiPVT for DPI radiography applications to support national safety, security, and safeguards.

Investigation of Internal X-ray Scatter within BiPVT and EJ-200

To better explain the predicted disparities in specific x-ray SRb values obtained via modeling of the duplex wire IQI, additional simulations were performed. These sought to estimate the relative amount of pixel crosstalk caused by the leakage of scattered particles (i.e. x-rays and electrons) across variable lengths of adjacent 2×2 mm pixels of BiPVT and EJ-200 when exposed to 150, 270, or 370 kVp x-rays. For these environments, internal scatter can include contributions from both photoelectrons and incoherent scatter, the latter contributing by either Compton electrons or the down-scattering of a photon to a lower energy and different direction, thereby increasing the likelihood it deposits its energy in a neighboring pixel. For each of these environments, internal scatter within BiPVT is expected to occur at higher rates than within EJ-200 due to its significantly greater electron density, as detailed in Table 4.3.

Simulations

MCNP6 was utilized to simulate nine pixels, each with pixel faces of 2×2 mm and arranged as a 3×3-pixel array. A 2×2 mm planar source located 10 cm from the array was aligned with the central pixel and directed all simulated particles only into that pixel. Particles were distributed uniformly across this plane and transited through vacuum to reach the array, thereby preventing scatter from occurring prior to interactions with the array material. No spacing was used to separate the arrays, so the design was equivalent to the TMESH3 configuration described earlier. Figure 4.18 provides an illustration of the design, although the thickness of the array shown is not representative of the values used.

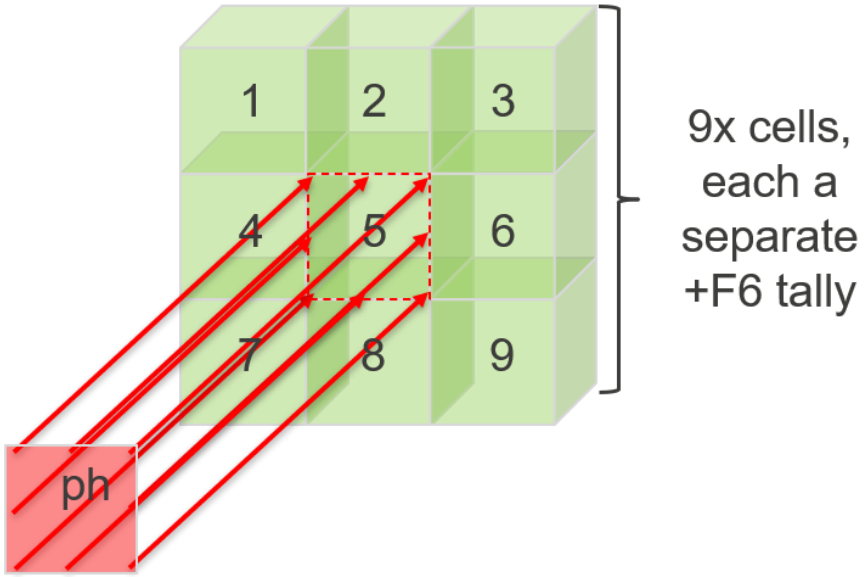


Figure 4.18. Conceptual image of the simulated array design used to estimate pixel crosstalk in BiPVT and EJ-200 for 150, 270, and 370 kVp x-ray fields. For each material and energy region the array was simulated at thicknesses of 10, 15, 20, or 25 mm, commensurate with the energies and thicknesses used in the duplex wire evaluations of SRb.

Source terms for 150, 270, and 370 kVp x-ray distributions matched those used in the duplex wire evaluations, and +F6 tallies recorded deposited energy within all nine of the pixels, individually. Lastly, variable array thickness was evaluated at 10, 15, 20, or 25 mm with 2M particles simulated. This enabled MCNP6 tallies of energy deposition to converge with uncertainties below 4% for all evaluations.

Results

MCNP6 returned estimates of energy deposition in units of MeV/g, and these values were normalized for pixel mass based on the specific material properties and volumes. Since image resolution is independent of particle interaction efficiency, all estimates of pixel crosstalk are presented here as a percentage of the energy deposited within the central pixel. For the purposes of this comparison, predictions of energy deposition within each pixel adjacent to the central pixel (pixels 2, 4, 6, and 8 in Figure 4.18) were averaged to provide a total estimate of pixel crosstalk in one direction. The values for each of these estimates are plotted in Figure 4.19.

When considering the effects of pixel energy crosstalk on SRb, a lower percentage of crosstalk energy in these simulations is expected to correlate with better SRb because it suggests a greater percentage of the deposited energy is effectively localized. It follows then, that a higher percentage of pixel crosstalk energy would correlate to worse values of SRb because a greater fraction of deposited energy within a given pixel is scattered into neighboring pixels, thereby reducing spatial resolution. Based upon this analysis, the simulated data offer a plausible explanation for the comparative performance of EJ-200 and BiPVT for the duplex wire evaluations. For the 150 kVp field, percentages of relative pixel crosstalk remain consistent between EJ-200 and BiPVT for all thicknesses at a difference of ~0.63%. This might indicate no significant change in relative SRb values is expected between 2×2 mm-pixel arrays made from BiPVT and EJ-200. Interestingly, this behavior is reflected in the SRb values estimated across all array thicknesses at 150 kVp in Table 4.17, in which all SRb values for BiPVT and EJ-200 agreed within the provided uncertainties.

In contrast, the percentage of pixel energy crosstalk at 270 kVp decreases for EJ-200 and increases for BiPVT. Additionally, the disparity between these percentages grows with increasing array thickness, shifting from a difference of 1.6% at 10mm to 1.78% at 25mm. This behavior suggests that BiPVT SRb values may be closer to those of EJ-200 at 10mm and further apart at 25mm, which is supported by the simulated results provided in Table 4.17. In fact, at a thickness of 25mm, EJ-200 is predicted to offer a statistically significant improvement in SRb over that provided by BiPVT.

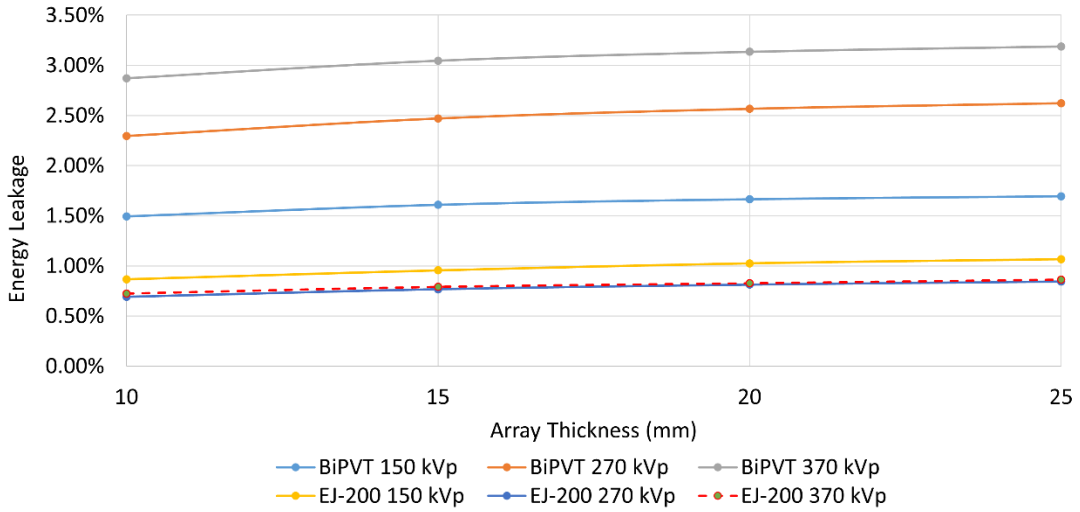


Figure 4.19. Plot of estimated pixel energy crosstalk to adjacent pixels as a fraction of total energy deposited in the central pixel.

Lastly, for the 370 kVp x-ray field, the estimated percentages of relative pixel crosstalk for EJ-200 and BiPVT are predicted to diverge to a greater extent than at 270 kVp. Specifically, the disparity in crosstalk percentages between the two grows from 2.15% at 10mm to 2.32% at a 25mm array thickness. As before, this behavior suggests EJ-200 may offer improved SRb over BiPVT at 25mm, while providing more equivalent values of SRb at shorter array thicknesses. Again, these relative percentages of pixel energy crosstalk at 370 kVp reflect the values simulated in Table 4.17, where EJ-200 was predicted to outperform BiPVT in SRb at array thicknesses of 20mm and 25mm. For 370 kVp x-rays interacting in pixels matching those of the physical arrays, specifically 2×2×19 mm, this equates to a total estimate of ~4.5% and ~18% pixel crosstalk in EJ-200 and BiPVT, respectively. Therefore, x-ray scatter within the BiPVT pixels is expected to degrade both measured and simulated SRb values.

Discussion

The simulated results demonstrate that, for pixels with 2×2 mm dimensions, crosstalk is expected to occur in BiPVT to a greater extent than for EJ-200. This is believed to be due to the higher electron density present within BiPVT relative to EJ-200, as previously calculated. This material property increases BiPVT's intrinsic efficiency for PE absorption, as well as the likelihood for incoherent scatter at higher x-ray energies. Photons and electrons from incoherent scatter typically possess greater probabilities for crossing pixel boundaries due to their higher average energies. Of course, this is true for both BiPVT and EJ-200; however, for particles scattered beyond initial pixel boundaries, BiPVT provides the greater probability for secondary interactions within the array due to its increased interaction efficiency, thereby contributing to pixel crosstalk. Interestingly, the reliance of EJ-200 upon signal generated almost entirely from incoherent scatter is concluded to be a benefit to its spatial resolution performance because down-scattered photons are less likely to interact again. The combined effects from PE electrons and incoherent scatter leaking into adjacent pixels are believed responsible for the simulated pixel crosstalk examined here, although the exact partition of leaked energy from these sources is not defined at this time.

Additionally, the relationship predicted between relative rates of pixel crosstalk in EJ-200 and BiPVT appears to follow previous evaluations of SRb simulated for each array across various x-rays energies and array thicknesses. Therefore, these simulations are believed to demonstrate the potential impact of higher probabilities of x-ray scatter and pixel crosstalk on evaluations of SRb for BiPVT, which are expected to degrade its measured spatial resolution relative to EJ-200. This is predicted to be especially impactful at 270 kVP for array thicknesses of 25mm and at 370 kVp at array thicknesses of 20mm and 25mm, as demonstrated in Table 4.17. Of course, the signal expected from BiPVT due to its significantly higher interaction probabilities for PE absorption will factor into evaluations of overall

performance; however, for the purposes of evaluating SRb, those benefits are not applied.

CHAPTER FIVE -

EXPERIMENT DESIGN ANALYSIS AND CONSIDERATIONS

This chapter addresses a series of topics and brief investigations that provide foundational support to conclusions drawn from analysis of the experimental and computational data. From the fabrication of the physical arrays to sources of DDA noise contribution, the analyses presented herein enable a more thorough understanding of the physical environment and its potential impact on the measurements. As such, these investigations and findings informed both the experimental design and initial predictions of array performance.

Array Fabrication

Pixel Dimensions

For both x-ray and neutron evaluations, a 2×2 mm pixel face was selected for the BiPVT, EJ-200, and EJ-256 materials due to expected scattered electron and proton pathlengths. Specifically, based on CSDA data [46] and an assumed EJ-200 density of 1.023 g/cm^3, neutron-induced 14 MeV protons recoil >2 mm. Therefore, if pixel face dimensions are too small, charged particles may routinely scatter beyond the pixel boundaries of incidence and deposit significant portions of their energy in adjacent pixels or outside the array. For example, protons scattered at 30° relative to the path of incident 14 MeV neutrons will depart at energies of ~10.5 MeV, which means they are expected to travel ~1.3 mm from the interaction site and ~0.65 mm orthogonal to the original neutron path. Therefore, protons scattered at 30° from anywhere within a pixel with a cross section <1.69 mm^2 (1.3×1.3 mm) may likely enter an adjacent pixel. Since TFT panels measuring light scintillations typically operate in integration mode, this effect would be expected to reduce the position and image resolution. Based on this understanding, a pixel dimension of 2×2 mm (4 mm^2 pixel cross section) is selected to reduce the likelihood of secondary particles depositing energy in neighboring pixels. This dimension was used for EJ-200, as well as the BiPVT and EJ-256, which have higher densities of 1.4 and 1.081 g/cm^3, respectively.

Fabrication Process

Based on these determinations, a small sample of LLNL BiPVT (6.85×19×21 mm) was cut, polished, and assembled into a 4×3-pixel array, with final individual pixel dimensions of 2×2×19 mm. All material cutting, polishing, and array assembly was conducted at Agile Technologies, Knoxville, TN. The cutting of the material was performed using a highly modified STC-22 (22 in) circular saw with computer-

controlled inputs for depth, speed, and number of cuts. The blade was 400 μm-thick and, with computer assisted positioning, provided positional cutting accuracy of ± 50 μm. An image of the original material, prior to cutting and array fabrication, is shown in Figure 5.1.

Due to the small amount of source material, the BiPVT array pixels were cut individually prior to polishing and assembly, which is not ideal for producing consistently uniform pixel polish, spacing, or dimensions within an array. Polishing consisted of smoothing the pixels on wet, fine sandpaper to reduce them all to 2 mm, followed by polishing with Buehler™ alumina to remove any remaining scratches. Alumina is simply aluminum oxide, typically at particle sizes <1 μm, and it can be purchased to polish a variety of surfaces and materials in either a powder or liquid form.

Unfortunately, several of the individually cut pixels, due to internal material stresses and strains, failed to remain perfectly straight, which is one of the risks in cutting individual pixels. Dual layered enhanced specular reflector (ESR), which consisted of two separate 0.065 mm layers of Vikuiti™ ESR separated by a layer of flat black paint, was used to separate and optically isolate each pixel. This ESR is assessed as providing >98% reflectivity [54], while the UV-cured adhesive, Dymax OP-20, is expected to only provide ~72% and ~76% optical transmission for emission wavelengths of 425 nm and 550 nm at thicknesses of 0.03 mm, which correspond to the peak emissions for EJ-200 and BiPVT, respectively [55]. The dual-layered ESR provided a measured thickness of ~0.25 mm; however, due to the minor deformations in several BiPVT pixels, a final average pixel pitch of 2.44 mm, measured using a Mitutoyo Toolmaker's Microscope, was the best that could be achieved for this array. This provided a calculated fractional active volume of ~67.2% for the array. Additionally, the process of trimming ESR to fit individual pixels and then stacking those into columns separated by larger sections of dual-layered ESR produced gaps in the Dymax adhesive and non-uniform bonding between the pixels and reflector. Images of the final BiPVT array are included in Figure 5.2.

To facilitate BiPVT array performance comparisons, EJ-200 was selected as an industry standard material. Consequently, a 3×4-pixel array of matching pixel dimensions was also fabricated from EJ-200 and EJ-256; however, both arrays benefited from superior manufacturing processes due to an abundance of source material. Specifically, rather than producing separately cut pixels, 2.25 mm plates of EJ-200 and EJ-256 were first cut and polished uniformly.

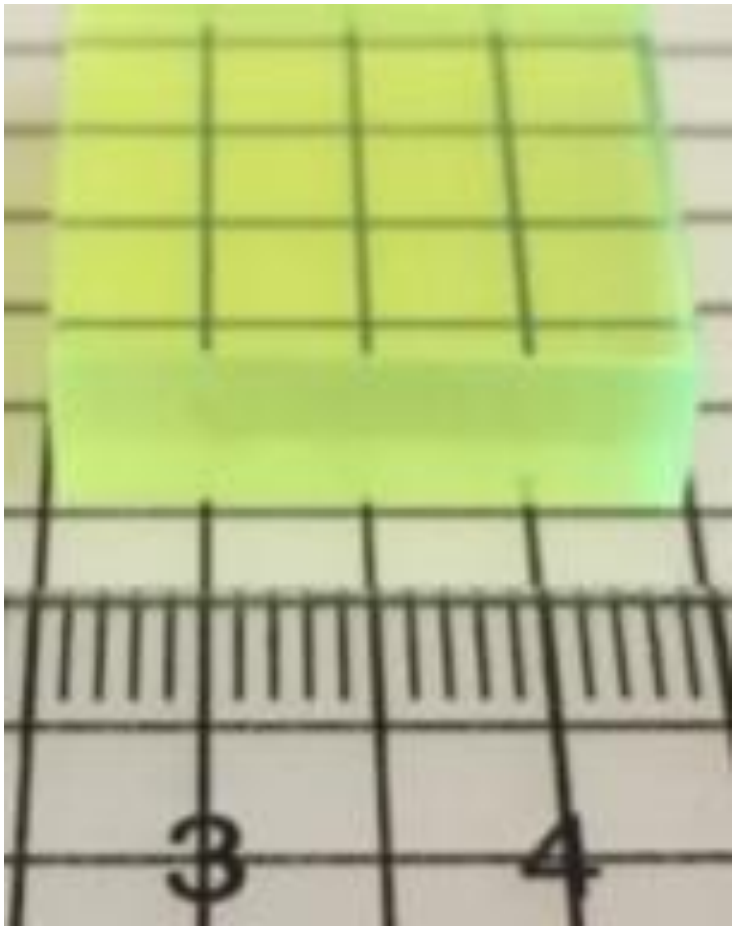


Figure 5.1. BiPVT source sample (6.85×19×21 mm) provided by LLNL.

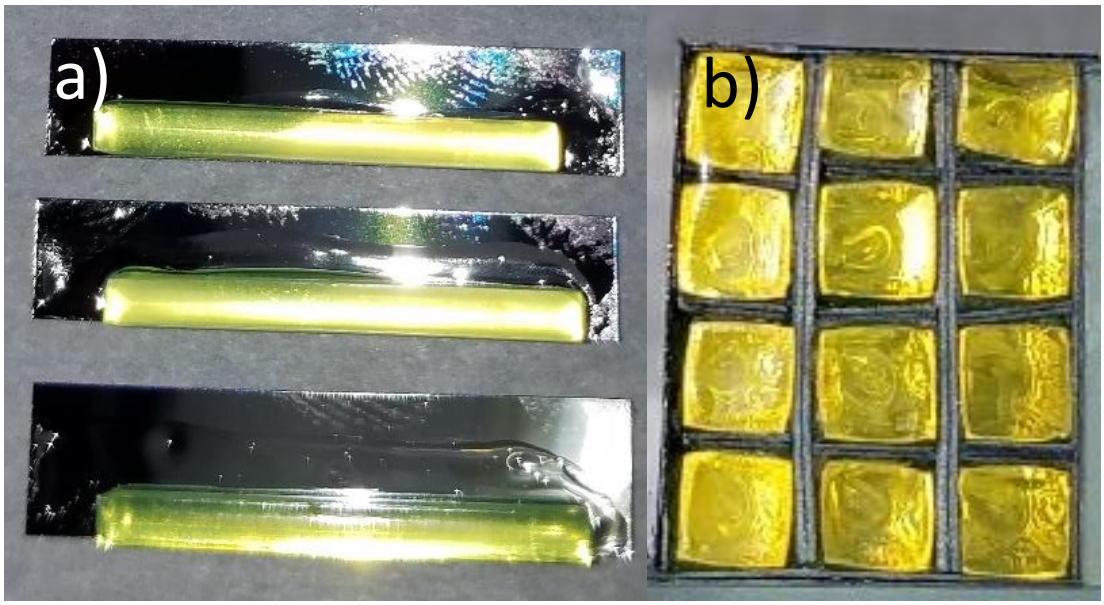


Figure 5.2. Images of the a) individual BiPVT pixels, adhesed to ESR using a UV-cured optically clear adhesive prior to trimming, and b) final BiPVT 4×3-pixel array face, which is placed in contact with the Varex radiographic panel.

Cutting of the material was performed using the same saw as described above, and polishing was completed using a flat surface and wetted P2500 and P3000 sandpaper until the plastic plates were ~2.1 mm thick. At that point, liquid alumina (0.5 μm) was used to further reduce and polish the plates uniformly to achieve a smooth finish and 2 mm thickness prior to ESR application and stacking. The higher-Z EJ-256 was found to require more time for polishing due to it being a slightly denser material. The adhered layers were then cut orthogonally into stacks of four pixels, which were polished again to 2 mm and then assembled with dual layered ESR into the final array. This methodology produced superior geometric uniformity, polish consistency, and ESR adhesion for the EJ-200 and EJ-256 arrays when compared to the BiPVT array. As such, the EJ-200 and EJ-256 array were both measured as providing an average pixel pitch of 2.28 mm without identifiable gaps in adhesive, which resulted in an average fractional active volume of 76.9%. Images of the EJ-200 plates and final array are shown in Figure 5.3.

The finished arrays were then affixed to 2.5 mm acrylic plastic to prevent change to their relative location between measurements. All array fabrication occurred at Agile Technologies, located in Knoxville, TN. An image of the final arrays, mounted to the acrylic plastic, is provided in Figure 5.4.

The arrays were then pressure-mounted to the a-Si receptor plate of a commercial Varex PaxScan 1515DXT-I Flat Panel Detector radiographic panel [56]. This first required the removal of the original proprietary DRZ conversion layer. Next, custom-made aluminum pieces attached to all four outer Varex panel sides, thereby extending the detector panel's light-tight enclosure vertically by 25.4 mm. Within this expanded volume, the BiPVT, EJ-256, and EJ-200 arrays were fixed in place against the a-Si photodetector using layers of foam, specifically cut to hold the arrays and acrylic plastic base. The a-Si TFT provided pixel pitches of 127 μm, so every 2×2 mm array pixel response would be the averaged response of ~240 photodetector pixels. The light-tight enclosure included another detector not addressed in this paper; however, its presence was included in all simulations. Lastly, the enclosure was covered and sealed with the original Varex 2.5 mm-thick carbon fiber plate. The location of the arrays within the aluminum enclosure and supporting foam is shown in Figure 5.5, although additional layers of foam and the cover plate are absent to enable viewing.

BiPVT Light Collection Degradation

Of note, the final expected light yield, optical transmissivity, and coupling efficiencies for the BiPVT array were impossible to predict and were expected to be inconsistent from pixel-to-pixel. This was largely due to the material novelty; however, the effect was compounded by the limited source amount, which necessitated pixel-by-pixel construction.

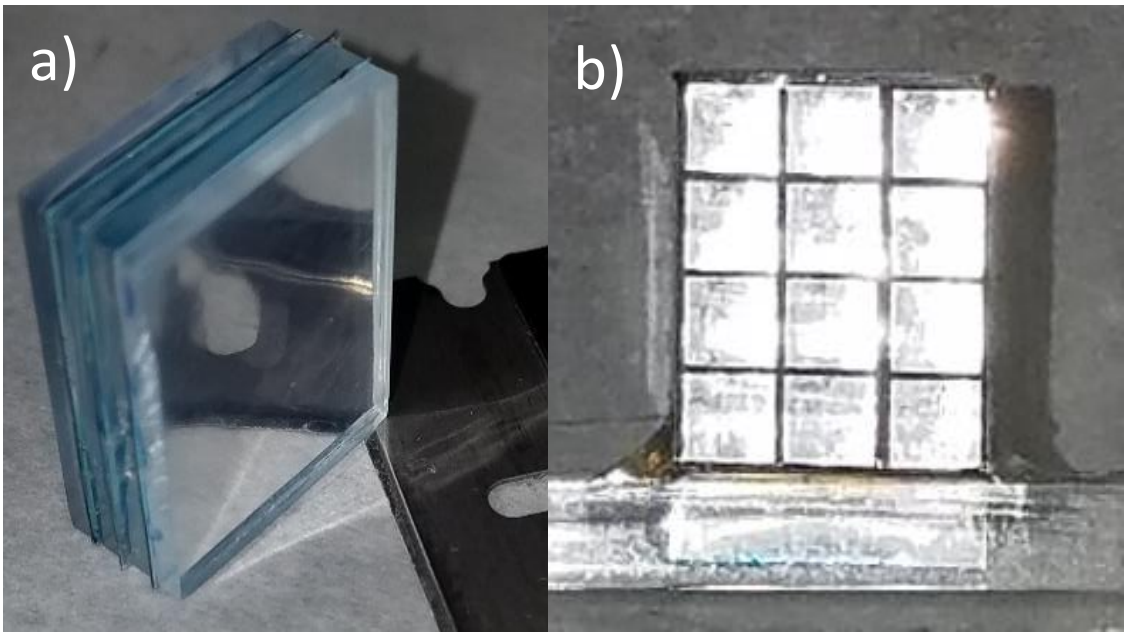


Figure 5.3. Images of EJ-200 a) cut, polished, and stacked into uniform plates (prior to the orthogonal cut creating the pixel stacks), and b) the final EJ-200 4×3-pixel array face, which contacts the Varex radiographic panel.

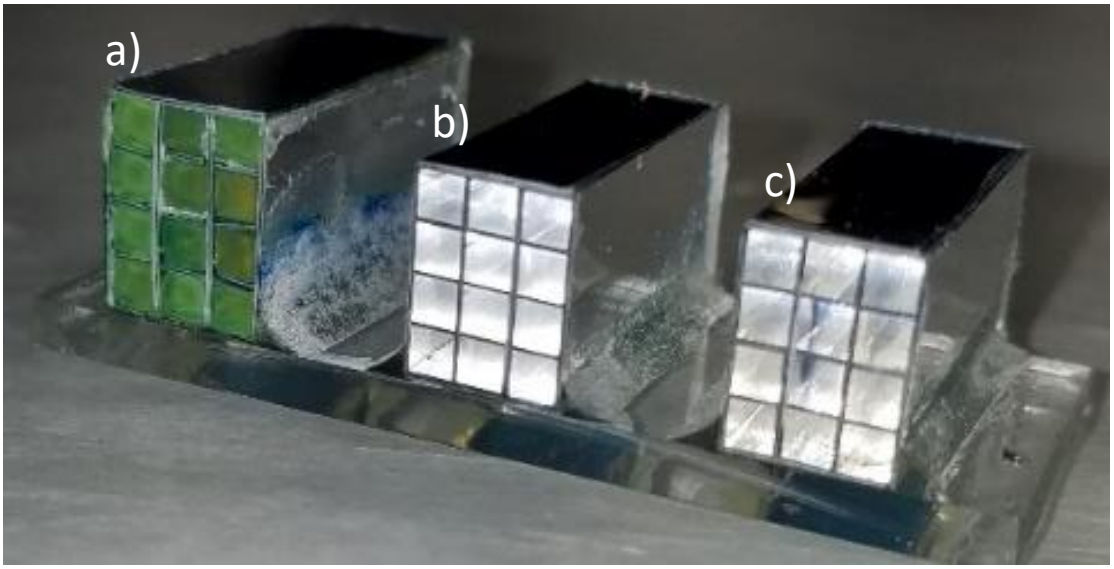


Figure 5.4. Images of the a) BiPVT, b) EJ-200, and c) EJ-256 finished arrays mounted on a 2.5 mm tall plate of polycarbonate plastic to prevent movement between measurements.

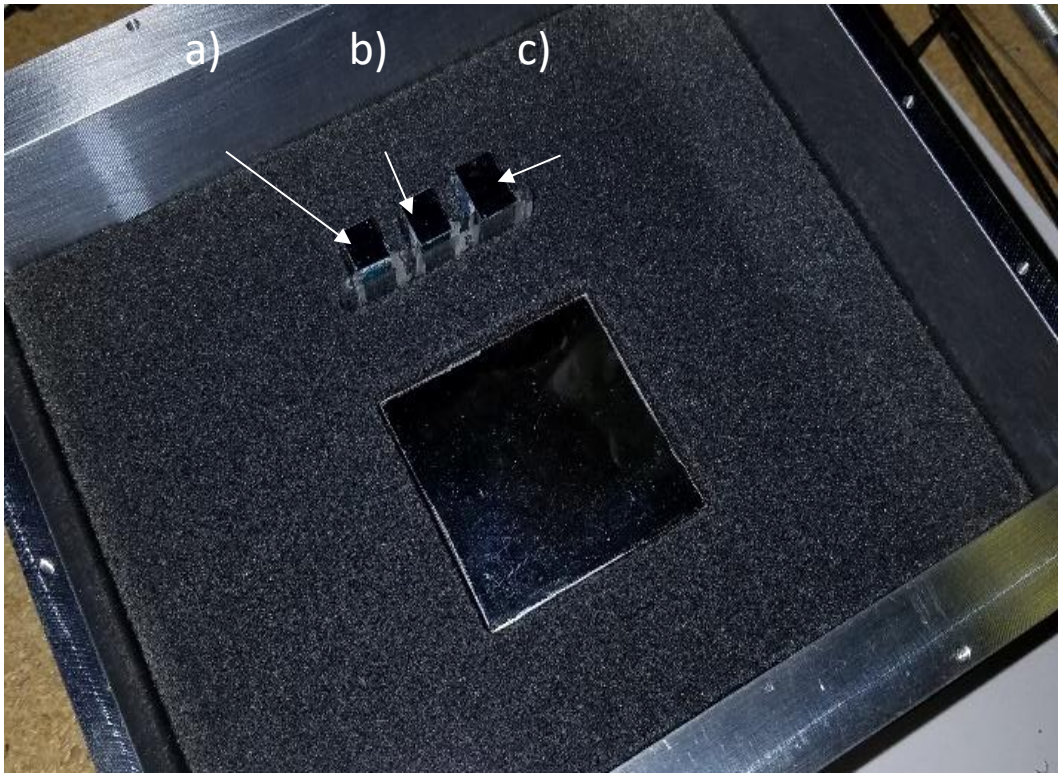


Figure 5.5. Images of the a) EJ-256, b) EJ-200, and c) BiPVT arrays within the aluminum light-tight enclosure, which is affixed to the sides of a Varex PaxScan 1515DXT-I Flat Panel Detector.

More specifically, BiPVT performance uncertainties were largely driven by imprecise pixel dimensions and alignment, as well as pixel occlusion following a final alumina polishing of the detector face. This final effect was entirely unexpected, and the alumina produced a halo-like “clouding” effect inside each BiPVT pixel, apparently along their entire length. This occurred due to inconsistent adhesion between the BiPVT and ESR layers, a byproduct of pixel-by-pixel construction, which produced thin gaps that drew in the alumina polishing solution by capillary action. The presence of the alumina, a white, opaque solution, thereby reduced ESR reflectivity by an unknown degree along the length of each pixel. Due to its presence along the surface of the BiPVT pixels, the alumina also became entrained within the BiPVT, which resulted in pixel ‘clouding.’ Fortunately, the halo-like occlusions largely dissipated after a few days, although some small deposits remained, which likely increased optical scatter and absorption within the pixels, thereby reducing array light collection. However, the greatest degradation to BiPVT array performance was expected from the reduction in array ESR reflectivity. Consequently, future BiPVT scintillator fabrication should utilize alternative methods than alumina to achieve highly polished surfaces, such as simply using finer sandpaper and buffing materials. Figure 5.6 demonstrates the presence of the occlusions, but these are also visible in the BiPVT array shown in Figure 5.4.

Lastly, these sources of experimental uncertainty did not exist in either the EJ-200 or EJ-256 arrays, which benefited from a more standardized array fabrication process, a direct result of greater source material availability.

Radiation Sources

The primary sources supporting the array performance comparisons discussed herein were high-energy bremsstrahlung photons and fast neutrons created from deuterium-tritium fission reactions. Both sources were provided using a separate radiation generating device (RGD) for each particle type, and the energies and reaction types leveraged were selected from other alternatives due to their specific application for dual-particle imaging.

X-ray Source

a) Physical

X-rays were generated by a Comet MXR-451/26 RGD, which uses a tungsten target and can provide up to 450 kVp at 10 mA. It also offers dual focal spots of 2.5 and 5.5 mm and a total of 5 mm of beryllium filtering with a 30˚ targeting angle.

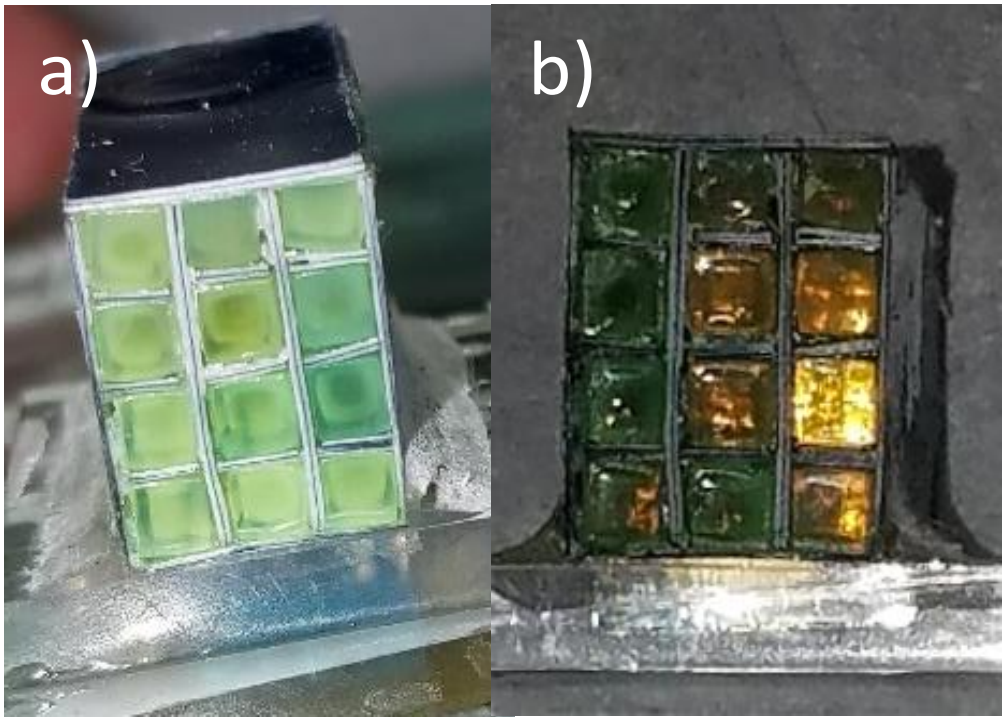


Figure 5.6. Images of the BiPVT array, including a) a "clouding" effect within the pixels due to alumina polishing, and b) after the clouding had largely dissipated. Image 'b)' also shows some small residual occlusions, although their contributions, as well as the degradation in ESR reflectivity, were impossible to quantify prior to experimental evaluation.

For the purposes of this research, the tube was operated at 370 kVp, a current of 3 mA, and a focal spot size of 5.5 mm at 1,000 mm from the face of the radiographic array. The focal spot size of 5.5 was selected due to manufacturer recommendations based on the energy and current used, despite the known benefits to spatial resolution from using smaller source size. These reasons are discussed in Chapter 7.

Although outside the bounds of traditional ASTM evaluation, an energy of 370 kVp was selected because it represents the practical upper limit for portable x-ray radiography. Additionally, due to the higher intrinsic efficiency of BiPVT for photoelectric absorption, a superior performance of the BiPVT array over those made from EJ-200 or EJ-256 at 370 kVp would guarantee the superior performance of equivalent arrays made from BiPVT at all lower energies. Therefore, a single assessment of BiPVT at 370 kVp would demonstrate its efficacy over the considered alternatives for all practical x-ray energies available. Of course, due to the previously discussed calculations of relative Z_{eff}, experiments to quantify the performance of BiPVT at lower x-ray energies will also be valuable. The distribution of bremsstrahlung x-rays produced by the MXR-451/26 RGD was provided by Comet and is shown in Figure 5.8.

b) Computational

The MXR-451/26 was simulated as a point source with a bremsstrahlung x-ray distribution adapted from the 450 kVp spectrum provided by Comet and shown in Figure 5.8. Additionally, the characteristic x-ray emission lines associated with $K_{\alpha 1}$, $K_{\alpha 2}$, and $K_{\beta 1}$ electron transitions in tungsten were also simulated, which produce x-rays at 59.3, 58.0, and 67.2 keV, respectively. Relative peak intensities were also maintained to ensure the accuracy of the simulated spectrum. Figure 5.9 shows a plot of the source spectrum used for all x-ray free-field and shielded simulations.

Neutron Source

a) Physical

The neutron source for all physical measurements was an ING-27 D-T neutron generator (S/N 5593661) resting upon a winched platform, which enabled precise height, leveling, and directional control of the generator. Using this device, the ING-27 was positioned ~100 cm above the floor and operated at ~80% of its maximum voltage, which produced 14.064 MeV neutrons isotopically at a rate of $\sim 4.4 \times 10^7$ neutrons per second. Neutron flux was tracked during each measurement using a pixelated alpha detector, which was located inside the generator vacuum 10 cm from the tritium target, as shown below in Figure 5.10.



Figure 5.7. Image of the Comet MXR-451/26. This RGD contains a bipolar oil-cooled x-ray tube with a tungsten anode and 5mm of beryllium beam shielding. It is designed specifically for NDA.

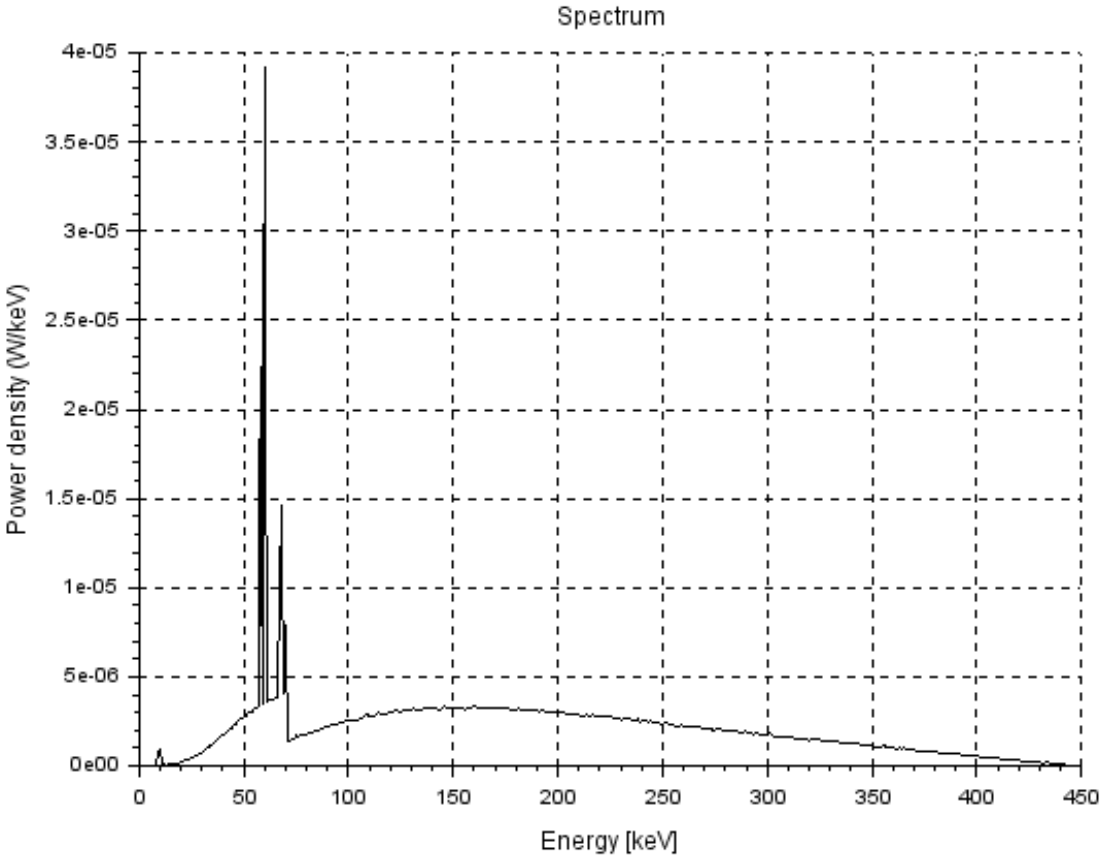


Figure 5.8. Image of the bremsstrahlung x-ray spectrum emitted by the Comet MXR-451/26 when operated at 450 kVp.

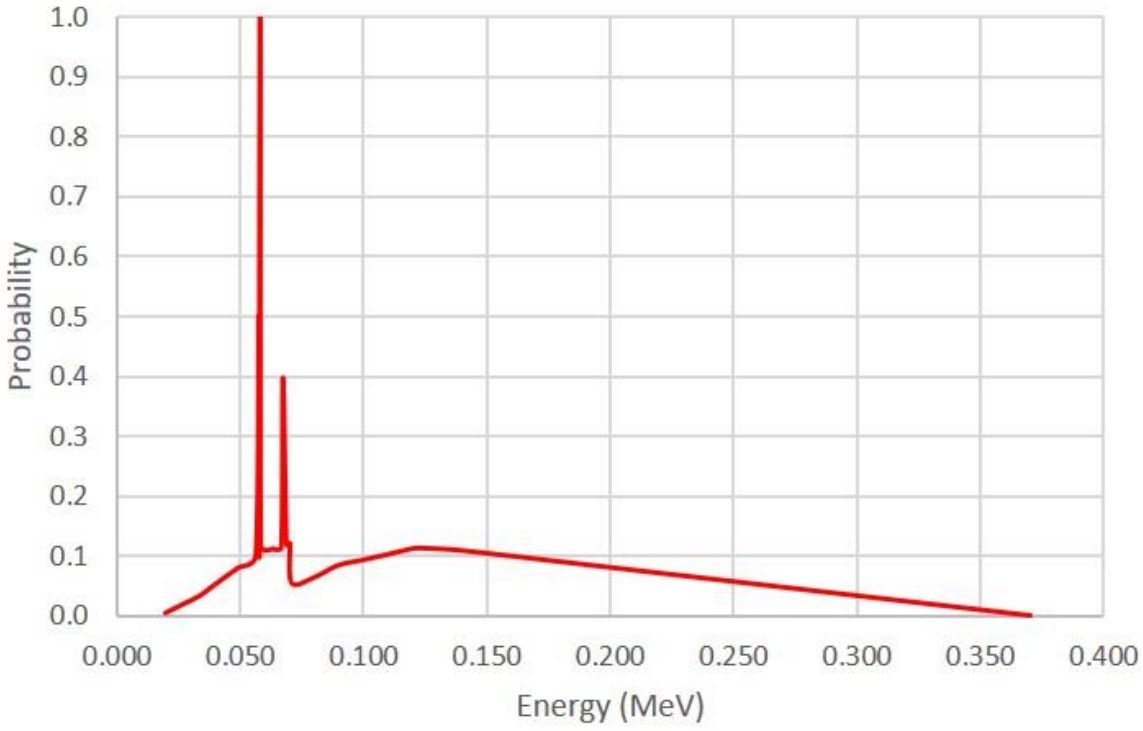


Figure 5.9. Simulated source spectrum for the MXR-451/26 RGD at 370 kVp.

Fluctuations in the rate of neutron production were present throughout the recorded measurements; however, these were monitored continuously, and the generator voltage was adjusted to maintain as consistent a rate of neutron production as possible. Prior measurements found that unmonitored neutron production rates varied by as much as 10% between measurements, so the continuous monitoring and adjustment of neutron production was expected to reduce this uncertainty below ±5% for most measurements.

Specifically, the alpha detector provided a total active area of 36 mm^2, which enabled estimates of neutron production over 4π. This was possible because each deuterium-tritium (D-T) fusion event produces a single neutron and an alpha, each travelling in opposing directions (180˚ opposite) at known energies. Therefore, it is possible to accurately calculate the rate and directionality of neutrons produced by the ING-27 using the rate and location of alpha particles detected by the paired pixelated array. Specifically, values of neutron production were calculated as 3,941× the alpha rate measured at the center pixel and 3,516× the alpha rate recorded in the corner pixels. Using the measured alpha interaction rates for each exposure, as well as the location-dependent graduated conversion values for neutrons across all alpha detector pixels, estimates of neutron flux were calculated in real time during operation, with the voltage adjusted to produce as steady a rate of neutrons as possible.

Lastly, to eliminate possible unwanted contributions from x-rays originating within the neutron generator, a 6.35 mm-thick plate of lead measuring ~10 cm on each side, was placed just outside of the generator housing, between the tritium target and the radiographic panel. It is now understood that low energy x-rays are emitted from neutron generators as part of the particle acceleration process, although more research is needed to better quantify their distribution. Although the precise spectrum of x-rays emitted by the ING-27 has not been measured, the maximum energy of x-rays emitted by D-T generators is not believed to exceed 140 keV. Prior research using this generator suggested x-rays were absent when the 6.35 mm-thick lead plate was used as a shield. This was substantiated experimentally by recording x-ray images using the Varex panel while its carbon fiber cover was shielded with 6.35 mm of lead. Specifically, image analyses revealed the 6.35 mm lead shield eliminated >98% of the measured signal across all arrays when exposed to 150 kVp. Since this thickness of lead is expected to produce only limited attenuation for the high-energy neutron emissions, as shown in the following section, it was selected to eliminate most lower energy photons emitted from the generator. However, the lead shield was factored into all simulations of radiographic response, and a separate computational study was performed to ensure neutron-induced lead photoluminescence from inelastic scatter would not contribute substantially to radiographic images.

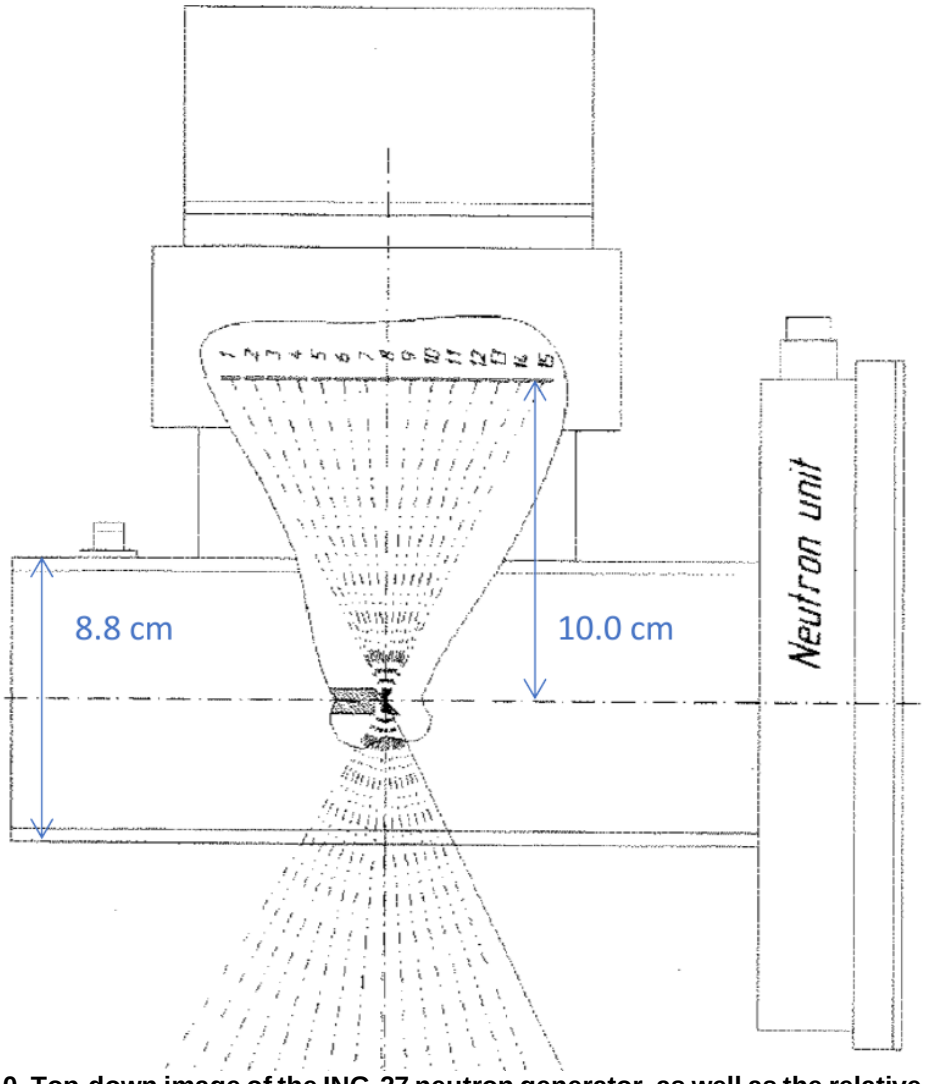


Figure 5.10. Top-down image of the ING-27 neutron generator, as well as the relative location of the pixelated alpha detector (top), which enables accurate calculations of neutron production and directionality (bottom) from measured alpha interaction rates and localities.

b) Computational

The physical ING-27 neutron source was simulated as a monoenergetic 14.064 MeV neutron point source located 103 cm from a concrete floor and 12.5 cm from the pixelated arrays, which were modeled within the aluminum housing of the Varex panel. Located between the source and each pixelated plastic array, the model included the 4 mm-thick aluminum housing of the generator, the 6.35 mm-thick lead plate used to remove x-ray contributions, and the 2.5 mm-thick carbon fiber plate covering the Varex panel. These materials and their relative positions are shown below in Figure 5.11.

Additionally, a separate analysis was performed to quantify the degree of energy deposition within the three arrays due to neutron-induced photoluminescence from the lead x-ray shield. Of course, these gamma rays may only contribute to radiographic images, or portions thereof, where the arrays are unshielded, such as free-field images. This is likely because the presence of the tungsten IQI, or similar high-Z object under investigation, would be expected to largely attenuate such emissions. Likewise, due to the intended purpose for which the evaluated BiPVT material will be used (i.e. neutron imaging of select portions of large, sealed high-Z objects), it is reasonable to predict these emissions will not meaningfully contribute to such neutron images. However, for the purposes of relative performance comparisons within a controlled environment, it is important to evaluate all potential contributions to the relative performance of each array.

Consequently, D-T neutron-induced photon fluence spectra were simulated for separate 150-second measurements within two rectangular volumes filled with air. These air volumes were similar in size and dimension to the combined three plastic arrays. Figure 5.12 shows the plotted photon spectra computed within each of these volumes, while Figure 5.13 demonstrates the relative position of each volume in physical space. The red spectrum in Figure 5.12 represents the estimated photon fluence in volume B, which is located between the lead plate and the carbon-fiber Varex panel cover (centered between the generator and the panel). The remaining spectra reflect photon fluences within air volume A, the same volume occupied by the plastic detector arrays and within the Varex panel. No other components of the experimental design were included (i.e. the arrays, aluminum panel sides, etc.) other than the D-T source, aluminum generator wall, lead plate, and carbon fiber Varex panel cover. Lastly, the carbon fiber cover and lead plate were removed in separate subsequent simulations to demonstrate their individual contributions to the photon fluence within volume A.

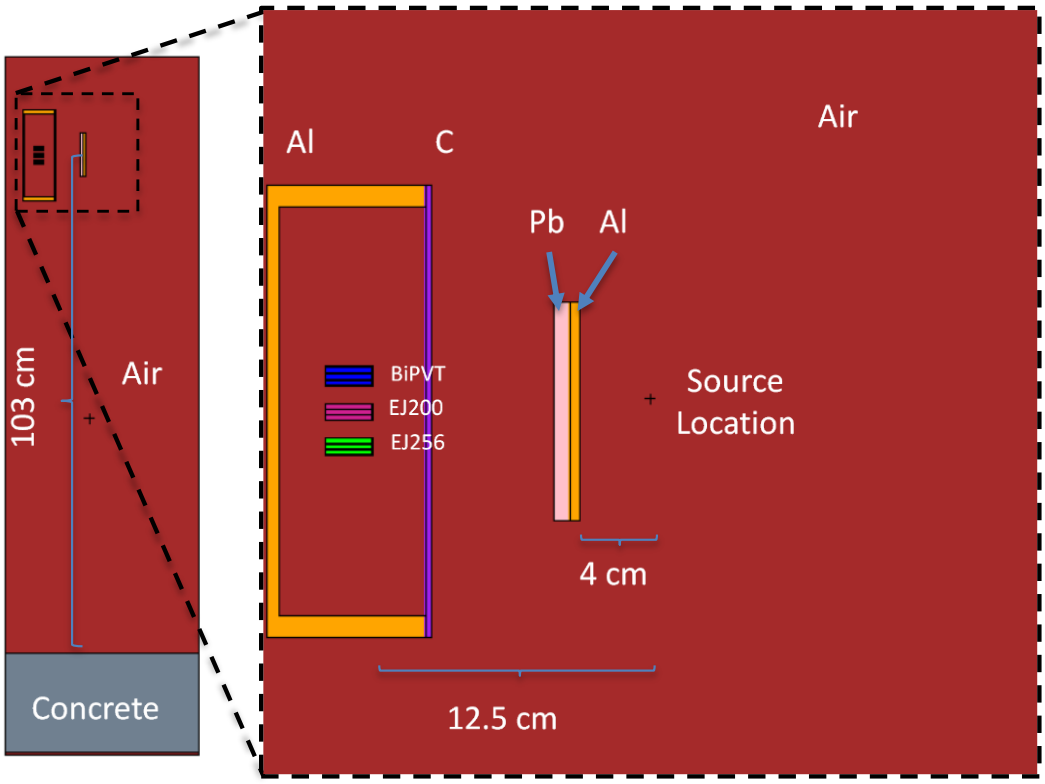


Figure 5.11. Simulated neutron source location relative to the Varex panel, plastic arrays, concrete floor, aluminum generator housing, and lead x-ray shield.

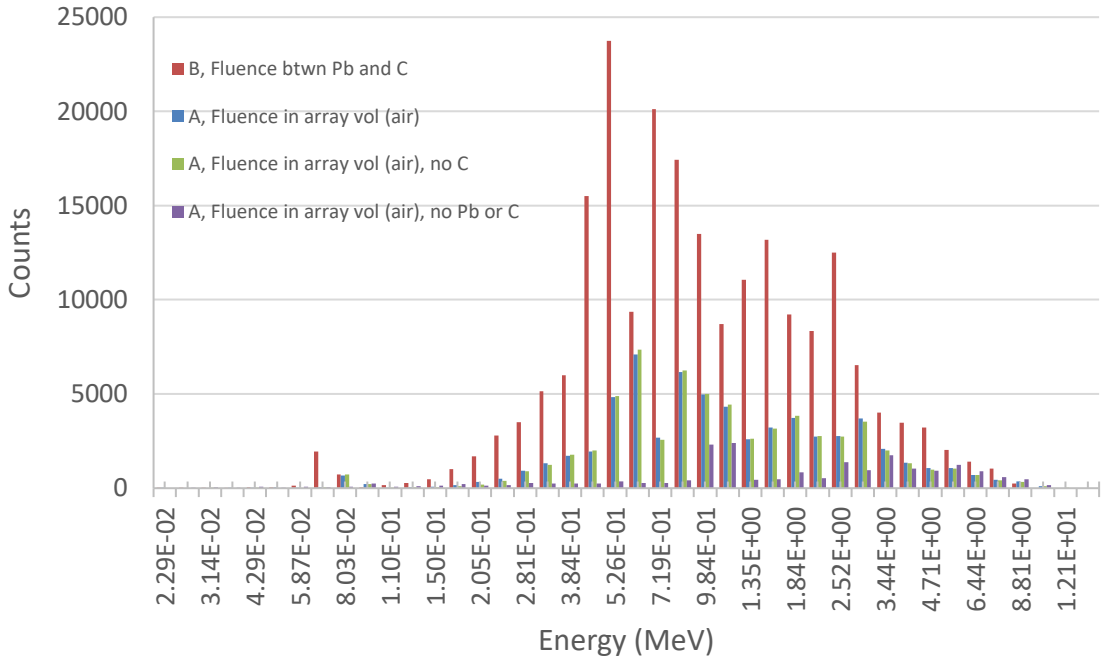


Figure 5.12. Simulated D-T neutron-induced photoluminescence spectra emitted from the 6.35 mm lead x-ray shield and present within two volumes of air per 150 second exposure. These spectra were measured within two different air volumes with different materials present in the simulations to account for their specific contributions to the spectra.

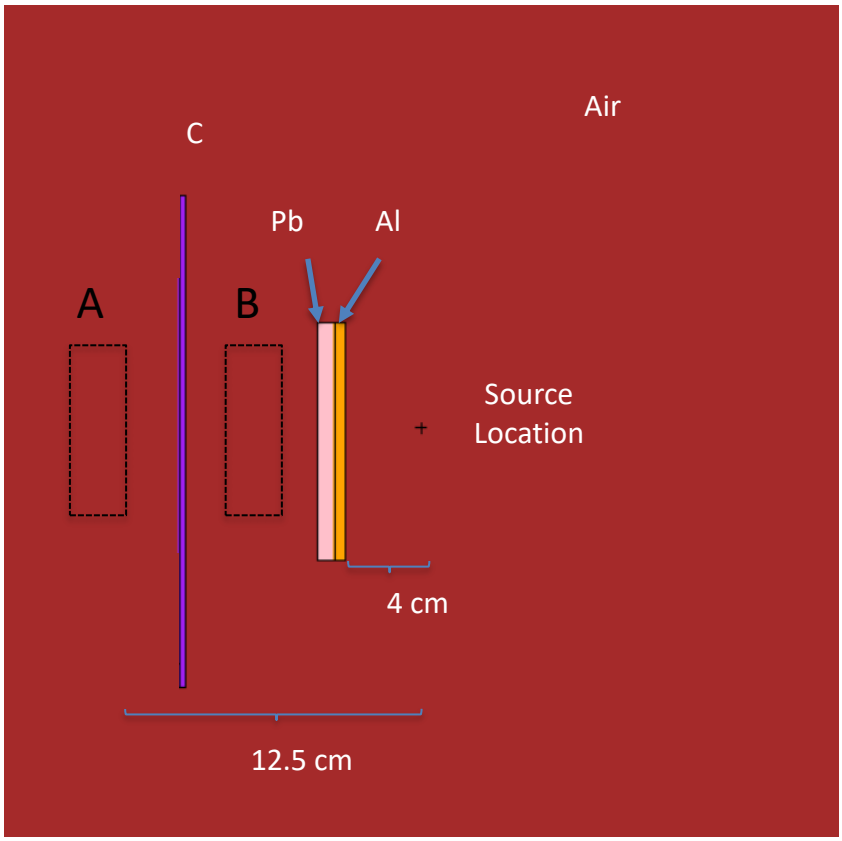


Figure 5.13. Simulated air volumes (A and B) used to predict relative photon fluence due to source 14.064 MeV neutron interactions within the lead x-ray shield. The purpose was to estimate material-specific energy depositions from these photoemissions within each of the plastic arrays and compare those values to expected neutron energy depositions.

This analysis demonstrates that the lead shield does indeed produce high-energy gamma-rays incident upon the array volume, and it enables quantification of their predicted energy contribution. Specifically, the simulation of photon fluence within volume A, with all materials present between the source and air volume, enables a prediction of the likely number of photons incident upon on each array for each 150 sec measurement, and these values can be used to predict average photon energy contributions to each material during free-field measurements. These calculations provide an early estimate of ~300 photons incident on each pixel per measurement window. When compared to current predictions of ~5,500 (n,p) interactions at this source to detector distance, photons would account for ~5.2% of the average number of total particle interactions expected within each pixel, assuming a 100% interaction rate. Based on these predictions, the expected photon emission spectra simulated within volume A, which is shown in blue in Figure 5.12, is used as a source term for additional MCNP6 simulations to predict the material-dependent deposited energy contributions within each array from these photons. These computed values are shown below in Table 5.1 along with proton recoil energy deposition estimates within the same arrays from simulated D-T neutron irradiation.

Therefore, the ratios of photon to proton energy deposition per particle listed in Table 5.1 suggest relatively low contributions to total energy deposition are to be expected from inelastic neutron scatter within the lead plate shielding. These contributions are predicted to be highest within the BiPVT, which seems reasonable due to it possessing the highest likelihood of the three materials for photon interaction at every practical energy. This is followed, predictably, by the lead-loaded EJ-256, with EJ-200 providing the lowest expected contribution to total energy deposition from photon interactions. Additionally, it is worth observing these values of expected photon energy contribution appear relatively similar, with EJ-200 and EJ-256 receiving 64% and 70% of the energy deposited estimated within BiPVT, respectively. These ratios are far greater than those witnessed in the x-ray simulations at 370 kVp, which is a direct reflection of the significantly higher average energy of this incident photon spectrum. At these energies, the benefits from the superior photoelectric absorption efficiency of BiPVT are largely mitigated, as Compton-scatter reactions dominate. As such, these simulation results appear consistent with the current understanding of high energy photon interactions and, therefore, seem reasonable.

Table 5.1. Simulated average energy deposition (MeV) within the three array pixels using a D-T neutron source, both from proton recoil events and photon interactions due to photoluminescence in the lead plate.

	BiPVT	EJ-200	EJ-256
Photon	1.2805E-06	7.32685E-07	8.08659E-07
Proton	5.5739E-05	4.97769E-05	5.00285E-05
Fraction	2.30%	1.47%	1.62%

Panel Noise Discussion and Study

To accurately quantify the degree of light collected during irradiation from any of the three arrays evaluated, the amount of noise present in the recorded images must be identified per pixel to support its efficient removal. Each pixel in a flat panel array consists of an a-Si photodiode paired with an a-Si TFT, with the TFT serving as a gate to allow or prevent integration of the generated signal into the capacitance of the photodiode. Pixels are arranged across the array in both rows and columns, with each connected by gate and data lines. When measuring an image, electron-hole pairs created in the photodiodes from incident photons are collected using an externally applied reverse voltage bias, and this signal continues to collect until positive voltage is applied to the gate line. This occurs at the end of a measured frame, and it allows the TFT to conduct the stored capacitance to the preamplifier and ADC where the measured signal from each pixel is read out. Sources of measured noise that occur during this process can generally be separated into contributions from statistical noise, pixel noise, and dark noise, although other sources in a DDA exist. Statistical noise arises from photons interacting stochastically with the photodetector. Thermal noise includes noise based on pixel size, temperature, and capacitance. Dark noise is the presence of measured "signal" even when no source of external radiation is present, which is also heavily related to panel temperature.

Statistical Noise

This is quantum noise generated from the statistical uncertainty of light collection over a specific measurement window, which is driven by the stochastic nature of radiation production and interaction in the scintillator. In the case of DDA images, this is also known as shot noise, and it includes the stochastic processes of light generation, light collection, and quantum efficiency within each array pixel. In applications involving large x-ray exposures, such as radiography, the SNR from flat panel imaging systems is generally limited by the quantum noise present [57].

For the purposes of the experiments detailed herein, this uncertainty is best represented as a Poisson distribution, which results when a small but constant probability of particle detection is present during the measurement window, and far more source particles pass through the detector array than are successfully detected [20, p. 73]. More specifically, this is the case when detecting interactions from particles emitted from an accelerator, wherein the binomial distribution for particle detection probability reduces to a Poisson probability function,

$$P(x) = \frac{\bar{x}^x e^{-\bar{x}}}{x!}, \qquad (18)$$

where $\bar{x}$ is the mean value of the distribution, and x is a measured value. For a Poisson distribution, the mean and variance are equal and represent the first moment of the distribution. Additionally, statistical noise increases as a function of signal intensity distribution, which implies that a signal distributed over a wider range of energies will result in a larger calculation of statistical noise than one distributed over fewer [20, p. 67]. As such, the root means square (rms) contribution from statistical noise to total noise can be estimated as,

$$\sigma_q = \sqrt{N_p}, \qquad (19)$$

where N_p is the number of electron-hole pairs generated per TFT pixel [58].

Thermal Noise

Known also as Johnson or kTC noise, thermal noise is a source of uncorrelated noise originating from the on and off switching of TFTs, with the dominant component due to interactions between the TFT switch and the photodiode [45]. Specifically, thermal noise is created from the TFT-on resistance, which produces random charge fluctuations [57]. Equations for thermal noise spectral density and the frequency-dependent transfer function of the pixel-preamplifier network simplify into

$$\sigma_{thermal} = \sqrt{kTC_{pd}}, \qquad (20)$$

where k is the Boltzman constant of 8.62 eV/K, T is the temperature in Kelvin (K), and C_{pd} represents photodiode capacitance (F), which is typically 20 pF [57, 45]. However, when the TFT switch is turned off, the noise calculated in Equation 20 is integrated into the photodiode capacitance. Then, when the switch is turned on again to record the next frame, the preamplifier samples the measured thermal noise, $\sigma_{thermal}$, as well as that from the previous frame. Assuming the temperature is constant between frames, this results in equal and uncorrelated noise contributions, thereby increasing thermal noise by up to a factor of $\sqrt{2}$. Consequently, the total TFT thermal noise (in units of e^-) can be determined from

$$\sigma_{kTC} = \frac{\sqrt{\alpha kTC_{pd}}}{q}, \qquad (21)$$

where α represents a constant between 1 and 2, depending on the rate of thermal noise duplication, and q is the charge per electron of 1.6×10^{-19} C/e^- .

Dark Noise

Experiments were conducted to quantify the dark noise present within the Varex panel and its positive relationship with increasing operating temperature. It was found that the temperature increase originates from the panel's power supply, which is logical. In addition to the time-dependent results of this study, this section

will detail the planned methodology for effectively accounting for and subtracting these contributions. However, it may be helpful to first define dark current and dark noise since these effects are related.

Dark Noise Definition

Dark current is defined as the current of electrons that exists in a photodiode when no photons are incident upon it [59]. In other words, even without photons incident on the photodiode, a certain number of electron-hole pairs are generated. Furthermore, dark generation of electrons and holes in the sensor depletion region is a stochastic process, so it is analogous to photon detection shot noise in that it has a similar statistical nature and distribution. As such, it can also be described in similar terms as

$$\sigma_{dark} = \sqrt{N_d}, \qquad (22)$$

where N_d is the dark current and σ_{dark} is the dark noise contribution within each frame [58]. Among other things, dark current is strongly correlated to temperature, with a well-established positive relationship between detector temperature and dark noise counts.

Dark Noise Study using the Varex 1515DXT-I Panel

This relationship was demonstrated and quantified experimentally using the Varex 1515DXT-I panel in a series of measurements devoid of external radiation quanta. In this way, these experiments offered a means to study the temperature-dependent noise measured by the panel. For the first experiment, the ambient temperature of the panel was 295 K and, immediately after plugging in the 1515DXT-I panel, an offset calibration was performed using the Varian Image Viewing and Acquisition (ViVa64) software, followed by two measurements (A and B) that took a total of 90 mins. Measurement A recorded 588× 5-sec (0.2 fps) exposures (49mins), and Measurement B recorded an additional 360× exposures (30 mins). The integrated ROI over which the noise was studied covered an area of 333×1152 pixels, roughly one third of the of the panel active surface, and without scintillating material in contact with it. The data consisted of two measurements separated by ~7.5 minutes, at which time no collection took place. Despite this, the data revealed no discontinuity in the thermal background, which indicated it continued to increase whether images were recorded or not.

The results revealed that dark noise contributions within the panel likely plateau over time, after roughly 180 minutes, which implied that measurements recorded after reaching thermal equilibrium would likely benefit from a more reliable subtraction of dark noise due to the greater stability in temperature. This enhanced understanding of the impact of heat helped facilitate an improved methodology for background subtraction, which resulted in a refinement of the proposed experimental design, as well as improved data collection and analysis techniques.

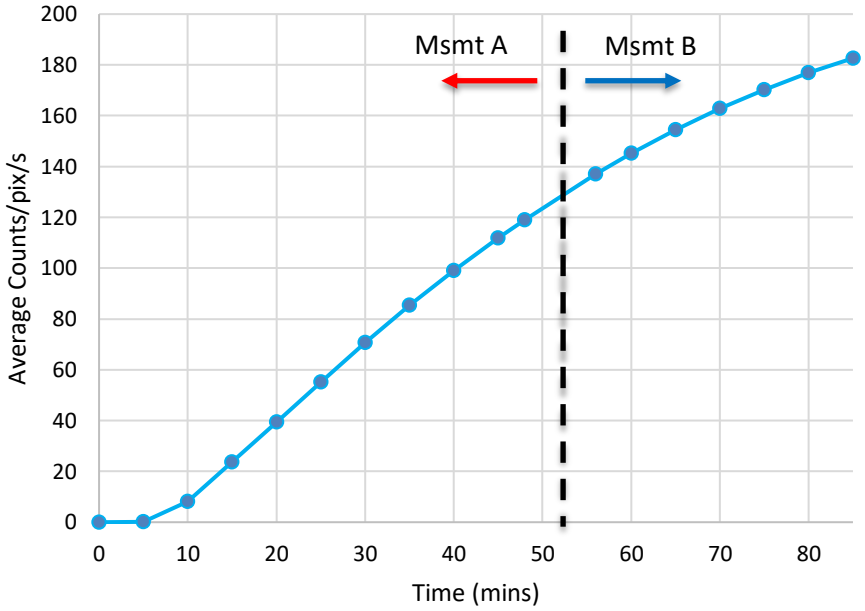


Figure 5.14. Plot of measured dark noise within the Varex 1515DXT-I panel over time as temperature increased.

The initial experiment was then repeated, this time to evaluate the effect of the Varian offset calibration during measurements. The ambient temperature of the panel was 293 K, and, immediately after plugging in the 1515DXT-I panel, an offset calibration was performed using the Varian software, followed by three measurements (A, B, and C) lasting a total of 170 mins. The data from this second series of experiments are plotted in orange, while the previous data from Figure 5.14 are plotted in blue. All three measurements consisted of 600× 5-sec (0.2 fps) exposures (50mins), each separated by 10 minutes; however, offset calibrations were performed between each measurement to reduce the accumulated dark noise. The integrated region used for both data matched the previously used 333×1152-pixel ROI.

The results in Figure 5.15 demonstrate the effectiveness of offset calibrations in reducing thermal background contributions, and the rates of increase in these dark noise measurements generally agree with the original data. The key difference appeared to be the exact time dark noise began to significantly appreciate following the arrival of power to the system. Disparities between data sets plotted in Figure 5.15 are likely due to a difference between the starting temperatures of the system and its electronics. Specifically, the data from Figure 5.14 was collected in the afternoon at a room temperature of ~72˚ F, while the data shown in Figure 5.15 was collected early in the morning at a room temperature of ~68˚ F.

The measured images were further analyzed to quantify the degree of dark noise biasing across the array to determine whether it occurred in a more uniform or localized manner. Four separate 1820-pixel ROIs were created and identified as Upper Left (UL), Bottom Left (BL), Bottom Right (BR), and Upper Right (UR). The average count rates of these ROI are plotted below, along with the original experimental results from the 333×1152 ROI (dark blue). Furthermore, this analysis resulted in the production of Figure 5.17, which demonstrates the same significant count rate bias toward the upper right (UR) region of the panel.

Additionally, analysis of the quadrants in Figure 5.17 revealed the ultimate source of the thermal effects as the panel power supply. Upon further consideration, this made sense because the UR quadrant is located nearest to the 15V input, as shown in Figure 5.18, which is a view of the back of the 1515DXT-I panel with the same quadrants superimposed.

Table 5.2. Measured count rates from the Varex 1515DXT-I (shown graphically in Figure 5.14) panel following an offset calibration as panel temperature (unmeasured) increased.

Measurement	Integral	Avg counts	$\frac{Avg\ counts}{pixel - sec}$	Time (mins)	Start (s)
1	29817	0.077726	0.001	0	1
2	1011938	2.637893	0.044	5	61
3	1.89E+08	491.4939	8.192	10	121
4	5.42E+08	1413.97	23.566	15	181
5	9.07E+08	2365.464	39.424	20	241
6	1.27E+09	3313.672	55.228	25	301
7	1.63E+09	4236.857	70.614	30	361
8	1.96E+09	5116.385	85.273	35	421
9	2.28E+09	5946.43	99.107	40	481
10	2.57E+09	6703.329	111.722	45	541
11	2.74E+09	7131.131	118.852	48	576
12	3.15E+09	8219.044	136.984	56	672
13	3.34E+09	8710.962	145.183	60	721
14	3.56E+09	9267.27	154.454	65	781
15	3.75E+09	9769.889	162.831	70	841
16	3.91E+09	10204.63	170.077	75	901
17	4.07E+09	10610.64	176.844	80	961
18	4.20E+09	10957.81	182.630	85	1021

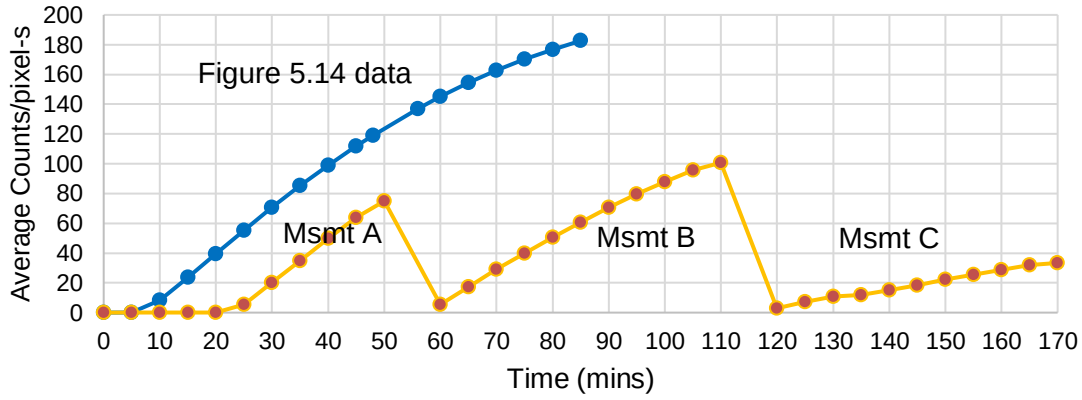


Figure 5.15. Plot of measured dark noise within the Varex 1515DXT-I panel over time as temperature increased. Offset calibrations were utilized between Measurements A, B, and C using the ViVa software package from Varian.

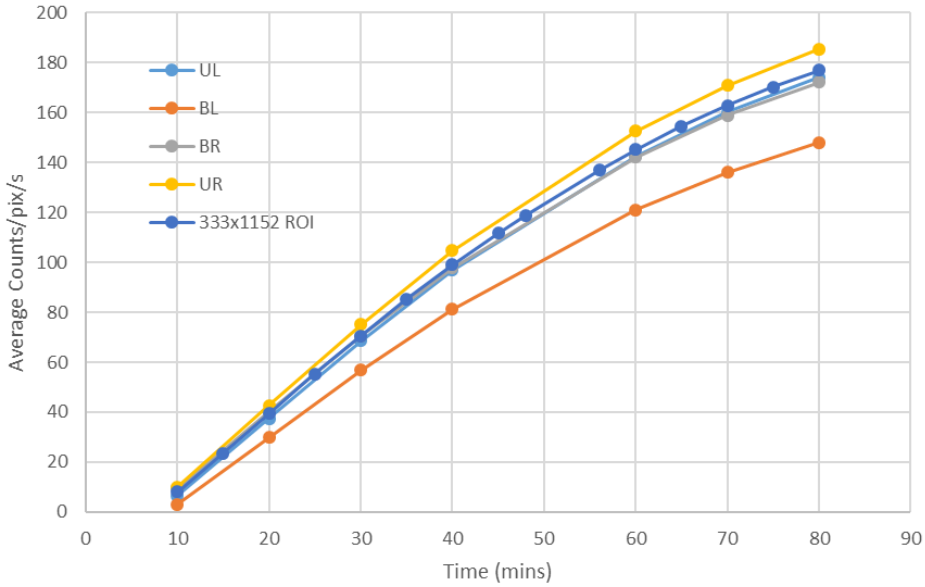


Figure 5.16. Image of measured dark noise within the Varex 1515DXT-I panel over time as temperature increased. The image reveals a count rate bias toward the upper right quadrant of the panel.

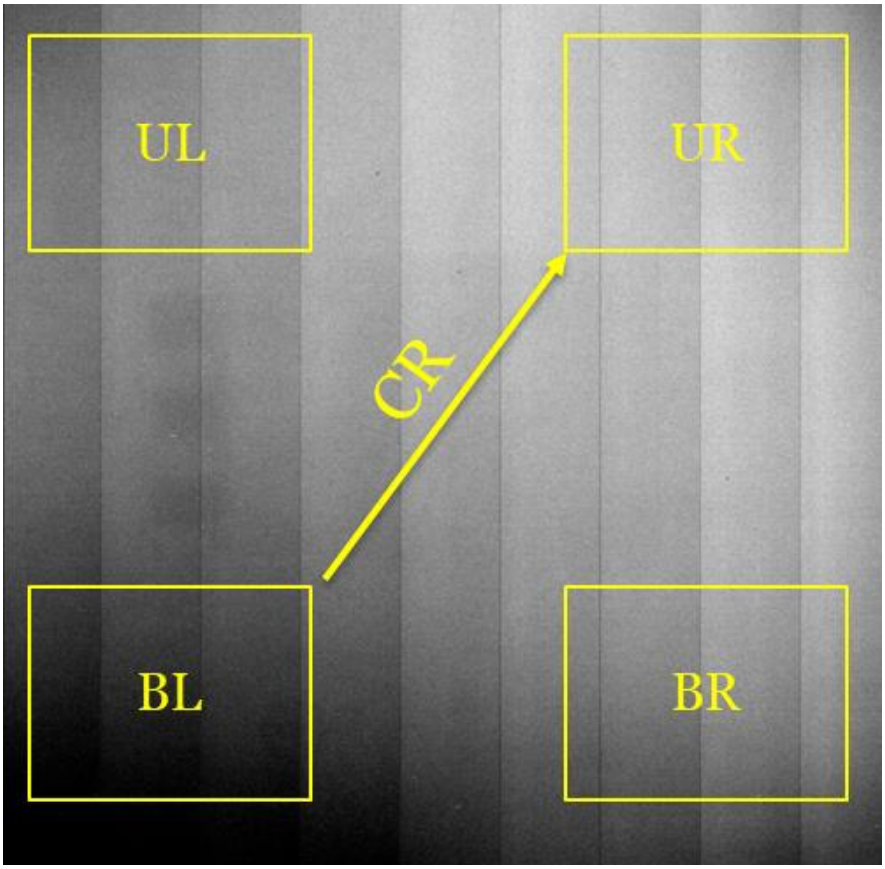


Figure 5.17. Image of measured dark noise within the Varex 1515DXT-I panel over time as temperature increased. The image reveals a count rate bias toward the upper right quadrant of the panel.

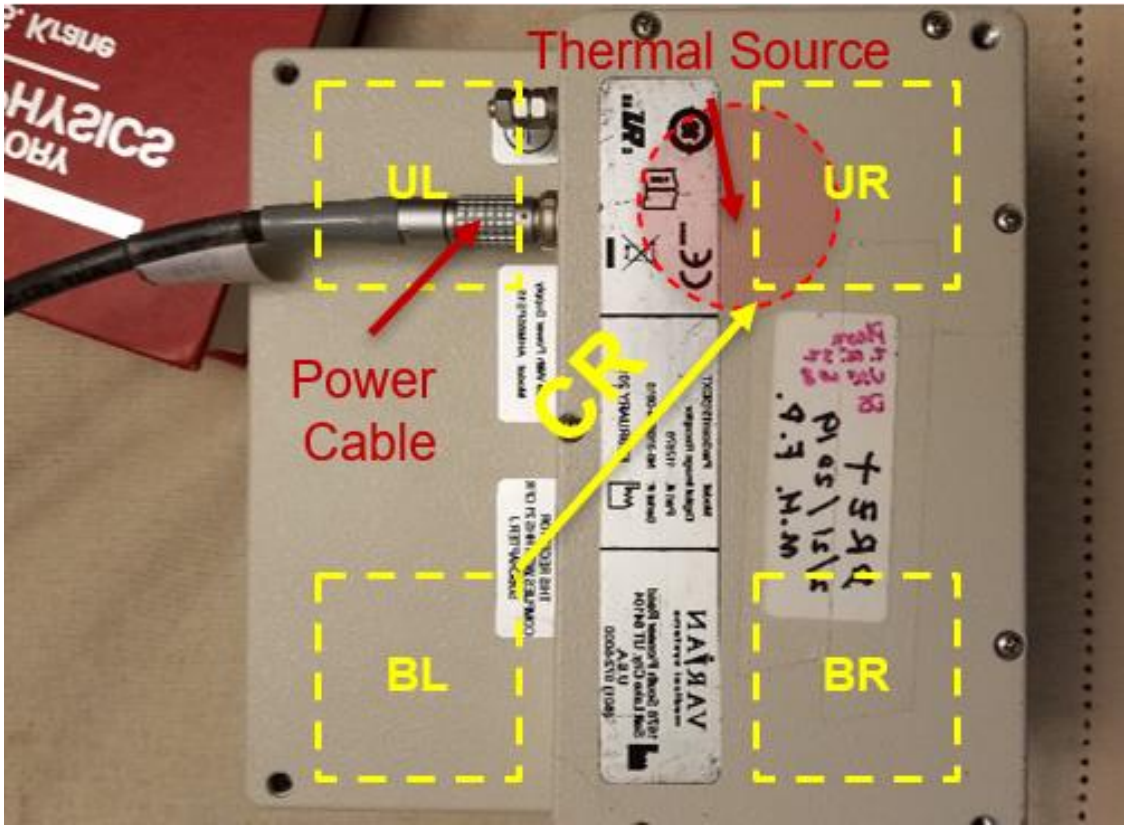


Figure 5.18. Image of the back of the Varex 1515DXT-I panel, with the quadrants from Figure 5.17 superimposed to show relative location. This analysis fully explains the source of thermal influence which affects dark noise across the Varex panel in a nonuniform manner.

These findings provided valuable information that informed the experimental design for the neutron measurements. Due to the saturation of the arrays with radiation during x-ray measurements, contributions from dark noise remain relatively small compared to the signal measured from the arrays and are subtracted via offset-correction. However, neutron measurements are expected to provide significantly reduced rates of signal compared to x-ray measurements, thereby reducing the expected SNR for each array.

Methodology for Dark Noise Subtraction

Therefore, to more effectively account for all noise contributions (so they may be reliably subtracted), the following procedures were employed for neutron measurements.

1) Plug in the panel and leave it running for as long as possible before recording any measurements or performing an offset calibration. The longer it is left running, the lower the expected rate of thermal change and, therefore, the lower the expected contributions from dark noise background. Tests suggested the panel should run for at least 10 minutes prior to recording measurements to enable the stabilization of the dark noise increase.

2) Perform an offset calibration using an equal number of dark images as the number of images planned for each measurement. In the case of the neutron measurements, this required an offset calibration of 30 frames recorded at a rate of 0.2 fps.

3) Record a dark measurement to ensure the calibration worked (Measurement D_1)

4) Record five (5) separate measurements (M_1-M_5)

5) Record a dark measurement to measure the rate of thermal background increase since the last measurement (Measurement D_2)

Steps 3-5 were repeated until all experimental measurements were recorded, each for 150 secs. These procedures, of course, increased the total time required to record each set of measurements; however, the quality of the data produced was significantly superior to measurements taken with shorter exposures.

To accurately estimate accumulating dark noise for each neutron measurement, a consistent 333×1152-pixel region was summed from the average of each 30-frame measurement set. This region represented ~1/3 of the panel surface area and was devoid of any scintillator material, so it only recorded accumulating panel noise. These values of summed dark noise accumulation were used to represent the relative noise present in the five images (M_{ir}) and dark images (D_{1r} and D_{2r}) for each measurement set.

Using these values, contributions from panel noise were estimated on a per TFT pixel basis for each measurement. This was accomplished by calculating the

fractional contributions (F_i and 1-F_i) of noise from the two dark images to each individual measurement by summing those contributions into a single estimate of background (B_i) and subtracting it from each measured image (M_i). This process produced offset corrected (M_{iOC}) difference images. The five offset corrected images were then averaged to produce a final measurement image for the free field and for all 15 shielded measurements. Therefore, each measurement was the average of 150 separate frames, which were offset corrected in groups of 30 frames. This process enabled the isolation of measured signal from background, which would otherwise have been obscured. Algebraically, this series of calculations is performed using,

$$F_i = \left(\frac{D_{2r} - M_{ir}}{D_{2r} - D_{1r}}\right), \quad (23)$$

$$B_i = F_i * D_1 + (1 - F_i) * D_2, \quad (24)$$

$$M_{iOC} = M_i - B_i. \quad (25)$$

This analysis was conducted across all measurement sets, each consisting of five 30-frame measurements bracketed by two dark 30-frame measurements.

Of course, due to the large amount of noise subtracted, this process resulted in some negative TFT pixel values, which necessitated normalization of the measured data. Specifically, pixel intensities were scaled by subtracting average background from a nearby 50×160-pixel void ROI without scintillator material present. Consequently, the final standard deviation for each array pixel was determined from the square root of the sum of the squares of standard deviation from each pixel signal and the void ROI. This resulted in larger recorded variances for measured signal, which necessitated longer exposures and a shorter SDD to achieve a free-field SNR greater than 1.0 for all the arrays.

In conclusion, specific contributions to noise are not individually quantified and summed for each experiment; however, for both x-ray and neutron environments, panel noise is subtracted to the greatest extent possible to provide the largest SNR measurable. In the case of x-ray measurements, this is achieved using offset correction via the subtraction of dark measurements, as per ASTM guidance [53, 60]. For neutron measurements, in which the produced signal is often below the dark noise, Equations 23-25 provide a methodology to quantify and subtract dark noise background on a per TFT pixel basis, thereby enabling the measurement of light collected from the scintillator arrays. Additionally, each averaged shielded measurement is divided by the averaged free-field measurement in both environments to normalize the measured DDA response, a common practice used for image calibration [60]. Analysis of a quotient image allows for equivalent

comparisons of calibrated performance, and it improves detection sensitivity by eliminating non-uniformities in pixel performance from the final images. Additionally, the use of offset correction and image averages further reduces noise in these calibrated images and represents some of the substantial advantages offered by DDAs over other imaging media, such as film [60].

CHAPTER SIX -

MATERIAL ANALYSES

This chapter documents several investigations of BiPVT, EJ-200, and EJ-256 with the goal of providing a more thorough understanding of the physics occurring, with respect to both the scintillation material and geometry. As such, these investigations and their associated conclusions informed predictions of array performance in both the x-ray and fast neutron environments.

Stopping Power and Proton Range

Proton range and linear stopping power evaluations were conducted both empirically and computationally for BiPVT, EJ-200, and EJ-256 to support early predictions of relative array performance and pixel crosstalk. These evaluations were conducted using equations for collisional stopping power, which are based upon the Bethe formula [20, p. 31] and exclude electrons from x-ray scatters due to their extremely short range.

Stopping Power Theory

Linear stopping power, S, is defined for a charged particle as the rate of change in its kinetic energy as it transits through a medium, divided by its length of travel within that medium. This is expressed algebraically as

$$S = -\frac{dE}{dx}. \qquad (26)$$

In the case of charged particles, including protons, *S* increases as velocity and kinetic energy decrease. This inverse relationship is reflected in the Bethe formula [20, p. 31],

$$-\frac{dE}{dx} = \frac{4\pi e^4 z^2}{m_0 v^2} NB, \qquad (27)$$

where *B* represents the expression,

$$B \equiv Z\left[ln\frac{2m_0v^2}{I} - ln\left(1-\frac{v^2}{c^2}\right) - \frac{v^2}{c^2}\right]. \qquad (28)$$

In Equations 27 and 28, *v* and *z* represent the velocity and charge of the incident particle, respectively, while *N* and *Z* represent the effective number density and

atomic number of the medium. Additionally, m_0 is the electron rest mass, e represents the electronic charge, and I is the average excitation and ionization potential of the medium, which is normally determined experimentally.

Of note, analytic solutions to the Bethe model have been shown to provide good agreement with experimental results in determining charged particle stopping power and range, which can reduce the reliance upon experimental material characterization in some circumstances [61]. For example, the National Institute of Standards and Technology (NIST) provides solutions to Equation 27 for a variety of light and heavy charged particles (HCP) within elemental matter and some compounds. In doing so, they utilize the Bethe-Bloch stopping model, which is derived in ICRU 49 [61] but will not be explicitly detailed here. In addition to the terms shown above, the Bethe-Bloch model used by NIST includes terms accounting for shell, density, and mean ionization energy corrections. Of these terms, by far the most impactful is the shell correction term, which corrects the theoretical assumption in the Bethe model that ion velocity is significantly greater than electron orbital velocity. This term is typically calculated from the incident particle's expected interaction with each elemental electron orbit, thereby making it dependent upon changing ion kinetic energy. Suffice to say, the Bethe-Bloch model is widely accepted as providing reliable estimates of stopping power and range for light ion transport through media, especially at energies above one MeV/nucleon [61]. This is particularly useful when accurate data on range and stopping power are desired without conducting physical experiments.

From Bethe-Bloch model calculations, NIST provides estimates of total stopping power, S, in units of MeV*cm^2/g, and this is further partitioned into contributions from both nuclear stopping power (S_n) and collisional stopping power (S_c),

$$S = S_n + S_c \left(\frac{MeV*cm^2}{g}\right). \qquad (29)$$

Of these two terms, S_n reflects the average rate of energy loss per unit path length due to the transfer of ion energy to recoiling atoms via elastic collisions, which is only appreciable at very low energies for protons. Alternatively, S_c, which is also known as *electronic* stopping power, refers to the average rate of energy loss per unit path length due to Coulomb collisions. These Coulombic interactions result in the ionization and excitation of atoms and molecules in the medium, and, therefore, represent the dominant form (>99%) of energy transfer from high-energy charged particles to the absorbing material at energies above one MeV/nucleon. As such, calculations of S_c offer very reasonable estimations of S for charged particles traveling at these kinetic energies.

Collisional Stopping Power

Fortunately, models exist to accurately predict the S_c for a given kinetic energy and incident particle within an elemental or compound medium. One of these is rooted in a geometric model of electronic collisions between incident charged particles and atomic or molecular electron clouds. Specifically, the geometric model leverages a cross-sectional view of charged particle reactions within a medium, treating electron orbitals as targets within an infinitesimal thickness of material, *dx*, within a slab of area, *A*. This would suggest the cross-sectional target areas, σ, are present in numbers n_v, per unit volume, and an incident number of charged particles, Φ, produces an incremental fluence, $d\Phi$, leading to reactions within the slab [62]. This concept is expressed mathematically as,

$$\frac{d\varphi}{\varphi} = \frac{dA}{A} = \frac{(n_v A dx)\sigma}{A} = n_v dx\sigma,\ \sigma = \frac{\frac{d\varphi}{\varphi}}{n_v dx} = \frac{\frac{d\varphi}{n_v dx}}{\varphi}. \qquad (30)$$

In other words, the reaction cross section can be described as the quotient of reaction probability for each incident charged particle and the number of those incident particles per unit area. The validity of this explanation is further explored in academic literature, along with the mathematical derivations of force and energy imparted to orbital electrons from incident particles [62]. These derivations rely upon the classical definition of the electron radius, r_0, as

$$r_0 = \frac{e^2}{4\pi\epsilon_0 m_e c^2}, \qquad (31)$$

where *e* represents the atomic electron charge, ϵ_0 is the permittivity of free space, and $m_e c^2$ is the electron rest mass (0.511 MeV/nucleon). Using Equation 31, the classical electron radius is calculated as 2.8179×10^{-15} m. Furthermore, application of the geometric model necessitates the estimation of, σ, the cross-sectional target area. For pure elements, this value can be approximated as *R* [63], which is defined as,

$$R = r_0 A^{\frac{1}{3}}. \qquad (32)$$

In the case of heterogenous compounds, these areas are derived using the basic molecular formula for each material, including any high-Z components present. Consequently, for the three materials of interest in this research, the A_{eff} values derived using Equation 11 and listed in Table 4.3 can be substituted in Equation 24 to approximate respective molecular cross-sectional areas.

Additionally, the Lorentz variable, β, which represents the fractional speed of light for a particle at a given kinetic energy, is utilized in expressions of stopping power to represent incident particle kinetic energy, *T*. This is shown mathematically as,

$$\beta^2 = \left[\frac{v}{c}\right]^2 = \frac{T(T+2Mc^2)}{(T+Mc^2)^2}, \qquad (33)$$

where *M* is the mass of the incident particle and *c* is the speed of light. One can immediately recognize the relevance of this term from its use in Equation 28.

Utilizing these terms and concepts, it is feasible to derive a single equation to estimate collisional stopping power, S_c, of a charged particle within a medium. This can be represented as,

$$S_c = 4\pi z^2 r_o{}^2 \left(\frac{m_e c^2}{\beta^2}\right) N_a \frac{Z}{M_m} ln\left[\frac{2m_e c^2 \gamma^2 \beta^2}{I}\right] - \beta^2, \qquad (34)$$

in which all utilized terms are consistent with those described in Equations 9, 27, 33, and the units are represented in MeV*cm^2/g, consistent with those for Equation 29. Of note, *Z* is represented here as the sum of constituent weight fractions multiplied by the respective quotient of atomic number and molar mass, as shown in Equation 9.

Components of Collisional Stopping Power

In this work, analytic methods are used to calculate the electron densities and mean excitation potentials of BiPVT, EJ-200, and EJ-256, which are important components of the analytic estimate of S_c. Fortunately, such data already exist for polyvinyl toluene plastic from NIST, which corresponds to the constituent make-up of EJ-200. This is advantageous, since it enables a direct comparison between the accepted NIST values and those derived analytically here for EJ-200. If these values are found to agree, it suggests the methodology applied to arrive at the values calculated for BiPVT and EJ-256 are likely also reasonable. As a means of further ensuring the accuracy of this approach, the same will also be done for water, since it occupies a place of special importance in health physics and stopping power calculations. As such, analytic values calculated for proton range and stopping power in water will also be compared to accepted values listed by NIST.

Collisional stopping power is heavily influenced by two primary factors, the electron density and mean excitation potential of the medium, and both values can be calculated analytically for compounds. The fact that S_c is heavily affected by electron density is intuitive, since atomic and molecular electrons provide the Coulombic forces which attenuate charged particles transiting through a medium. Equation 9 provides the solution to the term $N_a(Z/M_m)$ within Equation 34 but without the density term. And from this, the total number of electrons present (N_{et}) within each gram of the fictional element, which is also known as its electron density, may be calculated using Equation 9, as previously addressed in Chapter 4.

Lastly, the final variable needed to determine an approximate solution to charged particle stopping power via Equation 35 is the mean excitation potential of the compound, *I*. This value, in units of eV, represents the average of all electronic transition energies for a given atomic target, and an approximate value can be calculated for any compound if the ionization potentials are known for the constituent elements. The NIST website provides these values for hydrogen, carbon, bismuth, oxygen, and lead [46]. These values are provided below in Table 6.1. Consequently, these NIST values can be leveraged to estimate the overall ionization potential for each compound of interest using the Bragg additivity rule, which states

$$\ln I = \frac{\sum N_i Z_i \ln I_i}{\sum N_i Z_i}, \qquad (35)$$

where N_i is the relative number of atoms of each element of atomic number Z_i in the compound. This equation can be simplified by using the specific elemental weight percentages within the compound, as defined in Equation 5. This simplified equation is

$$\ln I = \sum w_i \ln I_i, \qquad (36)$$

where I_i represents the respective excitation potential of *i*-th element. Of note, S_c calculations are dependent upon the logarithm of *I*, which implies a direct but slowly varying relationship. These calculations result in values of mean excitation potential for the three materials of interest listed in Table 6.2, as well as two additional materials used to further validate the accuracy of this methodology.

Based upon the demonstrated agreement between calculated, NIST, and ICRU 90 values [64] for compound excitation potential, analytical stopping power values and proton range may now be calculated for all materials of interest. In the case of EJ-200, liquid water, and air, calculated values are compared against accepted NIST and ICRU values determined using the Bethe-Bloch model to demonstrate the accuracy of the analytical approach, while also highlighting the accepted degree of uncertainty between 'approved' values. However, before proton range can be calculated, it is necessary to first detail the MCNP6 simulations used to compute the equivalent values, so those results may also be considered and analyzed.

Simulation Methodology

MCNP6 was utilized to estimate proton range within each of the materials of interest. This was achieved by modeling each material separately as a series of 10×10×0.005 cm sheets (x,y,z), with the sheets stacked together along the z-axis to form a larger material slab with a total thickness of 2.5 mm. Therefore, 50 individual layers were used to simulate the larger object for each material, and each material was modeled and evaluated independently using the established densities and weight percentages provided above.

Table 6.1. Mean excitation potential, I, values for specific elements in units of eV [46]

Element	*I* (eV)
Hydrogen	19.2
Carbon	78
Oxygen	95
Lead	823
Bismuth	823

Table 6.2. Mean excitation potential, I, values for compounds in units of eV

Compound	Calculated *I* (eV)	NIST *I* (eV)	ICRU 90 (eV) [64]
BIPVT	116.4	N/A	N/A
EJ-256	78.6	N/A	N/A
EJ-200	69.2	64.7	N/A
Water	79.4	75.0	78.0 ± 2.0
Air	86.9	85.7	85.7 ± 1.7

A beam consisting of monoenergetic protons was then directed into the center (x,y) of each material slab along the z-axis, and the energy deposition from only protons was recorded for each layer within the slab using a F6 tally (F6:h). This computational design enabled estimations of proton penetration depth by analyzing proton populations and deposited energy within the material layers. By varying the initial energy of source protons, predictions of energy-dependent proton range could then be determined. A graphic depiction of this is provided in Figure 6.1.

Additionally, proton physics were utilized in these simulations using the PHYS:H card to ensure proper Coulombic interactions were modeled to reduce proton kinetic energy. These simulated effects reflect the same processes accounted for in the analytic calculations, which incorporate changing proton collisional stopping power across varying material depth. For all materials and energies considered, 1M particles were simulated, with estimates of proton energy deposition and particle count passing all ten statistical checks for tally fluctuation. All results were found to converge with <0.01 % uncertainty. These values were estimated for each material in separate simulations at varying proton energies of interest, and nothing existed within the simulations to otherwise perturb the path of the incident protons.

Of course, since the material layers were modeled at thicknesses of 50 μm, proton range estimation accuracy is constrained by that level of granularity. As such, final estimates of proton depth were determined at the center of the final layer reached by the protons, with uncertainty estimated at ± 25 μm for every measurement. Energy-dependent proton range values computed using MCNP6 are provided in the Results section.

Results

Analytic calculations and MCNP simulation results for proton range and stopping power are provided below, as well as the comparison of these values with NIST's Proton Stopping-power And Range (PSTAR) data listed online [46]. This comparison was conducted to verify the accuracy of the calculated and simulated results for both water and the PVT-based plastic scintillator, EJ-200, in Figures 6.2 and 6.3. If found to agree, this analysis would support the reliability of similar simulations and calculations for BiPVT and EJ-256, which do not appear in literature.

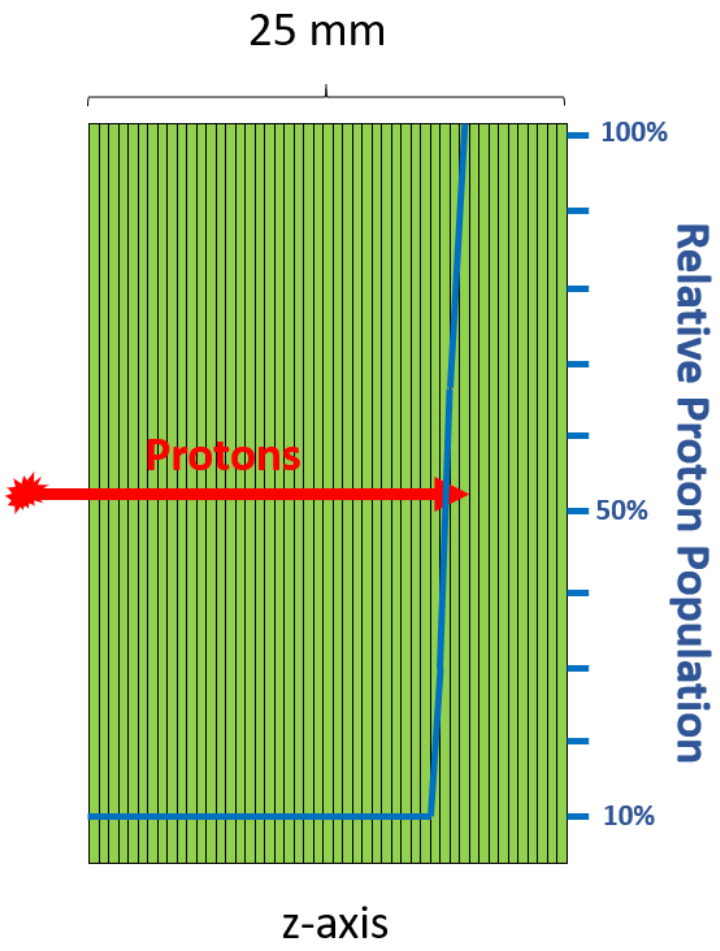


Figure 6.1. Conceptual diagram of the MCNP6 simulation methodology used to estimate energy-dependent proton range for the three scintillator materials. The diagram also illustrates the relative proton populations estimated within each layer of attenuating material, with the largest population present in the layer furthest from the source. In the methodology, the centroid of the furthest layer containing protons was used to estimate the maximum proton range at that energy.

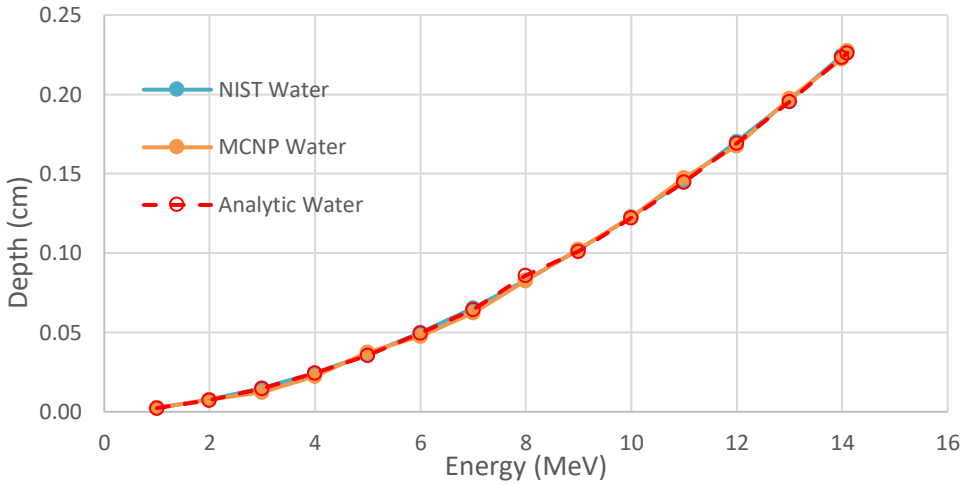


Figure 6.2. Estimated proton range values within liquid water for energies 1.0-14.1 MeV as reported by NIST [46], as well as the MCNP6 simulations and analytic calculations described herein for water.

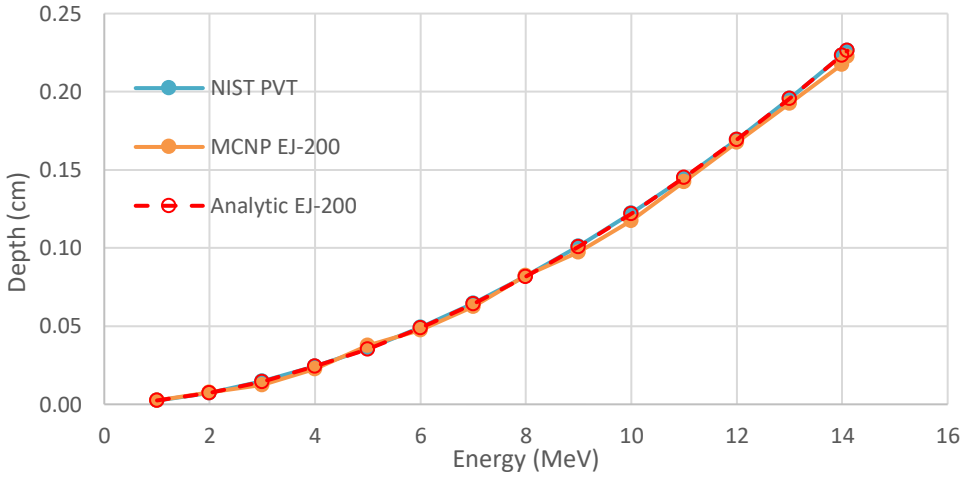


Figure 6.3. Estimated proton range values within PVT for energies 1.0-14.1 MeV as reported by NIST [46], as well as the MCNP6 simulations and analytic calculations described herein for EJ-200.

Comparisons of proton range predictions in water resulted in average differences between the approved NIST values and those determined from both MCNP simulation and analytic calculation of <1.25%. Likewise, differences for proton range in EJ-200 between MCNP simulations and analytic calculations both averaged <4% when compared with the NIST published values for PVT. Based upon these results, the same methodologies were applied to both BiPVT and EJ-256 to estimate energy-dependent proton range within these materials, with the results shown in Figures 6.4 and 6.5. Analytic and MCNP-derived estimates for proton range differed by an average of <7% for BiPVT and <4% for EJ-256 across all energies; however, these averages were heavily weighted by large disparities in estimated range at 1 and 2 MeV due to the 25 μm granularity of the MCNP estimates. Excluding those two energies for both materials reduces the average difference between measurements to <5% and ~2% for BiPVT and EJ-256, respectively. The calculated and simulated values of energy-dependent proton range are provided below in Table 6.3 for all four materials.

Therefore, analytic methods can provide accurate and reliable predictions of comparable proton range in EJ-200, EJ-256, BiPVT, and liquid water. The values for the three materials of primary interest are plotted in Figure 6.6 to highlight their disparities and how those differences in proton range increase as proton energy increases. The validated analytic estimates for proton range also enable reliable predictions of material collisional stopping power, S_c, as defined in Equation 29 for all three materials considered. As mentioned previously, predictions of S_c are valid estimates of total stopping power, S, for the energies considered (>1 MeV/nucleon). The evaluated values of S for each material are plotted in Figure 6.7 and listed in Table 6.4. Calculated values for the stopping power of liquid water differed by an average of ~1% when compared to the values provided by NIST, and a similar average disparity was found for the same comparison between EJ-200 and NIST plastic scintillator.

Lastly, these comparative predictions of proton recoil range facilitate an analysis of proton leakage and pixel crosstalk, which represent mechanisms reducing signal localization. An initial investigation, specifically for protons scattered within the center of a pixel toward an outer edge, can provide insight into the fraction of pixel cross-sectional area capable of attenuating a 7 MeV recoil proton, which is the average kinetic energy of recoil protons within a 14 MeV neutron environment. These values are listed below, and their potential relevance is discussed in greater detail within the next section.

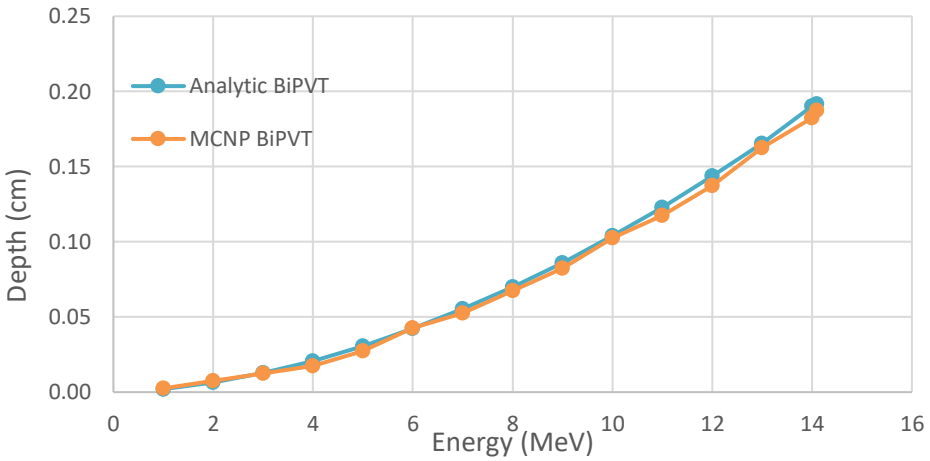


Figure 6.4. Estimated energy-dependent proton range within BiPVT derived both via MCNP simulation and analytically.

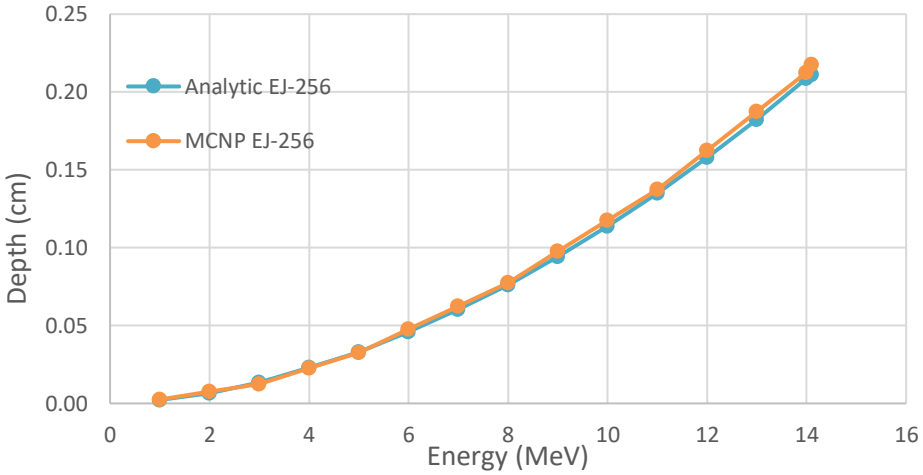


Figure 6.5. Estimated energy-dependent proton range within EJ-256 derived both via MCNP simulation and analytically.

Table 6.3. Simulated (MCNP) and calculated (Analytic) energy-dependent proton ranges (cm) for each material examined.

	MCNP				Analytic			
E (MeV)	BiPVT	EJ-200	EJ-256	Water	BiPVT	EJ-200	EJ-256	Water
1	0.0025	0.0025	0.0025	0.0025	0.0020	0.0025	0.0022	0.0024
2	0.0075	0.0075	0.0075	0.0075	0.0064	0.0072	0.0067	0.0074
3	0.0125	0.0125	0.0125	0.0125	0.0127	0.0144	0.0135	0.0148
4	0.0175	0.0225	0.0225	0.0225	0.0208	0.0245	0.0230	0.0243
5	0.0275	0.0375	0.0325	0.0375	0.0306	0.0354	0.0341	0.0356
6	0.0425	0.0475	0.0475	0.0475	0.0423	0.0489	0.0470	0.0495
7	0.0525	0.0625	0.0625	0.0625	0.0555	0.0644	0.0602	0.0646
8	0.0675	0.0825	0.0775	0.0825	0.0700	0.0818	0.0784	0.0858
9	0.0825	0.0975	0.0975	0.1025	0.0860	0.1008	0.0967	0.1011
10	0.1025	0.1175	0.1175	0.1225	0.1039	0.1218	0.1167	0.1222
11	0.1175	0.1425	0.1375	0.1475	0.1229	0.1452	0.1386	0.1448
12	0.1375	0.1675	0.1625	0.1675	0.1436	0.1692	0.1621	0.1694
13	0.1625	0.1925	0.1875	0.1975	0.1655	0.1955	0.1870	0.1955
14	0.1825	0.2175	0.2125	0.2225	0.1901	0.2232	0.2138	0.2234
14.1	0.1875	0.2225	0.2175	0.2275	0.1915	0.2262	0.2166	0.2262

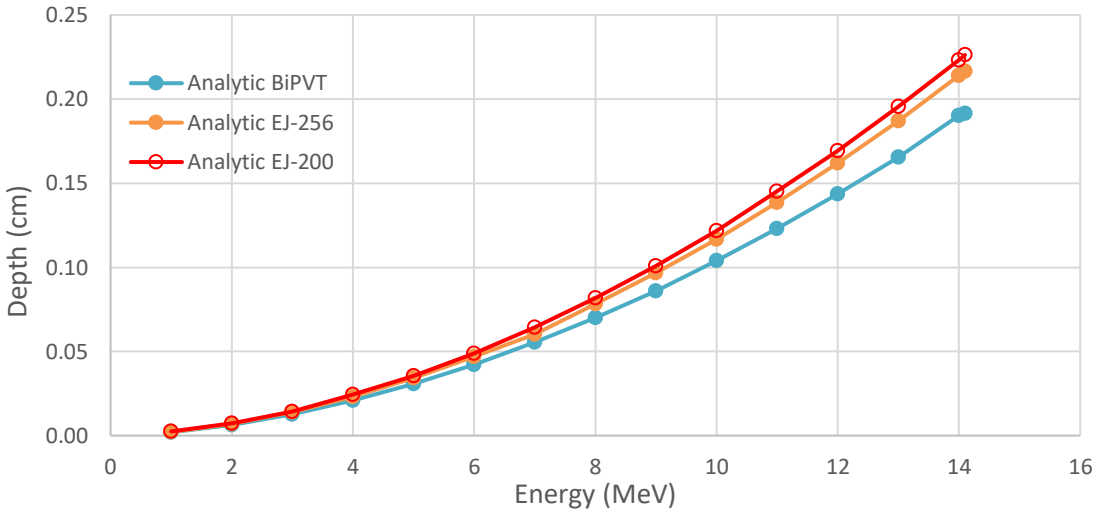


Figure 6.6. Comparative estimates of energy-dependent proton range within BiPVT, EJ-256, and EJ-200 derived via analytic methods.

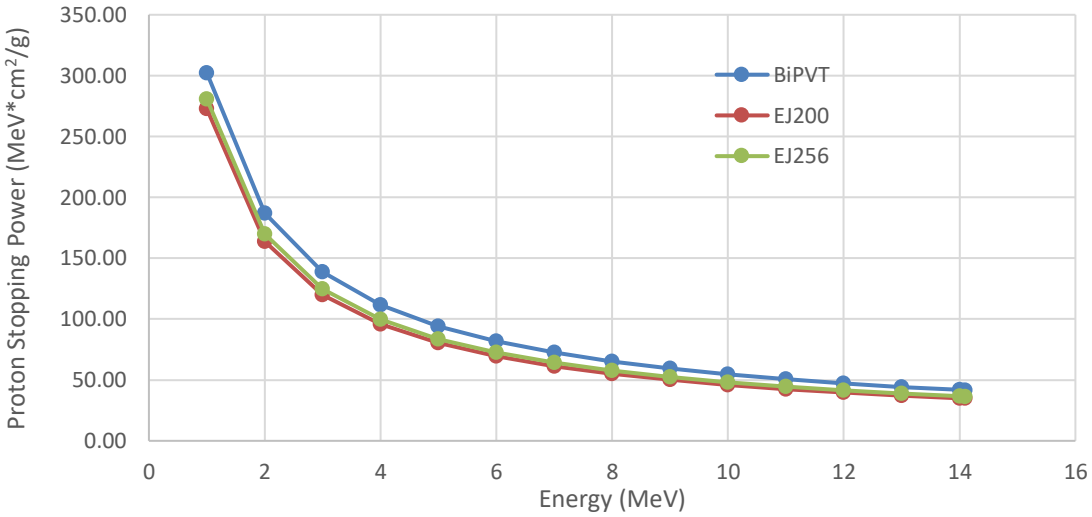


Figure 6.7. Comparative estimates of energy-dependent total proton stopping power, *S*, within BiPVT, EJ-256, and EJ-200 derived via analytic methods.

Table 6.4. Calculated energy-dependent stopping powers, *S*, for each material examined.

	Analytic Stopping Power (MeV*cm^2/g)			
E (MeV)	BiPVT	EJ-200	EJ-256	Water
1	302.26	272.70	280.66	269.79
2	187.13	163.88	169.80	162.86
3	138.90	120.07	124.79	119.57
4	111.76	95.86	99.81	95.58
5	94.15	80.33	83.74	80.16
6	81.72	69.44	72.46	69.34
7	72.43	61.35	64.07	61.29
8	65.20	55.08	57.56	55.05
9	59.40	50.07	52.35	50.06
10	54.63	45.97	48.08	45.97
11	50.64	42.54	44.51	42.55
12	47.24	39.62	41.47	39.64
13	44.31	37.12	38.86	37.15
14	41.76	34.94	36.59	34.97
14.1	41.52	34.74	36.38	34.77

Conclusions

The demonstrated agreement between NIST PSTAR data and those derived via both MCNP simulation and analytic calculation validates the employed theoretical methodology. In the case of EJ-200, a small portion of the disparity is attributable to minor differences in material density between PVT (1.031 g/cm^3) and EJ-200 (1.023 g/cm^3). Additionally, the limit of 25 μm on the fidelity of MCNP simulated estimates also contributes to the reported disparities for all materials, especially at lower energies. Despite this, the agreement between the theoretical calculations of proton range and those reported by NIST or simulated in MCNP is considered acceptable.

These results for proton range and stopping power confirm one anticipated relationship between the three materials. Specifically, protons of equivalent energy would be expected to travel furthest in EJ-200, followed by EJ-256, with BiPVT providing both the shortest range and, by extension, the greatest stopping power. This is due, however, to more than simply differences in material density, although it does follow that relationship. Although related, the far more significant contributor to differences in proton range is the comparative material electron density, which was calculated earlier and provided in Table 4.3. Consequently, the presence of high-Z-loading in both EJ-256 and BiPVT dramatically increases material electron density, which affects both the force and frequency of Coulombic collisional interactions between charged particles, including recoil protons, and orbital electrons within the media.

From these estimates, it is observed that a 14.1 MeV neutron imparting all or nearly all its initial kinetic energy to a proton in a single collision will produce a recoil proton traveling ~18% further in EJ-200 than in BiPVT. This equates to an additional distance of ~0.35 mm, which may seem insignificant due to the forward scatter required for such interactions in a pixel length of 19 mm; however, it implies BiPVT pixels benefit from a higher likelihood of attenuating high-energy recoil protons and collecting the light emitted by each.

Perhaps a more instructive analysis occurs when the average imparted energy of 7 MeV is considered. According to the analysis presented, such an interaction would provide an average difference in expected proton recoil distance of ~0.1 mm. Therefore, for protons scattered directly toward a pixel edge, the likelihood of full proton attenuation and subsequent light collection is directly linked to pixel cross-sectional area. For example, for pixels with cross-sections of 2×2 mm, only those protons scattering within the central 0.8 mm^2 of BiPVT (20% of the total cross-sectional area) will reliably deposit their full energy within the pixel. In the case of EJ-200, this active area reduces to ~0.05 mm^2, or ~12.25% of the total cross-sectional area.

Again, this only applies to protons scattered directly toward a pixel edge; however, the percentage of available area capable of facilitating proton attenuation and maximum light collection is expected to exponentially increase as pixel size increases. This relationship is demonstrated by the calculated percentage of cross-sectional area expected to fully attenuate a 7 MeV proton scattered toward the pixel edge, as shown in Table 6.5. Specifically, the table indicates the expected importance of shorter proton recoil range for arrays with small pixel dimensions, while it also demonstrates how the importance of proton recoil distance, especially for protons scattering directly toward the pixel edges, reduces exponentially as pixel dimension, and therefore pixel volume, increases. Lastly, this investigation provides the most accurate prediction of energy-dependent proton range and stopping power to date for the novel 21%-loaded BiPVT material. Unfortunately, no similar predictions of proton stopping power for EJ-256 were found in literature to support a direct comparison.

Analyses of Expected Photon and Neutron Interactions

X-rays

Building upon the calculations explained in Chapter 4, this analysis is intended to provide a rough prediction of relative light yield from each of the scintillators when exposed to 370 kVp bremsstrahlung spectrum of x-rays in the free field, without any attenuation or IQI employed.

Starting with x-ray generation, the tungsten target provides a radiative yield of ~3.02% for 370 keV electrons, as reported by NIST ESTAR [65]. Therefore, a current of 3 mA, or 3×10^{-3} c/s, is expected to emit ~33.522 J/s in bremsstrahlung x-rays, as calculated in Equation 37.

$$\frac{3\times10^{-3}\ \mathrm{c}}{sec}\times\frac{1\ e}{1.6\times10^{-19}\ \mathrm{c}}\times\frac{0.37\ e\ MeV}{e}\times\frac{0.0302\ \gamma\ MeV}{e\ MeV}\times\frac{1.6\times10^{-13}\ \mathrm{J}}{\gamma\ MeV}=33.522\frac{J}{sec},\quad(37)$$

Since each image was recorded for 0.5 seconds, 16.76 Joules (J) of bremsstrahlung x-rays, or ~1.05×10^{14} photons, were produced during each recorded image in 4π. At a SDD of 100 cm, the photon fluence is therefore calculated as 8.34×10^{8} photons per cm^2 at the arrays, so ~3.33×10^{7} photons were directly incident upon each 2×2 mm pixel face during each measurement. However, due to the presence of a collimating window in the MXR RGD, a significant fraction of lower energy photons would also be reflected through this window toward the arrays. Consequently, the calculated number of incident photons is likely very low. Additionally, due to the array proximity, the calculated values of photon flux are assumed as consistent across all three arrays.

Table 6.5. For each material, the fraction of pixel cross-section wherein a 7 MeV proton scattered directly toward a pixel edge is expected to fully attenuate and deposit light within the pixel. These values are provided for various pixel cross sectional areas (cm^2) and demonstrate the importance of proton recoil range within small pixel arrays.

Pixel side (cm)	Pixel Area (cm^2)	BiPVT	EJ-200	EJ-256
0.15	0.02	6.76%	N/A	N/A
0.20	0.04	19.80%	12.67%	15.85%
0.30	0.09	39.69%	32.57%	35.85%
0.40	0.16	52.20%	45.97%	48.87%
0.50	0.25	60.53%	55.12%	57.64%
0.60	0.36	66.42%	61.67%	63.90%
0.70	0.49	70.80%	66.59%	68.56%
0.80	0.64	74.18%	70.39%	72.17%
0.90	0.81	76.85%	73.43%	75.04%
1.00	1.00	79.03%	75.90%	77.37%

MCNP6 simulations provide predictions of energy deposition per incident photon within each pixel, and these values can be averaged across all twelve pixels for each material. Based upon such calculations, the average energy deposition in MeV per incident photon is listed in Table 6.6 for each of the three materials analyzed. Of note, the x-ray source was modeled as a point source collimated in a conical direction with a half angle of 8.11˚ and centered on the EJ-200 array. At the face of the DDA, this produced a circle of direct source exposure with a radius of 14 cm, which fully enclosed the DDA and the IQI. These MCNP estimates include corrections for the forward bias and directionality of the source term. The simulations also pass all ten statistical tests for tally fluctuation, and the reported solutions converge with <1% uncertainty.

Utilizing these computational predictions of average energy deposition per photon and the calculated number of photons incident upon each pixel from direct exposure in each measurement, a prediction of energy deposition from the source is possible. These values are provided in Table 6.7.

Light yield, as defined in Equation 5, is linearly related to energy deposition for x-ray measurements, although different materials produce light at varying rates. Table 6.8 provides the expected light yields for the three materials of interest in this analysis. Multiplying these values by the estimated energy deposition per pixel from Table 6.7 provides an estimate of the average number of photons emitted within each 2×2 mm pixel for each material per measurement. These calculated values are provided in Table 6.9.

Lastly, by multiplying the average quantum efficiency of the photodetector material across all emission wavelengths, a final comparison of relative light yield can be reached for each of the three arrays. Specifically, an a-Si TFT provides an average QE of 48.3% for the largely green emission spectrum of BiPVT, while EJ-200 and EJ-256, which share the same reported blue emission spectrum, average a QE of only 23.4% from a TFT [45]. Based upon these QE values, the final relative photon detection rates for each measurement can be calculated, and these values are reported in Table 6.10.

In conclusion, these values are only estimations of relative light detection because they rely upon a forward-scattered source term in a highly simplified simulated environment and do not account for the additional contributions from indirect x-rays emitted by the RGD. As such, the values reported here are expected to be far lower than those measured in a physical experiment, since the actual source is collimated and contributions from room return and other scattering surfaces may affect the final tallies.

Table 6.6. Average energy (MeV) deposited per incident photon within each pixel, as estimated by MCNP6 simulations.

Material	E_{dep} (MeV/photon)
BiPVT	4.097×10^{-5}
EJ-256	1.561×10^{-5}
EJ-200	4.111×10^{-6}

Table 6.7. Average predicted energy (MeV) deposited per pixel for each material of interest during each 0.5 sec measurement.

Material	E_{dep} (MeV)
BiPVT	1,364.3
EJ-256	519.8
EJ-200	136.9

Table 6.8. Reported light yields (ph/MeV) for BiPVT, EJ-256, and EJ-200 [9, 37, 36].

Material	Light Yield (photons/MeV)
BiPVT	20,000
EJ-256	5,200
EJ-200	10,000

Table 6.9. Estimated average number of photons emitted within each 2×2 mm pixel per measurement.

Material	Emitted Photons
BiPVT	2.729×10^{7}
EJ-256	2.703×10^{6}
EJ-200	1.369×10^{6}

Table 6.10. Estimated average number of photons detected within each 2×2 mm pixel per measurement.

Material	Detected Photons
BiPVT	1.318×10^{7}
EJ-256	6.325×10^{5}
EJ-200	3.203×10^{5}

Additionally, these estimates do not incorporate Zemax simulations of radiative light propagation through the pixel materials, which includes transmissivity, nor do they account for limiters to light collection within the physical BiPVT pixels, such as the documented occlusions and poor ESR reflectivity. Therefore, the experimental and computational ratios are expected to differ between BiPVT and the other two materials; however, due to the similarity of optical properties present within EJ-200 and EJ-256, specifically their identical optical emission spectra, virtually identical transmissivities, and equivalent manufacturing quality, the predicted ratio of measured signal may be close. As such, these estimates suggest EJ-256 may produce ~2× the signal as EJ-200 from 370 kVp free-field exposures.

D-T Neutrons

This portion of the analysis is intended to provide rough predictions of relative light yield from each of the scintillator pixels when exposed to 14.1 MeV neutrons from the ING-27 neutron generator, which was described previously in Chapter 5. As with the previous x-ray efficiency predictions, these calculations are for free-field scenarios without any neutron attenuation or IQI employed.

For these predictions, the Varex flat panel detector containing the three scintillator arrays is located ~5.7 cm from the edge of the D-T generator and x-ray shield, which were also described in Chapter 5. This provides a total SDD of ~12.5 cm and enables the use of the 2 in tungsten block IQI for shielded measurements, while also minimizing SDD and maximizing array solid angle. Since the D-T generator produces neutrons at a rate of 4.3×10^7 per second over 4π, this implies the neutron flux at the closest pixel face will be ~22,400 neutrons/cm^2-sec, or ~900 neutrons/pixel-sec for each 2×2 mm pixel face. However, only a small fraction of the incident neutrons are expected to interact with the arrays, while most will simply pass through the arrays without reaction.

Focusing solely on proton recoil reactions, the probability of a 14.064 MeV neutron interaction can be calculated for a given material using the macroscopic cross section for (n,p) interactions and the material depth. This is determined using,

$$F = 1 - \frac{Q}{Q_0} = 1 - e^{-N\sigma t}, \qquad (38)$$

which is a permutation of Equation 15, but one applied to neutrons. Here, F represents the fraction of neutrons expected to interact at least once within the material of thickness, t, in centimeters. Additionally, Q is the total number of penetrating neutrons, Q_o represents the initial number of neutrons incident on the material, N is the atomic number density (atoms/cm^3), and σ is the microscopic cross section for (n,p) elastic scatter. Together, $N\sigma$ represent the macroscopic cross section for a given neutron interaction, Σ.

For any compound material, such as those considered in this research, the macroscopic cross section, Σ, for a specific interaction is calculated by multiplying the material's atomic number density, N, by the sum of the products of the constituent material atomic fractions, A, and their respective microscopic cross sections by using the equation,

$$\Sigma = N \sum \sigma_i A_i, \quad (39)$$

Leveraging the atomic fractions and number densities provided in Tables 4.1 and 4.2, respectively, as well as Equations 38 and 39, the probability, F, for each incident 14.064 neutron to interact within 1.9 cm of material can be calculated for BiPVT, EJ-200 and EJ-256. These values are provided in Table 6.11 for (n,p) reactions. Using these values and the expected flux of source 14.064 MeV neutrons incident upon each pixel, the rate of (n,p) reactions from direct neutrons at a SDD of 12.5 cm can be estimated, both per second and for the 150-sec measurement windows expected during experimentation, as shown in Table 6.12.

Furthermore, the average energy imparted to a recoil proton, ΔE, can be calculated using the equation,

$$\Delta E = \left(\frac{1-\alpha}{2}\right) E_o, \quad (40)$$

where E_o represents the initial kinetic energy of the incident neutron, which has already been defined as 14.064 MeV for a D-T neutron source. In Equation 40, α is defined as,

$$\alpha = \left(\frac{A-1}{A+1}\right)^2, \quad (41)$$

for any atom with atomic number, A. Since the hydrogen nucleus consists of only a single proton (A=1), α is calculated as a value of 0, which implies ΔE=0.5 E_o. Therefore, the average kinetic energy imparted to recoil protons from elastic scattering interactions with source D-T neutrons is ~ 7 MeV. Using this value of average energy transfer, initial predictions of expected light generated per interaction can be made. Prior research suggests the light output from 7 MeV protons in BC-505 liquid scintillator is roughly 3.5 MeVee [66]. Therefore, by assuming this value is roughly consistent across all three materials, we can apply the light yield values listed in Table 6.8 for each material, thereby producing crude, relative predictions of light output from each (n,p) reaction.

Table 6.11. Calculated macroscopic cross sections and probabilities for 14.064 MeV (n,p) elastic scatter interaction within 1.9 cm of material.

Material	Σ (n,p)/cm	F (%)
BiPVT	0.03864	7.08
EJ-256	0.03574	6.56
EJ-200	0.03562	6.54

Table 6.12. Expected rate of (n,p) reactions from incident 14.064 MeV neutrons

Material	(n,p) rxns/pixel-sec	(n,p) rxns /pixel-measurement
BiPVT	63.72	9,558
EJ-256	59.04	8,856
EJ-200	58.86	8,829

Using these values, EJ-200 is expected to produce ~35,000 photons per (n,p) reaction, while BiPVT may be expected to produce an average of ~70,000 photons, and EJ-256 may produce up to ~18,200. Lastly, as discussed in the case of x-ray interactions, these values of photon detection must also be modified by the QE of the photodetector. The final calculated values of expected photon detection, including QE of the photodetector for each array, are provided in Table 6.13.

Of note, the estimate for BiPVT is likely low relative to EJ-200 and EJ-256, since the two latter materials lack the radiative deexcitation pathways present in BiPVT for molecules excited to triplet states. Additionally, since BC-505 is a fluid, thereby benefiting from molecular motion, it offers a substantially higher probability for triplet-triplet annihilation (TTA) events to occur along proton ionization tracks where triplet states are densely packed. TTA events produce two singlet-state molecules, one excited (S_1) and one deexcited (S_0), which offers another productive pathway for radiative emission in such circumstances. Consequently, MeVee predictions for BC-505 will likely overestimate photon production in EJ-200 and EJ-256. It is unknown at this time how light production in BiPVT may differ from that of BC-505 since it has not yet been measured.

When considering the 7 MeV proton recoil distances for each material shown in Fig. 6.6, the ions may be traveling any direction in 4π. As such, the fractional area of each 2×2 mm pixel (in 2-D) which ensures full proton energy deposition, regardless of recoil direction, becomes important, and these values are provided in Table 6.5. More importantly, protons deposit energy non-linearly as they transit materials. Despite creating straight and dense ionization trails, protons deposit greater amounts of energy as they lose kinetic energy, often depositing most of their energy within the last few nanometers of travel. This was demonstrated earlier in Chapter 6 via the Bethe-Bloch model calculations, hence the widespread application of proton beam therapies for cancer treatments. Consequently, the range of recoil protons is extremely important for predictions of energy and light localization within small pixels.

By applying a two-dimensional model to this problem, it is possible to provide a better analysis of expected photon production rates in the pixels. For example, in the case of the 2×2 mm EJ-200 pixels considered, only 12.67% of the pixel cross-section ensures 100% energy deposition from 7 MeV proton produced within. However, this estimate only applies to outwardly directed recoil protons, so it is artificially low.

Table 6.13. Expected average number of photons detected within each pixel per 150s measurement, assuming 100% localization of energy deposition and including QE.

Material	Ph/pixel-measurement
BiPVT	6.691×10^8
EJ-256	1.612×10^8
EJ-200	3.090×10^8

A better expression of the relationship between pixel cross-sectional area and the probability of retaining recoil proton energy can be found with simple a 2-D analysis. This explicitly considers the spacing between the region offering 100% probability of energy deposition at the center of each pixel and the pixel edge, which still provides a 50% probability for energy deposition because protons scattered inward over 2π at a pixel face will deposit their energy locally. Therefore, assuming protons recoil with equal likelihood across all 360˚ in a 2-D circle of radius, *R*, which is equal to the range of a 7 MeV proton, the probability, *P*, of 100% energy deposition at various distances from the pixel center may be calculated using the equations,

$$\theta = 2cos^{-1}\left(\frac{d}{R}\right), \quad (42)$$

and

$$P = \frac{\frac{1}{2}R^2(\theta - sin(\theta))}{\pi R^2}, \quad (43)$$

where θ is the central angle and *d* is the distance between the interaction point and the pixel edge. A 2-D diagram of this is provided as Figure 6.8.

Using these equations, probabilities of proton energy deposition for pixels with 2×2 mm cross-sectional area may be calculated for locations from the center of the pixel to its edge. These values for EJ-200, EJ-256, and BiPVT are calculated and plotted in the following figure, with respect to distance from the center of the pixel at 0 to the edge at 1 mm. These expected probabilities reduce even further at pixel corners, where one would only detect the full proton ionization track if scattered inward across π, with a probability of 25%. Fortunately, by convolving the 2-D probability in Figure 6.9, it is relatively simple to account for geometry changes in a 3-D model, as shown below for one quarter of a 2×2mm pixel of EJ-200 in Figure 6.10. These average 2-D probability areas are provided for each material in Table 6.14.

Of course, this analysis can be extended once more to incorporate pixel length, which would involve an additional dimension of probability. The below figure provides a 3-D plot of such a result for EJ-200, representing the probability volumes for one quarter of a pixel at 1 mm up to the edge. As such, Figure 6.11 provides a probability for the local detection of 7 MeV proton energy deposition for each of the four 3-D corners of a 2×2 mm pixel for lengths ≥ 2 mm. The material-specific probability volumes are provided in Table 6.15.

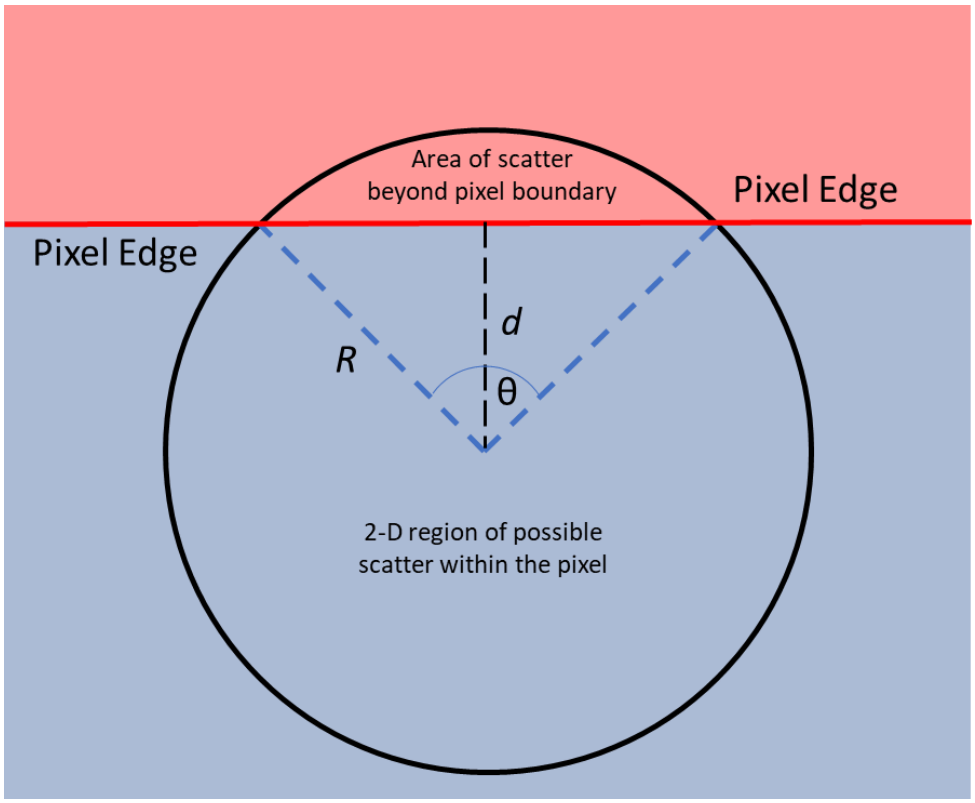


Figure 6.8. Image depicting a pixel edge and the values necessary for calculating the probability of proton energy deposition within the pixel based on *R*, *d*, and *θ*.

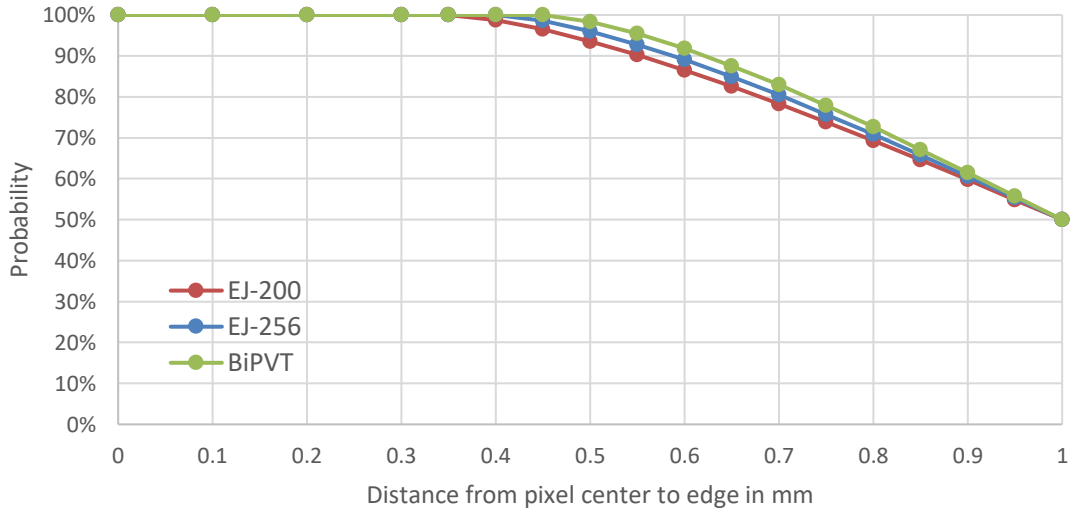


Figure 6.9. Plot of expected probabilities for a 7 MeV proton to deposit all kinetic energy locally within a 2×2mm pixel of EJ-200, EJ-256, or BiPVT, based on the distance of interaction from the pixel center (0 mm) to pixel edge (1 mm).

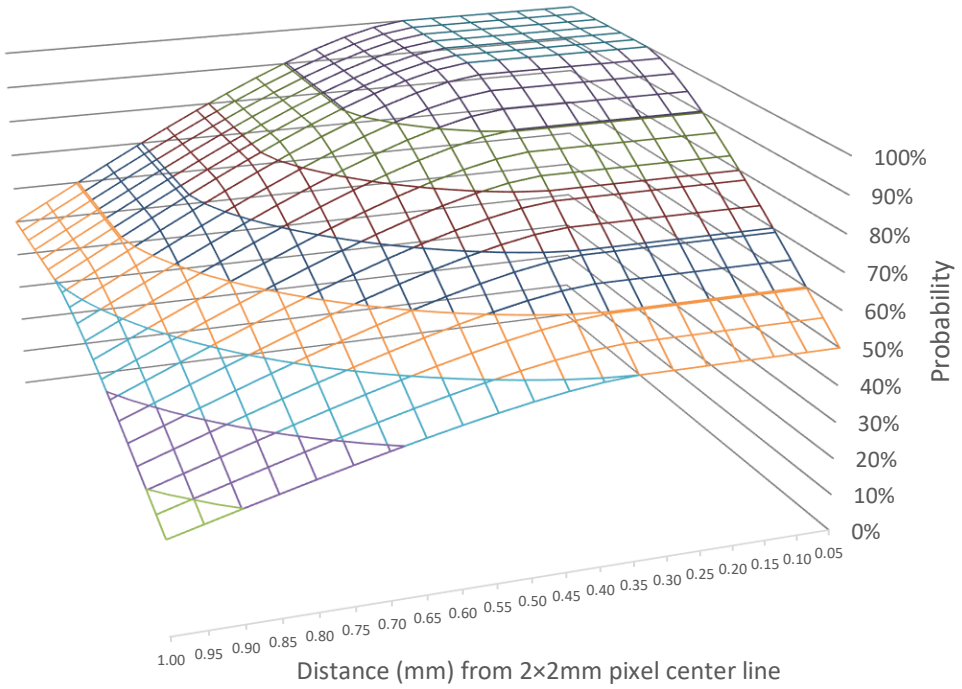


Figure 6.10. Expected probabilities for 7 MeV protons to deposit kinetic energy locally based on distance from a pixel edge within a 2×2mm pixel of EJ-200 in 2-D space. This graph represents one quarter of a pixel in 2-D, which is representative of the whole due to symmetry.

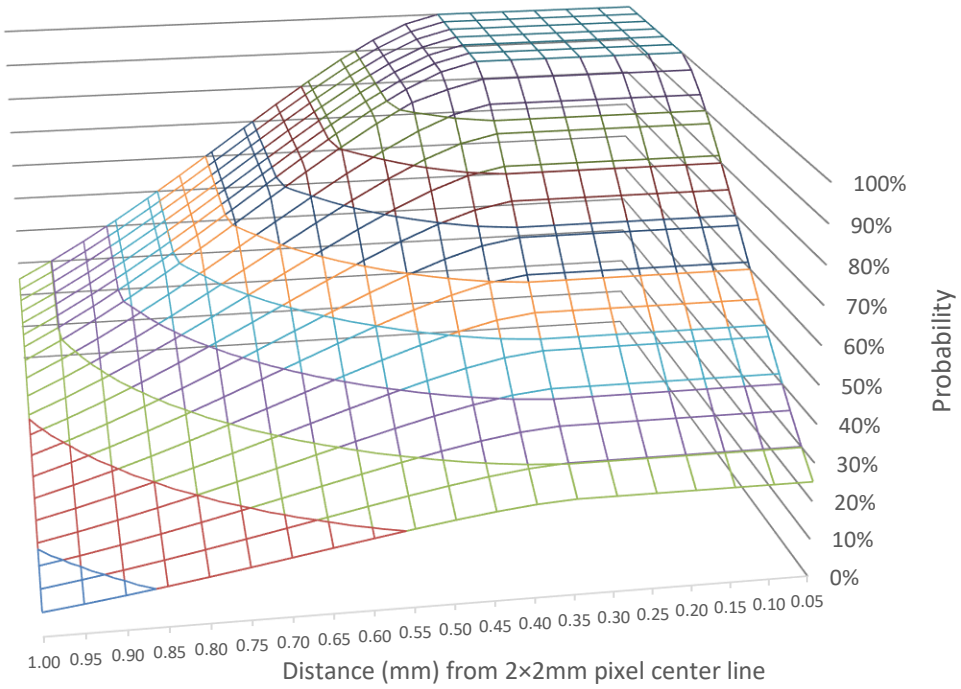


Figure 6.11. Expected probabilities for 7 MeV protons to deposit energy locally within a 2×2 mm pixel of EJ-200 based on distance from a pixel edge and corner in 3-D space. This graph represents one quarter of a pixel, which is representative of the whole due to symmetry.

Table 6.14. Analytically derived 2-D probabilities for full energy deposition and localization of 7 MeV recoil protons for pixels within a 2×2 mm pixel for each material of interest.

Material	Probability
BiPVT	76.9%
EJ-200	73.4%
EJ-256	75.1%

Table 6.15. Analytically derived probabilities for full energy deposition and localization of 7 MeV recoil protons for pixels within a 2×2×19 mm pixel for each material of interest.

Material	Probability
BiPVT	61.8%
EJ-200	56.2%
EJ-256	58.9%

In calculating the final probability volumes, the previously derived probabilities are applied to pixels with dimensions of 2×2×19 mm. As such, the 2-D probabilities for each material are valid estimates for 17 of the 19 mm of length, while the 3-D probability volumes previously demonstrated are appropriate for the final 1 mm at each pixel end. Applying this logic, the 3-D probability volumes for local energy deposition of 7 MeV proton recoil energy can be estimated for 2×2×19 mm for each material as shown in Table 6.16. These probability values enable updated calculations of predicted photon emission and expected light collection within these pixels. Of course, these estimates are still based on the interactions of 7 MeV protons created from elastic scatter with neutrons in each hydrogenous matrix, which is an extremely simplified estimate of proton behavior in these volumes. These values of predicted photon measurement are provided in Table 6.17.

Even though these are the most reasonable analytic predictions of photon light production available for the planned 150-sec measurement windows, it is anticipated these values are overpredictions for the reasons presented earlier. This is, of course, especially true for BiPVT, which is believed to produce ~20% of the detector response expected from x-ray simulations. This estimate would suggest that the BiPVT array may produce ~1×10^8 optical photons, putting its response below both EJ-200 and EJ-256. Despite the degraded performance of the BiPVT array, it is likely the ratios of measured light, especially between EJ-200 and EJ-256, will follow the relationships provided above. Consequently, there is value in performing these rough predictions.

Proton Pixel Crosstalk Study

Simulations

Just as in earlier simulations of x-ray pixel crosstalk, MCNP6 was used to estimate the relative rate of pixel crosstalk from proton recoils following 14.1 MeV neutron exposure within each of the three materials of interest, specifically BiPVT, EJ-256, and EJ-200. This was performed using separate simulations, each modeling a 3×3 array consisting of 2×2×19 mm pixels of material without ESR or spacing between adjacent pixels. Incident mono-energetic 14.1 MeV neutrons were collimated into a 2×2 mm plane directed at the center pixel in each array, so source neutrons only interacted with the central pixel of each simulated array, with neutrons evenly distributed across this plane. No other pixels in the arrays were exposed to the source of 14.1 MeV neutrons directly, so all estimates of deposited energy tallied in the outer pixels were assessed as resulting from neutron interactions within the center pixel. The results were estimated using particle specific tallies (F6: n,h), as well as a total energy tally (+F6), and neutron and proton physics cards were used in these simulations, as illustrated in Figure 6.12.

Table 6.16. Analytically derived probabilities for full energy deposition and localization of 7 MeV recoil protons for pixels within a 2×2×19 mm pixel for each material of interest.

Material	Probability
BiPVT	75.3%
EJ-200	71.6%
EJ-256	73.4%

Table 6.17. Expected rate of photon production within each pixel per measurement, considering the analytic probabilities of proton scatter for each material and 2×2 mm pixel in 3D space.

Material	Ph/Measurement
BiPVT	5.038×10^8
EJ-200	2.212×10^8
EJ-256	1.183×10^8

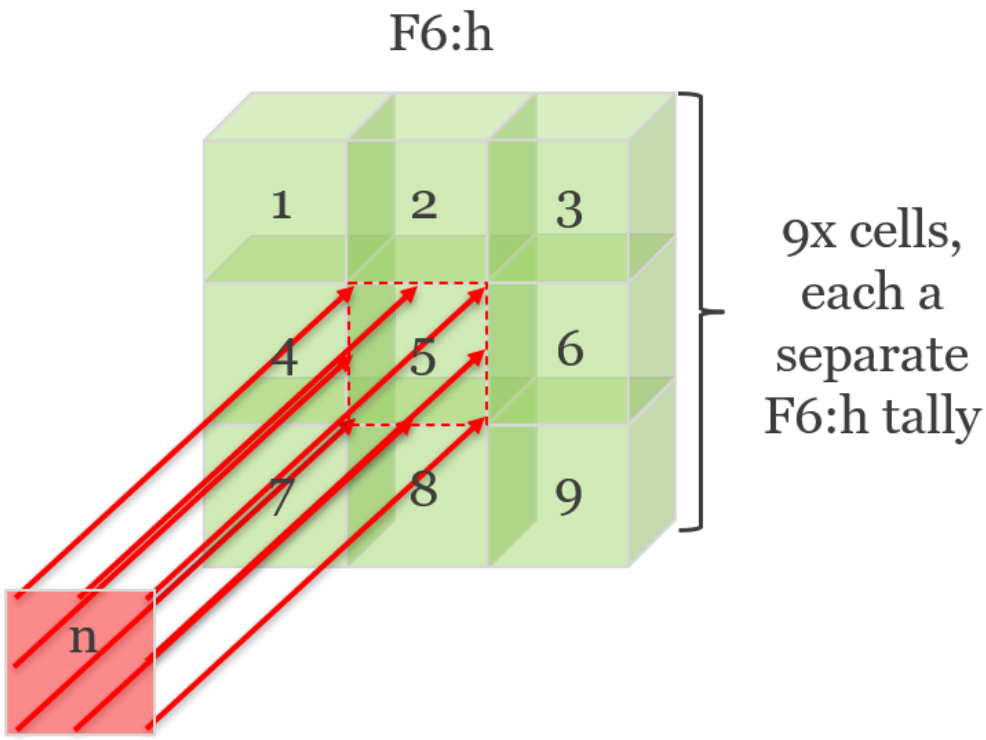


Figure 6.12. Depiction of the simulated methodology with incident 14.1 MeV neutrons striking the central pixel of each 3×3-pixel array. However, the pixel dimensions shown here are not representative; each material was evaluated as an array with individual pixel dimensions of 2×2×19 mm.

Particular attention was paid to proton energy deposition estimates within the outer pixels, since these were assessed as contributions from recoil protons originating from neutron elastic scatter with hydrogen atoms in the center pixel. This is similar to the analytical evaluation of proton leakage in the previous section. Therefore, the calculated ratio of deposited proton energy in the central pixel compared to that estimated within the entire array should provide a prediction of fractional proton pixel crosstalk for each material for these pixel dimensions.

Results

Computed tallies of proton energy deposition for each pixel were tallied by MCNP6 in units of MeV/g-source particle, so the values were first converted into simply units of deposited energy (MeV/source particle) using the material mass (g) of each pixel. The computed estimates of energy deposition were then summed for all cells in each array, and the ratios of proton energy estimated in just the center array pixel were calculated for each array. These estimated percentages are provided below in Table 6.18 and compared to the analytic values provided earlier in Table 6.17.

Conclusions

These simulations suggest the analytically derived values of proton energy localization overpredict the degree of proton crosstalk present within the pixelated arrays, which is likely due to the assumption that 7 MeV protons would scatter directly toward each pixel edge. In reality, a 7 MeV recoil proton would scatter at ~45˚ from the incident path of a 14.1 MeV neutron following elastic scatter, so it can be understood why the analytic calculations, based on the assumptions used, might overpredict proton pixel crosstalk. However, the analytic calculations do accurately predict proton energy localization performance based on the relative material. Specifically, MCNP6 simulations support the analytic determination that BiPVT will provide the greatest degree of proton energy localization, and, therefore, the least amount of proton pixel crosstalk of the three materials. Furthermore, both the analytic and simulated results predict EJ-256 will outperform EJ-200 in terms of proton localization, with its rate closer to that of EJ-200 than that of BiPVT. Lastly, simulated predictions of proton energy localization in EJ-200 match the analytic calculations in predicting that recoil protons created in this material are the least likely to deposit all their energy locally.

Table 6.18. Computationally derived estimates for the fraction of proton energy deposition within the center pixel of a 3×3-pixel array when exposed to 14.1 MeV. This is analogous to the analytic estimates performed above for the probability for full energy deposition and localization of 7 MeV recoil protons for pixels within a 2×2×19 mm pixel for each material of interest.

Material	Simulated Probabilities	Analytic Probabilities
BiPVT	81.1%	75.3%
EJ-200	79.5%	71.6%
EJ-256	79.8%	73.4%

CHAPTER SEVEN -

IMAGE ANALYSIS THEORY AND APPLICATION

Although computed tomography (CT) is not applied in this research, composite images (i.e. larger images constructed from multiple smaller images) are required for performance comparisons of the considered arrays due to their small size, which is largely a result of the limited quantity of novel material available for characterization. Consequently, the theory and procedures applied herein for x-ray and neutron digital detector array (DDA) performance comparisons are based on published American Society for Testing and Materials (ASTM) standards for the measurement of CT system performance. Edge response is measured using composite image data from a phantom of defined material and thickness, which produces differences in pixel modulation across the phantom's edge. In CT, this is provided by a circular phantom enabling a two-dimensional analysis of edge response; however, this research only examines a one-dimensional (1D) edge, so the phantom is offset from the pixel rows by a consistent angle selected between 2-5°, as per ASTM standards [67, 68, 48]. Ideally, this angular offset produces numerous array pixels measuring varying degrees of phantom attenuation, depending on the extent to which pixels are shielded by the phantom edge. The standard practice for characterizing CT system spatial resolution begins with measurements of a composite edge response function (ERF) [67]; however, one must first possess composite images to analyze.

Composite Image Production and Edge Response Measurement

Measured array responses using the Varex radiographic panel, as well as those estimated using MCNP6 and Zemax, are analyzed using ImageJ Image Processing and Analysis in Java (v1.52a) software. In the case of physical measurements, regions of interest (ROIs) are initially established over each individual 2×2 mm pixel for all three arrays from the free-field measurement, and these ROIs are used consistently to measure pixel response in all subsequent shielded measurements. Pixel measurements for all 15 shielded measurements are then off-set corrected and divided by the free-field measurement to eliminate any geometric distortion and measure only behavior in time and dose [53]. This last step is also used for the simulated responses provided by Zemax. After that, pixel responses are assembled to form the composite image of the measured shield response. Specifically, the 15 measurements, each composed of only 4×3-pixels, are combined into a thin, 4×45-pixel image of the shield edge response. Figure 7.1 provides two examples of these initial images for both BiPVT and EJ-200.



Figure 7.1. Image of initial, 4×45-pixel, composite images for a) BiPVT and b) EJ-200 measured in the 370 kVp x-ray environment.

However, these smaller composite images still provide too few pixels to support ERF analyses, which require a minimum of 256 pixels and pixel width of 11 across the measured edge [67]. Therefore, the smaller 4×45-pixel composite array images are expanded to 23×45 pixels by replicating the contrast values at commensurate distances across the measured edge, thereby producing a larger composite image for each array. This could only be accomplished with the use of a straight edge phantom, which facilitate contrast pattern replication at equivalent distances from the edge for both shielded and unshielded regions within each 4×45-pixel image. Figure 7.2 provides an example of this process.

These larger composite images are then imported into ImageJ to enable data analysis. Specifically, imported 23×45-pixel images are rotated to enable measurement of the edge profile, as illustrated below. A ROI is then established to measure as much of the edge as possible, with ROI minimums of 11-pixels across the edge and 256 pixels in total [63, 48]. ROI edge data are then averaged (top to bottom) to calculate the edge response.

Modulation Transfer Function and Spatial Resolution

Averaged values of edge response are then normalized, and interpolation is used to determine the edge response function (ERF), with bin sizes set at 10% of the pixel size used in the ROI [67]. An example ERF is provided in Figure 7.3.

A piecewise least-squared cubic fit of the ERF is then performed using the same number of values across the measured edge response. From these polynomial functions, the analytical derivative is calculated for each point to provide the line spread function (LSF), which is then normalized and centered on the ERF [67, 68]. This is represented mathematically as

$$LSF = \frac{d(ERF)}{dx}. \qquad (44)$$

An example of the LSF, superimposed on the ERF, is also shown in Figure 7.4. Next, the modulation transfer function (MTF) is calculated from the 1D Fourier Transform (FT) of the LSF using the equation,

$$MTF = FT\left(\frac{d(ERF)}{dx}\right) = FT(LSF). \qquad (45)$$

A 1D FT is used to move the data from the frequency to the spatial domain, so the MTF describes the change in modulation within an image signal as a function of modulation spatial frequency for the specific DDA.

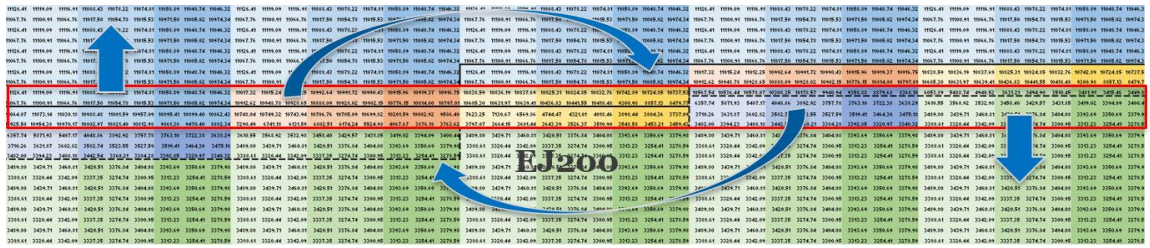


Figure 7.2. This image explains the systematic process of expanding a 4×45-pixel composite image into a 23×45-pixel composite image. Specifically, the red box highlights the original 4×45-pixel image, while the arrows, dashed boxes, and colors serve to illustrate what portions of the original image, at least for the 370 kVp x-ray measurements, are replicated to maintain the edge response. Additionally, fully shielded and fully unshielded portions are replicated to conserve the edge and broaden the image.

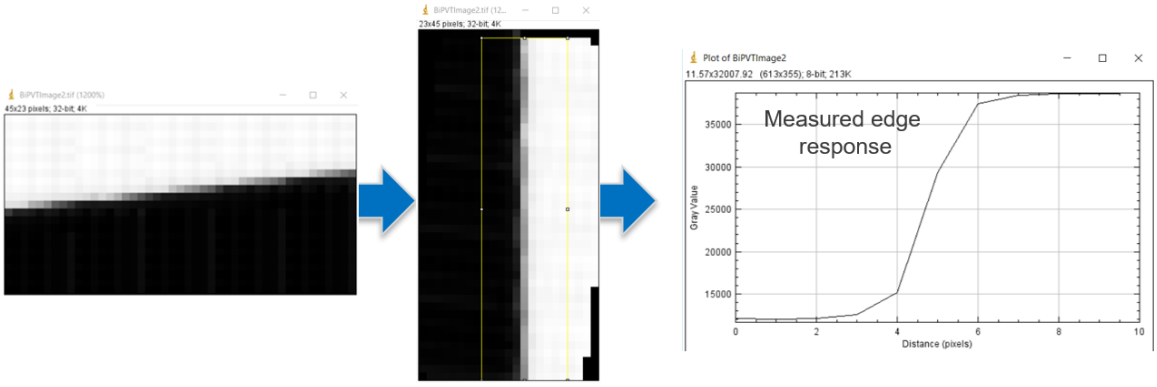


Figure 7.3. From left to right, example of a composite 23×45-pixel image imported into ImageJ. Next, the image is rotated until the IQI edge is vertical. Lastly, this enables a measurement of edge response within the highlighted ROI (yellow), which is applied consistently across all three arrays.

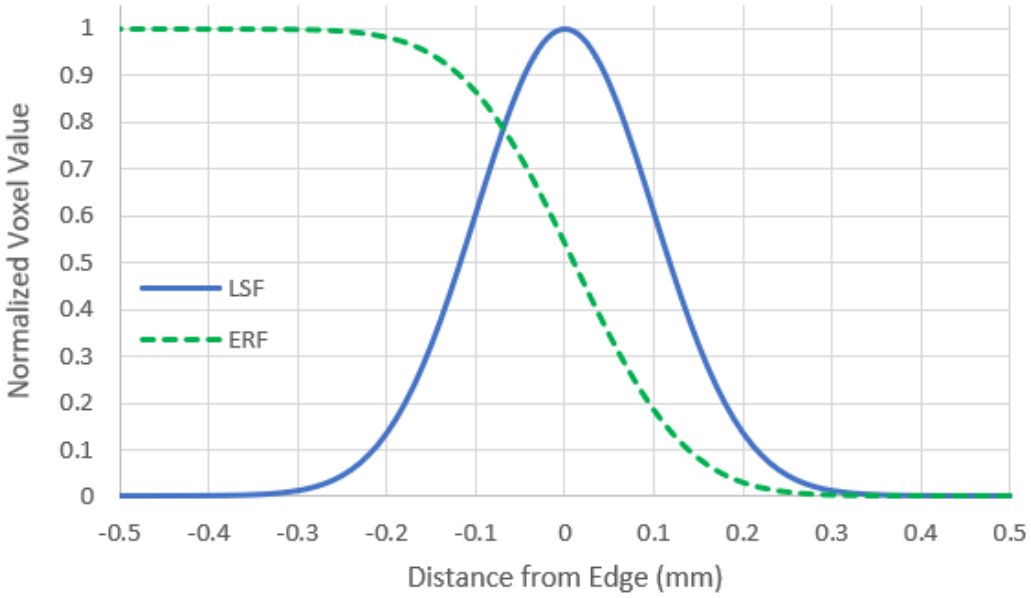


Figure 7.4. Expected Example plot of normalized edge response function (ERF) and line spread function (LSF).

MTF magnitudes are then normalized to unity at frequency zero, and a cut-off frequency at 10% of the MTF ($f_{10\%}$) enables a calculation of the DDA spatial resolution (SR) limit. Spatial frequency is represented in units of line pairs per millimeter (lp/mm), SR units are expressed in units of distance, such as mm. SR is calculated as one half the inverse of the spatial cut-off frequency ($f_{10\%}$), and it represents the limit of geometrical detail resolvable by the DDA with an uncertainty of ± 5% [67, 51, 69]. An example MTF, including the cut-off threshold for minimum SR, is provided in Figure 7.2.

Detector Signal-to-Noise Ratios Normalized

Since SR is calculated from the *normalized* MTF, information regarding the relative signal provided by different arrays is absent from any comparison based solely on this metric. Therefore, a more useful method for evaluating relative DDA performance relies on both the SR and the measured signal-to-noise ratio (SNR) of the DDA. The SNR is the quotient of mean value of the intensity (signal) and standard deviation (σ) of that intensity (noise) [51, 60]; however, when comparing radiography images produced by different arrays or panels, a more useful term for direct comparison is the detector SNR normalized (dSNRn). The equation for this is,

$$dSNRn = \frac{SNR \times \sqrt{2} \times 88.6\ \mu m}{SR}. \qquad (46)$$

Here the $\sqrt{2}$ term is used to correct the SNR, since the difference of two images is used for noise calculations. A value of 88.6 µm is consistent with phosphor film pixel widths, so its inclusion in dSNRn calculations standardizes DDA performance comparisons across multiple radiographic systems [51, 70]. The dSNRn is a useful indicator of DDA performance because it quantifies the exposure necessary to reach a full SNR [51, 60]. For a 16-bit image, this means ~50k contrast tones measured in the detector area, which avoids image overexposure. Typically, these values are expressed in plots of dSNRn vs. the square root of the exposure dose (mGy), with the slope of each line defining the DDA efficiency, as shown in Figure 7.3. However, if the exposure, beam filtering, and IQI are equivalent for two separate DDAs, then the dose terms cancel and leave just the dSNRn values to compare, with higher dSNRn values indicating superior DDA performance at that exposure. Traditional x-ray radiography DDA, such as TFT paired with gadolinium oxysulfide (Gd_2O_2S) or cesium iodide (CsI), typically yield SNR >200 and SR <200 µm. These systems provide dSNRn values well over 100 or even 1000 at certain exposures; however, such systems provide no capability to support fast neutron imaging, which constitutes the second half of this research to characterize BiPVT for DPI purposes. Therefore, x-ray dSNRn values produced by systems optimized for DPI are not expected to appear competitive when compared against traditional DDAs optimized solely for x-ray radiography.

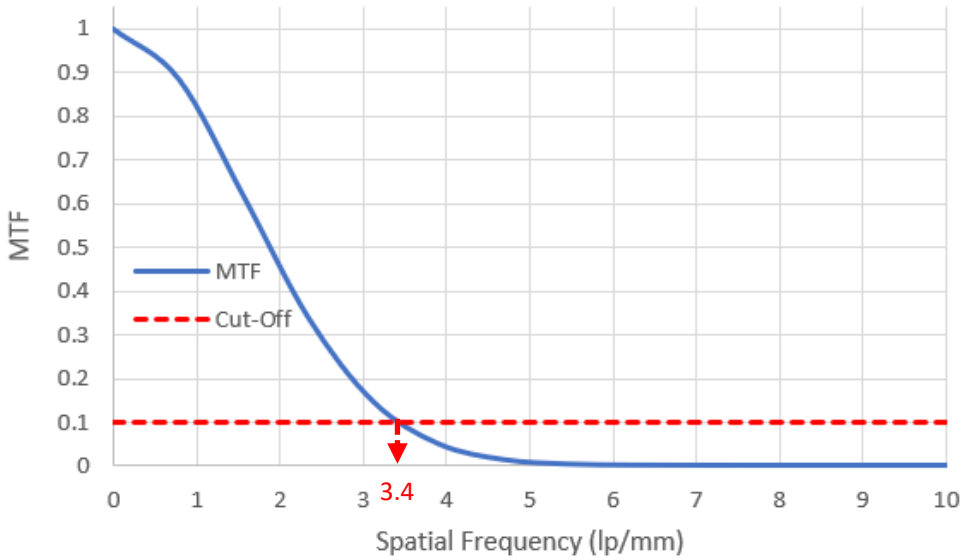


Figure 7.5. Example modulation transfer function (MTF), including the 10% cut-off threshold ($f_{10\%}$) which determines the value of spatial resolution (SR). In the case of this example, the MTF reaches 10% at a spatial frequency of 3.4 lp/mm, which equates to a hypothetical DDA SR value of 0.147 mm.

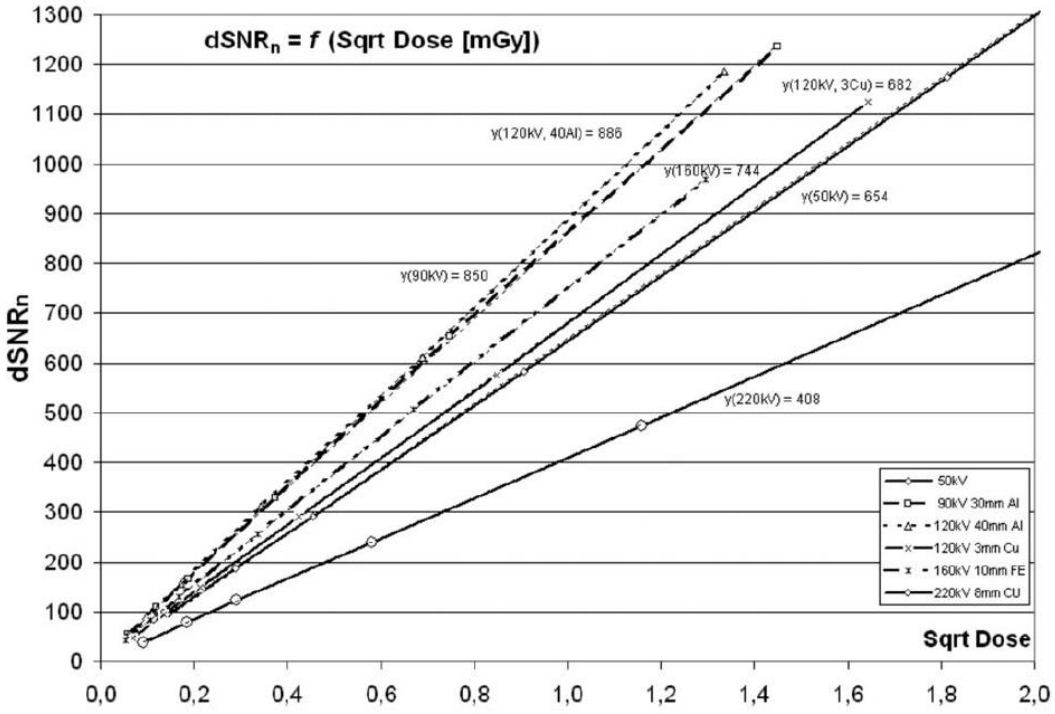


Figure 7.6. Example chart for efficiency test with difference images at different energy levels [53].

Factors Affecting Spatial Resolution

The SR of a DDA indicates the smallest geometrical detail resolvable by the imaging system, which is similar to DDA pixel size [60, 48, 49, 71]. For traditional DDAs evaluated in x-ray environments, this value is typically determined using a duplex wire gauge, also known as an image quality indicator (IQI) [48]. A duplex wire gauge enables the measurement and plotting of contrast modulation across increasingly smaller diameter wires using Equation 16. From these values of modulation, Equation 17 enables the calculation of SRb for the DDA system, which is analogous to SR calculated for a CT system. Traditional determinations of SR for a CT system rely upon a disk phantom, which is rotated and imaged with the axis of rotation normal to the scan plane [67]. This produces a series of pixels measuring the edge response of the disk phantom as it rotates, which are averaged to produce a 1-D edge response similar to that evaluated in the methodology described above. As such, a number of factors are known to affect the spatial resolution for any DDA, and the following is a list of some of those factors and how they can affect SR in a scintillator-based DDA.

Values of SR may be estimated for a given DDA by calculating the total unsharpness (U_t) of the system [72, 60], including the components of those terms. U_t is typically calculated using

$$U_t = \sqrt[3]{{U_i}^3 + {U_g}^3}, \qquad (47)$$

where U_i represents the inherent unsharpness and U_g represents the geometric unsharpness of the system. The inherent component refers to features of the DDA internal to the detector system, while the geometric term refers to external features, such as divergence of the incident radiation and object, detector, and source spacing [72].

Inherent Unsharpness

Pixel Pitch

Pixel pitch is the principal factor governing DDA SR because it defines the physical dimensions of the individual scintillator pixels [60]. Typically, smaller pixels provide better spatial resolution because they increase the spatial sampling rate, thereby increasing the spatial frequency at which image features may be resolved by the DDA. This comes at the cost of detection efficiency, however, since smaller pixels correspond to smaller individual active detector volumes, and a larger number of pixels in the same volume mean a higher percentage of material used to optically isolate those pixels. Despite this, lower detection efficiency does not typically impact SR because the processes by which SR is determined involves line pair and edge response normalization, both in the case of traditional x-ray IQI and CT. However, reduced pixel pitch can correspond to an increased possibility of internal scatter radiation, which will degrade DDA spatial resolution. Consequently, pixel

pitch for any DDA is typically optimized to provide the largest possible pitch necessary to detect the specific features of interest for the intended purpose of the DDA [60]. As such, pixel pitch should always provide the maximum detector volume possible, while minimizing the volume of material used to optically isolate the individual pixels. This maximizes the probability of particle detection while minimizing pixel spacing, which improves both SR and detection efficiency.

Internal Scatter Radiation

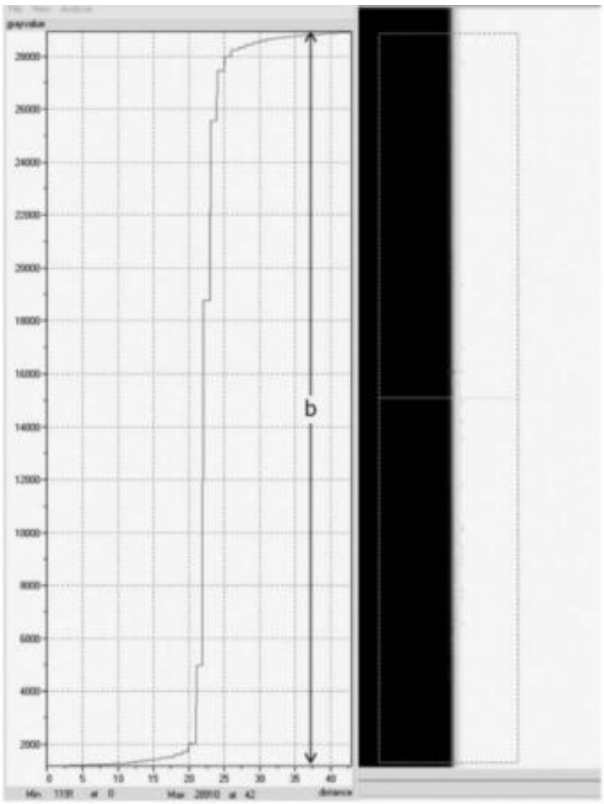
Internal scatter radiation (ISR) is defined as scattered radiation within the detector that occurs from the scintillator, photodiodes, electronics, shielding, or other detector hardware [60]. The amount of internal scatter can be affected by the thickness of the scintillator, since thicker scintillators allow for higher energy x-rays or neutrons to scatter more than once. This potentially allows incident particles to deposit portions of their energy in locations outside the initial interaction site, thereby contributing to noise. Pixel crosstalk, as it is discussed and defined above, is one such component of ISR. ASTM provides a standardized method for determining DDA ISR in x-ray environments, which includes measuring the edge response of a 16 mm-thick copper plate phantom when exposed to 220 kVp x-rays, with an 8 mm copper beam filter. From this, components of the edge response are measured and ISR is calculated in the manner shown in Figure 7.7.

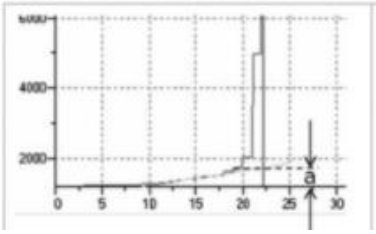
For the ASTM equation shown in Figure 7.7, *a* is defined as the long-range unsharpness contribution, and *b* is defined as the measured signal beside the copper plate [53]. Measurements of ISR for the three pixelated arrays were not performed as part of this research; however, now that simulated estimates of pixel crosstalk have identified ISR as a likely component affecting the SR of BiPVT, future analyses should consider the experimental quantification of ISR for similar high-Z loaded arrays.

Geometric Unsharpness

Source Size

Source size, or focal spot size, is inversely related to spatial resolution, so the larger the source of radiation the worse the expected SR for the image. This is because a larger area of emitted radiation produces a greater degree of possible angles for source radiation incidence upon the imaged feature and DDA. By increasing the dispersion of source radiation relative to the feature imaged, the response measured by the DDA is broadened, which results in decreased SR, as shown in Figure 7.8. This image demonstrates how differing source sizes can result in measurements of differing intensities for the same feature. As such, source size is a factor that affects geometric unsharpness.





The scatter radiation is calculated as follows
Internal scatter is measured as a = 531 ADUs;
the max. and min. signal level as 28910 and 1191 ADUs
with the difference max-min b = 27119 ADUs

ISR = (2*a /b) *100 [%]
= (2* 531 / 27119) *100% = 3,83% [160kV]

Figure 7.7. ASTM technique to calculate and quantify internal scatter radiation within a DDA [53].

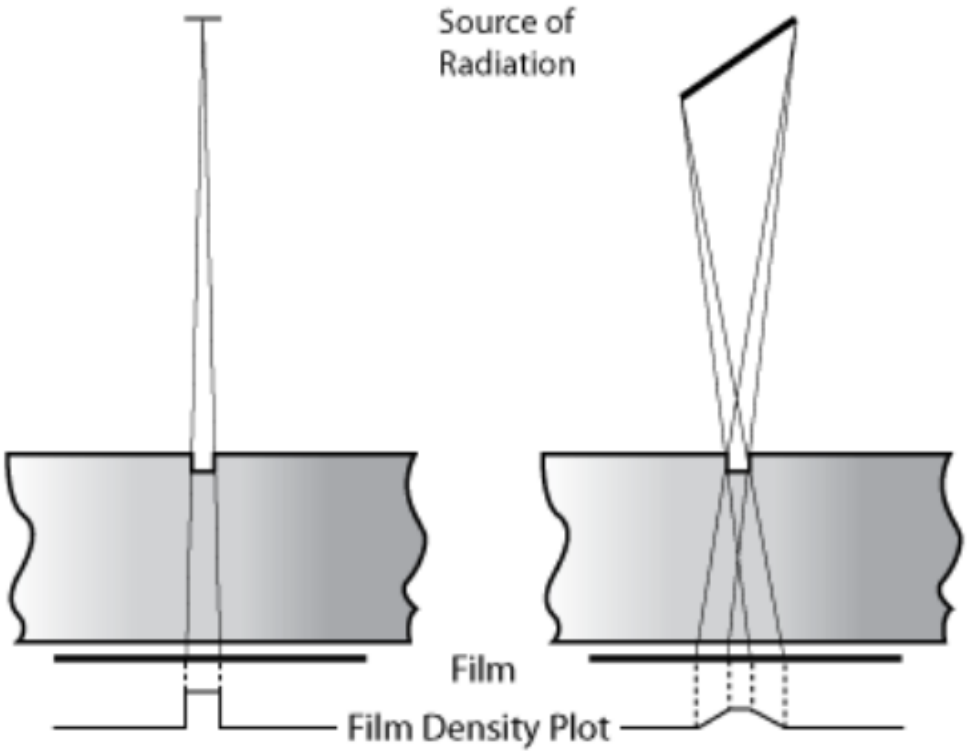


Figure 7.8. Two different source term sizes used in a hypothetical imaging system. The image demonstrates how SR is worsened when the source of radiation is larger [74].

Source-to-Object Distance
This is simply the distance from the source of radiation to the front of the object under examination; however, longer distances can be used to minimize the effects of larger source sizes. This can result in a process known as maximizing the "*L/D* ratio," where *L* is the source-to-object distance and *D* is the diameter of the source [73]. Therefore, the greater the *L/D* ratio, the more parallel the incident radiation when it interacts with the detector. As always, however, a tradeoff exists between the benefits of a more parallel source of radiation and the lower amount of particle flux as the ratio increases.

Object-to-Detector Distance
This is the final component of U_g, and it is defined as the distance from the detector to the surface of imaged object which is closest to the source of radiation [74]. Consequently, the term accounts for both the thickness of the imaged object as well as any distance between the detector and the object if one exists. This distance is usually minimized to reduce contributions to unsharpness.

With this understanding, U_g can be calculated for an imaging system using the equation

$$U_g = \frac{D*S}{L}, \qquad (48)$$

where *S* is defined as the object-to-detector distance [73, 74]. It follows that imaged objects placed closer to the detector face will result in less measured unsharpness than those placed further away, as illustrated in Figure 7.9.

Based upon these relative distances, a penumbra shadow is created for edge response measurements. This region is defined as the shadow cast on a DDA when incident radiation partly, but not wholly, interacts with the object. It represents a region of partial illumination between the umbra, or shielded region, and the free-field region. Obviously, thinner objects produce little to no penumbra when imaged near the DDA, but the larger the value of *S* (due to object distance from detector, object thickness, or both), the greater the contribution expected to geometric unsharpness.

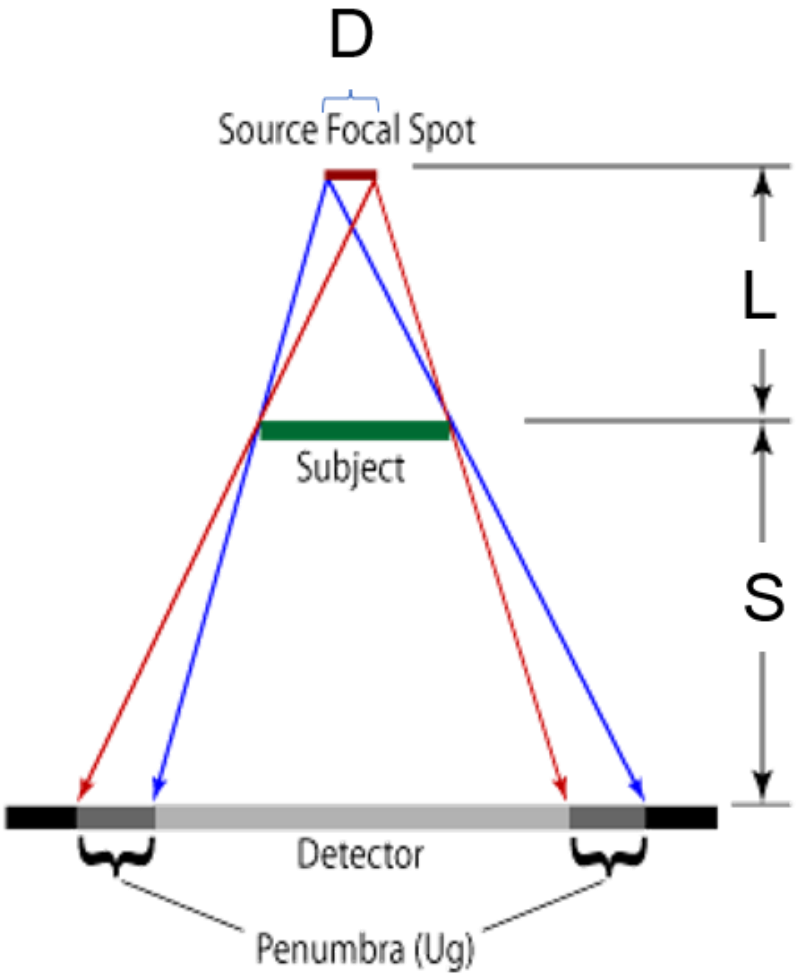


Figure 7.9. Image demonstrating the relationship between the three components of geometric unsharpness (U_g) and how their relative values affect spatial resolution. Adapted from [74].

CHAPTER EIGHT -
X-RAY RADIOGRAPHY CHARACTERIZATION USING A BISMUTH-LOADED POLYVINYL TOLUENE ARRAY

Abstract

[1]Novel organic plastic scintillators offer exciting opportunities for improvements in particle interaction efficiency, light yield, and pulse shape discrimination. One area of particular application for novel plastics may be in portable dual-particle imaging (DPI) systems for nuclear safety, security and safeguards purposes. One possible candidate material, a novel 21% Bismuth-loaded polyvinyl toluene (BiPVT), is computationally and experimentally evaluated in a 370 kVp x-ray field as a small, pixelated array and compared against similar evaluations of EJ-200, an industry standard material. MCNP6.2 software enables estimates of particle interaction and energy deposition within the materials, whereas Zemax OpticStudio software computes optical light transport within each pixelated array. Computational estimates are compared against experimental results for both materials, and the results suggest that BiPVT will provide improved performance over equivalent arrays made from EJ-200 for all practical x-ray environments supporting portable DPI.

Introduction

Current and future nuclear safety, security, and safeguarding efforts depend upon the accurate detection, localization, and identification of radioactive material. In terms of safety, the use of radioactive materials is common among multiple professional fields and disciplines, including nuclear research, medicine, and power generation. As such, the use of radioactive materials requires safe and careful handling procedures, technology, and environments to ensure minimal health risks are present for both radiation workers and the general public. For example, the removal, monitoring, and long-term storage of spent nuclear reactor fuel depends upon nuclear safety, and, in cases of contamination, radioactive sources must be reliably located and removed. From a safeguarding perspective, the control, measurement, and monitoring of all special nuclear material (SNM) is required in perpetuity to ensure reliable custody. Likewise, the detection and identification of illegal SNM production and acquisition routes are essential to nuclear security, and the transport of illicit SNM usually offers the best opportunities for their discovery. Furthermore, the continuous threat of terrorist radiological dispersion device (RDD) or improvised nuclear device (IND) use

[1] Chapter 8 has been accepted for publication in the *Journal of Radiation Effects, Research and Engineering* vol. 39, no. 1. *Authors:* A.W. Decker, C.J. Delzer, S. Hok, N.J. Cherepy, and J.P. Hayward. The dissertation author was the primary investigator and author.

requires technological capabilities that can detect, locate, and identify radioactive materials and SNM, despite the use of significant shielding to mask their presence.

An important part of the solution for this range of plausible and persistent challenges facing nuclear safety and security includes a variety of radiation imaging systems with dual-particle imaging (DPI) capabilities. This means the systems must reliably detect and discriminate between neutrons and high-energy photons, which together can offer more information that a single form of radiation imaging can provide alone [1, 2, 3, 4, 5, 6, 7]. Practical DPI systems should also offer durability, portability, and high detection efficiencies while also being low-cost. Fortunately, research to identify novel materials to enhance radiation imaging is widespread, and recent advances in organic scintillators provide some of the most exciting prospects for expanding the practical utility of DPI systems. In particular, plastics now exist that provide improved light yields and detection efficiencies, as well as traditional pulse shape discrimination (PSD) properties [8, 9, 10, 11, 12, 17, 45]. Such advancements, especially considering the low-cost and high durability benefits already associated with plastics, indicate that portable DPI systems may soon exist to answer these critical capability gaps.

One plastic scintillator produced at Lawrence Livermore National Laboratory (LLNL) is of particular interest. It is a 21% Bismuth-loaded polyvinyl toluene (BiPVT) that provides enhanced light yields over traditional plastics through the incorporation of iridium complex fluors. The novel fluors enable both singlet and triplet deexcitations via spin-orbit coupling, and this additional luminescence helps to mitigate the reduced light output typical of high-Z loaded plastics [9, 17]. Consequently, BiPVT generates ~20,000 ph/MeV in the green (~550 nm) compared to an upper limit of ~10,000 ph/MeV in the blue (~425 nm) from standard plastics, such as EJ-200. Lastly, BiPVT also benefits from an emission wavelength spectrum that couples well to the sensitivity of radiation hard a-Si thin-film transistor (TFT) based readouts, with quantum efficiencies of ~2× expected for BiPVT over traditional plastics that photoluminesce in the blue [45].

The potential benefits motivative this work, which describes both computational and experimental comparisons of BiPVT digital detector array (DDA) performance against DDA paired with an industry standard plastic scintillator, such as EJ-200, for x-ray radiography. The results described herein quantify the performance improvements expected from future systems leveraging BiPVT material for x-ray radiographic imaging, a critical component of DPI systems.

Theory

The standard practice for characterizing computed tomography (CT) system spatial resolution begins with measurements of a composite edge response function (ERF) [67]. Although CT is not applied in this research, composite images (those constructed from multiple smaller images) are required for performance

comparisons of the pixelated arrays considered. Consequently, the theory and procedures applied herein for x-ray digital detector array (DDA) performance comparisons are based on published American Society for Testing and Materials (ASTM) standards for the measurement of CT system performance. As such, traditional duplex wire image quality indicators (IQI) are not used; however, the theoretical basis for the performance measurement methodologies [67, 68, 60] is equivalent because both approaches calculate spatial resolution from the modulation transfer function (MTF). The reliance upon composite images in this work is largely due to the limited quantity of novel material available for characterization.

The edge response is measured from composite image data using a phantom of defined material and thickness to produce differences in pixel modulation at the phantom's edge. In CT, this is provided by a circular phantom providing a two-dimensional edge response; however, this research only examines a one-dimensional (1D) edge, so the phantom is offset from the pixel rows by a consistent angle selected between 2-5° [67, 68, 48]. Ideally, this produces numerous pixels measuring varying degrees of phantom attenuation, depending on the extent to which the pixels are shielded by the phantom edge. A region of interest (ROI) is then established to measure as much of the edge as possible, with ROI minimums of 11-pixels across the edge and 256 pixels, total [67, 48]. ROI edge data are then averaged to produce an average modulation response across the edge. The edge response data are normalized, and interpolation is used to determine the ERF, with bin sizes set at 10% of the pixel size for ROI with widths of 11 pixels [67]. An example ERF is provided in Figure 8.1.

A piecewise least-squared cubic fit of the ERF is then performed using the same number of values. From these polynomials, the analytical derivative is calculated to provide the line spread function (LSF), which is also normalized and centered on the ERF [67, 68]. This is represented mathematically as,

$$LSF = \frac{d(ERF)}{dx}. \qquad (48)$$

An example of the LSF, superimposed on the ERF, is also shown in Figure 8.1.

A 1D FT is used to shift the data from units of object space to units of spatial frequency, or cycles per distance. Therefore, the MTF describes the change in modulation within an image signal as a function of modulation spatial frequency for the specific DDA. MTF magnitudes are then normalized to unity at frequency zero, and a cut-off frequency at 10% of the MTF ($f_{10\%}$) represents the limit of spatial resolution (SR) for the DDA, with an accuracy of ± 5% [67]. SR is calculated as one half the inverse of the spatial frequency, and it represents the limit of geometrical detail that can be resolved by the DDA [48, 69]. An example MTF, including the cut-off threshold for minimum SR, is provided in Figure 8.2.

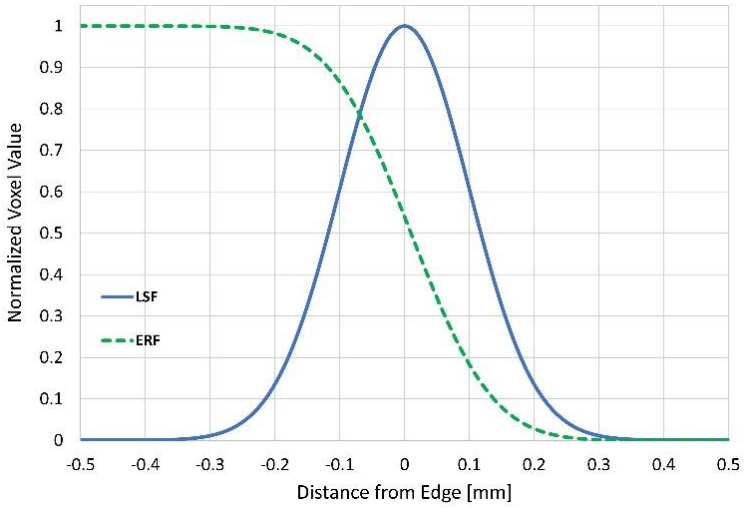


Figure 8.1. Expected Example plot of normalized edge response function (ERF) and line spread function (LSF).

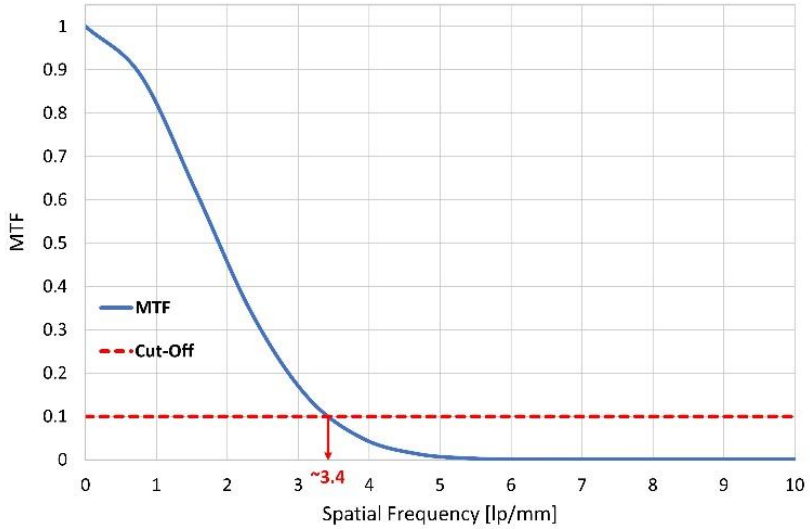


Figure 8.2. Example modulation transfer function (MTF), including the 10% cut-off threshold which determines the value of spatial resolution (SR). In the case of this example, the MTF reaches 10% at a spatial frequency ($f_{10\%}$) of 3.4 lp/mm, which equates to a hypothetical DDA SR value of 0.147 mm.

However, since SR is calculated from the normalized MTF, a more useful method for evaluating relative DDA performance relies on both the SR and the measured signal-to-noise ratio (SNR) of the DDA. The SNR is the quotient of mean value of the intensity (signal) and standard deviation (σ) of that intensity (noise) [60, 51]; however, in the case of radiography images, a more accurate equation is provided below, where

$$SNR = \frac{Mean\ intensity\ (difference\ image)}{\sigma(difference\ image)}, \qquad (49)$$

and the difference image is achieved by averaging the pixel intensities in the free-field (i.e., in the case of unshielded irradiation) and subtracting the same regions of the averaged intensities from the offset images (i.e., measured without irradiation) [51]. This process produces offset-corrected images; the process is analogous to correcting for background contributions in traditional radiation measurements. Together, these terms enable a calculation of the detector SNR-normalized (dSNRn) in the free-field, using

$$dSNRn = \frac{SNR \times \sqrt{2} \times 88.6\ \mu m}{SR}. \qquad (50)$$

The $\sqrt{2}$ term is used to correct the SNR, since the difference of two images is used for noise calculations, and 88.6 μm is consistent with phosphor film pixel widths, so it is included to standardize DDA performance comparisons across multiple radiographic systems [51, 70].

The quantity dSNRn is a useful indicator of DDA performance because it quantifies the exposure necessary to reach a full SNR [60, 51]. For a 16-bit image, this means ~50k contrast tones measured in the detector area, which avoids image overexposure. Typically, these values are expressed in plots of dSNRn vs. the square root of the exposure dose (mGy), with the slope of each line defining the DDA efficiency. However, if the exposure, beam filtering, and IQI are equivalent for two separate DDAs, then the dose terms cancel and leave just the dSNRn values to compare. Higher dSNRn values indicate higher DDA performance at a given exposure.

More traditional x-ray radiography DDA, such as TFT paired with gadolinium oxysulfide (DRZ) or cesium iodide, typically yields a SNR >200 and a SR <200 μm. These systems provide dSNRn values well over 100 or even 1000 at certain exposures; however, such systems provide no capability to support fast neutron imaging, which constitutes the second half of the research to characterize BiPVT for DPI purposes. Therefore, x-ray dSNRn values produced by systems optimized for DPI, although perhaps useful for comparisons against similar DPI systems, will not appear competitive against traditional DDAs optimized solely for x-ray radiography.

Lastly, for the purposes of future fast neutron characterizations, a 2×2 mm pixel face was selected for both the BiPVT and EJ-200 materials due to expected scattered proton pathlengths in future neutron experiments. If pixel face dimensions are too small, charged particles may routinely scatter beyond the pixel boundaries of incidence and deposit significant portions of their energy in adjacent pixels or outside the array. For example, protons scattered in EJ-200 (ρ = 1.032 g/cm^3) at 30° relative to the incident path of 14 MeV neutrons will depart at energies of ~10.5 MeV, which means they are expected to travel ~1.3 mm from the interaction site and ~0.65 mm orthogonal to the original neutron path. Therefore, protons scattered at 30° from anywhere within a pixel with a cross section <1.69 mm^2 (1.3×1.3 mm) will exit the pixel. Since TFT panels measuring scintillation operate in integration mode, this effect would reduce the position and image resolution. Based on this understanding, pixel dimensions of 2×2 mm (4 mm^2 pixel cross section) were selected. Additionally, a pixel depth of 19 mm was chosen for both arrays to maximize the probability of particle interactions, while also reducing the pixel aspect ratio below 10:1 to maximum light output versus image resolution [75]. These dimensions were used for both EJ-200 and BiPVT (ρ = 1.4 g/cm^3).

Experiment and Simulation Methodology

Array Fabrication

Based on these determinations, a small sample of LLNL BiPVT (6.85×19×21 mm) was cut, polished, and assembled into a 4×3-pixel array, with final individual pixel dimensions of 2×2×19 mm. An image of the original material, prior to array fabrication, is shown in Figure 8.3. Due to the small amount of source material, the BiPVT array pixels were cut individually prior to polishing and assembly, which is not ideal for producing consistently uniform pixel polish, spacing, or dimensions within an array. Dual layered enhanced specular reflector (ESR) was used to separate and optically isolate each pixel, with a final average pixel pitch of 2.44 mm for the BiPVT array, which is also relatively large. Images of the final BiPVT array are included in Figure 8.3.

To facilitate BiPVT array performance comparisons, EJ-200 was selected as an industry standard material. Consequently, a 4×3-pixel array of matching pixel dimensions was also fabricated from EJ-200; however, the EJ-200 array benefited from superior manufacturing processes due to an abundance of source material. Consequently, 2.25 mm plates of EJ-200 were cut and polished uniformly to 2 mm prior to ESR application and stacking. The adhered layers were then cut orthogonally into stacks of four pixels, which were polished again to 2 mm and then assembled with ESR layering into the final array. This process produced superior geometric uniformity, polish consistency, and ESR adhesion for the EJ-200 array, which produced an average pixel pitch of 2.28 mm.

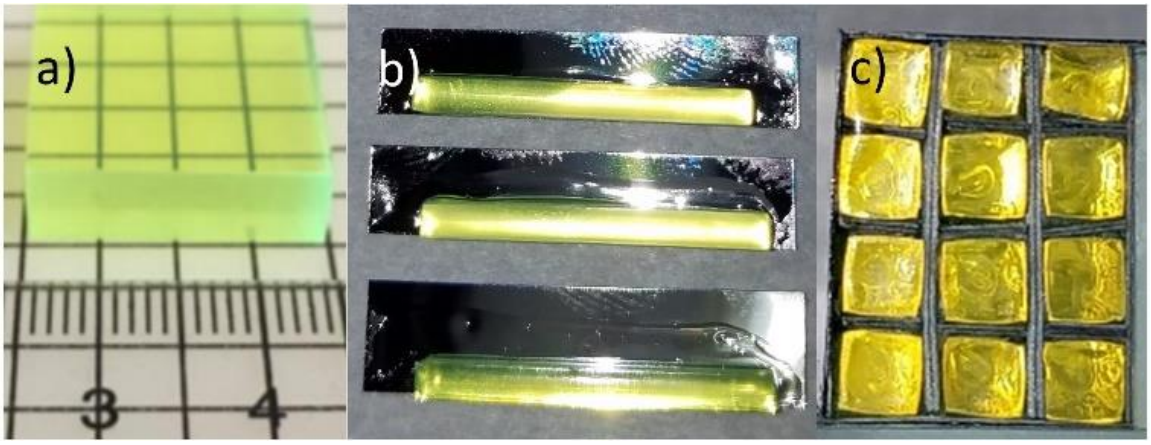


Figure 8.3. Images of a) the BiPVT source sample (6.85 × 19 × 21 mm) provided by LLNL, b) the individual BiPVT pixels, adhered to ESR, prior to trimming, and c) the final BiPVT 4×3-pixel array face, which is placed in contact with the Varex radiographic panel.

The finished arrays were then affixed to 2.5 mm acrylic plastic to help prevent any changes to their relative location between measurements. An image of the final arrays, mounted to the acrylic plastic, is provided in Figure 8.4. The arrays were then pressure mounted to the a-Si receptor plate of a commercial Varex PaxScan 1515DXT-I Flat Panel Detector radiographic panel [56]. This first required the removal of the original proprietary DRZ conversion layer. Next, custom-made aluminum pieces attached to all four outer Varex panel sides, thereby extending the detector panel's light-tight enclosure vertically by 25.4 mm. Within this expanded volume, the BiPVT and EJ-200 arrays were pressure mounted against the a-Si photodetector using layers of foam, specifically cut to hold the arrays and acrylic plastic base. The a-Si TFT provided pixel pitches of 127 μm^2, so every 2×2 mm array pixel response would be the averaged response of ~250 photodetector pixels. Lastly, the enclosure was covered and sealed with the original Varex 2.5 mm-thick carbon fiber plate.

Experiment Methodology

With the arrays pressure mounted and enclosed within the modified Varex 1515DXT-I radiographic panel, measurements within an x-ray field were recorded, with each measurement consisting of 40 separate images recorded at two frames per second (fps). The x-rays were generated by a Comet MXR-451/26 RGD with a tungsten target operated at 370 kVp, a current of 3 mA, and a focal spot size of 5.5 mm. Although outside the bounds of ASTM evaluation, 370 kVp was selected because it represents the practical upper energy limit for portable x-ray radiography. Therefore, a superior performance of BiPVT over EJ-200 at this energy would ensure the consistent superiority of BiPVT at every energy below, owing principally to the virtual absence of photoelectric absorption within EJ-200.

For all measurements, the source was centered on the panel at a source to detector distance (SDD) of 1,010 mm, in accordance with ASTM standards [51]. Shielded measurements utilizing a phantom edge were then recorded using the same process. A stainless-steel step wedge provided the measured phantom edge, specifically a consistent 6.35 mm thickness of steel above both arrays for each measurement. This was possible because the step widths were 13 mm and the edge consistently positioned at 5° off-axis to meet ASTM standards [60, 51]. A series of 15 shielded measurements were then recorded, with the phantom edge repositioned between measurements to provide an incrementally larger fraction of array shielding with each subsequent measurement. Consequently, the shielded measurements produced a range of array shielding in increments from 0-100%, all at 5° off-axis. These measurements were offset corrected and then divided by free-field values to normalize the data, a standard practice in imagery analysis to eliminate geometric distortion and only consider pixel behavior with respect to time and dose [51]. Using these measured contrast ratios, 4×45-pixel composite images of the steel wedge edge response were then assembled for both BiPVT and EJ-200.

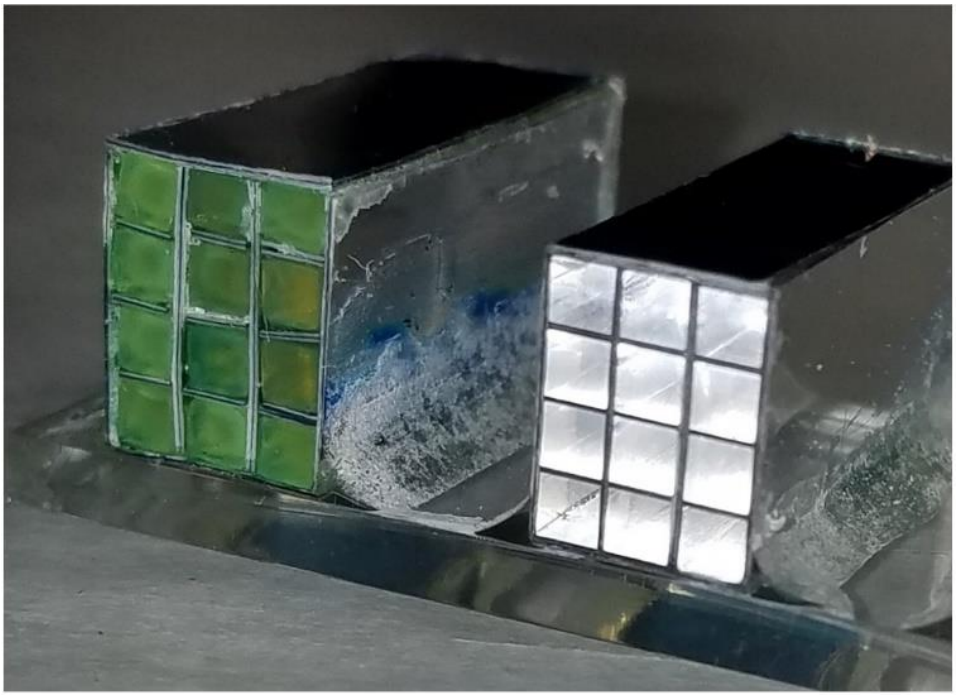


Figure 8.4. Image of the BiPVT (green) and EJ-200 (clear) 4×3-pixel arrays affixed to the acrylic plastic.

Lastly, both composite array images were expanded from 4×45-pixels to 23×45-pixels by replicating the contrast values at commensurate distances across the measured edge, thereby producing a larger composite image for each array. This could only be accomplished with the use of a straight edge as the phantom, which facilitated contrast pattern replication at equivalent distances from the edge for both shielded and unshielded regions within the original 4×45-pixel image. This step was necessary due to the limited volume of BiPVT available; however, identical pixel regions were used to expand the BiPVT and EJ-200 composite images.

Simulation Methodology

This research utilized two software programs to simulate particle energy deposition, pixel response, light transport, and quantum efficiency. Monte Carlo N-Particle Code v6.2 © (MCNP6) was leveraged to model particle transport, interactions with matter, and energy deposition within each pixel. MCNP6 also utilizes material cross section data from ENDF/B-VII, the most current library of cross section data available; however, MCNP6 cannot simulate optical light transport. Consequently, OpticStudio, a software package produced by Zemax, was utilized to simulate optical photon transport based on MCNP6 computations of energy deposition (J) within each pixel. OpticStudio utilizes Monte Carlo methods to model optical photon transport through complex optical systems. The software incorporates optical light absorption, emission, and transmissivity spectra, as well as material dimensions, density, refractive index, and surface reflectivity. OpticStudio also enabled incorporation of the photodetector quantum efficiency.

Once experimentation was complete, MCNP input decks were built to replicate the experiment geometry for all 15 measurements, matching the incrementally increasing fraction of shielded pixels used. Pixels were simulated as separate cells surrounded on five sides by ESR material, with the arrays affixed to 2.5 mm of acrylic plastic. Due to the lower manufacturing precision of the BiPVT pixels and array, individual BiPVT pixel dimensions were measured to micrometer accuracy using a Mitutoyo Toolmaker's Microscope. These values, both for pixel dimension and ESR spacing, informed the MCNP6 model of the BiPVT array. External to the arrays, the aluminum Varex panel housing, custom aluminum side attachments, and the carbon fiber cover were also replicated. The steel step wedge phantom was included for shielded simulations, and this was offset by 5° and shifted in position for each of the 15 separate shielded simulations, commensurate with the 15 experimental measurements. The first of such positions is shown in Figure 8.5, whereas in subsequent simulations the steel phantom was raised incrementally to shield more and more of the two arrays.

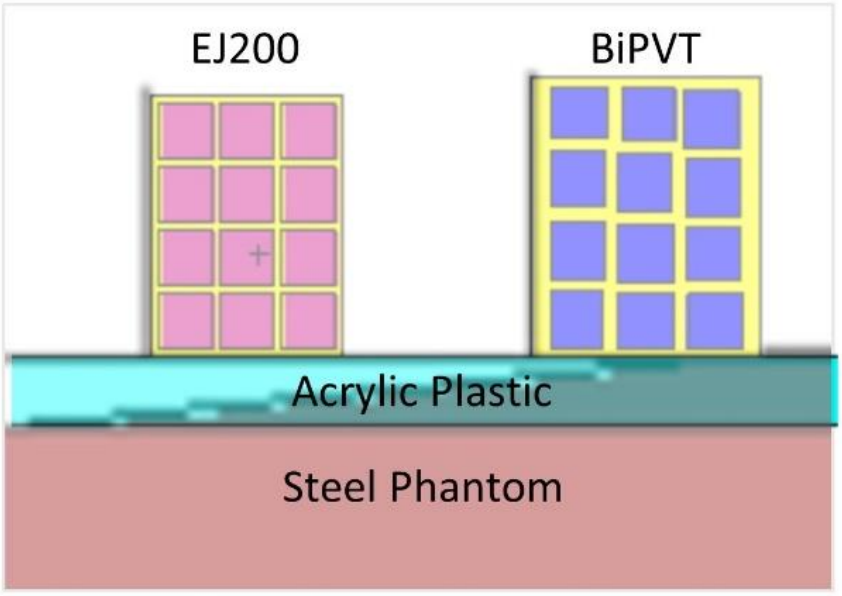


Figure 8.5. Example image of one shielded MCNP6 simulation, which includes the EJ-200 (pink) and BiPVT (blue) pixel arrays, as well as the steel step wedge phantom (brown) in one of the 15 positions, relative to the arrays. The acrylic plastic layer (light blue) and ESR material (yellow) are also shown.

Energy deposition within each pixel was estimated using +F6 tallies, and the x-ray source was based on a bremsstrahlung x-ray emission spectrum provided by Comet for the MXR-451/26 RGD. For shielded measurements, 40M particles were simulated and the results for each pixel passed all ten statistical checks for tally fluctuation.

MCNP predictions of energy deposition (J/pixel) informed OpticStudio simulations of photoluminescence and optical light transport by providing estimates of total photoemission energy. For BiPVT, OpticStudio simulated the primary emission, reabsorption, reemission, and transmissivity of optical light. These probabilities were determined beforehand from experimental data and were input into OpticStudio, along with the BiPVT material density of 1.4 g/cm^3. In all other respects, the BiPVT was modeled as a polycarbonate plastic, including the refractive index of 1.58.

For EJ-200, the photoemission spectrum listed on the Eljen Datasheet [36] was incorporated into OpticStudio, and a transmissivity of 100% was used for all wavelengths above 400 nm. Additionally, a refractive index of 1.58 and a material density of 1.023 g/cm^3 was also used [36]. Lastly, for all array simulations, OpticStudio incorporated the wavelength-dependent quantum efficiency of the TFT photodetector [45].

OpticStudio results for each array simulation were provided per pixel in units of incoherent irradiance (J/mm^2), and these were divided by free-field values to normalize the data. Using these ratios, 4×45-pixel composite images were then assembled for each material from the simulated responses using an identical methodology to that described in the experimental methodology. Likewise, using that same methodology, the 4×45-pixel composite images were expanded to 23×45-pixel images by replicating the contrast values at commensurate distances across the measured edge, thereby producing the larger composite image for each simulated array. Further analysis and results derived from the MCNP6 and OpticStudio simulations were acquired in an identical manner as those from the experimental measurements.

Analysis and Results

Experimental Data Analysis

All images recorded using the Varex radiographic panel were analyzed using the ImageJ Image Processing and Analysis in Java (v1.52a) software. Within ImageJ, ROIs were established over the individual pixels in both arrays, and the free-field measurement was analyzed. Pixel intensities for both arrays were then averaged from these ROI, and the standard deviation was calculated. These free-field intensity averages, as well as the SNRs calculated using Eq. 39, are listed in Table 8.1.

Table 8.1. Mean 2×2 mm pixel intensity and standard deviation measured for each array in the free-field (FF), as well as the SNRs calculated from those values.

	Mean (FF)	σ	SNR
BiPVT	41,807.4	1,871.7	22.3
EJ-200	11,098.9	639.4	17.4

Shielded pixel measurements utilized the same ROI used in the free-field analysis, and intensity values for each pixel from those 15 measurements were then exported for analysis. The expanded composite images measured for both materials, as described in the Methodology Section, are shown in Figure 8.6.

These 23×45-pixel composite images for BiPVT and EJ-200 facilitated edge response evaluations. In both images, an 11×44-pixel ROI (484 pixels, total) was centered over the edge to measure the normalized edge response. Through the deliberate application of procedures outlined in the Theory Section, the MTFs for both arrays were calculated from these experimentally measured composite images. Likewise, at the 10% cut-off, the SR values for both material arrays were calculated. The experimentally determined MTFs for both materials are plotted in Figure 8.8, and Table 8.2 lists the measured SR for each material, as well.

Computational Data Analysis

The computational data analysis methods matched those described in the Experimental Analysis precisely, including consistent use of the same pixel regions to expand the computational composite images to 23×45-pixels and identical 11×44-pixel ROI to analyze the edge response for both materials. The simulated 23×45-pixel composite images and associated edge responses for both materials are provided in Figure 8.7.

Material Evaluation Results

Figure 8.8 and Table 8.2 provide comparisons for the BiPVT and EJ-200 experimental and computational MTFs and SR values, respectively. Figure 8.8 also includes the cutoff threshold of 10% in both plots, at which point spatial resolution is assigned for the CT system. The experimental and computational values of SR agree within the associated error for both arrays, so the simulated results are found to agree with the experimental data. From these results, dSNRn calculations may be performed using Eq. 40. These calculated values are listed in Table 8.3.

These dSNRn results demonstrate that at 370 kVp, when using a 6.35 mm thick steel edge, the evaluated BiPVT array offers statistically equivalent x-ray radiographic performance when compared to an array of equivalent size made from EJ-200.

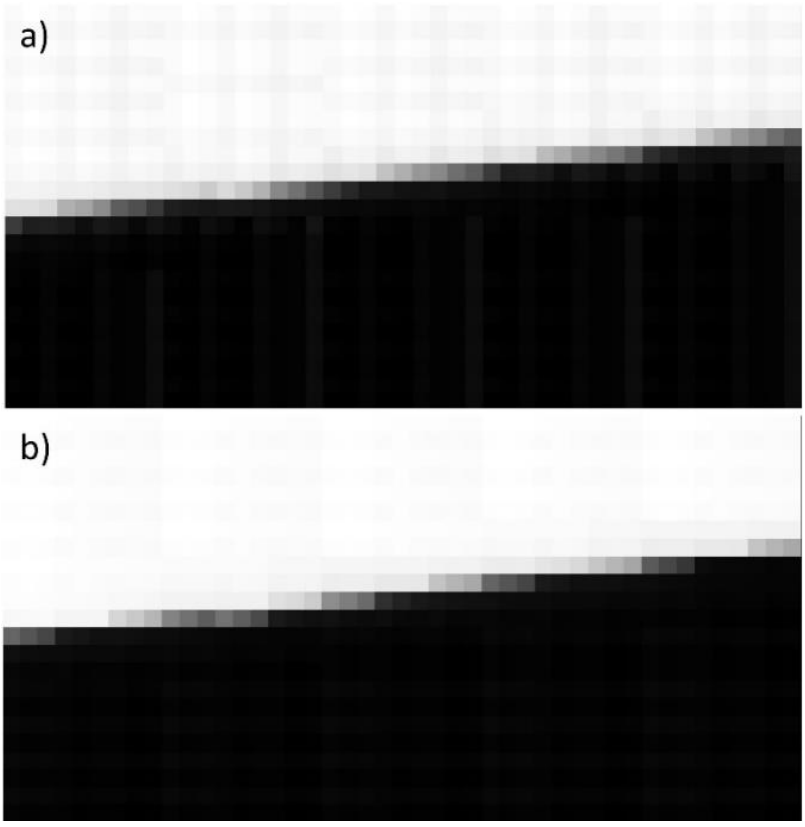


Figure 8.6. Images of the expanded a) BiPVT and b) EJ-200 23×45-pixel composite matrices. The expansion of the original 4×45-pixel composite image utilized repeating patterns at specific distances from the phantom edge to construct the expanded image response.

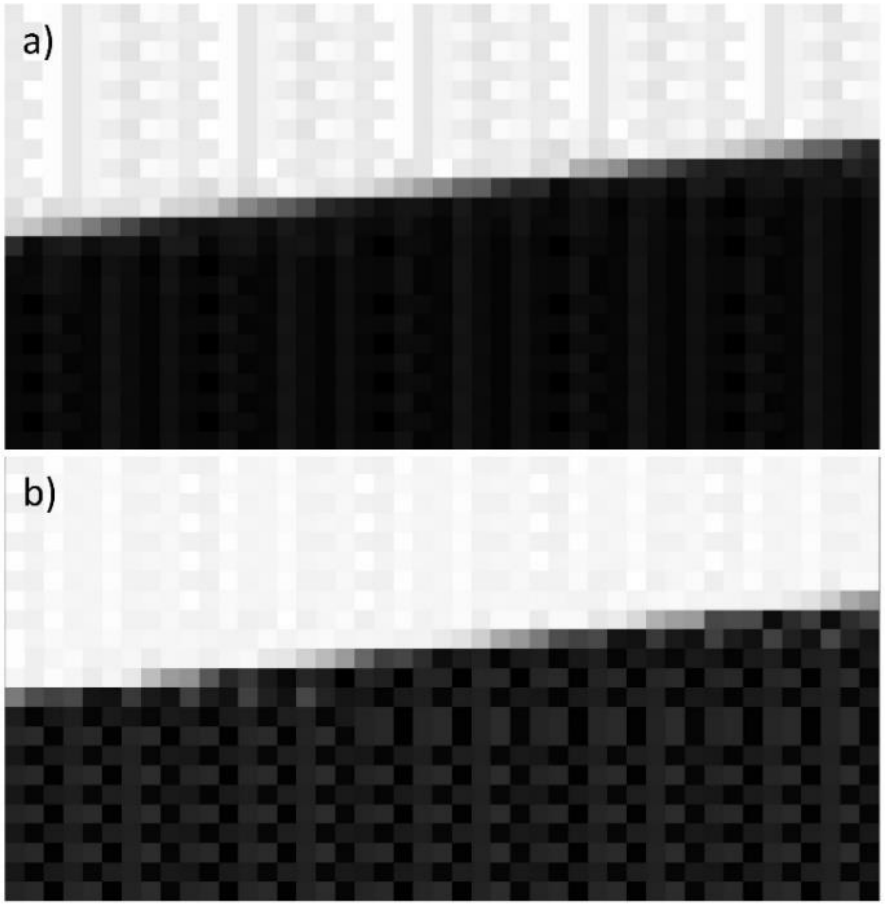


Figure 8.7. Images of the expanded a) BiPVT and b) EJ-200 23×45-pixel composite images.

Table 8.2. Experimentally and computationally determined values of SR for both material arrays, as well as the associated uncertainties.

	Experimental		Computational	
	$f_{10\%}$ (lp/mm)	SR ± 5%	$f_{10\%}$ (lp/mm)	SR ± 5%
BiPVT	0.202	2.48 ± 0.12 mm	0.193	2.59 ± 0.13 mm
EJ-200	0.262	1.91 ± 0.10 mm	0.273	1.83 ± 0.09 mm

Table 8.3. Experimentally and computationally determined values of dSNRn for both material arrays, as well as the associated uncertainties.

	SNR	SR (mm)	dSNRn
BiPVT	22.3	2.48	1.121 ± 0.056
EJ-200	17.4	1.91	1.131 ± 0.057

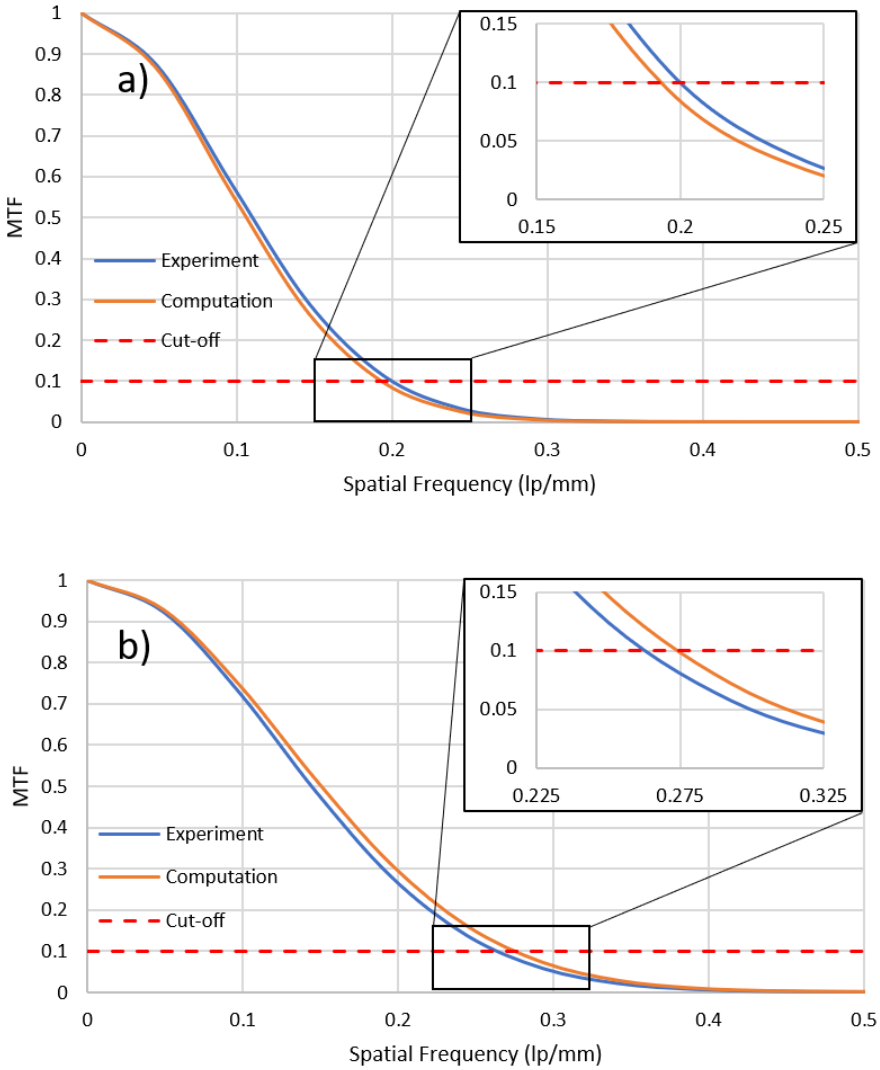


Figure 8.8. Plot of the experimental and computational MTFs for the a) BiPVT and b) EJ-200 composite images. Expanded sections demonstrate where the MTFs cross the 10% cutoff frequency ($f_{10\%}$) for spatial resolution determination based on ASTM standards for CT system performance evaluations [67].

Discussion

Of note, measured light yield, optical transmissivity, and geometric precision of the evaluated BiPVT array were all sub-optimal. These sources of reduced performance were largely driven by imprecise pixel dimensions and alignment (due to limited source material), as well as pixel occlusions that occurred following final alumina polishing of the array face. This final effect was entirely unexpected, with the alumina producing halo-shaped “clouding” effects inside each BiPVT pixel along their entire length. This effect can be seen in Figure 8.4, and it occurred due to the inconsistent adhesion between the BiPVT and ESR layers. This created thin gaps between the pixels and ESR that drew the alumina polishing solution in by capillary action. The presence of the alumina, a white, opaque solution, along the pixel sides reduced reflectivity and resulted in pixel clouding. Fortunately, the larger halo-shaped occlusions largely dissipated after a few days, although small occlusions remained.

Therefore, the greatest impact on measured BiPVT array performance is believed to be the degradation in reflectivity below that expected for ESR. Based upon MCNP6 and OpticStudio estimates of relative energy deposition and light transmission, this effect reduced the light collection efficiency of the BiPVT array by as much as ~80%. Without such degradation, the expected SNR of the BiPVT array could be conservatively estimated as twice that reported for EJ-200. This would provide a dSNRn value of 1.740 ± 0.087 for the BiPVT array, a significant improvement over that produced by EJ-200. This prediction of relative SNR is consistent with other arrays made from 21% Bi-loaded plastics. Of course, these sources of experimental uncertainty did not exist in the EJ-200 array, which benefited from a more standardized fabrication process, a direct result of greater source material availability. Consequently, future BiPVT scintillator array fabrication should not utilize either pixel-by-pixel construction or alumina to achieve a high polish.

Therefore, despite suffering from multiple sources of reduced light transport, at 370 kVp the BiPVT array demonstrated statistically equivalent performance when compared to a more ideally manufactured EJ-200 array. In terms of x-ray radiography, the performance superiority expected for a more ideally manufactured BiPVT array would only increase at lower source x-ray energies, primarily due to the extremely low intrinsic efficiency of EJ-200 for photoelectric absorption. Additionally, MTF and SR computed from the combination of MCNP and OpticStudio simulations are found to agree with experimental measurements and calculations, verifying the described simulations and methodologies.

Conclusions

In conclusion, at 370 kVp, the evaluated BiPVT array demonstrated equivalent performance when compared to a similar EJ-200 array. However, without the sources of performance degradation detailed herein, the BiPVT array would likely

have provided statistically superior performance to the EJ-200 array, and this performance advantage would only be expected to improve at lower x-ray energies. For ideally manufactured BiPVT arrays, simulations indicate these performance improvements may be >5× that of EJ-200 at 150 kVp and 270 kVp, two other energies relevant for portable x-ray radiography. These results support the use of BiPVT over other plastic alternatives, such as EJ-200, for portable DPI radiography. From the experimental and computational comparisons conducted herein, BiPVT is expected to offer significantly enhanced performance at all energies practical for portable x-ray radiography. These results support further investigation of BiPVT for DPI radiography applications to support national safety, security, and safeguards.

Acknowledgment

The authors thank the U.S. Army and the Department of Energy for supporting this research. The authors also thank Dr. Dan Shedlock and Varex Imaging for the use of a Varex Industrial PaxScan® 1515DXT-I flat panel detector, and Dr. Keith Vaigneur and Agile Technologies for their support and supervision during the fabrication of the evaluated arrays.

CHAPTER NINE -
SIMULATED X-RAY RADIOGRAPHIC PERFORMANCE OF A BISMUTH-LOADED PVT ARRAY

Abstract

[2] Recent material advancements in organic plastic scintillators enable marked increases in material detection efficiency, light yield, and pulse-shape discrimination properties. These advances may resolve significant capability gaps for low-cost, portable, and durable dual-particle imaging (DPI) systems for nuclear safety, security and safeguard purposes. One such material, a 21% bismuth-loaded PVT (BiPVT), is computationally evaluated as a small, pixelated radiographic array using MCNP® and Zemax OpticStudio®, and it is compared to identical evaluations of EJ-200 and EJ-256 arrays. MCNP software enables estimates of particle interaction and energy deposition, while OpticStudio computes optical light transport within each material. Computational estimates of spatial resolution and relative light collection at 370 kVp are found to agree with experimental results for both EJ-200 and EJ-256 arrays, thereby validating predictions of the same for the BiPVT array. As such, for equivalent exposures at 370 kVp, a BiPVT array may provide ~20× the light collection expected from EJ-200 and ~10× that expected from EJ-256. Similar comparisons of estimated light collection are also computed at 150 and 270 kVp, and these results suggest BiPVT will provide significantly improved performance over EJ-200 and EJ-256 across all energies practical for portable x-ray radiography.

Introduction

The accurate detection, localization, and identification of radioactive material is vital to current and future nuclear safety, security, and safeguarding efforts. From a safety standpoint, radioactive materials are employed ubiquitously for benign purposes across several fields, including nuclear research, medicine, and power generation. Consequently, use of such materials necessitates care and safety to ensure that health risks are minimized for both radiation workers and the public. For example, spent nuclear reactor fuel must be removed, stored, and monitored, and in cases of radioactive contamination, sources of radioactivity must be reliably located and removed. In terms of security, all produced special nuclear material (SNM) must be controlled, measured, and monitored in perpetuity to ensure proper custody. As such, identification of illicit SNM production and acquisition routes is vital to nuclear security, and transport of SNM often offers crucial opportunities for

[2] Chapter 9 has been published in the *Transactions in Nuclear Science*, vol. 67, no. 11. *Authors:* A.W. Decker, N.J. Cherepy, S. Hok, and J.P. Hayward. The dissertation author was the primary investigator and author.

detection. Similarly, the persistent threat posed by the use of a radiological dispersion device (RDD) or an improvised nuclear device (IND) necessitates technological capabilities to detect, locate, and identify radioactive materials and SNM, despite the possibility of significant shielding.

Due to the number of plausible safety and security challenges, an important part of the solution includes a range of radiation imaging systems with dual-particle imaging (DPI) capabilities, which means that they must reliably detect both incident high-energy photons and fast neutrons. As such, sources for DPI typically include both highly penetrating photons (>200 kVp) and 14.1-MeV D–T neutrons, due to the higher production rate over D–D neutrons. This dual-particle sensitivity offers important information that a single form of radiation detection and imaging cannot provide alone [76, 77, 78, 7, 6, 79, 4, 5, 1, 2]. DPI systems should also offer an attractive combination of ruggedness, portability, and high detection efficiency while remaining low cost. Fortunately, research and development in new materials to enhance radiation imaging is of widespread interest. Most notably, recent advances in organic scintillators provide some of the most exciting prospects for expanding the practical utility and versatility of DPI systems. Specifically, novel plastic scintillators offer improved light yield, detection efficiency, and pulse shape discrimination (PSD) properties [5, 8, 9, 10, 11]. These advancements, especially when paired with the well-known advantages of plastics, such as low cost and high durability, suggest substantial improvements in the field of portable radiation imaging are now attainable, especially for DPI.

One material of particular interest is triphenyl bismuth-loaded polyvinyl toluene (BiPVT) with 21 wt% bismuth produced at Lawrence Livermore National Laboratory (LLNL). Traditional plastics generally suffer from poor light yields and interaction efficiencies with X-rays due to low effective atomic numbers (Z_{eff}) [8]. However, since photoelectric absorption efficiencies scale as ~Z^4, high-Z loading dramatically improves the probability of these interactions. In addition to this benefit, BiPVT offers enhanced light yield over traditional high-Z sensitized plastics by incorporating an iridium-complex fluor, which enables triplet deexcitations through spin-orbit coupling [8, 12]. This additional radiative pathway helps mitigate the reduced light output typical of high-Z loaded plastics, allowing BiPVT to generate ~20,000 ph/MeV in the green (with peak emission at ~550 nm). This is a considerably higher light yield than the typical plastics commercially available for radiation detection applications, such as Eljen's PVT-based EJ-200 and EJ-256. Specifically, EJ-200 provides an upper limit of ~10,000 ph/MeV, while EJ-256, which includes 5 wt% lead, offers only ~5,200 ph/MeV, and both these materials photoluminescence in the blue (with peak emission at ~425 nm). Additionally, the emission wavelength spectrum of BiPVT couples well to the sensitivity of radiation hard amorphous silicon (a-Si) thin-film transistor (TFT)-based readouts, with an average of twice the expected quantum efficiency of EJ-200 and EJ-256 [9, 45, 37, 36].

These potential benefits justify computational comparisons of BiPVT-based digital detector array (DDA) performance and light collection against systems using industry standard materials for X-ray radiography. Results will quantify the potential performance improvements of future X-ray radiographic systems at 150, 270, and 370 kVp using BiPVT over the more traditional alternatives of EJ-200 and EJ-256.

Theory

The standard practice for characterizing computed tomography (CT) system SR begins with measurements of a composite edge response function (ERF) [67]. Although CT is not directly applied in this research, composite images (those constructed from the multiple smaller images) are required for performance comparisons of the pixelated arrays considered. Consequently, the theory and procedures applied herein for X-ray DDA performance comparisons are based on the published American Society for Testing and Materials (ASTM) standards for the measurement of CT system performance.

The edge response is measured from the composite image data using a phantom of defined material and thickness to produce a consistent line of pixel modulation at the phantom's edge. In CT, this is provided by a circular phantom providing a 2-D edge response; however, this research only examines a 1-D edge, so the phantom is offset from the pixel rows by a consistent angle selected between 2˚ and 5˚ [68, 48, 51]. Ideally, this produces numerous pixels measuring varying degrees of phantom attenuation, depending on the extent to which the pixels are shielded by the phantom edge. A region of interest (ROI) is then established to measure as much of the edge as possible, with ROI minimums of 11 pixels across the edge and 256 pixels in total [67, 68]. ROI edge data are then averaged to produce a modulation response across the edge. The averaged edge response data are normalized, and linear interpolation is used to determine the ERF, with bin sizes of 10% of the pixel size for ROI with widths of 11 pixels [67]. An example ERF is provided in Figure 9.1.

A least-squared cubic fit of the ERF is then performed using the same number of values. From this polynomial, the analytical derivative is calculated to provide the line spread function (LSF), which is also normalized and centered on the ERF [67, 68]. This is represented mathematically as,

$$LSF = \frac{d(ERF)}{dx}, \qquad (51)$$

and it represents the 1D profile across the edge. An example of the LSF, superimposed on the ERF, is shown in Figure 9.1.

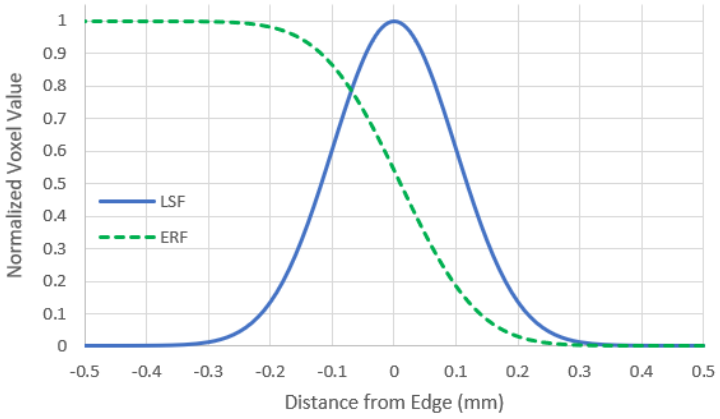


Figure 9.1. Example plot of normalized edge response function (ERF) and line spread function (LSF).

Next, the modulation transfer function (MTF) is calculated from the 1D Fourier Transform (FT) of the LSF using the equation,

$$MTF = FT\left(\frac{d(ERF)}{dx}\right) = FT(LSF). \quad (52)$$

The 1D FT is used to shift the data from units of object space to units of spatial frequency, or cycles per distance. Therefore, the MTF describes the change in modulation within an image signal as a function of modulation spatial frequency for the specific DDA. MTF magnitudes are then normalized to unity at frequency zero, and a cut-off at 10% of the MTF represents the limit of SR for the DDA, with an accuracy of ± 5% [67]. SR is calculated as the inverse of the spatial frequency, also known as the Nyquist frequency. The SR values represent the limit of geometrical detail that can be resolved by the DDA [51]. An example MTF, including the cut-off threshold for minimum SR, is provided in Figure 9.2.

Experiment and Simulation Methodology

A. Pixel Dimensions

Primarily for the purposes of future fast neutron characterizations, a 2×2 mm pixel face was selected for the BiPVT, EJ-200, and EJ-256 arrays due to expected scattered proton pathlengths. If pixel face dimensions are too small, charged particles may routinely scatter beyond the pixel boundaries of incidence and deposit significant portions of their energy in adjacent pixels or outside the array. For example, protons scattered at 30° relative to the path of incident 14 MeV neutrons will depart at energies of ~10.5 MeV, which means they are expected to travel ~1.3 mm from the interaction site and ~0.65 mm orthogonal to the original neutron path. Therefore, protons scattered at 30° from anywhere within a pixel with a cross section <1.69 mm^2 (1.3×1.3 mm) will exit the pixel. Since TFT panels measuring light scintillations operate in integration mode, this effect would reduce the position and image resolution. Based on this understanding, pixel face dimensions of 2×2 mm (4 mm^2 pixel cross section) were selected. Additionally, a pixel depth of 19 mm was chosen for both arrays to reduce pixel aspect ratio below 10:1.

These pixel dimensions were used for both experimental and computational array evaluations of EJ-200 and EJ-256, with these materials providing densities of 1.023 and 1.081 g/cm^3, respectively. BiPVT, with its higher density of 1.4 g/cm^3, was also simulated with these pixel dimensions.

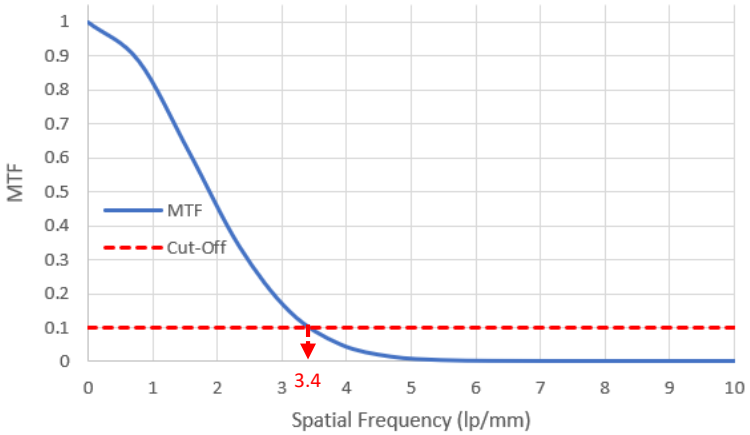


Figure 9.2. Example modulation transfer function (MTF). Values of spatial resolution (SR) are measured for the DDA at a 10% cut-off of the MTF. In the case of this example, the MTF reaches 10% at a spatial frequency of 3.4 lp/mm, which means the hypothetical DDA provides a SR of 0.294 mm.

B. EJ-200 and EJ-256 Array Fabrication

To facilitate predictions of BiPVT array performance, EJ-200 and EJ-256 were selected as representative industry standard materials. For this research, separate 4×3-pixel arrays were fabricated from both EJ-200 and EJ-256. In doing so, 2.25 mm plates of EJ-200 and EJ-256 were cut and polished uniformly to 2 mm thicknesses prior to the application of Vikuiti™ enhanced specular reflector (ESR) and stacking. The adhered layers were then cut orthogonally into three separate four-pixel stacks, which were each polished again to 2 mm thicknesses and assembled into the final arrays with ESR layers between each stack and on the five outer sides to optically isolate each pixel and the array. This process resulted in geometric uniformity (± 0.02 mm in all dimensions) and an average pixel pitch of 2.28 mm for each array. It also provided equivalent pixel polish and ESR adhesion across both arrays due to the use of identical procedures during their manufacture.

Both finished arrays were then affixed to a 2.5 mm-thick piece of acrylic plastic to prevent changes to their relative location between measurements. An image of the final arrays, mounted to the acrylic plastic, is provided in Figure 9.3. The arrays were then pressure-mounted to the a-Si receptor plate of a commercial Varex PaxScan® 1515DXT-I Flat Panel Detector radiographic panel [56]. This first required the removal of the original proprietary gadolinium oxysulfide (Gd_2O_2S) conversion layer. Next, custom-made aluminum pieces extended all four outer Varex panel sides, thereby expanding the detector panel's light-tight enclosure vertically by 25.4 mm. Within this expanded volume, the EJ-200 and EJ-256 arrays were compression mounted against the a-Si photodetector using layers of foam, specifically cut to hold the arrays and acrylic plastic base. The a-Si TFT provided pixel pitches of 127 μm^2, so every 2×2 mm array pixel response was the averaged response of ~250 photodetector pixels. Lastly, the enclosure was covered and sealed with the original Varex 2.5 mm-thick carbon fiber plate.

C. Experiment Methodology

With the arrays pressure mounted and enclosed within the modified Varex radiographic panel, measurements within an x-ray field were conducted, and each measurement consisted of 40 separate images recorded at two frames per second (fps). The x-rays were produced by a Comet MXR-451/26 radiation generating device (RGD) with a tungsten target operated at 370 kVp, a current of 3 mA, and a focal spot size of 5.5 mm. Although outside the bounds of typical ASTM evaluation, 370 kVp was selected because it represents the practical upper energy limit for portable x-ray radiography. Therefore, a superior performance of EJ-256 over EJ-200 at this energy would ensure the consistent superiority of EJ-256 at every energy below, owing principally to the extremely low intrinsic efficiency of EJ-200 for photoelectric absorption. As a high-Z loaded plastic, this same rationale applies to a BiPVT array.

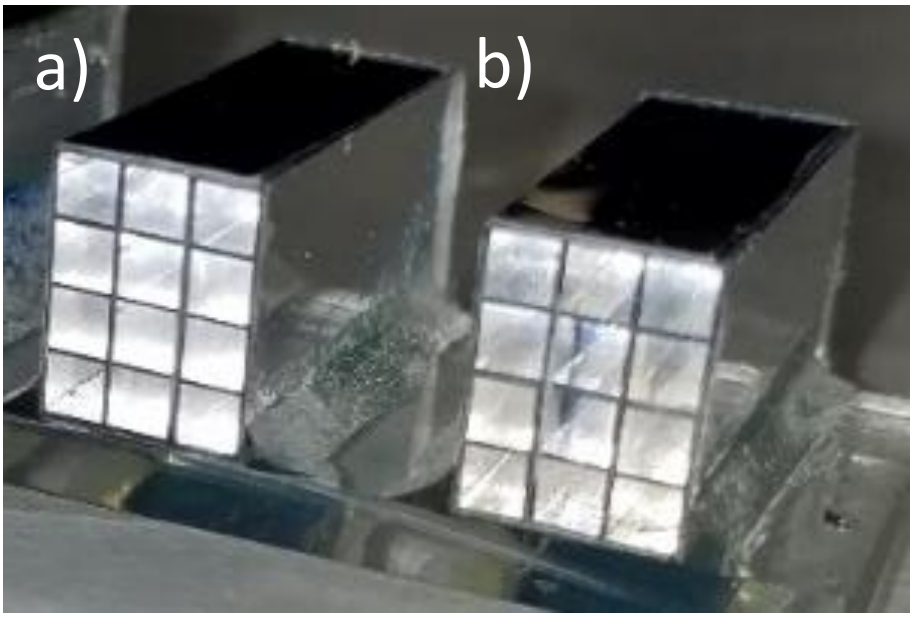


Figure 9.3. Image of the 4×3-pixel a) EJ-200 and b) EJ-256 arrays affixed to the acrylic plastic. Each 2×2×19 mm pixel is wrapped on five sides by ESR to maximize photoluminescent light collection by the photodetector.

For all measurements, the source was centered on the panel at a source to detector distance (SDD) of 1,010 mm, in accordance with ASTM standards [48]. Free-field (i.e. unshielded) measurements were recorded in this way for both arrays simultaneously, as well as dark measurements, which are necessary for image offset correction.

Shielded measurements utilizing a phantom edge were then recorded using the same process. A stainless-steel step wedge provided the measured phantom edge, specifically a consistent 6.35 mm thickness of steel above both arrays for each measurement. This was possible because the step widths were 13 mm, with the edge consistently positioned at 5° off-axis to meet ASTM standards [48, 51]. A series of 15 shielded measurements were then recorded, with the phantom edge repositioned between measurements to provide an incrementally larger fraction of array shielding with each subsequent measurement. Consequently, the shielded measurements produced a range of array shielding from 0-100%, all at 5° off-axis. These measurements were offset corrected and then divided by free-field values to normalize the data, a standard practice in imagery analysis to eliminate geometric distortion and only consider pixel behavior in respect to time and dose [53]. Using these measured contrast ratios, 4×45-pixel composite images of the steel wedge edge response were then assembled for both EJ-200 and EJ-256, which supported additional findings detailed in Section IV.

D. Simulation Methodology

This research utilized two software programs to simulate particle energy deposition, pixel response, light transport, and quantum efficiency. Monte Carlo N-Particle Code ® v6.2 (MCNP6) was leveraged to model particle transport, interactions with matter, and energy deposition within each pixel. MCNP6 also utilizes material cross section data from ENDF/B-VII, the most current library of cross section data available; however, MCNP6 cannot simulate optical light transport. Consequently, OpticStudio®, a software package produced by Zemax, was utilized to simulate optical photon transport based on MCNP6 computations of energy deposition (J) within each pixel. OpticStudio utilizes Monte Carlo methods to model optical photon transport through complex optical systems. The software incorporates optical light absorption, emission, and transmissivity spectra, as well as material dimensions, density, refractive index, and surface reflectivity. OpticStudio also enabled incorporation of the photodetector quantum efficiency.

Once experimentation was complete, MCNP6 input decks were built to replicate the experimental geometry for all three arrays and measurements, matching the incrementally increasing fraction of shielded pixels used during experimentation. Pixels were simulated as separate cells surrounded on five sides by ESR material,

with the arrays affixed to 2.5 mm of acrylic plastic. External to the arrays, the aluminum Varex panel housing, custom aluminum side attachments, and the carbon fiber cover were also replicated. The steel step wedge phantom was included for shielded simulations, and this was offset by 5° and shifted in position for each of the 15 separate shielded simulations, commensurate with the 15 experimental measurements. Energy deposition within each pixel was estimated using +F6 tallies, with BiPVT and EJ-256 simulated as homogenous PVT modified by the wt% of their respective high-Z constituent. The x-ray source was based on a bremsstrahlung x-ray emission spectrum provided by Comet for the MXR-451/26 RGD. For all computations, 40M particles were simulated and the results for each pixel passed all ten statistical checks for tally fluctuation.

MCNP6 estimates of energy deposition (J/pixel) informed OpticStudio simulations of photoluminescence and optical light transport by providing total photoemission energy. For BiPVT, OpticStudio simulated the primary emission, reabsorption, reemission, and transmissivity of optical light. Emissivity and transmissivity spectra for BiPVT were experimentally measured beforehand using a Horiba Jobin YvonFluorolog 3 Spectrofluorometer and a Cary 5000 UV-Vis-NIR Spectrophotometer, respectively, and the data are provided in Figure 9.4.

From the measured emissivity data in Figure 9.4, the primary and secondary emission spectra were estimated by fitting Gaussian functions to the data, with peaks at 457 and 550 nm, respectively. These were input into OpticStudio along with BiPVT transmissivity data and material density. As a material, BiPVT is a yellowish color, so the measured transmissivity data were not normalized to account for this property. In all other respects, the BiPVT was modeled as a polycarbonate plastic with a refractive index of 1.58.

For EJ-200 and EJ-256, the blue photoemission spectra listed on the respective Eljen Datasheets were incorporated into OpticStudio [36, 37]. Additionally, a refractive index of 1.58 and the respective material densities were incorporated. Also, due to the optical clarity of both materials, they were simulated as 100% transmissive across all emission wavelengths, which is a reasonable approximation. Lastly, for all array simulations, OpticStudio incorporated the wavelength-dependent quantum efficiency of the TFT photodetector [45].

OpticStudio results for each array simulation were provided per pixel in units of incoherent irradiance (J/mm^2), and these were divided by free-field values to normalize the data. Using these ratios, 4×45-pixel composite images were then assembled for each of the three materials from the simulated responses using an identical process to that described in the experiment methodology.

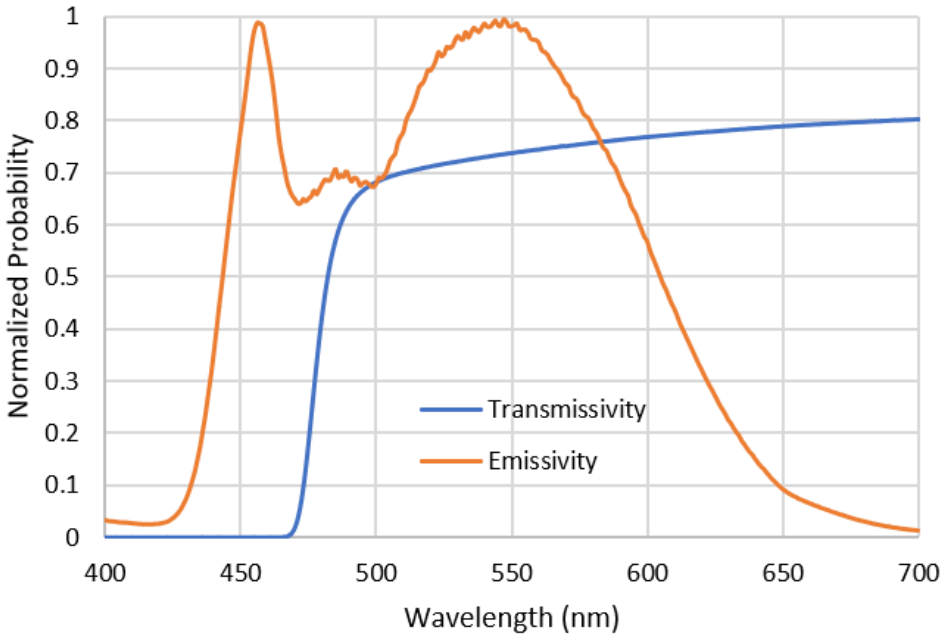


Figure 9.4. Plot of the measured BiPVT transmissivity and emissivity spectra. These data were analyzed and input into OpticStudio to facilitate simulation of the primary emission, reabsorption, reemission, and transmissivity of optical light within the BiPVT plastic.

Analysis and Results

A. Experimental Data Analysis

All images recorded using the Varex radiographic panel were analyzed using the ImageJ Image Processing and Analysis in Java (v1.52a) software. Every array measurement, whether dark, free-field, or shielded, was calculated from the average of 40 separate 16-bit images, each recorded by the Varex panel at two frames per second. All free-field and shielded measurements were then offset corrected by subtracting the dark (i.e. background) measurement, for reasons previously addressed [51].

Within ImageJ, ROIs were established over the individual pixels in both arrays, and pixel intensities and standard deviations were then averaged from these ROI for the free-field and fully shielded measurements. The average free-field pixel intensities for both materials are provided in Table 9.1. Shielded pixel measurements utilized the same ROI used in the free-field analysis, and the average fully shielded pixel intensities for both materials are provided in Table 9.2.

Pixel intensity values for each of the 15 shielded measurements were then exported for analysis. The shielded pixel intensity measurements were divided by the respective free-field pixel intensity measurements to produce intensity ratios for each array pixel, which was necessary for determining edge response. All 15 normalized array measurements for both EJ-200 and EJ-256 were then assembled to form composite 4×45-pixel images of the entire phantom edge, as shown in Figure 9.5. In these images, black corresponded to low signal due to the presence of the steel phantom.

Both composite array images were then expanded from 4×45-pixels to 23×45-pixels by replicating intensity values at commensurate distances across both sides of the measured edge, thereby producing a larger composite image for each array. This could only be accomplished with the use of a straight edge as the phantom, which facilitated contrast pattern replication at equivalent distances from the edge for both shielded and unshielded regions within the original 4×45-pixel image. This step was necessary due to the small size of the arrays; however, consistent pixel regions were used to expand the composite images for both EJ-200 and EJ-256, and these are shown in Figure 9.6.

The 23×45-pixel composite images for EJ-200 and EJ-256 facilitated edge response evaluations. In both images, an 11×44-pixel ROI (484 pixels, total) was centered over the edge to measure the normalized edge response. Through the application of the procedures outlined in Section II, the MTFs for both arrays were calculated from these experimentally measured composite images. Likewise, at the cut-off values of 10%, the SR values for both material arrays were calculated. The experimentally determined MTFs for both materials are plotted in Figure 9.9, and Table 9.3 lists the measured SR for each material, as well.

Table 9.1. Average 2×2 mm pixel intensity and standard deviation measured for each array when fully shielded by the 6.35 mm steel phantom.

Array Material	Mean	σ
EJ-256	21,626.88	1,204.5
EJ-200	11,098.9	639.4

Table 9.2. Average 2×2 mm pixel intensity and standard deviation measured for each array when fully shielded by the 6.35 mm steel phantom.

Array Material	Mean	σ
EJ-256	5,621.0	326.2
EJ-200	3,388.9	202.8



Figure 9.5. Measured composite 4×45-pixel images of a 6.35 mm-thick steel phantom edge for a) EJ-256 and b) EJ-200. These images were constructed from 15 separate measurements at varying degrees of array shielding, with the phantom edge offset from the pixel alignment at a 5˚ angle.

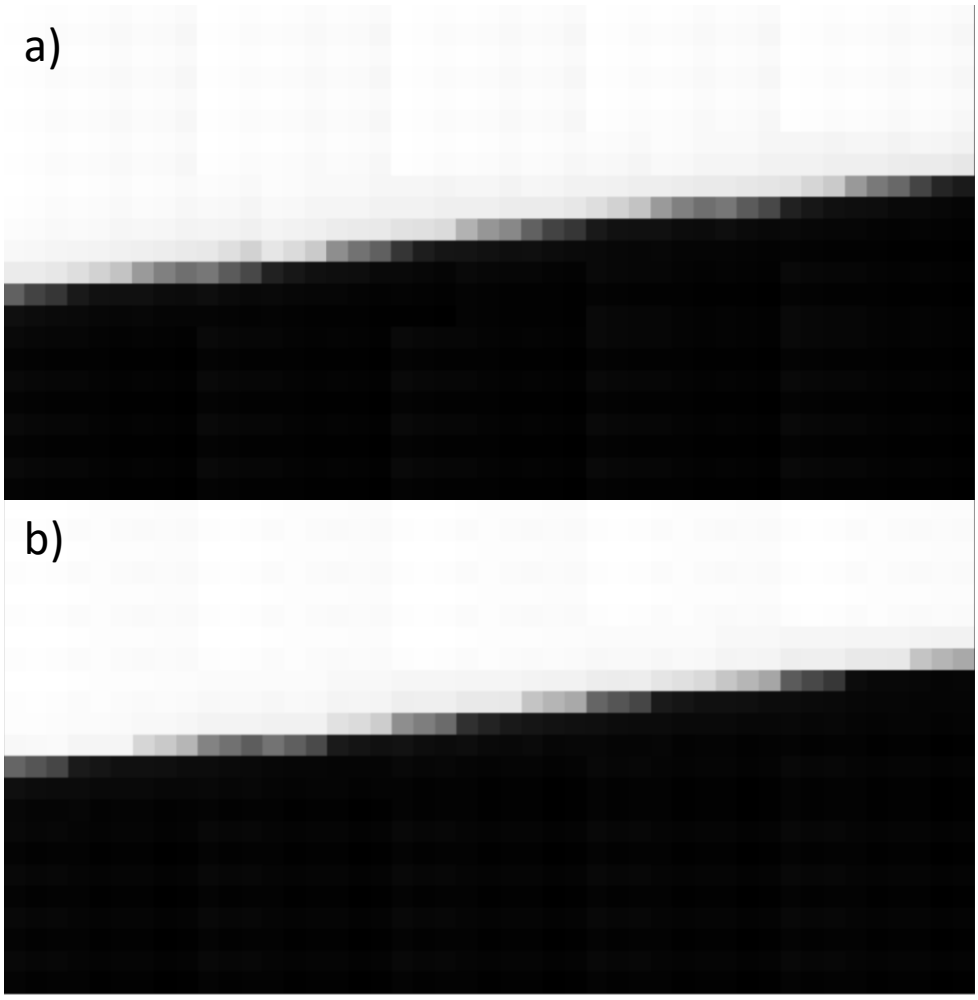


Figure 9.6. Images of the expanded a) EJ-256 and b) EJ-200 23×45-pixel composite matrices. Expansion of the original 4×45-pixel composite images, shown in Figure 9.5, utilized repeating patterns at specific distances from the phantom edge, which was necessary to facilitate calculations of the steel phantom ERF for each array.

B. Simulation Data Analysis

MCNP6 returned estimates of energy deposition per photon (MeV/g-photon) in every EJ-200, EJ-256 and BiPVT pixel for each of the 15 phantom locations, as well as for the free-field. Estimates of total energy deposition per pixel (J) were then calculated, and these values were incorporated in OpticStudio simulations as photoluminescent source energies. Lastly, OpticStudio computations provided estimates of incoherent irradiance (J/mm^2) detected by the TFT for each pixel. These computational estimates of irradiance were then and divided by the respective free-field estimates to produce normalized contrast ratios for each pixel measurement. The 15 normalized measurements for all three arrays were then assembled into composite 4×45-pixel images of the edge response for each material, as shown in Figure 9.7. The remaining data analysis methods matched those described in the Experimental Data Analysis section precisely, including consistent use of the same pixel regions to expand the computational composite images to 23×45-pixels and identical 11×44-pixel ROI to analyze the edge response for both materials. The simulated 23×45-pixel composite images and associated edge responses for both materials are provided in Figure 9.8.

C. Material Evaluation Results

Figure 9.9 and Table 9.3 provide comparisons for the EJ-256 and EJ-200 experimental and computational MTFs and SR values, as well as the simulated MTF and SR for the BiPVT array. Figure 9.9 also includes the cutoff threshold of 10% in all three plots, at which point spatial resolution is assigned for the CT system. For EJ-256 and EJ-200, the calculated experimental and computational SR values fall within the respective standard deviations; therefore, the simulated results are found to agree with the experimental data. This consistency in SR agreement supports the validity of computational predictions for BiPVT array SR, which are also listed in Table 9.3.

In terms of SR, this result suggests that BiPVT should reliably perform as well as EJ-256, while EJ-200 outperforms both by a statistically significant degree. Based upon investigation through simulation, the enhanced SR observed in EJ-200 is directly attributable to the increased rate of incoherent scatter present within the BiPVT and EJ-256 arrays at 370 kVp. Relative to EJ-200, this contributes to additional pixel crosstalk in both materials by increasing the rate of photoelectric absorption in neighboring pixels from scattered incident photons. Our simulations analyzed a variety of array thicknesses and x-ray energies, predicting that the BiPVT array will outperform EJ200 in terms of SR by an average of 9% at 150 kVp and provide statistically equivalent values at 270 kVp.

Additionally, since SR is calculated from the normalized edge response, this metric fails to consider each material's relative light yield and quantum efficiency, which are factors that significantly affect DDA response.



Figure 9.7. Simulated composite 4×45-pixel images of the 6.35 mm-thick steel phantom steel edge for a) EJ-256, b) EJ-200, and c) BiPVT. These images were assembled from 15 separate combined simulations of both MCNP6 and OpticStudio, each with varying degrees of array shielding, with the phantom edge offset at a 5˚ angle from the pixel alignment.

Table 9.3. Experimentally and computationally determined Nyquist values and spatial resolution (SR) for all three material arrays, as well as the associated standard deviation.

Array Material	Experimental		Computational	
	Nyquist (lp/mm)	SR ± 5% σ (mm)	Nyquist (lp/mm)	SR ± 5% σ (mm)
EJ-256	0.464	2.16 ± 0.11	0.474	2.11 ± 0.11
EJ-200	0.527	1.90 ± 0.10	0.543	1.85 ± 0.09
BiPVT	n/a	n/a	0.481	2.08 ± 0.10

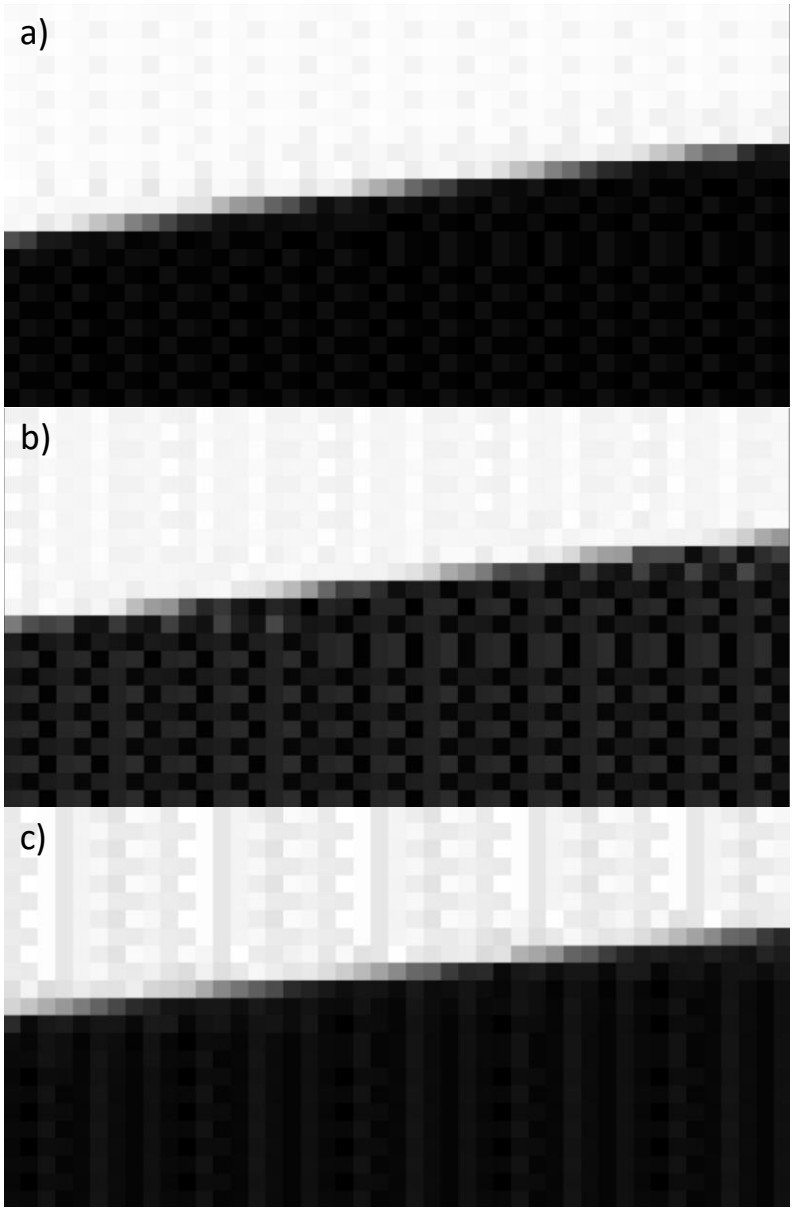


Figure 9.8. Images of the expanded a) EJ-256, b) EJ-200, and c) BiPVT 23×45-pixel composite images, computed from MCNP6 and OpticStudio.

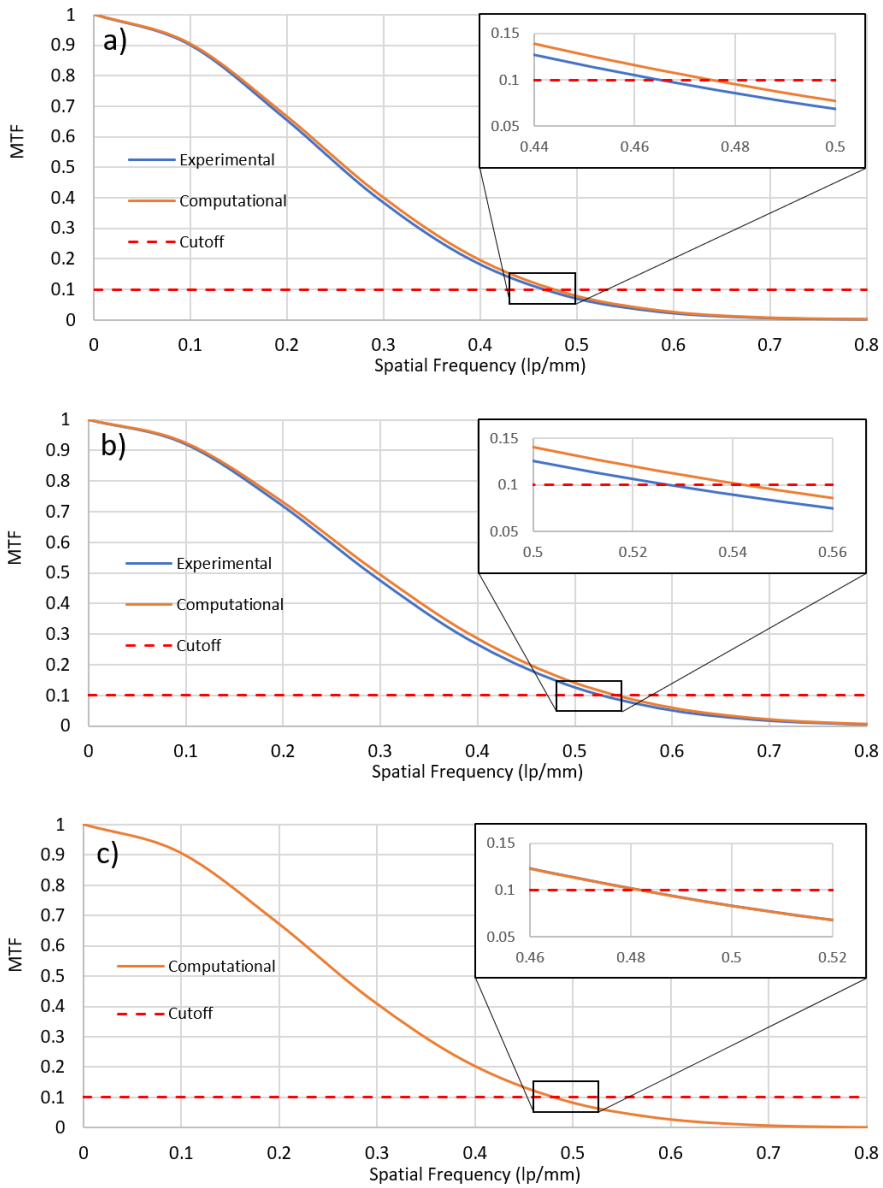


Figure 9.9. Plot of the experimental and computational MTFs for the a) EJ-256 and b) EJ-200 composite images, as well as the simulated MTF for c) BiPVT. Expanded sections highlight where the MTFs cross the 10% cutoff threshold for spatial resolution (SR) determination in ASTM standards for CT system performance evaluations [67].

Specifically, BiPVT provides light yield ratios (per MeV) of 2.0× and 3.9× those of EJ-200 and EJ-256, respectively. Additionally, the average quantum efficiency for BiPVT across its emission spectrum is 2.0× that of EJ-200 and EJ-256. Using these light yield and quantum efficiency ratios, MCNP6 and OpticStudio estimates of energy deposition and light transport can be used to predict relative DDA responses for all three materials.

To validate the accuracy of this approach, estimates of relative DDA response were computed for EJ-200 and EJ-256 and compared to ratios of the measured values in Tables 9.1 and 9.2. The results, both for the free-field and shielded environments, are listed in Table 9.4. The incorporation of EJ-200 and EJ-256 light yields and calculated quantum efficiencies with MCNP6 and OpticStudio simulations provide relative DDA responses that agree with the measured data within the experimental uncertainties. These findings support the validity of identical computational evaluations using BiPVT, as well as the predicted relative DDA response of BiPVT versus EJ-200 and EJ-256 at different x-ray energies considered for portable radiography. The results of comparative BiPVT response are listed in Table 9.5.

Discussion

The predicted pixel intensity ratios listed in Table 9.5 quantify the degree to which the higher Z-loaded BiPVT is expected to increase light collection across multiple x-ray energies (kVp). Therefore, despite the slightly better SR offered by EJ-200 at 370 kVp, these light collection yield estimates suggest BiPVT will significantly outperform both EJ-200 and EJ-256 at all x-ray energies practical for portable radiographic DPI. This is primarily due to the material's higher relative intrinsic efficiency for photoelectric absorption, its enhanced light yield, and its superior quantum efficiency when paired with a DDA. It is noteworthy to mention that the use of iridium-complexes in BiPVT, while greatly increasing light output, will likely introduce some additional cost compared with plastics without this constituent.

Conclusion

In conclusion, when exposed to all x-ray fields practical for portable radiography, the light collection expected from a BiPVT-paired DDA has been quantified and is significantly greater than that produced by an equivalent array made from EJ-200 or EJ-256. These findings are evident when utilizing a computational methodology that leverages MCNP6 for particle transport and energy deposition, as well as OpticStudio for scintillation and light transport. Computed results from this methodology are verified herein against physical measurements of MTF, SR, and light collection ratios of EJ-256 and EJ-200, thereby validating the simulation methodology.

Table 9.4. Comparative ratios of average pixel intensity for the EJ-256 and EJ-200 arrays in the free-field and shielded environments (6.35 mm of steel).

		Experimental ± σ	Computational
$\frac{EJ-256}{EJ-200}$	Free-field	1.95 ± 0.16	1.97
$\frac{EJ-256}{EJ-200}$	Shielded	1.67 ± 0.14	1.63

Table 9.5. Computational ratios of average pixel intensities for BiPVT vs. EJ-200 and EJ-256 at 150, 270, and 370 kV, both in the free-field and a fully shielded environment (6.35 mm of steel).

Array Ratios		Bremsstrahlung Energies		
		150 kV	270 kV	370 kV
$\frac{\text{BiPVT}}{EJ\ 200}$	Free-field	36.28	26.75	19.93
	Shielded	49.42	27.72	17.54
$\frac{\text{BiPVT}}{EJ\ 256}$	Free-field	7.27	10.38	10.09
	Shielded	8.86	11.20	10.75

These quantified improvements in BiPVT detector response translate directly into shorter measurement times and, therefore, less dose per measurement, which is optimal for portable radiography scenarios. Consequently, the simulated results support the use of BiPVT over other plastic alternatives, such as EJ-200 and EJ-256, for DPI radiography applications supporting national nuclear safety, security, and safeguards. Comparative evaluations between the BiPVT, EJ-256, and EJ-200 arrays in fast neutron fields will follow.

Acknowledgement

The authors would like to thank the U.S. Army and the Department of Energy, including award DE-NA0003180, for supporting this research. The authors also thank Dr. Dan Shedlock and Varex Imaging for the use of a Varex Industrial PaxScan® 1515DXT-I flat panel detector and Dr. Keith Vaigneur at Agile Technologies for his assistance and supervision during the fabrication of the evaluated arrays.

CHAPTER TEN -

FAST NEUTRON RADIOGRAPHC PERFORMANCE OF A SMALL BISMUTH-LOADED PVT ARRAY

Abstract

Some novel plastic scintillators offer substantial improvements in light-yield, detection efficiency, and pulse-shape discrimination over more traditional plastic materials. One promising application for select organic scintillators is in low-cost, portable, and durable dual-particle imaging (DPI) systems to support nuclear safety, security, and safeguards purposes. However, candidate materials should first undergo investigation utilizing industry standards to quantify and evaluate their capabilities. In this work, a 21% bismuth-loaded polyvinyl toluene (BiPVT) fabricated by Lawrence Livermore National Laboratory (LLNL) was computationally and experimentally evaluated as a small, pixelated radiographic array, with individual pixel dimensions of 2×2×19 mm. For comparison, the same evaluations were conducted for two same-sized arrays made from EJ-200 and EJ-256. ASTM standard test methods and practices were utilized to calculate the modulation transfer function and spatial resolution for each array, both from measured and simulated data. Measurements were recorded by pressure coupling all three arrays to a commercial a-Si digital radiographic panel, and computational models leveraged MCNP6 and OpticStudio to replicate the experimental design. Simulated and experimental results were compared for all three arrays in a 14.1 MeV neutron environment. The experimental results suggest BiPVT will outperform a nearly identical array made from EJ-256; however, the evaluated BiPVT array does not match the performance of a similar one made from EJ-200. These findings suggest that portable DPI systems utilizing BiPVT hold promise over other more traditional material alternatives.

Introduction

Recent advancements in organic plastic scintillators have produced several novel materials offering enhanced light yields, particle interaction efficiencies, and pulse shape discrimination properties [3, 8, 9, 10, 17]. These new materials, by virtue of their comparative performance advantages over more traditional plastics, may significantly improve the detection, localization, and identification of radiation sources, which remain vital tasks in many industries, such as nuclear power, medical imaging, and national security. Specifically, in terms of nuclear security, the reliable detection and localization of dangerous and potentially illicit radiation sources is of the highest priority, and plastic scintillators are used ubiquitously in

portal monitors, cargo scanners, large imagers, and in other forms of radiation detectors [1, 2, 4, 5, 6, 7].

This demonstrated reliance on plastics is largely due to the advantageous balance they offer in detection efficiency, considering their affordability in scalable volumes, as well as their durability and fast time response. However, the three principal drawbacks commonly associated with organic plastics are their relatively lower light yields, energy resolutions, and gamma detection efficiencies per unit volume [3, 9, 10]. However, for the purposes of dual-particle imaging (DPI), which is the focus of this work, the two principal considerations are light yield and efficiency.

Light Yield

Light yield is an important metric for comparing scintillators since it impacts fundamental system performance properties such as resolution and signal-to-noise ratio. Light yield is defined as,

$$\textit{Light Yield} = \frac{\#\ of\ scintillation\ photons}{energy\ of\ particle\ (MeV)}. \quad (53)$$

Traditional plastics made from a polyvinyl toluene (PVT) matrix, such as EJ-200, typically emit ~10^4 photons per MeV in the blue (with peak emission at ~425 nm) [36]. This light yield is considerably less than the ~3.8×10^4 photons per MeV emitted from NaI(Tl), an inorganic crystal widely used for x-ray and gamma detection and long considered a benchmark for scintillator performance comparisons.

Efficiency

Traditional plastics, such as EJ-200, are very sensitive to fast neutron detection, which predominantly occurs via proton recoil events due to their high hydrogen content. Likewise, a centimeter-scale thickness of EJ-200 offers reasonable efficiency for high energy photons interacting via Compton scatter. However, due primarily to its atomic constituents, EJ-200 delivers extremely low intrinsic efficiency for photoelectric (PE) absorption. Efforts to overcome this shortcoming result in high-Z loaded variants, such as EJ-256, which is a commercially available 5% Pb-loaded PVT plastic [37]. The presence of high-Z loading within an organic matrix improves photon detection efficiencies across nearly all energies by raising both the aggregate material density and its effective atomic number (Z_{eff}). This is important because PE is heavily governed by a power relationship with Z, with the probability of interaction defined as,

$$Probability_{PE} = \frac{{Z_{eff}}^n}{{Energy_{photon}}^{3.5}}. \quad (54)$$

where *n* is typically a value between 4 and 5 [9]. Therefore, even minor increases

in a material's Z_{eff} can significantly increase PE interaction rates at lower energies. Unfortunately, the benefits of high-Z loading are typically offset by degraded light yields, which occur due to increased rates of triplet molecular excited states forming from ionization events. Compared to useful singlet states, which facilitate prompt fluorescence, the more common triplet molecular states cannot radiatively deexcite in traditional plastics due to spin-forbidden electron transitions. Therefore, they must either non-radiatively relax or radiate via triplet-triplet annihilation, which is statistically unlikely [9]. For example, at just 5% Pb-loading, EJ-256 produces only 52% of the light yield expected from the unsensitized EJ-200 at an identical emission spectrum [36, 37]. In terms of radiographic applications, light yield directly impacts the efficiency of image production, since detection media with higher light outputs typically produce optimal images (those with ~50k contrast shades) in less time than detection materials producing less light at equivalent exposures. Therefore, higher material light yields facilitate greater imaging efficiency because this process requires less time and/or a lower radiation exposure.

Additionally, the ability to reliably detect both photons and neutrons across broad energy regions offers considerable benefits in the field of nuclear security by allowing a variety of future systems to operate with just a single detector material. Such dual particle sensitivity would provide important information that a single form of radiation detection and imaging cannot provide alone [8, 9, 10, 17, 1, 6]. For radiographic applications, the material in question must reliably detect incident fast neutrons (14.1 MeV) and high-energy photons (>200 keV). Furthermore, due to the number of plausible safety and security challenges our nation faces today, an important part of the solution would likely include a range of radiation imaging systems with DPI capabilities. Therefore, the development of such a material would likely reduce future system costs, improve the likelihood of dangerous and/or illicit radioactive material detection, and thereby contribute substantially to increasing the security of our nation and allies.

Novel Contributions

This research examines one such candidate material, which was designed and produced at Lawrence Livermore National Laboratory (LLNL). It is a 21% bismuth-loaded PVT plastic (BiPVT), and it is unique in that it pairs high Bi-loading with an iridium-complex fluor that facilitates radiative triplet deexcitation through spin-orbit coupling [9]. Consequently, this composition produces a light yield of ~2×10^4 photons per MeV in the green (with peak emission at ~550 nm), thereby partially mitigating the depressed light yields typical of other high-Z sensitized plastics. Lastly, the green photoluminescence emission spectrum from BiPVT pairs particularly well with commercially available radiation-hardened amorphous silicon (a-Si) photodetectors, with expected average improvements in quantum efficiency (QE) of ~2× that of scintillators emitting in the blue [45].

These potential benefits motivative this research, which describes both experimental and computational comparisons of BiPVT digital detector array (DDA) fast neutron radiography performance against the same DDA paired with industry standard plastic scintillators, specifically EJ-200 and EJ-256. Evaluations of comparative x-ray performance have already been performed and provide experimental and computational analyses of spatial resolution (SR) for EJ-200 and EJ-256 at the cut-off frequency ($f_{10\%}$) of the modulation transfer function (MTF).

Based upon investigation through simulation, the enhanced SR observed in EJ-200 is directly attributable to the increased rate of incoherent scatter present within the BiPVT and EJ-256 arrays at 370 kVp. Relative to EJ-200, this contributes to additional pixel crosstalk in both materials by increasing the rate of photoelectric absorption in neighboring pixels from scattered incident photons. The simulations analyzed a variety of array thicknesses and x-ray energies, predicting that the BiPVT array will provide equivalent SR to EJ-200 at 150 kVp and provide statistically equivalent values at 270 kVp for thicknesses up to 20 mm. These analyses, as well as the values provided in Table 10.1, supersede those previously published [80] but do not alter the final conclusions, which determined BiPVT will provide marked performance improvements over EJ-200 and EJ-256 at all energies practical for portable x-ray radiography [80, 81]. As such, the results described herein serve to further quantify the comparative performance of future systems leveraging BiPVT material for fast neutron radiography, a critical component of DPI systems.

Theory

Although computed tomography (CT) is not applied in this research, composite images (i.e. larger images constructed from multiple smaller images) are required for performance comparisons of the considered arrays due to their small size, which is largely a result of the limited quantity of novel material available for characterization. Consequently, the theory and procedures applied herein for neutron DDA performance comparisons are based on published American Society for Testing and Materials (ASTM) standards for the measurement of CT system performance. The standard practice for characterizing CT system performance begins with measurements of a composite edge response function (ERF) [67].

Modulation Transfer Function and Spatial Resolution

The edge response is measured from composite image data from a phantom of defined material and thickness, which produces differences in pixel modulation across the phantom's edge.

Table 10.1. Experimentally and computationally determined $f_{10\%}$ and spatial resolution (SR) values for all three material arrays evaluated in a 370 kVp x-ray field, as well as the associated errors.

Array Material	Experimental		Computational	
	$f_{10\%}$ (lp/mm)	SR ± 5% σ (mm)	$f_{10\%}$ (lp/mm)	SR ± 5% σ (mm)
EJ-256	0.212	2.36 ± 0.12	0.208	2.40 ± 0.12
EJ-200	0.270	1.85 ± 0.09	0.276	1.81 ± 0.09
BiPVT	n/a	n/a	0.210	2.38 ± 0.12

In CT, this is provided by a circular phantom enabling a two-dimensional analysis of edge response; however, this research only examines a one-dimensional (1D) edge, so the phantom is offset from the pixel rows by a consistent angle selected between 2-5°, as per ASTM standards [48, 53]. Ideally, this angular offset produces numerous array pixels measuring varying degrees of phantom attenuation, depending on the extent to which pixels are shielded by the phantom edge. A region of interest (ROI) is then established to measure as much of the edge as possible, with ROI minimums of 11-pixels across the edge and 256 pixels in total [67]. ROI edge data are then averaged to calculate modulation response across the edge. This average edge response is normalized, and interpolation is used to determine the ERF, with bin sizes set at 10% of the pixel size used in the ROI [67]. A piecewise least-squared cubic fit of the ERF is then performed using the same number of values. From this series of third order polynomials, the analytical derivative is calculated to provide the line spread function (LSF), which is also normalized and centered on the ERF [67, 68]. This is represented mathematically as,

$$LSF = \frac{d(ERF)}{dx}. \quad (55)$$

An example of the LSF, superimposed on the ERF, is also shown in Figure 10.1. Next, the modulation transfer function (MTF) is calculated from the 1D Fourier Transform (FT) of the LSF using the equation,

$$MTF = FT\left(\frac{d(ERF)}{dx}\right) = FT(LSF). \quad (56)$$

The 1D FT is used to shift the data from units of object space to units of spatial frequency, or cycles per distance. Therefore, the MTF describes the change in modulation within an image signal as a function of modulation spatial frequency for the specific DDA. MTF magnitudes are then normalized to unity at frequency zero, and a cut-off at 10% of the MTF ($f_{10\%}$) represents the limit of spatial resolution (SR) for the DDA, with an accuracy of ± 5% [67]. SR is calculated as one half the inverse of the $f_{10\%}$, and it represents the limit of geometrical detail that can be resolved by the DDA [67, 71, 69]. An example MTF, including the cut-off threshold for minimum SR, is provided in Figure 10.2.

Normalized Signal-to-Noise Ratio

However, since SR is calculated from the normalized MTF, information regarding the relative intensity of different arrays is absent from any comparison based solely on this metric. Therefore, a more useful method for evaluating relative DDA performance relies on both the SR and the measured signal-to-noise ratio (SNR) of the DDA.

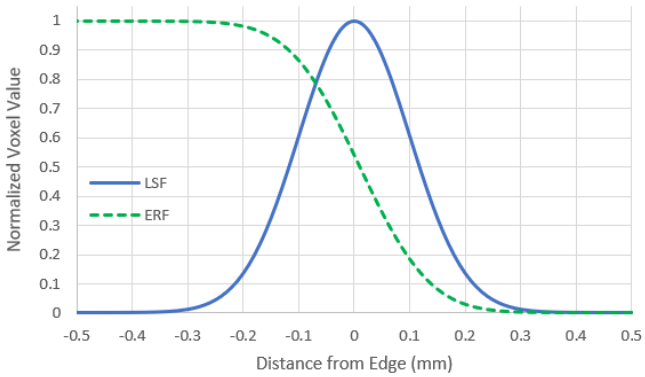


Figure 10.1 Example plots of normalized edge response function (ERF) and line spread function (LSF).

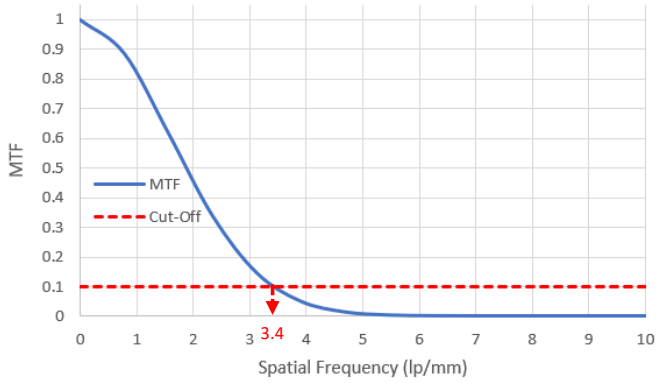


Figure 10.2 Example modulation transfer function (MTF). Values of spatial resolution (SR) are measured for the DDA at a 10% cut-off of the MTF($f_{10\%}$). In this example, the MTF reaches $f_{10\%}$ at a spatial frequency of 3.4 lp/mm, which means the hypothetical DDA provides a SR of 0.147 mm.

The SNR is the quotient of mean value of the intensity (signal) and standard deviation (σ) of that intensity (noise) [48]; however, in the case of radiography images, a more accurate equation is,

$$SNR = \frac{Mean\ intensity\ (difference\ image)}{\sigma(difference\ image)}, \quad (57)$$

where the difference image is achieved by averaging the pixel intensities in the free-field (i.e. in the case of unshielded irradiation) and subtracting the same regions of the averaged intensities from dark images (i.e. those measured without irradiation) [53]. This process produces offset-corrected images and is analogous to correcting for background contributions in traditional radiation measurements. Together, these terms enable a calculation of the detector SNR-normalized (dSNRn) in the free-field, using

$$dSNRn = \frac{SNR \times \sqrt{2} \times 88.6\ \mu m}{SR}. \quad (58)$$

The $\sqrt{2}$ term is used to correct the SNR, since the difference of two images is used for noise calculations, and 88.6 µm is consistent with phosphor film pixel widths, so its inclusion in dSNRn calculations standardizes DDA performance comparisons across multiple radiographic systems [53]. The dSNRn is a useful indicator of DDA performance because it quantifies the exposure necessary to reach a full SNR. For a 16-bit image, this means ~50k contrast tones measured in the detector area, which avoids image overexposure. In the case of x-ray radiography, these values are expressed in plots of dSNRn vs. the square root of the exposure dose (mGy), with the slope of each line defining DDA efficiency. However, if the exposure, beam filtering, and image quality indicator (IQI) are all equivalent for separate DDAs, then the dose terms cancel and only the dSNRn values are left to compare, with higher dSNRn values indicating superior DDA performance at that exposure.

Traditional x-ray radiography DDA, such as thin film transistor (TFT) paired with gadolinium oxysulfide (Gd_2O_2S) or cesium iodide (CsI), typically yield SNR >200 and SR <200 µm. These systems provide dSNRn values well over 100 or even 1000 at certain exposures; however, such systems provide no capability to support fast neutron imaging. Therefore, x-ray and neutron dSNRn values for systems optimized for DPI are typically significantly lower and do not appear competitive when compared against traditional DDAs optimized solely for x-ray radiography.

Pixel Size

For the purposes of fast neutron characterization, a 2×2 mm pixel face was selected for all three materials due to the expected pathlengths of scattered protons. If pixel face dimensions are too small, recoil charged particles may

routinely scatter beyond pixel boundaries and deposit significant portions of their energy in adjacent pixels or outside the array. For example, protons scattered in EJ-200 (ρ = 1.023 g/cm^3) at 30° relative to the incident path of 14.1 MeV neutrons will recoil at energies of ~10.5 MeV, which means they are expected to travel ~1.3 mm from the interaction site and ~0.65 mm orthogonal to the original neutron path. Therefore, protons scattered at 30° from anywhere within a pixel with a cross section <1.69 mm^2 (1.3×1.3 mm) will likely exit the pixel. Since TFT photodetector panels operate in integration mode, this result would reduce position and image resolution. Based on this understanding, pixel dimensions of 2×2 mm (a 4 mm^2 pixel cross section) were selected. Additionally, a pixel depth of 19 mm was chosen for all three arrays to maximize the probability of particle interactions while also reducing pixel aspect ratio below 10:1, which is expected to maximize light output versus image resolution [75]. These dimensions were used for EJ-200, EJ-256 (ρ = 1.081 g/cm^3), and BiPVT (ρ = 1.4 g/cm^3).

Dark Noise Subtraction

Use of a-Si TFT panels to measure radiographic response inherently includes contributions from dark noise in all recorded images. Any meaningful impact from this noise is typically eliminated via subtraction of a dark measurement and, in the case of x-ray images, any remaining contributions are minor compared to the measured response. However, in the case of neutron transmission imaging, the signal may often fail to surmount the accumulating dark noise, so noise discrimination and subtraction becomes less straightforward. Additionally, digital panel noise was found to aggregate non-linearly over time in the Varex 1515DXT-I panel. In fact, the total noise appears to plateau after ~180 minutes of continuous operation in a dark field, which represents roughly the time required for the panel to reach a stable operating temperature. Therefore, due to the strong dependence of dark noise on temperature, measurements conducted after 180 mins of panel operation may produce more stable and easily subtracted image noise.

Experiment and Simulation Methodology

Array Fabrication

Based upon optimal pixel size determinations, a small sample of LLNL BiPVT (6.85×19×21 mm) was cut, polished, and assembled into a 4×3-pixel array, with final individual pixel dimensions of 2×2×19 mm. An image of the original material, prior to array fabrication, is shown in Figure 10.3. Dual layered Vikuiti™ enhanced specular reflector (ESR) was used to optically isolate each pixel, with a final average pixel pitch of 2.44 mm for the BiPVT array. Images of the final BiPVT array are provided in Figure 10.3.

To facilitate BiPVT array performance comparisons, EJ-200 and EJ-256 were selected for comparative characterizations as industry standard materials. Consequently, 4×3-pixel arrays of matching pixel dimensions (2×2×19 mm) were fabricated from each material.

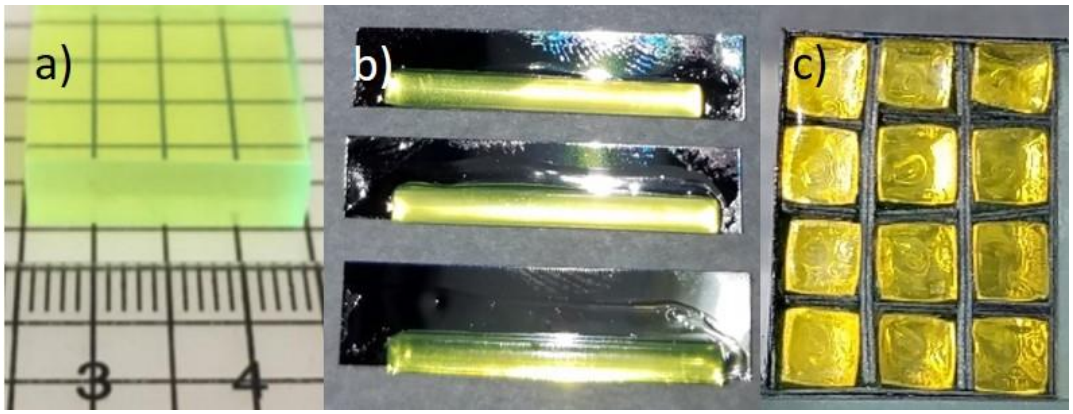


Figure 10.3 Images of a) BiPVT source sample (6.85×19×21 mm) provided by LLNL, b) individual BiPVT pixels, adhered to ESR, prior to trimming, and c) the final BiPVT 4×3-pixel array face, which pressure-mounted to the Varex radiographic panel.

The three arrays were then affixed to a section of 2.5 mm tall acrylic plastic to prevent changes in their relative location or orientation between measurements. An image of the final arrays, mounted to the acrylic plastic, is provided in Figure 10.4.

This process resulted in much improved geometric uniformity and an average pixel pitch of 2.28 mm for each array. It also provided equivalent pixel polish and ESR adhesion across both arrays due to the use of identical procedures during their manufacture.

The three arrays were then paired with a commercial radiographic Varex PaxScan 1515DXT-I Flat Panel Detector for all measurements [56]. This first required the removal of the original proprietary gadolinium oxysulfide (Gd_2O_2S) conversion layer, followed by the attachment of custom aluminum components to all four outer sides of the Varex panel, thereby extending the panel's light-tight enclosure by 25.4 mm orthogonal to the TFT. Within this expanded volume, the BiPVT, EJ-200, and EJ-256 arrays were pressure mounted against the a-Si photodetector using layers of custom-cut foam to hold the arrays in place. The a-Si TFT provided pixel pitches of 127 μm^2, so every measured 2×2 mm array pixel response was averaged from the response of ~250 photodetector pixels. Lastly, the enclosure was sealed using the Varex panel's original 2.5 mm-thick carbon fiber plate.

Experiment Methodology

With the arrays pressure mounted and enclosed within the modified Varex radiographic panel, measurements within a fast neutron field were conducted, and each measurement consisted of the average of 30 separate images recorded at 0.2 frames per second (fps). The neutrons were produced by an ING-27 D-T neutron generator (S/N 5593661), which was positioned ~100 cm above the floor and operated at ~80% of its maximum voltage. This produced 14.1 MeV neutrons at a rate of ~4.4×10^7 neutrons per second. Also, to eliminate possible unwanted contributions from x-rays, a 0.635 cm-thick plate of lead measuring ~10 cm on each side, was placed just outside of the generator housing, between the 5 mm-wide tritium target and the radiographic panel. Although the x-ray spectrum emitted by the ING-27 is yet to be precisely measured and quantified, current research suggests it does not exceed 140 kVp. Prior x-ray image evaluations using a 6.35 mm lead shield eliminated >98% of the measured signal across all three arrays when exposed to 150 kVp, therefore contributions from x-rays are believed to be minor. Since this small thickness of lead produces virtually no attenuation of the emitted 14.1 MeV neutrons, it was selected to ensure the elimination of potential x-ray contributions.

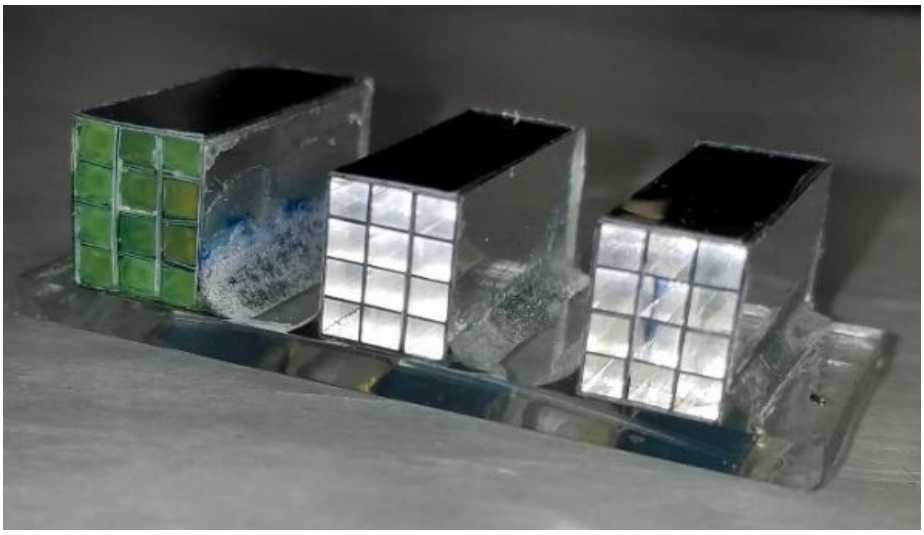


Figure 10.4 Image of the BiPVT (left), EJ-200 (center), and EJ-256 (right) 4×3-pixel arrays affixed to acrylic plastic.

For every measurement, the neutron source was centered on a specific array at a consistent source to detector distance (SDD) of 12.5 cm to maximize array solid angle and minimize necessary exposure times. Due to this proximity, however, separate sets of measurements, each with the source centered on a different array, were required to measure comparable free-field and edge response data. Shielded array measurements utilized a 5.08 cm-thick tungsten block placed against the panel's outer carbon fiber plate, ~1.75 cm from the arrays inside. The phantom provided a uniform shield thickness for all three arrays, and the edge was consistently positioned at 5° off-axis to meet ASTM standards [48, 53]. A series of 15 shielded measurements were recorded, with the phantom edge repositioned between each measurement to provide an incrementally larger fraction of array shielding than the previous measurement. This process required the use of a Velmex® motorized slide, which enabled uniform movement of the phantom in 0.775 mm increments between measurements. Consequently, this produced a range of shielding measurements for each array between 0-100%, all at 5° off-axis.

In terms of dark noise subtraction, 180 mins was not allowable prior to each series of measurements, so the panel was simply operated for ~30 mins before measurements were recorded. This allowed for both a reduction and stabilization in the rate of dark noise aggregation prior to experimentation. To accurately quantify accumulating dark noise, a consistent 333×1152-pixel region was summed from each averaged 30-frame measurement. This region represented ~1/3 of the panel surface area and was devoid of any scintillator material, so it only recorded accumulating panel noise. Measurements were conducted in sets of five (M_1-M_5) and these were each bracketed between two dark measurements without neutron emission present. The summed values of dark noise accumulation from the 333×1152-pixel regions represented noise in each 150-sec measurements (M_{1r}-M_{5r}) and in the dark measurements (D_{1r} and D_{2r}).

Using these values, contributions from panel noise were estimated on a per TFT pixel basis for each measurement. This was accomplished by calculating the fractional contributions (F_i and 1-F_i) of noise from the two dark images to each individual measurement by summing those contributions into a single estimate of background (B_i) and subtracting it from each measured image (M_i). This process produced offset corrected (M_{iOC}) difference images. The five offset corrected images were then averaged to produce a final measurement image (M_f) for the free field and for all 15 shielded measurements. Therefore, each measurement was the average of 150 separate frames, which were offset corrected in groups of 30 frames. This process enabled the isolation of measured signal from background, which would otherwise have been obscured. Algebraically, this series of calculations is performed using,

$$F_i = \left(\frac{D_{2r} - M_{ir}}{D_{2r} - D_{1r}}\right), \quad (59)$$

$$B_i = F_i * D_1 + (1 - F_i) * D_2, \quad (60)$$

$$M_{iOC} = M_i - B_i, \quad (61)$$

$$M_f = \frac{\sum M_{iOC}}{5}. \quad (62)$$

This analysis was conducted separately across all measurement sets. Of course, due to the large amount of noise subtracted relative to signal, this process resulted in some negative TFT pixel values and larger variances, which necessitated longer exposures and a shorter SDD to minimize those effects due to the small pixel volumes evaluated.

Shielded measurements were then gain-corrected by dividing them by free-field (i.e. unshielded) values to normalize the images, a standard practice in imagery analysis to correct for variable pixel performance [60]. Using these measured contrast ratios, 4×45-pixel composite images of the tungsten edge response were then assembled from the BiPVT, EJ-200, and EJ-256 array measurements.

Lastly, the composite array images were expanded from 4×45-pixels to 23×45-pixels by replicating contrast values at commensurate distances across the measured edge, thereby producing larger composite images for each array. This could only be accomplished by using a 1D straight-edge phantom, which supported additional findings detailed in Section IV.

Simulation Methodology

This research utilized two software programs to simulate particle energy deposition, pixel response, light transport, and quantum efficiency. Monte Carlo N-Particle Code© v6.2 (MCNP6) was leveraged to model particle transport, interactions with matter, and energy deposition within each pixel. MCNP6 also utilizes material cross section data from ENDF/B-VII, the most current library of cross section data available; however, MCNP6 cannot simulate optical light transport. Consequently, OpticStudio®, a software package produced by Zemax, was utilized to simulate optical photon transport based on MCNP6 computations of energy deposition (J) within each pixel. OpticStudio utilizes Monte Carlo methods to model optical photon transport through complex optical systems. The software incorporates optical light absorption, emission, and transmissivity spectra, as well as material dimensions, density, refractive index, and surface reflectivity. OpticStudio also enabled incorporation of the wavelength-dependent photodetector quantum efficiency into estimated results.

Once experimentation was complete, MCNP6 input decks were built to replicate the experimental geometry for all three arrays and measurements. Pixels were simulated as separate cells surrounded on five sides by ESR material, with the arrays affixed to 2.5 mm of acrylic plastic. External to the arrays, the aluminum Varex panel housing, custom aluminum side attachments, and the carbon fiber cover were also replicated. The tungsten phantom was included for all shielded simulations, and this was offset by 5° and shifted in position for each of the 15 separate shielded simulations. Simulations matched the incrementally increasing fraction of array pixels shielded by the tungsten IQI during experimentation using a transformation (TR) card to uniformly rotate and shift the tungsten block between simulations.

Additionally, the lead x-ray shield, located between the tritium target and DDA, was included in all simulations of radiographic response, and a separate computational study was performed to predict the fractional energy deposited from neutron-induced lead photoluminescence. These simulations found that gammas emitted from neutron inelastic scatter within the lead plate may account for ~2.3% of the total energy deposited in the BiPVT pixels and ~1.5% and ~1.6% of the energy deposited in EJ-200 and EJ-256, respectively.

Energy deposition within each pixel was estimated using +F6 tallies, with BiPVT and EJ-256 simulated as homogenous PVT modified by the wt% of their respective high-Z constituent. The source was simulated as 5 mm-wide circular surface and produced 14.1 MeV neutrons isotopically; however, forward bias was applied with lower particle weights to direct most particles into a 25.16˚ cone, thereby reducing computation time. Proton, neutron, electron, and photon physics cards were also employed, and deposited proton recoil energy was estimated separately, as well as photon energy originating from neutron inelastic scattering within the tungsten and panel components. In all cases, 15M particles were simulated with the source centered on each array at a SDD of 12.5 cm for all 15 measurements to match the experimental design. Results for the pixels passed all ten statistical checks for tally fluctuation with average uncertainties across all pixels of ~2.5% and ~4% for the unshielded and fully shielded configurations, respectively.

MCNP6 estimates of energy deposition (J/pixel) informed OpticStudio simulations of photoluminescence and optical light transport by providing total photoemission energy. For BiPVT, OpticStudio simulated the primary emission, reabsorption, reemission, and transmissivity of optical light. Emissivity and transmissivity spectra for BiPVT were experimentally measured beforehand using a Horiba Jobin YvonFluorolog 3 Spectrofluorometer and a Cary 5000 UV-Vis-NIR Spectrophotometer, respectively, and the data are provided in Figure 10.5.

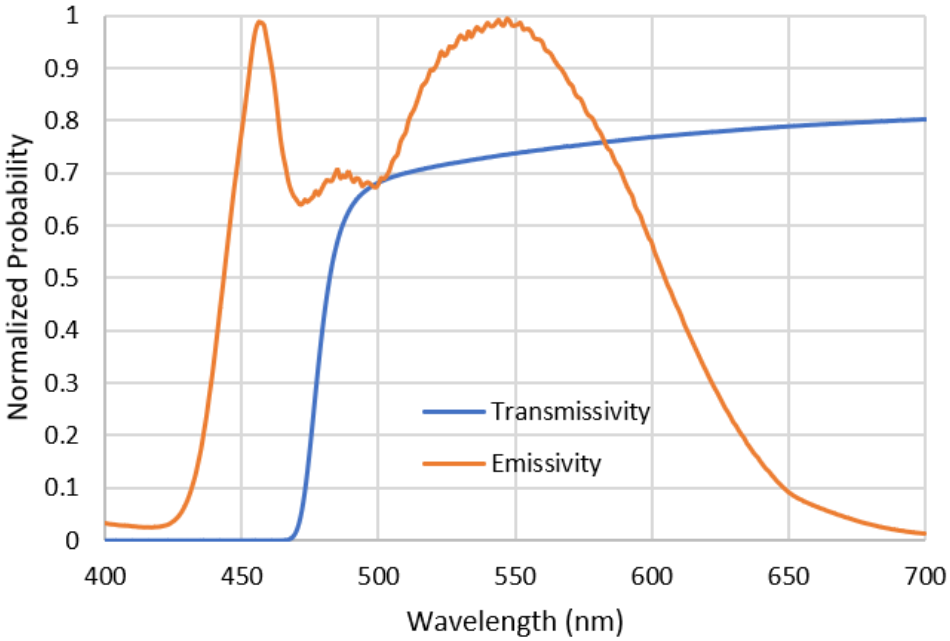


Figure 10.5 Plot of the measured BiPVT transmissivity and emissivity spectra. These data were analyzed and input into OpticStudio to facilitate simulation of the primary emission, reabsorption, reemission, and transmissivity of optical light within the BiPVT plastic.

From the measured emissivity data in Figure 10.5, the primary and secondary emission spectra were estimated by fitting Gaussian functions to the data, with peaks at 457 and 550 nm, respectively. These were input into OpticStudio along with BiPVT transmissivity data and material density. As a material, BiPVT is a yellowish color, so the measured transmissivity data were not normalized to account for this property. In all other respects, the BiPVT was modeled as a polycarbonate plastic with a refractive index of 1.58.

For EJ-200 and EJ-256, the blue photoemission spectra listed on the respective Eljen Datasheets were incorporated into OpticStudio, and a refractive index of 1.58 and the respective material densities were incorporated [36, 37]. Also, due to the optical clarity of both materials, they were simulated as 100% transmissive across all emission wavelengths, which is a reasonable approximation. Lastly, for all array simulations, OpticStudio incorporated the wavelength-dependent quantum efficiency of the TFT photodetector [45].

OpticStudio estimates for each array simulation were provided per 2×2mm pixel in units of incoherent irradiance (J/mm^2), and these were divided by free-field values to normalize the data in the same way gain correction was used for the experimental data. Using these ratios, 4×45-pixel composite images were then assembled for each of the three materials from the simulated responses using an identical methodology to that described for the experiment data analysis.

Analysis and Results

Experiment Data Analysis

All images recorded using the Varex radiographic panel were analyzed using MATLAB© (R2018b) and ImageJ Image Processing and Analysis in Java (v1.52a) software. Every array measurement, whether free-field or shielded, was calculated from the average of 150 separate 16-bit images, each recorded by the Varex panel at one frame per five seconds (0.2 fps). Dark measurements were recorded at the same rate but averaged from 30 separate images, each. The free-field and shielded measurements were then offset corrected using the specific calculated backgrounds (i.e. B_i), which were obtained using MATLAB software and the methodology explained in Section II.

Then, within ImageJ, ROIs were established over the individual pixels, and pixel intensities and standard deviations were averaged from these ROI for the free-field and fully shielded measurements. The average free-field pixel intensities were scaled by subtracting average background from a nearby ROI, and signal standard deviation was determined from the square root of the sum of the squares of standard deviation for both pixel signal and remaining background. These values are provided for all three materials in Table 10.2.

Table 10.2. Average 2×2 mm pixel intensity, standard deviation, and SNR measured for each array during five-second exposures in the free-field (FF).

Array Material	Mean	σ	SNR
EJ-200	7.12	3.16	2.26
BiPVT	4.85	3.08	1.58
EJ-256	3.30	3.02	1.09

Shielded pixel measurements utilized the same ROI used in the free-field analysis, and the average fully shielded pixel intensities for both materials are provided in Table 10.3. Lastly, the shielded images were all gain corrected by dividing each by the corresponding free-field array image, and the pixel intensity ratios for each of the 15 shielded measurements were then exported for analysis. The 15 measurements for BiPVT, EJ-200, and EJ-256 were assembled to form composite 4×45-pixel images of the entire phantom edge, as shown in Figure 10.6. In these images, black corresponds to low signal due to the presence of the tungsten phantom.

Of the 45× total measurements, three fully shielded measurements (two for BiPVT and one for EJ-256) were identified as suffering from unusually low signal, with disparities >10% from neighboring fully shielded measurements. Consequently, these measurements were considered outliers, so they were normalized using the ratio of average signal within other fully shielded measurements. The unexpectedly low signal present in these measurements was attributed to low average neutron flux. This was the only change made to the measured data, and the changes are highlighted in Figure 10.6. These composite array images were then expanded from 4×45-pixels to 20×45-pixels by replicating intensity values at commensurate distances across both sides of the measured edge, thereby producing a larger composite edge image. This could only be accomplished with the use of a straight edge phantom, which facilitated contrast pattern replication at equivalent distances from the edge for both shielded and unshielded regions within the original 4×45-pixel image. This step was necessary due to the small size of the arrays. Expanded images of the tungsten edge are shown in Figure 10.7.

The 20×45-pixel composite images facilitated edge response evaluations. For all three images, a 13×45-pixel ROI (585 pixels, total) was centered over the edge to measure the normalized edge response. Through the application of the procedures outlined in Section II, MTFs for both arrays were calculated from these experimentally measured composite images. Likewise, at the cut-off frequency, $f_{10\%}$, SR values for both material arrays were calculated. The experimentally determined MTFs for both materials are provided in Section C below, as well as the measured SR for each material.

Simulation Data Analysis

MCNP6 returned separate estimates of energy deposition per neutron (MeV/g-neutron) within every EJ-200, BiPVT, and EJ-256 pixel for each of the 15 phantom locations, as well as for the free-field. These values were then normalized based on pixel mass (g) and estimates of total energy deposition per pixel (J) were calculated and input into OpticStudio as photoluminescent source energies. OpticStudio simulations then returned estimates of incoherent irradiance (J/mm^2) detected by the simulated TFT for each 2×2 mm pixel.

Table 10.3. Average 2×2 mm pixel intensity, standard deviation, and SNR measured for each array during five-second exposures when fully shielded by the 5.08 cm tungsten phantom.

Array Material	Mean	σ	SNR
EJ-200	3.86	3.01	1.28
BiPVT	2.13	2.97	0.72
EJ-256	1.16	3.05	0.38

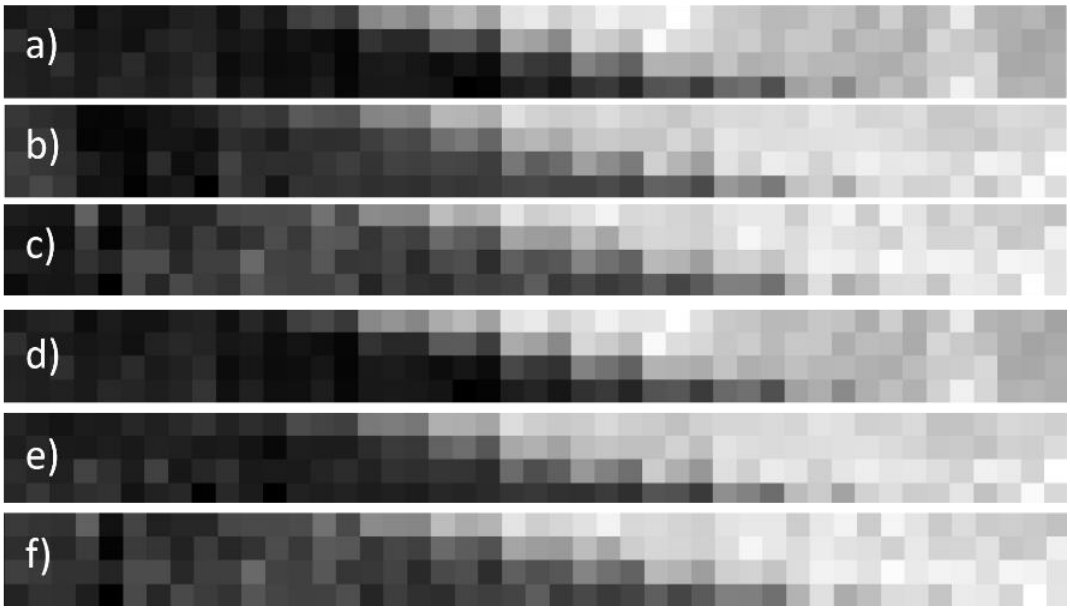


Figure 10.6 Measured composite 4×45-pixel images of a 5.08 cm-thick tungsten phantom edge for a) EJ-200 b) BiPVT and c) EJ-256. These images were constructed from 15 separate measurements at varying degrees of array shielding, with the phantom edge offset from the pixel alignment at a 5˚ angle. Pixel intensity normalization occurred for a total of three fully shielded measurements (two for BiPVT and one for EJ-256), as reflected in the final composite 4×45-pixel images for d) EJ-200 e) BiPVT and f) EJ-256.

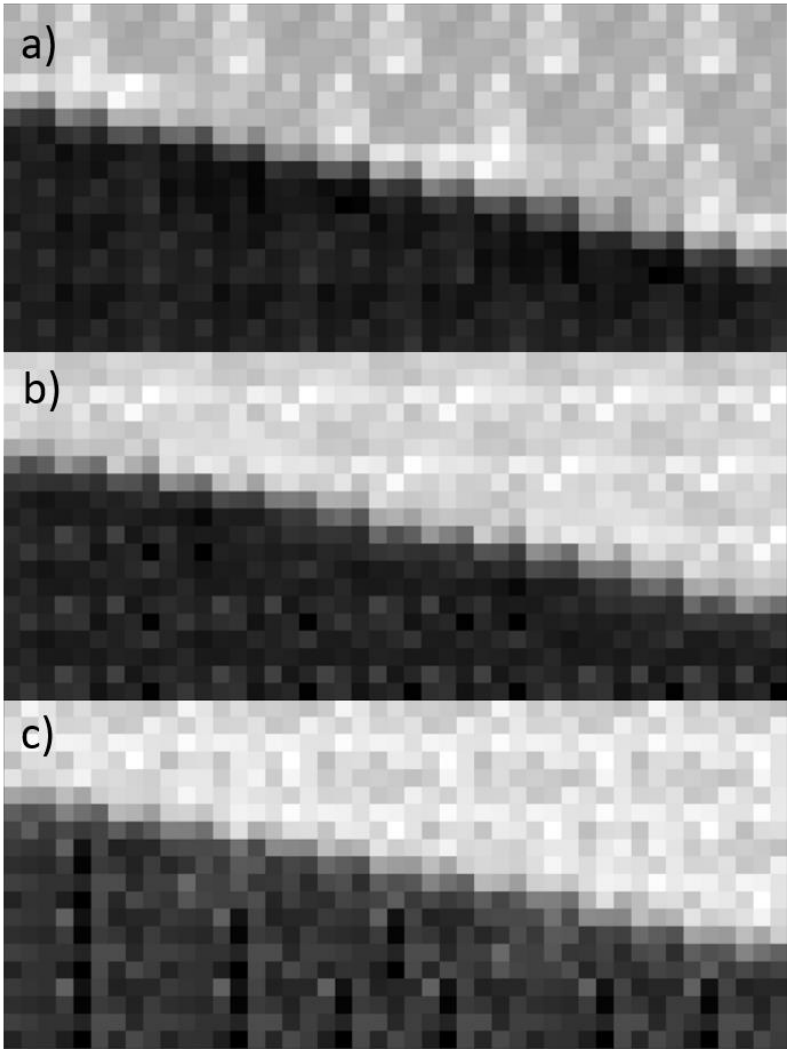


Figure 10.7 Images of the expanded a) EJ-200, b) BiPVT, and c) EJ-256 20×45-pixel composite matrices. Expansion of the final 4×45-pixel composite images, shown in Figure 10.6 (d-f), utilized repeating patterns at specific distances from the phantom edge, which was necessary to facilitate calculations of the tungsten phantom ERF for each array.

The computational estimates of irradiance were then divided by the respective free-field estimate to produce normalized contrast ratios for each pixel measurement. The 15 normalized measurements for all three arrays were then assembled into composite 4×45-pixel images of the edge response for each material, as shown in Figure 10.8. The remaining data analysis methods matched those described in the Experimental Data Analysis precisely, including consistent use of the same pixel regions to expand the simulated composite images to 20×45-pixels and identical 13×44-pixel ROI to analyze the edge response for all three materials. The simulated 20×45-pixel composite images and associated edge responses for both materials are provided in Figure 10.9.

Material Evaluation Results

Figure 10.10 and Table 10.4 provide comparisons of experimental and computational MTFs and SR values for the EJ-200, BiPVT, and EJ-256 arrays. Figure 10.10 also includes the cutoff frequency threshold, $f_{10\%}$, for all three plots, at which point spatial resolution is assigned for the CT system using the process described in Section II.

For all three arrays, the calculated experimental and computational SR values fall outside of the assigned uncertainties of the other, which means the simulated results are found *not* to agree with the respective experimental results. This disagreement between measured and estimated SR is believed largely due to a shortcoming in the simulation data analysis methodology, specifically the evaluation of edge response using values of total energy deposited from both recoil protons and photons (i.e. the +F6 tally in MCNP6). In other words, even if the energy values were partitioned at input, OpticStudio cannot simulate different rates of energy-dependent fluorescence and phosphorescence based on specific portions of energy deposited by photons and protons, respectively; it is not a radiation transport code. It only knows to treat energy deposition as originating from photon interactions and cannot simulate the energy dependent phosphorescence and quenching phenomena associated with proton recoil, a purpose for which it was not designed.

Furthermore, the energy-dependent light output response necessary to accomplish such a simulation remains unquantified at this time for BiPVT and, it is believed, for EJ-256. In other words, relative LY (in terms of response vs. MeV_{ee}) is still unknown for these two materials, which makes accurate simulation of their optical response to fast neutrons impossible. In the case of EJ-200, a limited number of studies address comparative light response to fast neutrons [82, 83, 84]; however, a review of the available literature did not provide a thorough accounting of optical light response up to 14.1 MeV. The most recent of these provided quantification of proton recoil response from 0.064-3.863 MeV [84], which is still below that needed to support the analysis here.

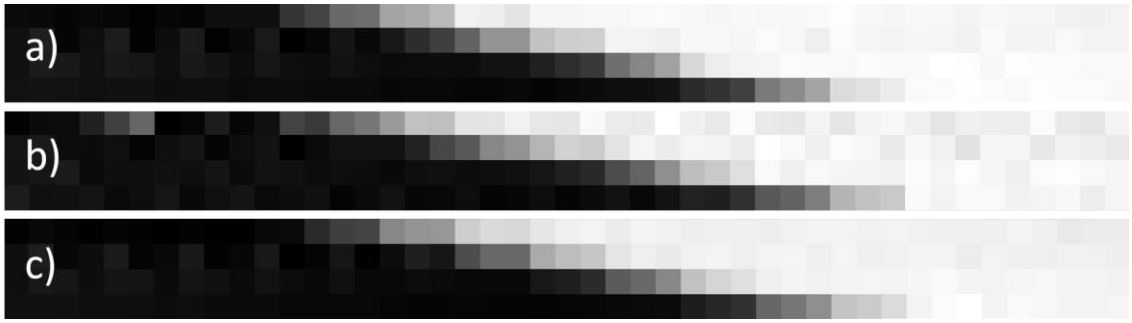


Figure 10.8 Simulated composite 4×45-pixel images of the 5.08 cm-thick tungsten phantom edge for a) EJ-200, b) BiPVT, and c) EJ-256. These images were assembled from 15 separate combined simulations of both MCNP6 and OpticStudio, each with varying degrees of array shielding, with the phantom edge offset at a 5˚ angle from the pixel alignment.

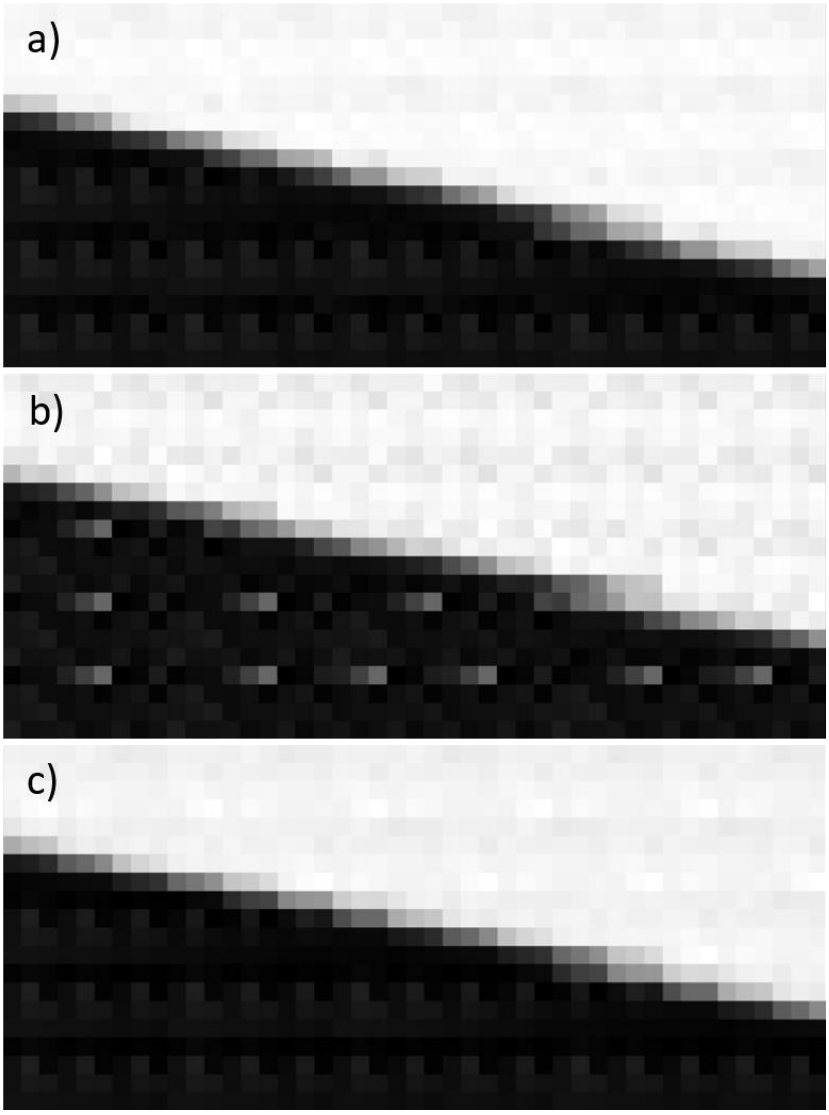


Figure 10.9 Images of the expanded a) EJ-200, b) BiPVT, and c) EJ-256 20×45-pixel composite images, computed from MCNP6 and OpticStudio. These are created from the original 4×45-pixel composite images, shown in Figure 10.8, using repeating patterns at specific distances from the phantom edge.

Table 10.4. Experimentally and computationally determined $f_{10\%}$ frequencies and spatial resolution (SR) values for all three material arrays, as well as the associated uncertainty.

Array Material	Experimental		Computational	
	$f_{10\%}$ (lp/mm)	SR ± 5% (mm)	$f_{10\%}$ (lp/mm)	SR ± 5% (mm)
EJ-200	0.165	3.03 ± 0.15	0.192	2.60 ± 0.13
BiPVT	0.141	3.55 ± 0.18	0.182	2.75 ± 0.14
EJ-256	0.158	3.16 ± 0.16	0.197	2.54 ± 0.13

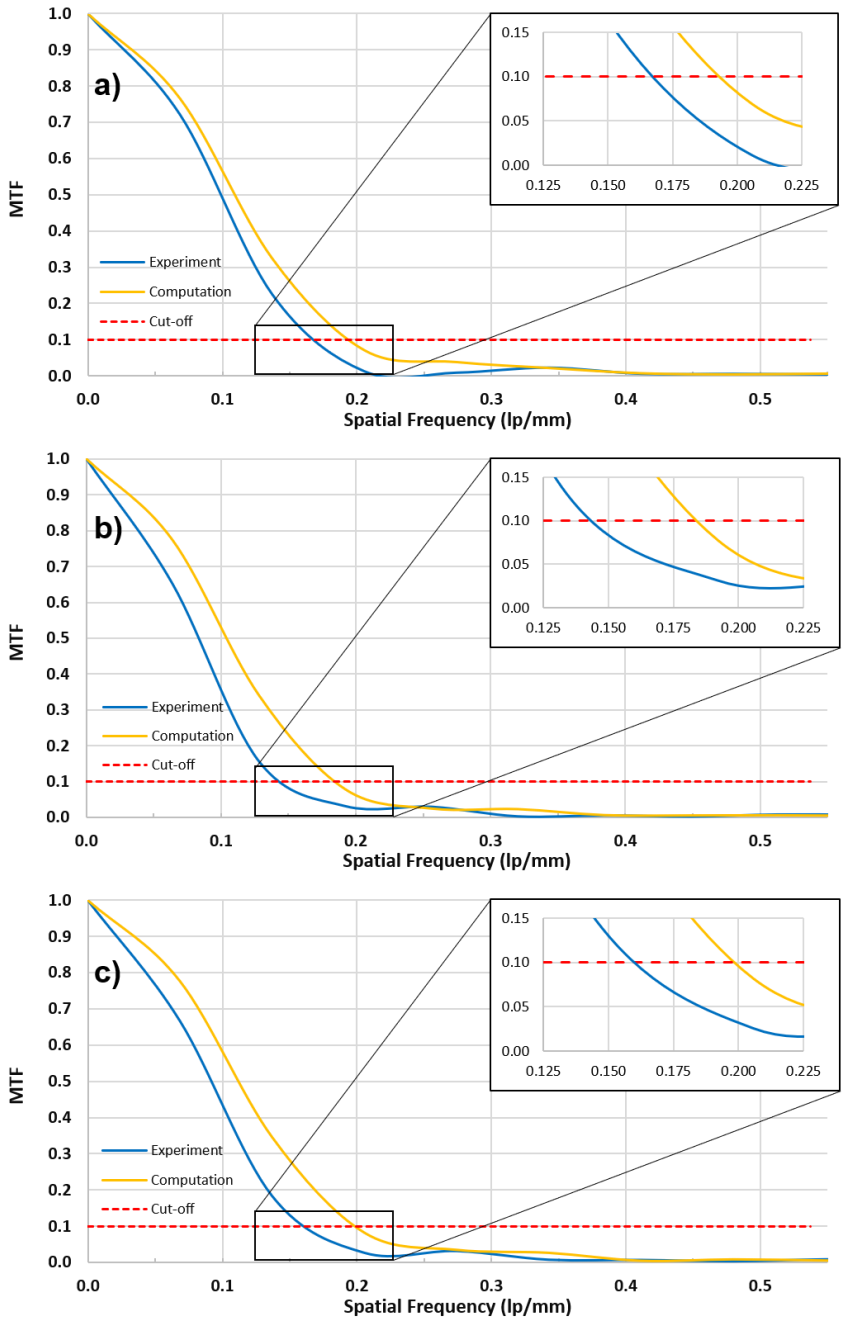


Figure 10.10 Plot of the experimental and computational MTFs for the a) EJ-200, b) BiPVT, and c) EJ-256 composite images. Expanded sections highlight where the MTFs cross the $f_{10\%}$ cutoff threshold for spatial resolution (SR) determination in ASTM standards for CT system performance evaluations [67].

Of note, a 2006 study of light response from proton recoils in BC-505 [66] may be used to predict relative light response from fast neutrons in EJ-200; however, these values are likely an overestimation for the plastic due to BC-505 being a liquid, and liquids are known to facilitate larger rates of TTA due to the fluid nature of their organic matrices [66]. Consequently, a more accurate estimate of simulated SR performance for these arrays cannot be made at this time.

Lastly, on the topic of SR, although the experimental and computational results fail to agree with the measured values and the ability to predict precise SR values for these materials is challenging, the simulated results do provide accurate estimates of relative performance. Specifically, the computational and experimental values of SR both return statistically equivalent performance for EJ-200 and EJ-256, while BiPVT is predicted and evaluated as providing poorer values of SR than the other two arrays.

The reasons for this performance disparity are believed to be due to both the larger pixel pitch of the BiPVT array (2.44 vs. 2.28 mm), as well as contributions from gammas emitted from the tungsten phantom, which are emitted following neutron inelastic scatter within the tungsten. The effect of the former was quantified via simulation, with BiPVT estimated to provide a SR value of 2.55 ± 0.13 if its pixel pitch was reduced to 2.28 mm. This implies that an equivalently manufactured BiPVT array may, according to simulation, provide statistically equivalent SR performance to both EJ-200 and EJ-256 in fast neutron environments. Furthermore, MTF evaluation of the measured BiPVT 20x45-pixel composite image using the 2.28 mm pixel spacing of EJ-200 and EJ-256 return an adjusted experimental SR value of 3.31 ± 0.17 for the array, which is markedly closer to the values reported for both EJ-200 and EJ-256. Therefore, it is assessed that a BiPVT array with an equivalent pixel pitch to that of EJ-200 and EJ-256 may return statistically equivalent values of SR in fast neutron environments, as predicted by the MCNP6 and OpticStudio simulations.

As for the influence of gamma rays, this effect is more difficult to quantify; however, due to its higher Z_{eff}, BiPVT provides significantly higher intrinsic efficiencies for photoelectric absorption and Compton scatter than the two other materials evaluated. Furthermore, contributions from internal scatter radiation are recognized contributors to geometric unsharpness within DDAs, which degrades SR performance [19]. Therefore, it is reasonable to suspect pixel crosstalk from gamma ray interactions within the pixels may likely contribute to the poorer SR values of BiPVT. In fact, it has been shown previously, and addressed earlier herein, that incoherent scatter within the BiPVT pixels can substantially degrade array SR performance when compared to both EJ-200 and EJ-256 [15].

Since SR is calculated from the normalized edge response, this metric fails to consider each material's relative light yield and quantum efficiency, which are

factors that significantly affect DDA response. As discussed in Section II, measurements of SR and SNR facilitate comparative evaluations of dSNRn, which is necessary to provide a more complete comparison of array performance. Calculations of dSNRn utilize Eq. 6 and the measured values provided in Tables 10.2 and 10.4. The calculations of dSNR are provided in Table 10.5 for each evaluated array. These values of dSNRn demonstrate that, for 14.1 MeV neutron fields, EJ-200 provides a statistically superior value of dSNRn over BiPVT and EJ-256, while BiPVT provides statistically improved performance over EJ-256.

Discussion

The measured dSNRn values listed in Table 10.5 quantify the degree to which the EJ-200 array outperforms the higher Z-loaded BiPVT array. However, Table 10.5 also demonstrates the BiPVT array outperforms the EJ-256 array, despite its higher Z-loading, larger pixel pitch, and poorer geometric uniformity. As reflected in the measured values of SR and SNR, this result is mostly due to the impressive light response of the BiPVT array, despite its documented light collection challenges. The superior brightness of the BiPVT over the EJ-256 is attributed to the incorporation of the iridium-complex in the organic matrix, which provides radiative pathways for electrons excited to triplet states. This produces an ~3.9× light yield increase over EJ-256 per MeVee; however, it is worth mentioning the use of iridium-complexes in BiPVT, while significantly increasing light output, also introduces additional cost compared with plastics where this constituent is absent. Lastly, the green photoluminescence emission spectrum from BiPVT pairs well with a-Si TFT of the Varex panel, which provides an improved quantum efficiency over the EJ-200 and EJ-256 blue emissions.

As such, it is unknown at this time whether a more ideally manufactured BiPVT might outperform a similarly sized and manufactured array made of EJ-200; however, it is believed possible.

Conclusion

In conclusion, when exposed to 14.1 MeV neutrons, the evaluated BiPVT array outperforms a similarly sized EJ-256 array in terms of dSNRn values, while one comprised of EJ-200 outperforms both alternatives. It is assessed that a more ideally manufactured BiPVT array would undoubtable provide improved performance; however, it is unknown at this time whether its performance would match that of EJ-200 in fast neutron environments. Regardless, the demonstrated advantage of BiPVT over that of EJ-256 in 14.1 MeV environments suggests it is a far better candidate for DPI systems, especially considering its predicted performance across a variety of x-ray energies [80]. Due to these advantages, BiPVT may provide better overall performance for DPI purposes than EJ-200, despite the comparative performance documented here.

Table 10.5. Comparative SNR, SR, and dSNRn values for all three arrays calculated from measured values of $f_{10\%}$ from the MTF and using Eq. 6.

	SNR	SR	dSNRn
EJ-200	2.26	3.03 ± 0.15	0.0935 ± 0.005
BiPVT	1.58	3.55 ± 0.18	0.0558 ± 0.003
EJ-256	1.09	3.16 ± 0.16	0.0432 ± 0.002

These quantified improvements in BiPVT detector response translate directly into shorter measurement times across both particle types and, therefore, less dose per measurement, which is optimal for portable radiography scenarios. Consequently, these results support the consideration of BiPVT over other plastic alternatives, such as EJ-200 and EJ-256, for DPI radiography applications supporting national nuclear safety, security, and safeguards.

Acknowledgement
The authors would like to thank the U.S. Army and the Department of Energy, including award DE-NA0003180, for supporting this research. The authors also thank Dr. Dan Shedlock and Varex Imaging for the use of a Varex Industrial PaxScan® 1515DXT-I flat panel detector and Dr. Keith Vaigneur at Agile Technologies for his assistance and supervision during the fabrication of the evaluated arrays.

CHAPTER ELEVEN -

CHARACTERIZATION OF A NOVEL PLASTIC ARRAY IN BOTH X-RAY AND FAST NEUTRON ENVIRONMENTS

Abstract

This chapter describes the measured performance of an array made of Ir-Bi-Plastic, which is a novel material produced by Dr. Nerine Cherepy's team at LLNL. The array arrived at UTK fully manufactured and wrapped with an 8×8-pixel configuration and an average pixel pitch of 5.25 mm. Consequently, the previously utilized methodologies for performance characterization in both the x-ray and fast neutron environments were applied to this array. This chapter details those investigations and results, as well as the suspected reasons for the relative performance of the Ir-Bi-Plastic in each radiation field. Modeling and simulation data were not estimated for the performance of this array due to time constraints, and this chapter is intended to outline a future journal submission to publish the results of these investigations.

Theory

Although computed tomography (CT) is not applied in this research, composite images (i.e. larger images constructed from multiple smaller images) are required for performance comparisons of the considered array due to its relatively small size and pixel count, which are a direct result of the limited quantity of novel material available for characterization. Consequently, the theory and procedures applied herein for x-ray and neutron DDA performance comparisons are based on published American Society for Testing and Materials (ASTM) standards for the measurement of CT system performance. The standard practice for characterizing CT system performance begins with measurements of a composite edge response function (ERF) [67].

Modulation Transfer Function and Spatial Resolution

Edge response is measured from composite image data using a phantom of defined material and thickness, which produces differences in pixel modulation across the phantom's edge when it is imaged. In CT, this is provided by a circular phantom enabling a two-dimensional analysis of edge response; however, this research only examines a one-dimensional (1D) edge, so the phantom is offset from the pixel rows by a consistent angle selected between 2-5°, as per ASTM standards [53, 48]. Ideally, this angular offset produces numerous array pixels measuring varying degrees of phantom attenuation, depending on the extent by which the pixels are shielded by the phantom edge. A region of interest (ROI) is then established to measure as much of the edge as possible, with suggested ROI minimums of 11-pixels across the edge and 256 pixels in total [67]. ROI edge data are then averaged to calculate the contrast response across the edge. This

average edge response is normalized, and interpolation is used to determine the edge response function (ERF) with suggested bin sizes of 10% the pixel size used in the ROI [67].

A piecewise least-squared cubic fit of the ERF is then performed using the same number of values. From this series of third order polynomials, the analytical derivative is calculated to provide the line spread function (LSF), which is also normalized and centered on the ERF [67] [68]. This is represented mathematically as,

$$LSF = \frac{d(ERF)}{dx}. \quad (63)$$

An example of the LSF, superimposed on the ERF, is also shown in Figure 11.1. Next, the modulation transfer function (MTF) is calculated from the 1D Fourier Transform (FT) of the LSF using the equation,

$$MTF = FT\left(\frac{d(ERF)}{dx}\right) = FT(LSF). \quad (64)$$

The 1D FT is used to shift the data from units of object space to units of spatial frequency, or cycles per distance. Therefore, the MTF describes the change in modulation within an image signal as a function of modulation spatial frequency for the specific DDA. MTF magnitudes are then normalized to unity at frequency zero, and a cut-off at 10% of the MTF ($f_{10\%}$) represents the limit of spatial resolution (SR) for the DDA, with an accuracy of ± 5% [67]. SR is calculated as one half the inverse of the $f_{10\%}$, and it represents the limit of geometrical detail that can be resolved by the DDA [67] [68] [71]. An example MTF, including the cut-off threshold for minimum SR, is provided in Figure 11.2.

Detector Signal-to-Noise Ratio Normalized

However, since SR is calculated from the normalized MTF, information regarding the relative intensity of different arrays is absent from any comparison based solely on this metric. Therefore, a more useful method for evaluating relative DDA performance relies on both the SR and the measured signal-to-noise ratio (SNR) of the DDA. The SNR is the quotient of mean value of the intensity (signal) and standard deviation (σ) of that intensity (noise) [53]; however, in the case of radiography images, a more accurate equation is,

$$SNR = \frac{Mean\ intensity\ (difference\ image)}{\sigma(difference\ image)}, \quad (65)$$

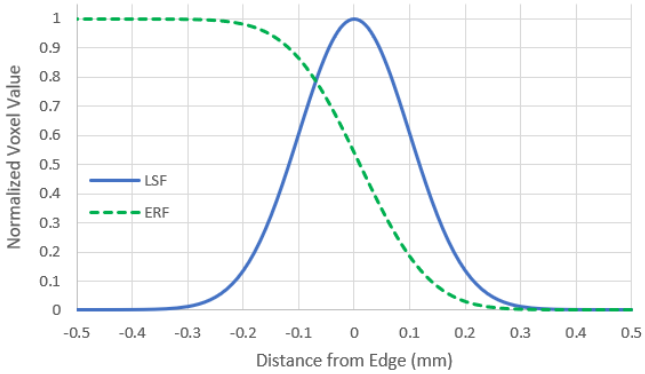


Figure 11.1. Example plots of normalized edge response function (ERF) and line spread function (LSF).

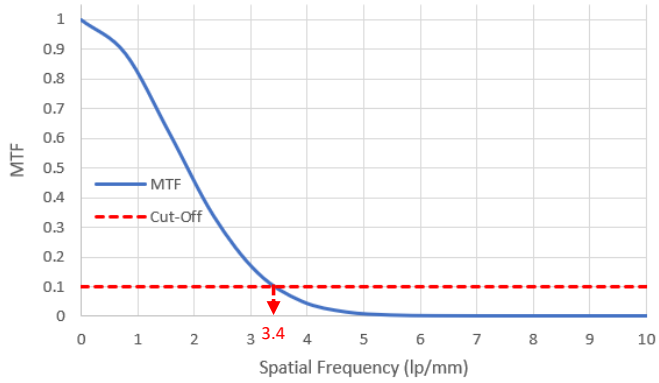


Figure 11.2 Example modulation transfer function (MTF). Values of spatial resolution (SR) are measured for the DDA at a 10% cut-off of the MTF ($f_{10\%}$). In this example, the MTF reaches $f_{10\%}$ at a spatial frequency of 3.4 lp/mm, which means the hypothetical DDA provides a SR of 0.147 mm.

where the difference image is achieved by averaging the pixel intensities in the free-field (i.e. in the case of unshielded irradiation) and subtracting the same regions of averaged intensities from dark images (i.e. those measured without irradiation) [53]. This process produces background-subtracted images and is analogous to correcting for background contributions in traditional radiation measurements. Together, these terms enable a calculation of the detector SNR-normalized (dSNRn) in the free-field, using

$$dSNRn = \frac{SNR \times \sqrt{2} \times 88.6\ \mu m}{SR}. \qquad (66)$$

The $\sqrt{2}$ term is used to correct the SNR, since the difference of two images is used for noise calculations, and 88.6 µm is consistent with phosphor film pixel widths, so its inclusion in dSNRn calculations standardizes DDA performance comparisons across multiple radiographic systems [53]. The dSNRn is a useful indicator of DDA performance because it quantifies the exposure necessary to reach a full SNR. For a 16-bit image, this means ~50k contrast tones measured in the detector area, which avoids image overexposure. In the case of x-ray radiography, these values are expressed in plots of dSNRn vs. the square root of the exposure dose (mGy), with the slope of each line defining DDA efficiency. However, if the exposure, beam filtering, and phantom or image quality indicator (IQI) are all equivalent for separate DDAs, then the dose terms cancel and only the dSNRn values are left to compare, with higher dSNRn values indicating superior DDA performance at that exposure.

Traditional x-ray radiography DDA, such as thin film transistor (TFT) paired with gadolinium oxysulfide (Gd_2O_2S) or cesium iodide (CsI), typically yield SNR >200 and SR <200 µm. These systems provide dSNRn values well over 100 or even 1000 at certain exposures; however, such systems provide no capability to support fast neutron imaging. Therefore, x-ray dSNRn values produced by systems optimized for DPI are typically much lower and do not appear competitive when compared against traditional DDAs optimized solely for x-ray radiography.

Description of the Evaluated Arrays

The novel material evaluated is identified as Ir-Bi-Plastic by LLNL, and its atomic fractions are listed as 48.19% hydrogen, 43.45% carbon, 6.59% oxygen, 0.8% nitrogen, 0.8% bismuth, and 0.16% iridium. The produces a material with 21% bismuth-loading by weight, which dramatically enhances its intrinsic efficiency for photoelectric absorption over more traditional low-Z plastics, such as EJ-200. Additionally, the inclusion of FIracac, an iridium-complex fluor, facilitates radiative triplet deexcitation through spin-orbit coupling within the organic matrix. These combined effects produce a light yield of ~2.4×10^4 photons per MeV (with peak emission in the green at ~520 nm), which is ~2.4× the brightness of EJ-200 [36],

thereby partially mitigating the depressed light yields typical of other high-Z sensitized plastics.

This is quite useful in x-ray environments; however, the iridium-complex is predicted to also benefit light yields measured in fast neutron environments. In these environments the dominant source of photoluminescence in plastics is typically proton recoil events, and ionization quenching is known to degrade scintillator brightness. This is especially true at lower proton kinetic energies when a greater fraction of proton energy is deposited per unit distance traveled. The result is a higher density of triplet molecular excited states compared to singlet. In traditional plastics, molecules excited to the triplet state are unable to radiatively deexcite due to spin-forbidden transitions, and, although triplet-triplet annihilation (TTA) can be a productive process in these conditions, it results in depressed light yields. Consequently, the presence of an iridium-complex provides additional pathways for triplet states to radiatively deexcite besides just TTA, which is expected to increase scintillator light yield within fast neutron environments.

Lastly, the green photoluminescence emission spectrum from Ir-Bi-Plastic pairs well with commercially available radiation-hardened amorphous silicon (a-Si) photodetectors, with expected average improvements in quantum efficiency (QE) of ~2× that of scintillators emitting in the blue [45].

The evaluated array measures 42×42×20 mm with individual pixel faces of 5×5 mm, which provides an 8×8-pixel array with pixel pitches of 5.25 mm. Furthermore, the cured plastic has a density of 1.15 g/cm^3, and WhiteOptics® White 98 Film, a diffuse reflector, is used to optically isolate each pixel [85]. Of note, however, the reflector used internal to the array is only present across 19 of its 20 mm thickness, leaving the final 1 mm of each array pixel closest to the TFT unsegmented and without optical isolation. This design is expected to allow optical crosstalk within the final 1 mm of the array, which may degrade SR; however, it is unknown whether these effects are quantified relative to a similar array with complete optical isolation and physical segmentation. Lastly, the exterior of the Ir-Bi-Plastic array was wrapped on five sides with Teflon tape, another diffuse reflector.

For the purposes of fast neutron characterization, a 5×5 mm pixel face is advantageous for improved energy localization due to the expected pathlengths of scattered protons. If pixel face dimensions are too small, recoil charged particles may routinely scatter beyond pixel boundaries, thereby depositing significant portions of their energy in adjacent pixels or outside the array. For example, protons scattered in EJ-200 (ρ = 1.023 g/cm^3) at 30° relative to the incident path of 14.1 MeV neutrons will recoil at energies of ~10.5 MeV, which means they are expected to travel ~1.3 mm from the interaction site and ~0.65 mm orthogonal to the original neutron path.

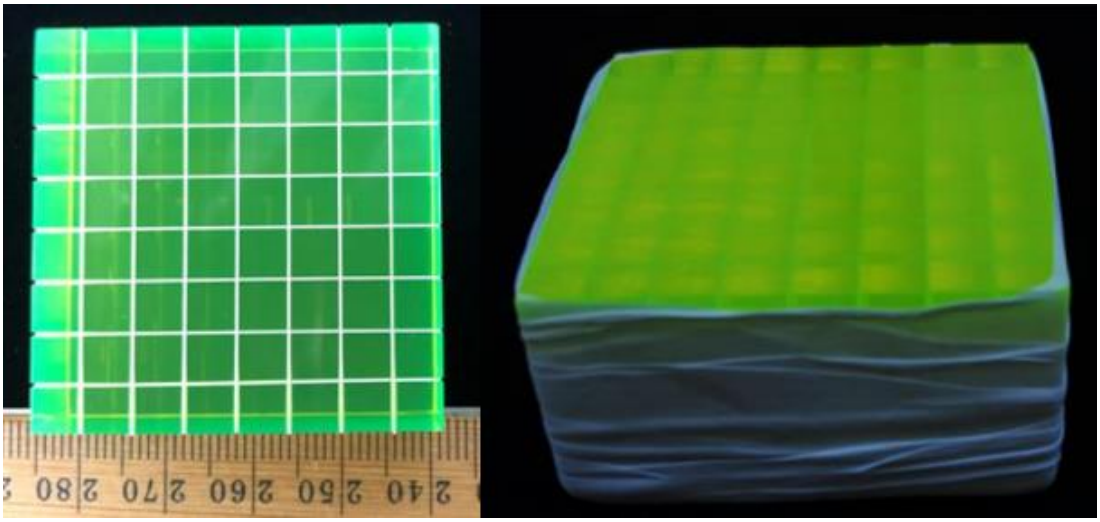


Figure 11.3 Images of the 8×8-pixel evaluated Ir-Bi-Plastic array. The segmented side is shown on the left prior to external Teflon tape wrapping. The image on the right shows the uncut face after external wrapping, which was placed in contact with the a-Si TFT array.

Therefore, protons scattered at 30° from anywhere within a pixel with a cross section <1.69 mm^2 (1.3×1.3 mm) will likely exit the pixel. Since TFT photodetector panels operate in integration mode, this result would reduce position and image resolution. Based on this understanding, the Ir-Bi-Plastic pixel dimensions of 5×5 mm (a 25 mm^2 pixel cross section) are expected to increase proton recoil energy localization over an array with a smaller pixel pitch. Of course, this benefit comes at the cost of reduced SR due to its larger pixel pitch. It is unknown whether a study designed to optimize pixel pitch versus proton recoil in a fast neutron environment has been conducted for this material.

Dark Noise Subtraction

Use of a-Si TFT panels to measure radiographic response inherently includes contributions from dark noise in all recorded images. Any meaningful impact from this noise is typically eliminated via subtraction of a dark measurement and, in the case of x-ray images, remaining contributions are minor compared to the measured response. However, in the case of neutron transmission imaging, the signal may often fail to surmount the accumulating dark noise, so noise discrimination and subtraction becomes less straightforward. Additionally, digital panel noise was found to aggregate non-linearly over time in the Varex 1515DXT-I panel. In fact, the total noise appears to plateau after ~180 minutes of continuous operation in a dark field, which represents roughly the time required for the panel to reach a stable operating temperature. Therefore, due to the strong dependence of dark noise on temperature, neutron response measurements conducted after 180 mins of panel operation may produce more stable and easily subtracted image noise.

Experiment Methodology

Detector Set-up

The Ir-Bi-Plastic array was paired with a commercial radiographic Varex PaxScan 1515DXT-I Flat Panel Detector for all measurements [56]. This first required the removal of the original proprietary gadolinium oxysulfide (Gd_2O_2S) conversion layer, followed by the attachment of custom aluminum components to all four outer sides of the Varex panel, thereby extending the panel's light-tight enclosure by 25.4 mm orthogonal to the TFT. Within this expanded volume, the Ir-Bi-Plastic array was pressure mounted against the a-Si photodetector using layers of custom-cut foam to hold the arrays in place. The a-Si TFT provided pixel pitches of 127 µm, so every 5×5 mm pixel response was averaged from the measured response of ~1,520 photodetector pixels. Lastly, the enclosure was sealed using the Varex panel's original 2.5 mm-thick carbon fiber plate.

X-Ray Experiment Methodology

With the arrays pressure mounted and enclosed within the modified Varex radiographic panel, measurements within an x-ray field were conducted, and each measurement consisted of 40 separate images recorded at two frames per second

(fps). The x-rays were produced by a Comet MXR-451/26 radiation generating device (RGD) with a tungsten target operated at 150, 200, 270, 300, and 370 kVp, at a current of 0.3 mA, and a focal spot size of 5.5 mm. These energies were selected for SNR analysis because 150, 270, and 370 kVp correspond to commercially available x-ray RGDs that support portable x-ray interrogation. For all measurements, the source was centered on the panel at a source to detector distance (SDD) of 1,010 mm, in accordance with ASTM standards [53]. Free-field (i.e. unshielded) measurements were also recorded in this way, as well as dark measurements, which are necessary for x-ray image offset correction.

Shielded measurements utilizing a phantom edge were then recorded using the same process but only at 370 kVp. This energy was selected because it represents the practical upper energy limit for portable x-ray radiography. Additionally, due to the high-Z loading of the Ir-Bi-Plastic, contributions to pixel crosstalk from incoherent scatter are expected to be highest at 370 kVp compared to the lower energies. Therefore, since internal scatter radiation is known to degrade DDA SR performance [53], 370 kVp was selected to provide a conservative estimate for array SR performance.

A 6.35 mm-thick stainless-steel plate provided the measured phantom edge, and a total of 5 shielded measurements were then recorded. The phantom edge was repositioned between measurements by 3.6 mm to provide an incrementally larger fraction of array shielding with each subsequent measurement. Consequently, the shielded measurements produced a range of array shielding from 0-100%, all at 5° off-axis. These measurements were background-subtracted and then divided by free-field values to offset-correct the data, a standard practice in imagery analysis to normalize variable pixel performance. Using these measured contrast ratios, an 8×40-pixel composite image of the steel edge response was the assembled. Lastly, the composite array image was then expanded from 8×40-pixels to 24×40-pixels by replicating contrast values at commensurate distances across the measured edge, thereby producing a larger composite image. This could only be accomplished by using a 1D straight-edge phantom, which supported the additional evaluations detailed in the Theory Section.

Neutron Experiment Methodology

With the array pressure mounted and enclosed within the modified Varex radiographic panel, measurements within a fast neutron field were conducted, with each measurement consisting of the average of 30 separate images recorded at 0.2 frames per second (fps). The neutrons were produced by an ING-27 D-T neutron generator (S/N 5593661), which was positioned ~100 cm above the floor and operated at ~80% of its maximum high voltage. This produced 14.1 MeV neutrons at a rate of ~4.4×10^{7} neutrons per second with uncertainties estimated

at ± 5%. Also, to eliminate possible unwanted contributions from x-rays, a 0.635 cm-thick plate of lead measuring ~10 cm on each side, was placed just outside of the generator housing, between the 5 mm-wide tritium target and the radiographic panel. Although the x-ray spectrum emitted by the ING-27 is yet to be precisely measured and quantified, current research suggests it does not exceed 140 kVp. Prior x-ray image evaluations using a 6.35 mm lead shield eliminated ~99.5% of the measured signal from the Ir-Bi-Plastic array, therefore contributions from x-rays are believed to be minor. Since the small thickness of lead produces virtually no attenuation of the emitted 14.1 MeV neutrons, it was selected to ensure the elimination of potential x-ray contributions.

For every measurement, the neutron source was centered on the Ir-Bi-Plastic array at a source to detector distance (SDD) of 12.4 cm to maximize array solid angle and minimize necessary exposure times. Shielded array measurements utilized a 5.08 cm-thick tungsten block placed against the panel's outer carbon fiber plate, ~1.75 cm from the array inside. The phantom provided a uniform shield thickness, and the edge was consistently positioned at 5° off-axis to meet ASTM standards [48, 53]. A series of 5 shielded measurements were recorded, with the phantom edge repositioned between each measurement to provide an incrementally larger fraction of array shielding than the previous measurement. This process required the use of a Velmex® motorized slide, which enabled uniform movement of the phantom in 3.6 mm increments. This distance was chosen to produce a continuous edge response across multiple images, which provided a range of pixel shielding measurements between 0-100%, all at 5° off-axis.

In terms of dark noise subtraction, 180 mins was not allowable prior to each series of measurements, so the panel was simply operated for ~30 mins before measurements were recorded. This allowed for both a reduction and stabilization in the rate of dark noise aggregation prior to experimentation. To accurately quantify accumulating dark noise, a consistent 333×1152-pixel region was summed from each averaged 30-frame measurement. This region represented ~1/3 of the panel surface area and was devoid of any scintillator material, so it only recorded accumulating panel noise. Measurements were conducted in sets of five (M_1-M_5) and these were each bracketed between two dark measurements without neutron emission present. The summed values of dark noise accumulation from the 333×1152-pixel regions represented noise in each 150-sec measurements (M_{1r}-M_{5r}) and in the dark measurements (D_{1r} and D_{2r}).

Using these values, contributions from panel noise were estimated on a per TFT pixel basis for each measurement. This was accomplished by calculating the fractional contributions (F_i and 1-F_i) of noise from the two dark images to each individual measurement by summing those contributions into a single estimate of background (B_i) and subtracting it from each measured image (M_i). This process

produced offset corrected (M_{iOC}) difference images. The five offset corrected images were then averaged to produce a final measurement image (M_f) for the free field and for all 15 shielded measurements. Therefore, each measurement was the average of 150 separate frames, which were offset corrected in groups of 30 frames. This process enabled the isolation of measured signal from background, which would otherwise have been obscured. Algebraically, this series of calculations is performed using,

$$F_i = \left(\frac{D_{2r} - M_{ir}}{D_{2r} - D_{1r}}\right), \quad (67)$$

$$B_i = F_i * D_1 + (1 - F_i) * D_2, \quad (68)$$

$$M_{iOC} = M_i - B_i, \quad (69)$$

$$M_f = \frac{\sum M_{iOC}}{5}. \quad (70)$$

This analysis was conducted separately across all measurement sets. Of course, due to the large amount of noise subtracted, this process resulted in some negative TFT pixel values and larger variances, which necessitated longer exposures and a shorter SDD to minimize those effects due to the small pixel volumes evaluated. The shielded measurements were then normalized by dividing each by the free-field (i.e. unshielded) measurement, a common process in image analysis [60]. to normalize the images for the reasons stated above. Using these measured contrast ratios, an 8×40-pixel composite image of the tungsten edge response was assembled from the Ir-Bi-Plastic array measurements. Lastly, the composite array image was then expanded from 8×40-pixels to 24×40-pixels by replicating contrast values at commensurate distances across the measured edge, following the same process used in the x-ray methodology.

Analysis and Results

X-Ray Analysis and Image Construction

All images recorded using the Varex radiographic panel were analyzed using ImageJ Image Processing and Analysis in Java (v1.52a) software. Every array measurement, whether dark, free-field, or shielded, was calculated from the average of 40 separate 16-bit images, each recorded by the Varex panel at two frames per second. All free-field and shielded measurements were then background-corrected by subtracting the dark (i.e. background) measurement, for reasons previously addressed [53].

Within ImageJ, ROIs were established over the individual 64 pixels, and pixel intensities and standard deviations were then averaged from these ROI for the

free-field and fully shielded measurements. The average free-field pixel intensities for the Ir-Bi-Plastic at each x-ray energy are provided in Table 11.1.

Shielded pixel measurements utilized the same ROI used in the free-field analysis, and the pixel intensity values for the five shielded measurements were also exported for analysis. These were divided by the free-field pixel intensity measurements to produce ratios for each array pixel, which was necessary for determining normalized edge response. The five normalized array measurements for the Ir-Bi-Plastic were then assembled to form the composite 8×40-pixel images of the entire phantom edge, as shown in Figure 11.4. In this image, black corresponds to low signal due to the presence of the steel phantom. As detailed above, the composite x-ray image was then expanded from 8×40-pixels to 24×40-pixels. This step was necessary due to the small size of the array, and the expanded image of the steel edge is shown in Figure 11.5.

D-T Neutron Analysis and Image Construction

Neutron response images were recorded using the Varex radiographic panel and analyzed using MATLAB© (R2018b) and ImageJ Image Processing and Analysis in Java (v1.52a) software. Array measurements, whether free-field or shielded, were calculated from the average of 150 separate 16-bit images, each recorded by the Varex panel at one frame per five seconds (0.2 fps). Dark measurements were recorded at the same rate but averaged from 30 separate images each. The free-field and shielded measurements were then background-subtracted using the specific calculated backgrounds (i.e. B_i), which were obtained using MATLAB software and the methodology explained in Section II. Lastly, the shielded images were all off-set corrected by dividing each by the free-field image, just as in the case of the x-ray measurements.

Then, within ImageJ, ROIs were established over the individual pixels using the offset-corrected images, and pixel intensities and standard deviations were averaged from these ROI for the free-field and fully shielded measurements. The average free-field pixel intensities were scaled by subtracting average background from a nearby void ROI without scintillator material present, and total standard deviation was determined from the square root of the sum of the squares of standard deviation from both Ir-Bi-Plastic pixel signal and void ROI. These average measured values from the 5×5 mm pixels are provided in Table 11.2.

Shielded pixel measurements utilized the same ROIs used in the free-field neutron analysis, as well as those used for the x-ray analysis. As in the case of the x-ray analysis, pixel intensity values for each of the five shielded measurements were exported for analysis and divided by the neutron free-field pixel measurements to produce ratios for each array pixel. These normalized values of pixel intensity were then assembled to form composite 8×40-pixel image of the entire phantom edge, as shown in Figure 11.6.

Table 11.1. Experimentally measured average pixel intensities, standard deviations, and calculated SNR for the Ir-Bi-Plastic when exposed to the considered x-ray bremsstrahlung spectra.

X-ray Energy (kVp)	Mean	σ	SNR
150	9,618.5	218.4	44.0
200	16,445.0	376.1	43.7
270	27,163.2	627.7	43.3
300	31,747.3	735.9	43.1
370	43,307.2	1008.9	42.9

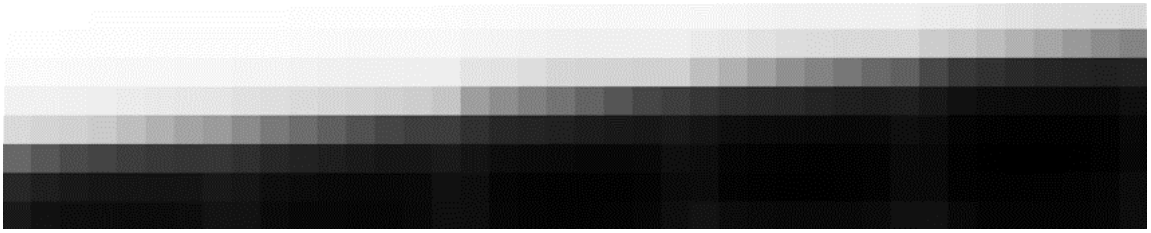


Figure 11.4 Measured composite 8×40-pixel images of a 0.635 cm-thick steel phantom edge using the 8×8-pixel Ir-Bi-Plastic array in a 370 kVp x-ray field. This image was constructed from five separate measurements at varying degrees of array shielding, with the phantom edge offset from the pixel alignment at a 5˚ angle.

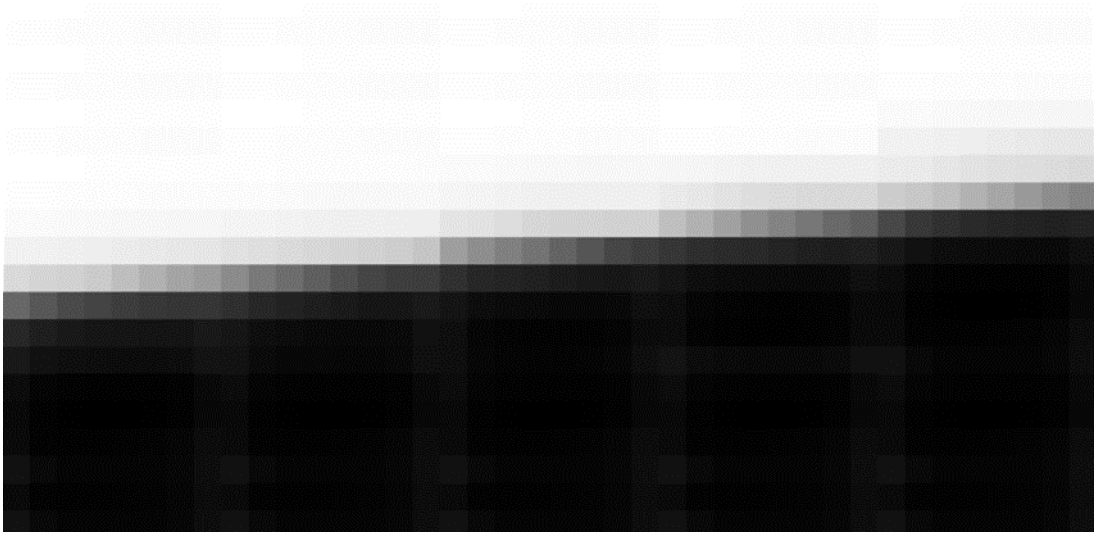


Figure 11.5 Image of the expanded 24×40-pixel composite image of the 0.635 cm-thick steel phantom edge using the 8×8-pixel Ir-Bi-Plastic array in a 370 kVp x-ray field. Expansion of the original 8×40-pixel composite image, shown in Figure 11.4, utilized repeating patterns at specific distances from the phantom edge, which was necessary to facilitate calculations of the steel phantom ERF.

Table 11.2. Experimentally measured average pixel intensities, standard deviations, and calculated SNR for the Ir-Bi-Plastic when exposed to 14.1 MeV neutrons at a SDD of 12.5 cm.

Neutron Energy	Mean	σ	SNR
14.1 MeV	44.57	2.73	16.35

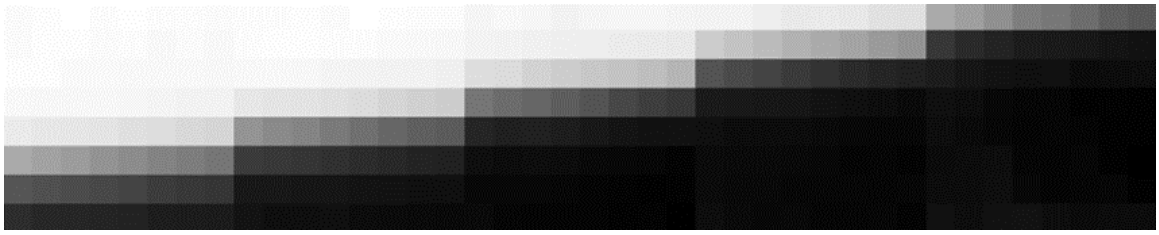


Figure 11.6 Measured composite 8×40-pixel images of a 5.08 cm-thick tungsten phantom edge using the 8×8-pixel Ir-Bi-Plastic array in a 14.1 MeV neutron field. This image was constructed from five separate measurements at varying degrees of array shielding, with the phantom edge offset from the pixel alignment at a 5˚ angle.

This composite array image was then expanded to 24×40-pixels, mimicking the process of replicating intensity patterns at commensurate distances from the edge used in the x-ray analysis. This resulted in an expanded image of the tungsten edge to support edge response analysis, specifically determinations of MTF and SR from the cut-off frequency ($f_{10\%}$) for the neutron environment. The expanded image is shown in Figure 11.7.

The 24×40-pixel composite images facilitated edge response evaluations using a 13×40-pixel ROI (520 pixels, total), which was centered across the edge to measure the normalized edge response. Through the application of the procedures outlined in Section II, the MTFs for the Ir-Bi-Plastic array were calculated from the experimentally measured composite x-ray and neutron images. Likewise, at the spatial frequency cut-off of $f_{10\%}$, a SR values for the array were calculated for each environment. The experimentally determined MTFs for the array in the 370 kVp x-ray and 14.1 MeV environments are provided in the Results section below, as well as the measured SR.

Ir-Bi-Plastic Performance Results

Figure 11.8 provides a comparison of the experimentally determined MTFs and SR values for the Ir-Bi-Plastic array in the 370 kVp x-ray and 14.1 MeV neutron environment. Figure 11.8 also includes the cutoff frequency threshold, $f_{10\%}$, at which point spatial resolution is assigned for the CT system using the process described in Section II. These calculated values of SR are provided in Table 11.3. The measured values of SR demonstrate superior performance of the Ir-Bi-Plastic array in the evaluated x-ray environment, which is likely attributable (at least partially) to differences in the x-ray and neutron experimental design. Specifically, the neutron experiment involved an SDD $1/8^{th}$ that of the x-ray experiment, as well as a phantom 8× as thick. These factors can combine to reduce image sharpness

However, since SR is calculated from the normalized edge response, this metric fails to consider the material's light output within each environment, which significantly affects DDA response. As discussed in Section II, measurements of SR and SNR facilitate comparative evaluations of dSNRn, which is necessary to provide a more complete comparison of array performance. Calculations of dSNRn utilize Eq. 6 and the measured values provided in Tables 11.1-11.3. The calculations of dSNR are provided in Table 11.4 for the two environments considered.

The reported values of dSNRn demonstrate the Ir-Bi-Plastic provides statistically improved performance in 370 kVp x-ray fields when compared to 14.1 MeV neutron fields. As discussed earlier, these calculated values of dSNRn for the Ir-Bi-Plastic array are predicted to be conservative since values of SR will likely decrease at lower x-ray energies due to decreasing ratio of incoherent scatter to photoelectric absorption.

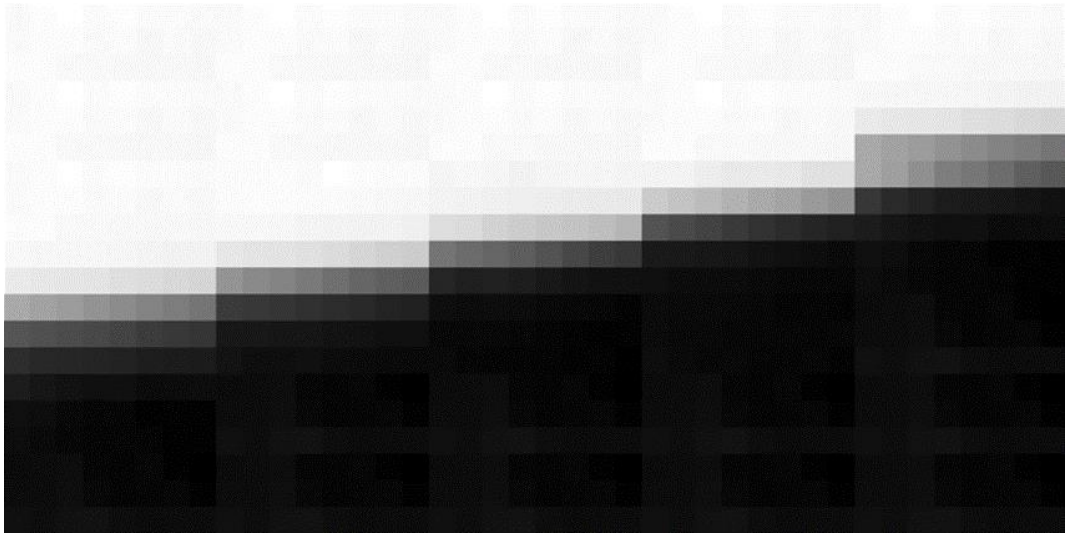


Figure 11.7 Image of the expanded 24×40-pixel composite image of the 5.08 cm-thick tungsten phantom edge using the 8×8-pixel Ir-Bi-Plastic array in a 14.1 MeV neutron field. Expansion of the original 8×40-pixel composite image, shown in Figure 11.6, utilized repeating patterns at specific distances from the phantom edge, which was necessary to facilitate calculations of the tungsten phantom ERF.

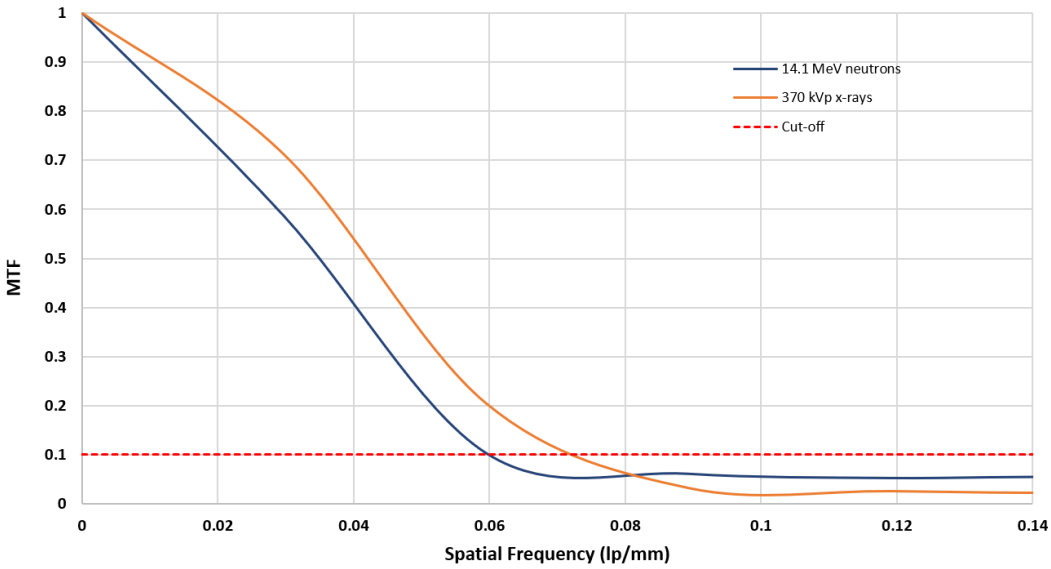


Figure 11.8 Plot of the experimental MTFs measured for 14.1 MeV neutron environment using a 5.08 cm-thick tungsten block and the 370 kVp x-ray field using a 0.635 cm-thick stell plate. Included with these MTFs is the $f_{10\%}$ cutoff frequency used for determinations of spatial resolution (SR) according to ASTM standards for CT system performance evaluations [67].

Table 11.3. Experimentally measured values of SR for the Ir-Bi-Plastic in both the 14.1 MeV neutron and 370 kVp x-ray environments.

Radiation Field	$f_{10\%}$ (lp/mm)	SR ± 5% (mm)
370 kVp x-ray	0.071	7.08 ± 0.35
14.1 MeV neutron	0.060	8.36 ± 0.42

Table 11.4. Experimentally measured values of dSNRn for the Ir-Bi-Plastic for both 14.1 MeV neutron and 370 kVp x-ray environments.

Radiation Field	SNR	SR	dSNRn
370 kVp x-ray	42.91	7.08 ± 0.35	0.759 ± 0.038
14.1 MeV neutron	16.35	8.36 ± 0.42	0.245 ± 0.012

As mentioned earlier, incoherent scatter is a suspected contributor to pixel crosstalk, which degrades deposited energy localization and thereby worsens SR. Lower x-ray energies would thereby result in improved (i.e. lower) values of SR, which would increase calculated dSNRn values. Additionally, the smaller contribution from slightly increased SNR at lower x-ray energies, as shown in Table 11.1, would also contribute to larger dSNRn values at lower x-ray energies.

Despite the higher dSNRn value measured within the x-ray environment, the Ir-Bi-Plastic outperformed an EJ-200 array of similar thickness but smaller pixel pitch in the fast neutron environment. Specifically, an EJ-200 array with 2×2×19 mm pixels and an average pitch of 2.28 mm was evaluated using a similar methodology, including an identical Varex panel, phantom, generator, SDD, and exposure. The EJ-200 array produced a dSNRn value of only 0.0947 ± 0.005, which is less than half the dSNRn value calculated for the Ir-Bi-Plastic array. This measured performance disparity suggests arrays made from Ir-Bi-Plastic may also offer substantially improved performance in neutron, as well as x-ray, environments over low-Z plastics like EJ-200. Furthermore, this performance is assessed as due to the significantly larger SNR provided by the Ir-Bi-Plastic, which measured 16.35 versus the 2.26 measured for the EJ-200 array with smaller pixel pitch. Assuming all else is equal, SNR should scale as the square root of pixel area [60], suggesting a similarly sized array of EJ-200 would only provide a SNR of only 5.65. This dramatically increased signal from the novel material is believed to be a direct result of the iridium-complex, which enables radiative deexcitation of triplet molecular states populated from proton recoil events. In traditional plastics, such as EJ-200, these excited states typically relax via non-radiative means. Regardless, further experimental and computational evaluations are necessary to more equivalently determine the relative performance of the Ir-Bi-Plastic compared to more traditional plastics, such as EJ-200 and EJ-256.

Discussion and Conclusion

This research sought to experimentally characterize the performance of an array made from a novel Ir-Bi-Plastic within x-ray and fast neutron environments. The results suggest this array is more ideally suited to transmission radiography purposes within x-ray fields, and, due to its high-Z loading and the documented light yield of similar bismuth-loaded plastics [9], it will likely outperform comparable arrays made from more traditional plastics, such as EJ-200.

Additionally, the dSNRn measured from the array in the 14.1 MeV neutron environment is markedly greater than that measured from an EJ-200 array of similar thickness. Therefore, it is likely that, due to the presence of the iridium-complex, the Ir-Bi-Plastic will also outperform comparable arrays made from EJ-200 in fast neutron environments. These findings suggest the Ir-Bi-Plastic may offer significantly enhanced performance over EJ-200 as a material for DPI applications.

These quantified evaluations of detector response translate directly into shorter measurement times across both particle types and, therefore, less dose per measurement, which is optimal for portable radiography scenarios. Consequently, these results support further comparative study of the Ir-Bi-Plastic against other plastic alternatives, such as EJ-200. If the performance advantage of Ir-Bi-Plastic is as expected, it may prove an exceptional candidate material for DPI radiography applications supporting national nuclear safety, security, and safeguards.

Acknowledgement

The authors would like to thank the U.S. Army and the Department of Energy, including award DE-NA0003180, for supporting this research. The authors also thank Dr. Dan Shedlock and Varex Imaging for the use of a Varex Industrial PaxScan® 1515DXT-I flat panel detector.

CHAPTER TWELVE -
CONCLUSIONS AND RECOMMENDATIONS FOR FUTURE WORK

Conclusions

This research sought to measure the performance of BiPVT for DPI applications using only a small sample of the novel material. As such, the available material was cut and reassembled as a 4×3 pixelated array and paired with a TFT radiographic panel. However, to quantify the *relative* performance of BiPVT in both x-ray and fast neutron environments, two additional arrays were also manufactured from EJ-200 and EJ-256 to provide comparable measures of performance. Together these three arrays were assessed experimentally and computationally for performance in both x-ray and fast neutron environments. Due to the small sizes of the arrays, this was accomplished using multiple measurements of each array with varying degrees of shielding. The individual measurements were then assembled into composite images to facilitate additional analyses of performance. Simulations were conducted to provide a better understanding of the physical reasons behind the measurements of relative performance, and, in the case of the x-ray environment, these were used to predict the likely relative performance of a more ideally manufactured BiPVT array at various x-ray energies.

X-Ray Environment

In terms of calculated dSNRn, at 370 kVp the evaluated BiPVT array demonstrated equivalent performance compared to a similar array made from EJ-200, and it outperformed an equivalent EJ-256 array. However, without the sources of performance degradation detailed above, the BiPVT array would likely have provided statistically superior performance to the EJ-200 array, and this performance advantage would only be expected to improve at lower x-ray energies. For ideally manufactured BiPVT arrays, simulations indicate these performance improvements may be >5× that of EJ-200 at 150 kVp and 270 kVp, two other energies relevant for portable x-ray radiography [80]. These results support the use of BiPVT over other plastic alternatives, such as EJ-200 and EJ-256, for x-ray radiography. These results support the further investigation and quantification of relative BiPVT performance for x-ray radiography applications to support national safety, security, and safeguards.

Neutron Environment

In a 14.1 MeV neutron environment, the evaluated BiPVT array outperformed a similarly sized EJ-256 array in terms of dSNRn values. However, one comprised of EJ-200 outperformed both alternatives in the current study. It is assessed that a more ideally manufactured BiPVT array would undoubtable provide improved performance; however, it is unknown at this time whether that performance would match that of EJ-200 in fast neutron environments. Regardless, the demonstrated advantage of BiPVT over that of EJ-256 in 14.1 MeV environments suggests it represents a better material for fast neutron radiography purposes.

Improved DDA performance, in terms of SR and detector response, translates directly into shorter measurement times across both particle types and, therefore, less dose per measurement, which is optimal for portable DPI radiography scenarios. Consequently, the combined results from the included x-ray and neutron measurements and simulations support the consideration of BiPVT over other plastic alternatives, such as EJ-200 and EJ-256. The conclusions herein suggest BiPVT may likely provide better overall performance for DPI purposes than EJ-200, despite the comparative performances documented here.

Ir-Bi-Plastic Array Evaluation

This research sought to experimentally characterize the performance of a novel Ir-Bi-Plastic array within x-ray and fast neutron environments. The dSNRn results suggest the array is more ideally suited to transmission radiography purposes within x-ray fields, and, due to its high-Z loading and the documented light yield of similar Bi-loaded plastics [9], it is expected to outperform comparable arrays made from more traditional plastics, such as EJ-200. Additionally, the dSNRn measured from the array in the 14.1 MeV neutron environment is markedly greater than that measured from an array of similar thickness made from EJ-200. Therefore, it is likely that, due to the presence of the iridium-complex, the Ir-Bi-Plastic will also outperform comparable arrays made from EJ-200 in fast neutron environments. These findings suggest the Ir-Bi-Plastic may offer significantly enhanced performance as a material for DPI applications over other traditional plastics, such as EJ-200.

Recommendations for Future Work

The recommendations for future work regarding 21% bismuth-loaded plastics paired with iridium fluorophores apply equally to both the BiPVT and the newer, better manufactured 64-pixel Ir-Bi-Plastic array. As a material, the Ir-Bi-Plastic offers a higher LY than the BiPVT due to its pairing with FIracac, and it remains free of pixel clouding and other sources of optical light attenuation and scatter. As an array, it provides a greater total volume, larger pixels, and improved optical reflector compared to the evaluated BiPVT array, as well as offering a uniform

geometric structure and a smooth array face surface. Consequently, acquisition of a similarly constructed array made from BiPVT would support future comparative analysis in both x-ray and fast neutron environments.

Using these arrays, future work requiring limited preparation time and expense could include fabrication and testing of equivalent 64-pixel arrays made from EJ-200 and EJ-256. Evaluations of SR and dSNRn could be conducted at x-ray energies of 150, 270, and 370 kVp to provide directly comparable values for each material. It is expected these results would quantifiably demonstrate the superior performance of bismuth-loaded plastics over those of EJ-200 and EJ-256. Additionally, values of Z_{eff} for the Ir-Bi-Plastic are expected to likely follow those calculated herein for BiPVT. Therefore, future investigations could attempt to verify those predicted rates of PE absorption in BiPVT and/or Ir-Bi-Plastic by measuring light yield when exposed to mono-energetic photon sources, particularly at 20 and 100 keV.

For future neutron measurements, similar performance evaluations could be conducted in a 14.1 MeV neutron environment using equivalent BiPVT and Ir-Bi-Plastic, and EJ-200 arrays to decisively conclude relative performance. Future investigations using fast neutrons would benefit greatly, however, from a better understanding of the relationship between the energy deposited by incident fast neutrons and the light produced in the bismuth-loaded plastics. Since proton light yield varies non-linearly with respect to recoil energy (due to quenching effects in plastic scintillators), it becomes even more important to quantify this relationship for these novel materials. The presence of the iridium fluorophore in their organic matrices facilitates radiative deexcitation pathways for excited triplet state molecules, which suggests they will both offer significantly different proton energy-dependent light yields than traditional plastics, such as EJ-200. This relationship must be better understood to enable accurate modeling of both BiPVT and Ir-Bi-Plastic performance in fast neutron environments, which would greatly assist future efforts to optimize arrays made from either material for neutron transmission imagery purposes.

Lastly, work must also be completed on identifying the specific DPI missions and applications for which bismuth-loaded plastics may provide superior performance. Therefore, coordination must occur with U.S. government agencies to identify a specific test criteria and environment in which a BiPVT or Ir-Bi-Plastic array could be evaluated. These conditions would allow its measured performance to be compared against current x-ray and neutron imaging techniques and technologies. However, based upon any identified test criteria, any bismuth-loaded plastic array must first be optimized, in terms of pixel size, pitch, and array thickness, to provide the best possible performance in both environments.

WORKS CITED

[1] M. Licata, M. J. Joyce, I. Tsitsimpelis, D. Clark and B. A. Shippen, "The potential of real-time, fast neutron and γ radiography for the characterization of low-mass, solid-phase media," *Nuclear Instruments and Methods in Physics Research Section A: Accelerators, Spectrometers, Detectors and Associated Equipment,* Dec. 2018.

[2] M. Licata and M. J. Joyce, "Concealed nuclear material identification via combined fast-neutron/y-ray computed tomography (FNGCT): a Monte Carlo study," *J. Inst.,* vol. vol. 13, no. no. 2, p. pp. P02013–P02013, Feb. 2018.

[3] W. C. Chuirazzi, et al., "Evaluation of polyvinyl toluene scintillators for fast neutron imaging," *J Radioanal Nucl Chem,* vol. vol. 318, no. no. 1, p. pp. 543–551, Oct. 2018.

[4] J. Rahon, A. Danagoulian, T. D. MacDonald, Z. S. Hartwig and R. C. Lanza, "Spectroscopic neutron radiography for a cargo scanning system," *Nuclear Instruments and Methods in Physics Research Section A: Accelerators, Spectrometers, Detectors and Associated Equipment,* vol. vol. 820, p. pp. 141–145, Jun. 2016.

[5] C. C. Lawrence, M. Febbraro, M. Flaska, S. A. Pozzi and F. D. Becchetti, "Warhead verification as inverse problem: Applications of neutron spectrum unfolding from organic-scintillator measurements," *Journal of Applied Physics,* vol. vol. 120, no. no. 6, Aug. 2016.

[6] R. C. Runkle, T. A. White, E. A. Miller, J. A. Caggiano and B. A. Collins, "Photon and neutron interrogation techniques for chemical explosives detection in air cargo: A critical review," *Nuclear Instruments and Methods in Physics Research Section A: Accelerators, Spectrometers, Detectors and Associated Equipment,* vol. vol. 603, no. no. 3, p. pp. 510–528, May 2009.

[7] B. D. Sowerby and J. R. Tickner, "Recent advances in fast neutron radiography for cargo inspection," *Nuclear Instruments and Methods in Physics Research Section A: Accelerators, Spectrometers, Detectors and Associated Equipment,* vol. vol. 580, no. no. 1, p. pp. 510–528, May 2009.

[8] N. P. Zaitseva, et al., "Recent developments in plastic scintillators with pulse shape discrimination," *Nuclear Instruments and Methods in Physics Research Section A: Accelerators, Spectrometers, Detectors and Associated Equipment,* vol. vol. 889, p. pp. 97–104, May 2018.

[9] T. J. Hajagos, C. Liu, N. J. Cherepy and Q. Pei, "High-Z Sensitized Plastic Scintillators: A Review," *Advanced Materials,* vol. vol. 30, no. no. 27, p. p. 1706956, Jul. 2018.

[10] G. H. V. Bertrand, M. Hamel, S. Normand and F. Sguerra, "Pulse shape discrimination between (fast or thermal) neutrons and gamma rays with plastic scintillators: State of the art," *Nuclear Instruments and Methods in Physics Research Section A: Accelerators, Spectrometers, Detectors and Associated Equipment,* vol. vol. 776, p. pp. 114–128, Mar. 2015.

[11] P. Schuster and E. Brubaker, "Investigating the Anisotropic Scintillation Response in Anthracene through Neutron, Gamma-Ray, and Muon Measurements," *IEEE Transactions on Nuclear Science,* vol. vol. 63, no. no. 3, p. pp. 1942–1954, Jun. 2016.

[12] N. Zaitseva, et al., "Plastic scintillators with efficient neutron/gamma pulse shape discrimination," *Nuclear Instruments and Methods in Physics Research Section A: Accelerators, Spectrometers, Detectors and Associated Equipment,* vol. vol. 668, p. pp. 88–93, Mar. 2012.

[13] C. Dujardin, et al., "Needs, Trends, and Advances in Inorganic Scintillators," *IEEE Transactions on Nuclear Science,* vol. vol. 65, no. no. 8, p. pp. 1977–1997, Aug. 2018.

[14] U. Bravar, et al., "Design and Testing of a Position-Sensitive Plastic Scintillator Detector for Fast Neutron Imaging," *IEEE Transactions on Nuclear Science,* vol. vol. 53, no. no. 6, p. pp. 3894–3903, Dec. 2006.

[15] M. G. Paff, S. D. Clarke and S. A. Pozzi, "Organic liquid scintillation detector shape and volume impact on radiation portal monitors," *Nuclear Instruments and Methods in Physics Research Section A: Accelerators, Spectrometers, Detectors and Associated Equipment,* vol. vol. 825, p. pp. 31–39, Jul. 2016.

[16] M. G. Paff, M. L. Ruch, A. Poitrasson-Riviere, A. Sagadevan, S. D. Clarke and S. Pozzi, "Organic liquid scintillation detectors for on-the-fly neutron/gamma alarming and radionuclide identification in a pedestrian radiation portal monitor," *Nuclear Instruments and Methods in Physics Research Section A: Accelerators, Spectrometers, Detectors and Associated Equipment,* vol. vol. 789, p. pp. 16–27, Jul. 2015.

[17] N. J. Cherepy, et al., "Bismuth- and lithium-loaded plastic scintillators for gamma and neutron detection," *Nuclear Instruments and Methods in Physics Research Section A: Accelerators, Spectrometers, Detectors and Associated Equipment,* vol. vol. 778, p. pp. 126–132, Apr. 2015.

[18] W. M. Steinberger, M. L. Ruch, A. Di-Fulvio, S. D. Clarke and S. A. Pozzi, "Timing performance of organic scintillators coupled to silicon photomultipliers," *Nuclear Instruments and Methods in Physics Research Section A: Accelerators, Spectrometers, Detectors and Associated Equipment,* vol. vol. 922, p. pp. 185–192, Apr. 2019.

[19] V. Geppert-Kleinrath, et al., "liquid VI scintillator cell for fast-gated neutron imaging," *Review of Scientific Instruments,* vol. vol. 89, no. no. 10, p. p. 10I142, Oct. 2018..

[20] G. Knoll, Radiation Detection and Measurement, Hoboken, NJ USA: John Wiley & Sons, 2010.

[21] M. T. Andrews, C. R. Bates, E. A. McKigney, C. J. Solomon and A. Sood, "Organic scintillator detector response simulations with DRiFT," *Nuclear Instruments and Methods in Physics Research Section A: Accelerators,*

Spectrometers, Detectors and Associated Equipment, vol. vol. 830, p. pp. 466–472, Sep. 2016.

[22] A. Baitenov, A. Iakovlev and D. Beznosko, "Technical manual: a survey of scintillating medium for high-energy particle detection," *arXiv:1601.00086 [hep-ex, physics:physics],* Jan. 2016.

[23] C. S. Sosa, S. J. Thompson, D. L. Chichester, P. F. Schuster, S. D. Clarke and S. A. Pozzi, "Improved neutron–gamma discrimination at low-light output events using conical trans-stilbene," *Nuclear Instruments and Methods in Physics Research Section A: Accelerators, Spectrometers, Detectors and Associated Equipment,* vol. vol. 916, p. pp. 42–46, Feb. 2019.

[24] M. P. Taggart and P. J. Sellin, "Comparison of the pulse shape discrimination performance of plastic scintillators coupled to a SiPM," *Nuclear Instruments and Methods in Physics Research Section A: Accelerators, Spectrometers, Detectors and Associated Equipment,* vol. vol. 908, p. Nov. 2018, pp. 148–154.

[25] M. J. Joyce, et al., "Fast neutron tomography with real-time pulse-shape discrimination in organic scintillation detectors," *Nuclear Instruments and Methods in Physics Research Section A: Accelerators, Spectrometers, Detectors and Associated Equipment,* vol. vol. 834, p. pp. 36–45, Oct. 2016.

[26] R. Zboray, R. Adams and Z. Kis, "Scintillator screen development for fast neutron radiography and tomography and its application at the beamline of the 10 MW BNC research reactor," *Applied Radiation and Isotopes,* vol. vol. 140, p. pp. 215–223, Oct. 2018.

[27] R. Zboray, R. Adams and Z. Kis, "Fast neutron radiography and tomography at a 10MW research reactor beamline," *Applied Radiation and Isotopes,* vol. vol. 119, p. pp. 43–50, Jan. 2017.

[28] S. Sen, et al., "Organic–Inorganic Composite Films Based on Gd 3 Ga 3 Al 2 O 12 :Ce Scintillator Nanoparticles for X-ray Imaging Applications," *ACS Applied Materials & Interfaces,* vol. vol. 9, no. no. 42, p. pp. 37310–37320, Oct. 2017.

[29] M. J. Cieślak, K. A. A. Gamage and R. Glover, "Coded-aperture imaging systems: Past, present and future development – A review," *Radiation Measurements,* vol. vol. 92, p. pp. 59–71, Sep. 2016.

[30] J. Yorkston, "Recent developments in digital radiography detectors," *Nuclear Instruments and Methods in Physics Research Section A: Accelerators, Spectrometers, Detectors and Associated Equipment,* vol. vol. 580, no. no. 2, p. pp. 974–985, Oct. 2007.

[31] E. H. Lehmann, P. Vontobel, G. Frei and C. Brönnimann, "Neutron imaging—detector options and practical results," *Nuclear Instruments and Methods in Physics Research Section A: Accelerators, Spectrometers, Detectors and Associated Equipment,* vol. vol. 531, no. no. 1, p. pp. 228–237, Sep. 2004.

[32] R. Adams, R. Zboray and H. M. Prasser, "A novel fast-neutron tomography system based on a plastic scintillator array and a compact D–D neutron generator," *Applied Radiation and Isotopes,* vol. vol. 107, p. pp. 1–7, Jan. 2016.

[33] M. Grodzicka-Kobylka, et al., "Study of n-γ discrimination by zero-crossing method with SiPM based scintillation detectors," *Nuclear Instruments and Methods in Physics Research Section A: Accelerators, Spectrometers, Detectors and Associated Equipment,* vol. vol. 883, p. pp. 159–165, Mar. 2018.

[34] R. Lewandowski, L. Cao and a. D. Turkoglu, "Noise evaluation of a digital neutron imaging device," *Nuclear Instruments and Methods in Physics Research Section A: Accelerators, Spectrometers, Detectors and Associated Equipment,* vol. vol. 674, p. pp. 46–50, May 2012.

[35] A. Poitrasson-Rivière, M. C. Hamel, J. K. Polack, M. Flaska, S. D. Clarke and S. A. Pozzi, "Dual-particle imaging system based on simultaneous detection of photon and neutron collision events," *Nuclear Instruments and Methods in Physics Research Section A: Accelerators, Spectrometers, Detectors and Associated Equipment,* vol. vol. 760, p. pp. 40–45, Oct. 2014.

[36] Eljen Technologies, "EJ-200, EJ-204, EJ-208, EJ-212 Data Sheet," [Online]. Available: https://eljentechnology.com/products/plastic-scintillators/ej-200-ej-204-ej-208-ej-212.

[37] Eljen Technologies, "Lead-Loaded EJ-256 Data Sheet," [Online]. Available: https://eljentechnology.com/products/plastic-scintillators/ej-256.

[38] R. J. McConn, et al., "Compendium of Material Composition Data for Radiation Transport," PNNL, 2011.

[39] NIST, "NIST XCOM," 6 Jan 2021. [Online]. Available: https://physics.nist.gov/PhysRefData/Xcom/html/xcom1.html.

[40] "WebQC.org," 24 February 2021. [Online]. Available: https://www.webqc.org/molecular-weight-of-CH2CH%28C6H4CH3%29.html.

[41] V. B. N. Singh, "Effective Atomic Weight, Effective Atomic Numbers and Effective Electron Densities of Hydride and Borohydride Metals for Fusion Reactor Shielding," *Journal of Fusion Energy,* pp. 10.1007/s10894-014-9679-4., 2014.

[42] R. C. Murty, "Effective Atomic Numbers of Heterogenous Materials," *Nature,* vol. vol. 207, pp. pp. 398-399, 1965.

[43] S. R. Manohara, S. M. Hanagodimath, K. S. Thind and L. Gerward, "On the effective atomic number and electron density: A comprehensive set of formulas for all types of materials and energies above 1 keV," *Nuclear Instruments and Methodsin Physics Research,* vol. vol. 266, pp. pp. 3906-3912, 2008.

[44] M. L. Taylor, "Robust determination of effective atomic numbers for electron interactions with TLD-100 and TLD-100H thermoluminescent dosimeteres," *Nuclear Instruments and Methods in Physics Research,* vol. 269, pp. pp. 770-773, 2011.

[45] R. L. Weisfield, "Amorphous Silicon TFT X-Ray Image Sensors," in *Electron Devices Meeting, Conference Paper*, 1998.

[46] National Institute of Standards and Technology, "Proton stopping-power and range (PSTAR) tables," [Online]. Available: https://physics.nist.gov/PhysRefData/Star/Text/PSTAR.html. [Accessed 1 Feb 2020].

[47] R. Golden, "Pulsed X-ray Technology Truths and Myths," Golden, [Online]. Available: https://www.ndtma.org/wp-content/uploads/2014/02/Golden.pdf . [Accessed 26 August 2019].

[48] ASTM International, "ASTM E2002-15 Standard Practice for Determining Total Image Unsharpness and Basic Spatial Resolution in Radiography and Radioscopy," ASTM International, West Conshohocken, PA, 2015.

[49] ASTM International, "ASTM E747-18 Standard Practice for Design, Manufacture and Material Grouping Classification of Wire Image Quality Indicators (IQI) Used for Radiology," ASTM International, West Conshohocken, PA, 2018.

[50] S. R. Cherry, J. A. Sorenson and M. E. Phelps, Physics in Nuclear Medicine (Fourth Edition), W.B. Saunders, 2012.

[51] ASTM International, "ASTM E2597/E2597M-14 Standard Practice for Manufacuring Characterization of Digital Detector Arrays," ASTM International, West Conshohocken, 2014.

[52] Zemax LLC, "Zemax User's Guide, Getting Started with OpticStudio," Zemax, http://customers.zemax.com/ZMXLLC/media/PDFLibrary/Brochures/OpticStudio16_GettingStarted.pdf?ext=.pdf, 2018.

[53] ASTM International, "E2597-07 Standard Practice for Characterization of Digital Detector Arrays," ASTM International, West Conshohocken, PA, 2013.

[54] 3M Optical Systems, "Vikuiti (TM) Enhanced Specular Reflector Data Sheet," 3M Optical Systems, St. Paul, 2010.

[55] Dymax, "Dymax Optical Adhesives," Dymax Corporation, 2014.

[56] Varex Industrial, "Pax Scan 1515DXT-I Flat Panel Detector Data Sheet," [Online]. Available: https://www.vareximaging.com/products/flat-panel-detectors/1515dxt . [Accessed 01 September 2019].

[57] M. Maolinbay, Y. El-Mohri, L. E. Antonuk, K. W. Jee, S. Narif, X. Rong and Q. Zhao, "Additive noise properties of active flat-panel imagers," *Medical*

Physics, vol. 27, no. https://doi.org/10.1118/1.1286721, pp. 1841-1854, 2000.

[58] J. Tan, "4T CMOS Active Pixel Sensors under Ionizing Radiation," Ipskamp Drukker B.V, Dissertation, Shanghai, 2013.

[59] R. Hui, Introduction to Fiber-Optic Communications, London: Elsevier, 2020.

[60] ASTM International, "E2736-17 Standard Guide for Digital Detector Array Radiography," ASTM International, West Conshohocken, PA, 2017.

[61] M. J. Berger, et al., "Report 49," *Journal of the International Commission on Radiation Units and Measurements,* vol. 25, no. 2, 1993.

[62] J. E. Turner, Atoms, Radiation, and Radiation Protection, Weinheim: John Wiley & Sons, 2007.

[63] P. A. Tipler and G. Mosca, Physics for Scientists and Engineers, New York: W. H. Freeman and Company, 2008.

[64] ICRU, "Report 90," *Journal of the International Commission on Radiation Units and Measurements,* vol. 14, no. 1, 2016.

[65] National Institute of Standards and Technology, "Electron stopping-power and range (ESTAR) tables," NIST, [Online]. Available: https://physics.nist.gov/PhysRefData/Star/Text/ESTAR.html. [Accessed 01 September 2019].

[66] R. E. Pywell, et al., "Ligth output response of BC-505 liquid scintillator," *Nuclear Instruments and Methods in Physics Research,* pp. 725-730, 2006.

[67] ASTM International, "E1695-95 Standard Test Method for Measurement of Computed Tomography (CT) System Performance," ASTM International, West Conshohocken, PA, 2013.

[68] ASTM International, "E1441-19 Standard Guide for Computed Tomography(CT)," ASTM International, West Conshohocken, PA, 2019.

[69] P. Lasch and D. Nauman, "Spatial resolution in infrared microspectroscopic imaging of tissue," *Biochimica et Biophysica Acta,* no. 1758, pp. 814-829, 2006.

[70] ASTM International, "E1815-18 Standard Test Method for Classification of Film Systems for Industrial Radiography," ASTM International, West Conshohocken, PA, 2018.

[71] ASTM International, "E2737-10 Standard Practice for Digital Detector Array Performance Evaluations and Long Term Stability," ASTM International, West Conshohocken, 2015.

[72] M. Hawesworth and J. Walker, "Review: Radiography with Neutrons," *Journal of Material Science,* vol. 4, pp. 817-835, 1969.

[73] A. Swift, "The Design of a Fast Neutron Radiography System for Non-Destructive Analysis of Thick, Dense Objects," PhD diss, University of Tennessee, Knoxville, 2016, http://trace.tennessee.edu/utk_graddiss/3753.

[74] Center for Nondestructive Evaluation, "Physics of Nondestructive Evaluation: X-rays," Iowa State University, [Online]. Available: https://www.nde-ed.org/Physics/X-Ray/GeometricUnsharp.xhtml. [Accessed 28 February 2021].

[75] K. Pauwels, E. Auffray, S. Gundacker, A. Knapitsch and P. Lecoq, "Effect of aspect ratio on the light output of scintillators," *IEEE Transactions on Nuclear Science,* vol. 59, no. 5, pp. 2340-2345, 2012.

[76] F. Brooks, R. Pringle and B. L. Funt, "Pulse Shape Discrimination in a Plastic Scintillator," *IRE Transactions in Nuclear Science,* vol. 7, no. 2-3, pp. 35-38, 1960.

[77] A. D. Volpi, "High-Resolution Fast-Neutron and Gamma Digital Radiography," *IEEE Transactions in Nuclear Science,* vol. 23, no. 1, pp. 350-353, 1976.

[78] M. Balasko, E. Svab and G. Endrczy, "Comparison of Neutron Radiography with Other Nondestructive Methods," *IEEE Transactions in Nuclear Science,* vol. 52, no. 1, pp. 330-333, 2005.

[79] Shaw, T.J., et al., "Improvement in SNM Detection Performance by Fusion of Data from Multiple Inspection Systems," *IEEE Transactions in Nuclear Science,* vol. 56, no. 3, pp. 939-943, 2009.

[80] A. Decker, N. Cherepy, S. Hok and J. Hayward, "Simulated X-Ray Radiographic Performance Characterization of a Bismuth-Loaded PVT Array," *Transactions on Nuclear Science,* vol. 67, no. 11, pp. 2329-2336, 2020.

[81] A. Decker, C. Delzer, N. Cherepy, S. Hok and J. Hayward, "X-Ray Radiographic Characterization using a Bismuth-loaded Polyvinyl Toluene Array," *Accepted for publication in the Journal of Radiation Effects, Research and Engineering,* vol. 39, no. 1, pp. 11-21, 2021.

[82] M. Hamel, et al., "A Fluorocarbon Plastic Scintillator for Heutron Detection: Proof of Concept," *Nuclear Instruments and Methods in Physics Research,* vol. A, no. 768, pp. 26-31, 2014.

[83] A.H. Tkaczyk, et al., "Characterization of EJ-200 Plastic Scintillators as Active Background Shield for Cosmogenic Radiation," *Nuclear Instruments and Methods in Physics Research,* vol. A, no. 882, pp. 96-104, 2018.

[84] T.A. LaPlace, et al., "Low Energy Light Yield of Fast Plastic Scintillators," *Nuclear Instruments and Methods in Physics Research,* vol. A, no. 954, 2020.

[85] White Optics, "White 98 Film Data Sheet," WhiteOptics, Conyers, GA, 2020.

VITA

Andrew W. Decker graduated from the United States Military Academy at West Point, NY in 2002, commissioned as a Military Intelligence (MI) Officer, and was initially assigned to Ft. Wainwright, AK. There he served as a platoon leader, company executive officer, and squadron intelligence officer for the 172nd Stryker Brigade Combat Team (172nd SBCT). In 2005, he deployed with the 172nd SBCT to support Operation Iraqi Freedom as the reconnaissance and target acquisition squadron intelligence officer. Following redeployment, he was assigned to the US Army Intelligence Center at Ft. Huachuca, AZ, where he served on the Commanding General's staff before completing the MI Captain's Career Course. Afterwards he deployed again in 2009 to Iraq as an intelligence advisor to the 9th Iraqi Army (Mech). During this time, he was assessed into the US Army's Nuclear and Counterproliferation Branch (FA52). After redeployment and a brief assignment as a staff intelligence officer with I Corps at Ft. Lewis, WA, Andrew was assigned to the Air Force Institute of Technology to earn a MS in Nuclear Engineering. His thesis research initiated a DTRA effort to verify and validate computational estimates for modern military vehicle radiation protection factors (RPFs). From 2014-18, he served as Deputy Director of the DTRA Nuclear Science and Engineering Research Center at West Point, NY, where he also led and advanced DTRA RPF research. Andrew is married to the former Ms. Jill Graff, and, on 02 June 2021, they will celebrate their 19th wedding anniversary. Andrew and Jill are both originally from Port Angeles, WA, and they have two daughters, Ashlyn (16) and Siena (12).